UNIVERSITAT POLITÈCNICA DE VALÈNCIA

UNIVERSITAT POLITÈCNICA DE VALÈNCIA

Design and Optimisation of a Virtual Prototype of a Ground Transportation System at Very High-Speeds in Conditions Close to Vacuum

PhD Thesis

Author: Federico Lluesma Rodríguez
Thesis director: Dr Sergio Hoyas Calvo
Thesis director (company): Dr Manuel Zaera Sanz

September 2022

Contents

List of Figures

List of Tables

Acknowledgements

This thesis is the result of four years of hard work, sacrifice and frustration. The road to a PhD is difficult, but it is known that, without effort, good results are not reached. The conclusion of this period is one of the most satisfactory achievements in my life, or even the best.

I want to acknowledge my thesis director at the university, Sergio Hoyas. I have worked with him for seven years since I started my BSc thesis in 2015. Not only is he one of the best researchers I have ever met, but he is also an incredible person who always thinks about others.

Special mention to my Zeleros' supervisors, Iván Temoatzin González during the first three years and Manuel Zaera during the last. I also want to thank all the colleagues from Zeleros. They have largely helped during the elaboration of this work.

I started researching the hyperloop in 2016, when I entered the university team Hyperloop UPV before Zeleros was founded. That decision absolutely changed my life. Ángel Benedicto, Daniel Orient, David Pistoni, Germán Torres and Juan Vicén, along with professor Vicente Dolz, were the creators of the hyperloop adventure in Valencia. I cannot be grateful enough to them as my studies and career have been focused on the hyperloop for more than six years.

Finally, I want to remark on the importance of my family and friends. Surely, I would not be here without them. They have supported me in the good and, especially, in the bad moments. Their help has been priceless, not only during the thesis period, but also during my entire life.

This work is partially funded by Ministerio de Ciencia, Innovación y Universidades under the grant "Doctorandos Industriales" number DI-17-09616.

Esta tesis es el resultado del duro trabajo, sacrificio y frustración durante cuatro años. El camino del doctorando es difícil, pero es sabido que sin esfuerzo no se consiguen resultados. La conclusión de este periodo es uno de los logros más satisfactorios en mi vida, o incluso el mejor.

Quiero reconocer a mi director de tesis en la universidad, Sergio Hoyas. He trabajo con él durante siete años, desde que comencé mi Trabajo Fin de Grado en 2015. No solamente es uno de los mejores investigadores que he conocido, si no que es también una persona increíble que siempre piensa en los demás.

También quiero realizar una mención especial a mis supervisores de Zeleros, Iván Temoatzin González durante los tres primeros años y Manuel Zaera durante el último. Quiero también agradecer a los compañeros de Zeleros. Han sido de una ayuda inestimable durante la elaboración del presente trabajo.

Comencé mi investigación sobre el hyperloop en 2016, cuanto entré en el equipo universitario Hyperloop UPV antes que Zeleros fuera fundada. Ángel Benedicto, Daniel Orient, David Pistoni, Germán Torres y Juan Vicén, junto con el profesor Vicente Dolz, fueron los creadores de esta aventura en Valencia. No les puedo agradecer lo suficiente, ya que mis estudios y carrera has estado centradas en el hyperloop durante más de seis años.

Finalmente, quiero remarcar la importancia de mi familia y amigos. Sin duda, no

estaría aquí si no fuera por ellos. Me han apoyado en los buenos y, especialmente, en los malos momentos. Su ayuda no tiene precio, no solamente durante el periodo de mi tesis, si no durante toda mi vida.

Este trabajo es fundado parcialmente por el Ministerio de Ciencia, Innovación y Universidades bajo la ayuda "Doctorandos Industriales" número DI-17-09616.

Resumen

Hyperloop es considerado el quinto medio de transporte, después del coche, barco, tren y avión. Consiste en una capsula de levitación magnética que viaja dentro de un tubo en el que la presión de aire ha sido reducida. Entonces, la fricción con el suelo y resistencia aerodinámica son minimizadas, alcanzando ultra altas velocidades a nivel de tierra.

Actualmente hay en desarrollo varios trenes maglev y conceptos hyperloop. La mayoría proponen levitar usando Suspensión Electromagnética (EMS). Zeleros, la compañía donde esta Tesis ha sido realizada, tiene una propuesta similar. Zeleros usa un EMS Híbrido (HEMS), combinando imanes y electroimanes para reducir los requerimientos de energía. Respecto a la propulsión, la propuesta es única ya que hace uso de un compresor de la industria aeroespacial. Simulaciones CFD prueban que usar un compresor reduce considerablemente la resistencia aerodinámica en el ambiente cerrado, ya que el efecto pistón es mitigado. Para el mismo tamaño de tubo y presión, un hyperloop con compresor requiere hasta 70 % menos potencia. En otros términos, si la misma potencia es instalada en el vehículo, el diámetro de la infraestructura puede ser 2.8 veces más pequeño.

Esta Tesis desarrolla un simulador 0D para evaluar el rendimiento de la solución hyperloop propuesta. Resolver su aerodinámica requiere solucionar un fujo interno y externo de Fanno. El último combina efectos de Couette y Poiseuille en un dominio anular. Así, se desarrolla un modelo simplificado para flujos de Fanno, acelerando así el modelado básico. Esta aproximación matemática incluye información de la velocidad de la pared y de la forma del dominio, evitando integrar un sistema de EDOs. La solución tiene una desviación en la ratio de presiones de 5 % respecto a CFD, y del 10 % en la longitud crítica.

El simulador modela toda la termodinámica del vehículo, incluyendo el compresor, conductos, turbina, tobera y flujo externo. Este modelado es similar al del ciclo de Bryton, sin cámara de combustión. Además, se incluye un modelo para predecir la masa y longitud de la cápsula y sus componentes. Así, las pérdidas de fricción y requerimientos de potencia y energía son obtenidos. Estos resultados presentan una desviación máxima del 20 % respecto a CFD.

Además, un proceso de optimización para encontrar la solución más eficiente se ha desarrollado con el código, para vehículos de 50 y 150 pasajeros. Se ha encontrado que es más beneficioso absorber menos gasto másico con el compresor, ya que la energía requerida para comprimir el flujo interno es más alta que las pérdidas en el canal externo. Comparando el consumo de energía específico de esta solución con otros medios de transporte, el hyperloop se encuentra cercano al rendimiento de los maglev. Éste es, también, entre tres y cinco veces más eficiente que los aviones. Además, es más competitivo que el avión en términos de velocidad media en una ruta hasta los 800 km.

Por último, se desarrolla un modelo similar para un sistema de escala media. Este prototipo, cuya velocidad objetivo es de 500 km/h, es diseñado por Zeleros previo al sistema de escala real. Su simulador incluye además los efectos transitorios y la termodinámica del tubo, asumiendo una velocidad del sonido infinita. Gracias a este código, se puede obtener el rendimiento en una misión. Inicialmente, el prototipo incrementa la presión del tubo aguas arriba, y la reduce aguas abajo debido al efecto pistón, generando una velocidad inducida. Al final de la misión, el flujo puede ser transferido otra vez, y las presiones se equilibran otra vez. Este modelo también predice el par y potencia del motor eléctrico, además de los parámetros de la batería (voltaje, corriente y profundidad de descarga).

Resum

Hyperloop és considerat el cinquè mitjà de transport, després del cotxe, vaixell, tren i avió. Consisteix en una càpsula de levitació magnètica que viatja dins d'un tub on la pressió d'aire es reduïda. Aleshores, la fricció amb el sòl i resistència aerodinàmica són minimitzades, aconseguint ultra altes velocitats a nivell de terra.

Actualment hi ha en desenvolupament diversos trens maglev i conceptes hyperloop. La majoria proposen levitar usant Suspensió Electromagnètica (EMS). Zeleros, la companyia on aquesta Tesi ha sigut realitzada, té una proposta similar. En particular, el concepte de Zeleros utilitza un EMS Híbrid (HEMS), combinant imants i electroimants per reduir els requeriments d'energia. Pel que fa a la propulsió, la proposta és única, ja que fa ús d'un compressor de la indústria aeroespacial. Simulacions CFD proven que utilitzar un compressor redueix considerablement la resistència aerodinàmica en un ambient tancat, ja que l'efecte pistó és mitigat. Per a la mateixa grandària de tub i pressió, un hyperloop amb compressor requereix fins a 70 % menys potència. En altres termes, si la mateixa potència és instal·lada al vehicle, el diàmetre de la infraestructura pot ser 2.8 vegades més menut.

Aquesta Tesi desenvolupa un simulador 0D per avaluar el rendiment de la solució hyperloop proposada. Resoldre l'aerodinàmica del hyperloop requereix solucionar un flux intern i extern de Fanno. L'últim combina efectes de Couette i Poiseuille en un domini anular. Així, es desenvolupa un model simplificat per a fluxos de Fanno, accelerant així el modelatge bàsic. Aquesta aproximació matemàtica inclou informació de la velocitat de la paret i de la forma del domini, evitant integrar un sistema de EDOs. La solució té una desviació a la ràtio de pressions de 5 % respecte a CFD, i del 10 % a la longitud crítica.

El simulador modela tota la termodinàmica del vehicle, incloent-hi el compressor, conductes, turbina, tovera i flux extern. Aquest modelat es similar al del cicle de Bryton, sense càmera de combustió. A més, s'inclou un model per predir la massa i la longitud de la càpsula i els seus components. Així, les pèrdues de fricció i requeriments de potència i energia són obtinguts. Aquests resultats presenten una desviació màxima del 20 % comparat amb CFD.

A més, un procés d'optimització per trobar la solució més eficient ha estat desenvolupat amb el codi, per a vehicles de 50 i 150 passatgers. S'ha trobat que és més beneficiós absorbir menys massa amb el compressor, ja que l'energia requerida per comprimir el flux intern és més alta que les pèrdues al canal extern. Comparant el consum d'energia específic d'aquesta solució amb altres mitjans de transport, el hyperloop és proper al rendiment dels maglev. Aquest també és entre tres i cinc vegades més eficient que els avions. A més, és més competitiu en termes de velocitat mitjana en una ruta fins a 800 km.

Finalment, es desenvolupa un model semblant per a un sistema d'escala mitjana. Aquest prototip, la velocitat objectiu del qual és de 500 km/h, és dissenyat per Zeleros previ al sistema d'escala real. El seu simulador inclou a més els efectes transitoris i la termodinàmica del tub, assumint una velocitat del so infinita. Gràcies a aquest codi, es pot obtenir el rendiment en una missió. Inicialment, el prototip incrementa la pressió del tub aigües amunt, i la redueix aigües avall degut a l'efecte pistó, generant una velocitat induïda. Al final de la missió, el flux pot ser transferit una altra vegada, i les pressions s'equilibren una altra vegada. Aquest model també prediu el parell i potència del motor elèctric, a més dels paràmetres de la bateria (voltatge, corrent i profunditat de descàrrega).

Abstract

Hyperloop is considered the fifth means of transportation, after the car, boat, train and plane. It consists of a magnetically levitating capsule that travels within a tube in which the air pressure has been reduced. Thus, the ground friction and aerodynamic drag are minimised, reaching ultra high-speeds at ground level.

Several maglev trains and hyperloop concepts being developed currently. Most of them propose levitating using Electromagnetic Suspension (EMS). Zeleros, the company where this Thesis was done, has a similar approach. It employs a Hybrid EMS (HEMS)In particular, the Zeleros approach employs a Hybrid EMS (HEMS), combining permanent and electromagnets to reduce energy requirements. As for the propulsion, the approach is unique as it uses a compressor from the aeronautical industry. CFD simulations prove that using a compressor considerably reduces the aerodynamic drag in the closed environment, as the piston effect gets mitigated. For the same tube size and pressure, a hyperloop with compressor requires up to 70 % less power. In other terms, if the same power is installed on the vehicle, the infrastructure diameter can be 2.8 times smaller.

This Thesis develops a 0D simulator to evaluate the performance of the proposed hyperloop solution. Solving the aerodynamics of the hyperloop requires solving internal and external Fanno flows. For the latter, the flow combines Couette and Poiseuille effects in an annular domain. Thus, a simplified model for Fanno flows is developed to accelerate the basic modelling. This mathematical approach includes the information of the wall speed and the shape of the domain, avoiding integrating an ODE system. The solution has a deviation in the pressure ratio of 5 % and 10 % in the critical length regarding CFD.

The simulator models all the vehicle thermodynamics, including the compressor, duct, turbine, nozzle, and external flow. This modelling is similar to a Bryton cycle, without a combustion chamber. Also, a model to predict the mass and length of the capsule and its components is included. Thus, the friction losses and the energy and power requirements can be extracted. These outputs are compared with CFD results, with a maximum deviation of 20 %.

Moreover, an optimisation process is conducted with the code to find the most efficient solution for 50- and 150-passenger vehicles. It is found that shallowing less mass flow with the compressor is better, as the energy required to compress the internal flow is higher than the losses on the external channel. Comparing the specific energy consumption of this solution with other means of transportation, the hyperloop is close to the maglev performance. It is also between three and five times more efficient than aeroplanes. Furthermore, the hyperloop is more competitive than the plane in terms of average speed on a route, up to 800 km.

The last part of this work develops a similar model for a middle-scale system. This prototype, which aims to reach 500 km/h, is being designed by Zeleros before the real-scale one. Its simulator also includes the transient effects and the tube thermodynamics, assuming an infinite sound speed. Thanks to this code, the performance in a mission is obtained. The prototype initially increases the upstream tube pressure and reduces the downstream one due to the piston effect, generating an induced speed. At the end of the mission, the flow can be transferred again, and the pressures equilibrate again. This model also predicts the electric motor torque and power and the battery parameters (voltage, current, and deep of discharge).

Abbreviations

CFD	Computational Fluid Dynamics
BR	Blockage Ratio
HL	Hyperloop
ETT	Evacuated Tube Transport
HSR	High-Speed Rail
UHSR	Ultra High-Speed Rail
LIM	Linear Induction Motor
LSM	Linear Synchronous Motor
LSRM	Linear Switched Reluctance Motor
EDS	Electrodynamic Suspension
EMS	Electromagnetic Suspension
HEMS	Hybrid Electromagnetic Suspension
HTS	High Temperature Superconductor
HPC	Hyperloop Pod Competition
EHW	European Hyperloop Week
dof	Degree of freedom
maglev	Magnetic Levitating (train)

Chapter 1

Introduction

Humans have had the necessity of travelling since they were known as *homo sapiens* 300,000 years ago. Although the first settlements were fixed, humans became nomads again relatively soon after. Two thousand years ago, Greeks and Romans had already created roads for people to move from one place to another. In fact, nowadays many European highways are built over ancient roads.

In our current society, the displacement necessities are still growing. Modern large-scale and fast means of transportation, i. e. aeroplanes and High-Speed Rail (HSR), are not enough in our fast-moving non-conformist society. Air traffic may increase up to 76 % from 2022 to 2050, according to EUROCONTROL [1], which will mean the saturation of the air space and an impossible increase in the fuel demand. However, if one looks at the railway as the transport replacement for aeroplanes, several problems arise. The maximum commercial train speed is around 300 km/h, a third of the one from the aeroplanes [2]. The use of Ultra High-Speed Railway (UHSR) seems not to be the solution as the current HSR faces several problems when trying to increase the commercial speed: maintenance cost due to the wear of the rail, wheels, and catenary-pantograph; instabilities of the rail-wheel system; and power transfer from the catenary to the train [3].

For these reasons mentioned above, it is necessary to develop a new concept that could fit the current necessities, also considering the decarbonisation of transport as a major goal of technology development. Here is where a new high-speed transportation system comes into play. In particular, this thesis studies an ultra-high-speed ground transportation system in conditions close to vacuum. Since the release of the Hyperloop Alpha by Elon Musk in 2013 [4], this system is commonly known as *hyperloop*. The development in recent years has proved that this new technology can be the solution to the transport problems modern society is facing. This step forward to industry 4.0 requires changing how travels are conceived again, as happened more than a century ago with the railway and the air services.

Hyperloop was born as a modern system that can move people or goods at ultra high-speeds connecting cities like a metro connecting points within an urban area (see figure 1.1). The hyperloop speed is closer to the one of the plane, with the frequency of the rail system.

Despite the name given by Elon Musk to this system, hyperloop cannot be considered

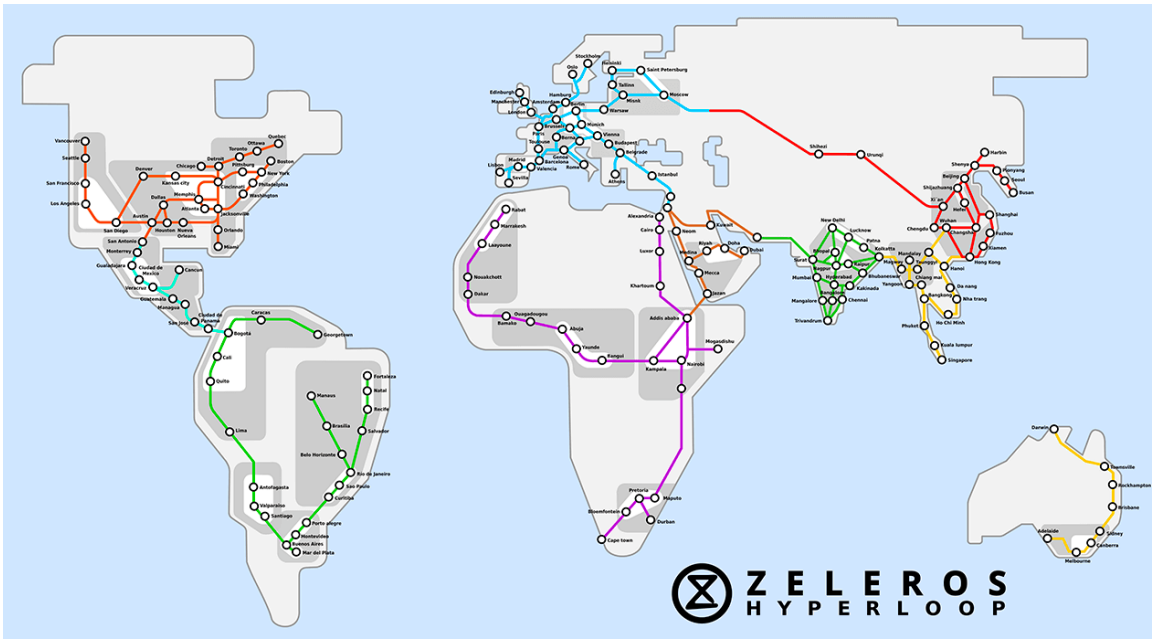

Figure 1.1: Analogy between a metro network and a global hyperloop network. Source: elaborated by Zeleros.

an invention of the XXI century. Developments of primitive hyperloop concepts were done during previous centuries, XIX and XX, naming this system as *Vactrain*, *Evacuated Tube Transport* (ETT) or *Atmospheric Railway*.

In spite of its aeronautical background, hyperloop can be considered a magnetic levitation train travelling inside a tube in which part of the air has been removed to reduce the pressure and thus the drag. This is why this chapter presents a brief historical reminder of how and when the trains were invented. Furthermore, it is stated when the magnetic levitation was invented and when low-pressure conditions were considered for this system.

Currently, hyperloop is being researched by several private companies and public institutions. In particular, the solution described in this thesis is the one proposed by the Spanish hyperloop company *Zeleros*, to which this industrial PhD belongs to. *Zeleros* aims to develop a feasible commercial solution for hyperloop transport, including magnetic levitation and aerodynamic propulsion in the vehicle. This PhD is focused on describing the hyperloop simulator developed for the company.

1.1 Objectives

First, the thesis aims to conduct a literature review to know which hyperloop technologies have been applied in other means of transportation. Moreover, a research is conducted about other hyperloop-alike projects studied in the past or being developed, highlighting the technical solutions they propose. If any information is published from these projects, their dynamics models will also be referenced.

Before presenting the main objectives of the project, an analysis of the solution proposed by *Zeleros*, focusing on why it is a better approach for tube transportation, will be made. In particular, the strengths in using aerodynamic propulsion with respect to closed vehicles using other propulsion systems will be analysed.

Then, a mathematical model of the *Zeleros* concept is being elaborated. The goal is to have a model which predicts the behaviour of the *Zeleros* concept under different boundary conditions: speed, route distance, temperature, number of passengers... The model will simulate only one instant in a mission, being as generic as possible.

Once the model is made, another goal will be to optimise several parameters using an optimisation algorithm, as the model has more degrees of freedom than restrictions. The problem can be closed by searching for the optimum of a specific parameter (typically the consumed energy or the installed power).

This simulator will be useful for comparing the behaviour of the analysed model with other hyperloop concepts or even other means of transportation. It will allow to also compute a reference vehicle in terms of mass, length, energy consumption, battery size...

With the conclusions learnt from the first model, another model is elaborated using the requirements of the middle-scale prototype developed by *Zeleros*. In this case, a point is insufficient, but the entire mission must be simulated, as the track is fully defined. More subsystem models are included as they have already been designed, and their mathematical behaviour is known. In this case, the optimisation process is not as relevant as the vehicle is already defined. The model will allow knowing the performance of the chosen integrated design.

With this simulator, the curves of the prototype in a generic mission will be computed. The speed and acceleration profiles, energy consumed, tube pressure, tube temperature and several other parameters will be analysed for the mission.

Finally, the lessons learnt from modelling this type of technology will be stated. The improvements in the models and their further application will also be described.

1.2 Before the locomotive

The first approximation to using something to guide vehicles is considered to have been developed in Greece more than 2600 years ago [5]. Then, our ancestors developed what can be considered the first sights of the railway idea. They thought that creating a pair of furrows on the path (separated 1.5 meters) helped their wheel vehicles (such as the Diolkos, seen in figure 1.2) circulate with less effort and more organised. Curiously, the width of the track was similar to the modern ones.

In the XVI century, something similar to rails started to be extended due to the necessities of the mining industry. They were wooden-made and were used to convey materials inside the mines. Again, they noticed that using a guidance system for the carts was better than conducting them on the uneven floor. More advanced developments were conducted in the following century to achieve the first railways working within the mines in England in 1650 (page 1 of [6]). There is an indication that in 1676 the developments in England made it possible to have straight and parallel tracks due to the addition of cross timbers, similar to the current ones. These small carriages to transport minerals were still of small

Figure 1.2: Diolkos canal from Greece, dated VII century b.C. Reference: `https://www.cienciahistorica.com/2017/03/22/petrocarril-la-antigua-grecia/`.

width.

However, it was not until 1760 that the rail, as it nowadays is known, was born (page 1 of [6]), with the same track width as the current one. An iron surface was added to the wood to reduce its wear. Starting from that point, the concept of rail evolved, and soon (in 1767), all the track was made of cast iron, introduced by Coal-brookdale Iron Company. The wrought-iron rail was first used in 1805 in Newcastle, although it had little consideration until 1820.

Once the society of that age noted that using a rail to guide the carriage was an improvement, their next step was to substitute human or animal force in favour of machines, giving birth to the first locomotives.

1.3 Origins of the locomotive

The first idea of the locomotive was suggested by James Watt in 1759 [6]. His idea was to use a steam engine to propel wheeled carriages, which was patented in 1784. Watt proposed using the steam machine by condensation for this purpose instead of high-pressure steam because he was concerned about the hazards of the pressure. However, in 1784 his assistant, William Murdoch, constructed a small prototype of a steam carriage using a non-condensing steam engine. Afterwards, in 1802 Richard Treventhick patented the application of the non-condensing high-pressure machine based only on steam expansion force to propel railroads. First, he applied the steam engine to carriages on normal roads. However, after experimenting in several places (chapter 3 of [7]), he confined his invention to a railway.

In 1804 Treventhick patented a second engine, and so, during the following years, many patents and new inventors improved the engine model.

Not only was the machinery enhanced, but also engineers started to consider the contact with the rail, which in the first prototypes was very poor. To avoid slipping at those early stages, Blinkinsop added a rack to the side of the rail with his patent in 1811 [7]. However, this idea was discarded soon after, leading to more advanced solutions.

The concept of the boogie was first presented by the Chapman brothers in their patent in 1812. However, it was not until 1825 that a company, Wyliam Railway, employed this concept on their machine.

Then, people started to consider that the idea of the locomotive was practical enough not only to convey minerals but to create a commercial service to transport goods and people from one place to another [5].

In 1825, the first railway line in the world was inaugurated, which connected Stockton and Darlington. It has 20 kilometres and still used horses sometimes. However, in 1830, the 50 kilometres line from Liverpool to Manchester (see figure 1.3) completely suppressed animal power use. This second line used improved locomotives, more powerful and lighter than the previous one, and was considered high speed (24 km/h) at that time.

Figure 1.3: Liverpool to Manchester coach. Reference: `https://commons.wikimedia.org/wiki/File:Liverpool_and_Manchester_Railway_coach.jpg`, retrieved on 02-10-2020. Author: G-13114. This file is licensed under the Creative Commons Attribution-Share Alike 4.0 International.

After its successful implementation in England, the locomotives were sent to France in 1829. Consequently, the railway was extended throughout Europe and the rest of the world in a few years.

This expansion was an essential improvement in people and goods transport, but it also led to the use of the same time across Europe. Until then, each city had its own time, and the travels between them were so slow that no necessity to unify the hour was required. However, since the invention of the locomotive, higher speeds could be achieved. The time invested in travelling decreased significantly, and the first coordinated time was created.

1.4 Origins of the electric locomotives

The steam locomotive was not a unique consideration for the first trains [8]. In 1838, the Scottish inventor Robert Davidson [9] developed the first electric locomotive, a coach equipped with batteries that powered the wheels up to 6.4 km/h.

Davidson made an electric locomotive model in 1837, named *Galvani*. His idea was based on the recent invention from Faraday in 1837: the electric motor. The battery technology used was zinc-acid. In 1842 the four-wheel locomotive was successfully tested on the Edinburgh-Glasgow line up to 6.4 km/h without any payload. However, battery technology at that time was in an early development stage. They were too expensive and had to be replaced each discharge, as the lead-acid accumulator was not invented until the 1850s. His invention was too early, and no companies showed interest in continuing this path.

It was not until the 1880s decade that the electric locomotives started to grow. In 1879, the first electric train was built in Berlin thanks to the inventor Werner von Siemens. It was 300 m long and reached 13 km/h with 2.2 kW provided by a third rail, not having batteries on board. Two years later, in 1881, thanks also to Siemens, the first electric tram line was opened in Lichterfelde, near Berlin. It already used a catenary, removing the third rail. In 1883 it was released in Brighton (UK), and then it was expanded throughout the world.

At that time, one problem arose with the growth of steam locomotives: the smoke they generated, especially crossing tunnels in urban areas. A initiative was to convert from steam to electric ones and making it underground, leading to the first line of the London Tube in 1890. It used electric machines built by Mather and Pratt. This phenomenon also increased the growth of electrification, particularly for underground trains.

In 1894, the Hungarian engineer Kálmán Kandó developed AC three-phase high voltage motors for electric locomotives. He also developed new transformers that allowed the trains to be fed directly from the public electric network. Thanks to the same engineer, the first complete electric line opened was a 106 km line (Valtellina line) in Italy in 1902. On the whole, Europe expanded at first the electrification of the mountainous regions due to the uneasy supply of coal.

In the US, the first electrification was conducted on a 10 km segment between Baltimore and Ohio in 1895. The project was stopped after a crash; however, New York started to operate electric locomotives in 1904.

Electric trains were proven to be the solution for rail transport in the following years.

However, due to the Second World War, the development of combustion engines for military vehicles promoted the slight application of this technology to locomotives during the XX century [10]. By the end of the century, the use of fossil fuels applied to trains had expanded, although nowadays it is known that it is not the future of rail transport.

1.5 Origins of Evacuated Tube Transport

The history of Evacuated Tube Transport (ETT) began over 200 years ago, parallel to the steam locomotives. In 1799, the English inventor George Medhurst ([7] chapter 2) first proposed moving passenger carriages through a tunnel using variations in pressure levels. The system was called "Atmospheric Railway". Some people were aware of the potential of the ETT as a future means of transportation, as shown in the satiric drawing from 1828 represented in figure 1.4.

Figure 1.4: March of Intellect, 1828 (est.). Creator: William Heath. `https://www.bl.uk/romantics-and-victorians/articles/inventing-the-future`. Reproduced under a Creative Commons Attribution-NonCommercial-ShareAlike 4.0 International (CC BY-NC-SA 4.0) licence. © The Trustees of the British Museum.

Medhurst did several developments between his first patent in 1799 and his death in 1827:

- 1799. Medhurst was granted the first patent for good transport through tubes. He defined his invention as "a condensing wind-engine, capable of being applied to all kinds of purposes, in which steam, water, wind, or horses are employed."[1].
- 1800. Medhurst patented the Aeolian engine, by which a carriage could be propelled by compressed air contained in a reservoir beneath the vehicle. He also described an engine powered by gas produced by exploding small quantities of gunpowder at defined intervals in the cylinder.
- 1805. Medhurst made another publication of the Aeolian Engine [11].
- 1810. In this document, Medhurst described an iron tube six feet high and five feet wide that included rails to conduct four-wheel carriages transporting goods thanks to an overpressure behind them [12], without a driver.
- 1812. Medhurst refined his previous design for larger carriages [13].
- 1827. Medhurst included in his design not only the overpressure downstream but the pressure reduction upstream to increase the efficiency of the system. However, he did not consider compressibility effects or the aerodynamic resistance [14].

After Medhurst ([7] chap 2), Lemuel Wright obtained a patent in 1828 for applying compressed air to power machinery, while Mann was granted another patent in 1829 for the application of compressed air to the motive power of carriages.

1.5.1 Atmospheric railway

The first implementation of the concept of using compressed air to move carriages was called *atmospheric railway*. It consisted of a pipe in the ground, instead of covering the whole train inside a tunnel, in which pressure differences on the pipe propelled a piston. This piston is externally attached to the carriage, transmitting the movement. However, these ideas were not put into practice by Medhurst.

Henry Pinkus launched a project for the National Pneumatic Railway Association in 1835 [15], and in 1837 experimented unsuccessfully with a line alongside the Kensington Canal with a small vacuum tube. One year later, Samuel Clegg [15] was also unsuccessful in producing a commercial system. In 1839 the Samuda Brothers conducted two experiments based on the atmospheric railway from Clegg and patented their concept.

The first successful test was reported in 1844 in Ireland [16] (see figure 1.6). That line ended up being the first commercial application [15] of this system, in 1848, between Kingstown and Dalkey. The pressure of this line had to be provided by a huge (for that year) stationary steam engine (110 HP) placed at Dalkey [17]. It was closed down in 1854.

In France [18], a concession to the Pereire brothers resulted in a 19 km line opened in 1837 using a steam locomotive, which tried to connect Paris with Saint Germain. However, due to climbing problems, it could not reach Saint German. In 1847 it was opened a 1.5 km extension of the line, powered by a piston as the concept of atmospheric railway, reached its

[1] `https://www.gracesguide.co.uk/George_Medhurst#cite_note-1`

final destination. There was a cylinder of 63 cm in diameter. Two stem engines provided 200 HP to the pumps, enforcing up to 35 km/h during the ascent. It was abandoned in 1860 due to more powerful locomotives.

By his part, in 1846 in England [15], Isambard Kingdom Brunel developed an extension of the 83 km line between Forest Hill and West Croydon on the London and Croydon Railway, although it was soon discontinued.

After its unsuccessful first line, Brunel built in 1847 another extension of the South Devon Railway between Exeter and Plymouth (see figure 1.5). The section from Exeter to Newton [15] was completed using stationary engines every 3.2 km instead of a huge engine at the beginning. The trains ran at approximately 32 km/h using fifteen pipes for the flat sections and twenty-two for the steeper gradients west of Newton. In this extension, the stationary pumping engines also sucked air from upstream of the piston. However, the technology used to seal did not prevent air from leaking. This problem, and that many trains ran considerably late, enforced that the system lasted less than a year: in 1848 (with experimental services from September 1847) from February to September. The system was never expanded beyond Newton, although several engine houses were already built.

Other reasons why the atmospheric train failed at that time were the following [15]:

- Failure of the tube seals, possibly due to rats eating the leather sealing strip greased with tallow.
- Shunting the trains into atmospheric formation was difficult or cumbersome.
- The pumping stations were spaces a few kilometres and had to run for longer than expected to accommodate late-running trains, converting the system too expensive to operate.
- The hill-climbing abilities of the system were not adequately tested. Brunel only tested the system on an even track.
- There had to be gaps in the atmospheric tubes at points and special arrangements at level crossings.
- Telegraphy was not advanced enough to coordinate the pump stations and trains.

Atmospheric railways have not disappeared yet. Aeromovel Corporation of Brazil developed an automated people mover at the end of the XX century that works on the same principle. It started its operation in 2013 at Porto Alegre Airport, Brazil. A similar system is installed in Taman Mini Indonesia Indah, Jakarta, Indonesia. More information about this system is provided in section 1.7.1.

Figure 1.5: On the left Totnes railway station atmospheric pumping house, South Devon, England. Reference: `https://commons.wikimedia.org/wiki/File:Totnes_railway_station_atmospheric_pumping_house,_South_Devon,_England.jpg`, retrieved on 05-10-2020. Author: Rosser1954. This file is licensed under the Creative Commons Attribution-Share Alike 4.0 International. On the right, Brunel's Atmospheric Railway at Didcot Railway Centre. Reference: `https://commons.wikimedia.org/wiki/File:Brunel%27s_Atmospheric_Railway.jpg`, retrieved on 05-10-2020. Author: Chowells commonswiki. This file is licensed under the Creative Commons Attribution-Share Alike 3.0 Unported license.

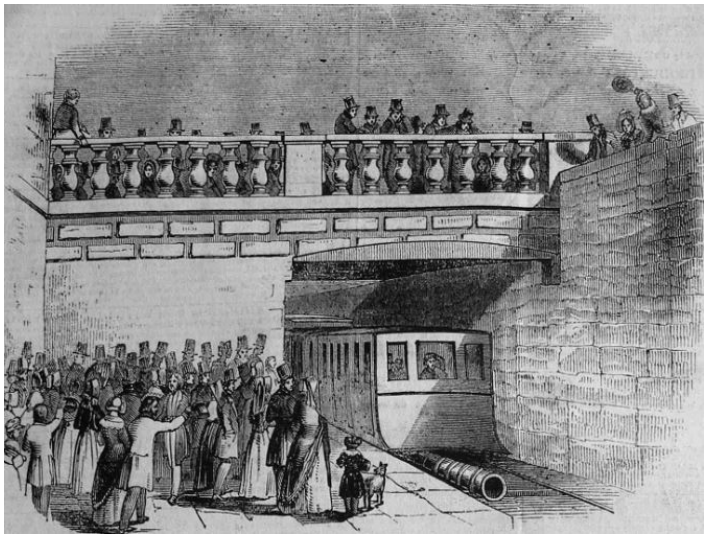

Figure 1.6: The Kingstown and Dalkey atmospheric railway art concept, as published in the London News newspaper in 1844. Reference: [16].

1.5.2 Pneumatic railway

The previously explained concept, the *atmospheric railway*, was based on using the air pressure within a small cylinder (compared to the wagons) to enforce the movement of a train. Following this concept in the second half of the XIX century, inventors started thinking about an alternative solution, still using air pressure. It was proposed to enclose all the trains inside the tubes, instead of only a piston attached to it. It is important to mention that Medhurst had already mentioned this way of powering the trains in his publications at the beginning of the century [12, 13, 14].

The first experimental version of the pneumatic railway was performed in 1824 by a man known as Vallance [19]. He built a short line with a pipe of 1.8 m diameter and rails inside at the bottom. Although this system worked, it did not have commercial success.

It was Wiliam Lamson Stickney, based on a previous invention from Wiliam Murdoch [20] around 1799, who used this vacuum concept in the commercial application of package transportation. He started with a system called Lamson tubes. He aimed to transport different goods within buildings and factories and even supported the postal service in some cities. They were a net of small tubes either pressurised at the beginning or depressurised at the end.

Although Murdock and Medhurst had already died, in 1854, Josiah Latimer Clark was issued a patent for conveying letters or parcels between places by air pressure and vacuum. One year before, he had built 200 meters on the London Stock Exchange of pneumatic tubes [21].

At the end of the century, William Stickney Lamson saw the great potential of the pneumatic tube system and, in the 1890s, bought several major companies building this system, such as the Lamson Pneumatic Tube Company [22]. Thanks to him, nowadays, this system is known as Lamson tubes.

Actually, after the successful demonstration in London, several postal services around the world used this system[2]:

- Between 1865 and 1976 in Berlin, up to 400 km.
- Between 1866 and 1984 in Paris, up to 467 km.
- Between 1875 and 1956 in Vienna.
- Between 1887 and 2002 in Prague. Stopped due to floods.
- Between 1897 and 1953 in New York City.

Another of the first approximations to the concept [15] was used for moving packages in tubes beneath the streets of London by the Pneumatic Despatch Company [23] created in 1859, using the same concept as the Lamson tubes. They operated between 1863 and 1874, which was different from the initial concept, as those tubes were considerably smaller than this new one, which was 610 mm in diameter. The goal was the same, to transport packages, letters and parcels within sealed tubes beneath the city.

[2] `http://douglas-self.com/MUSEUM/COMMS/pneumess/pneumess.htm`, last accessed 14-08-2022.

The first full-scale trial was at Battersea during the summer of 1861, where a 422-meter long tube was installed, with curves of up to a 91-meter radius and gradients of up to 4.5 %. A 610 mm narrow gauge track was cast inside the tube, where wheeled capsules that weighed 3 tonnes fitted inside. A 6.4 m diameter fan provided the required 30 HP to reach up to 60 km/h.

A permanent line of similar characteristics was constructed between Euston railway station and the North West District Post Office in Eversholt Street, approximately 500-meter long. It started to be tested on January 15th, 1863 and entered into service on February 20th 1863 (see the photo in figure 1.7). Thirteen journeys with a capsule conveying up to 35 bags of mail were transported every day. The Pneumatic Despatch Company charged the Post Office for each service.

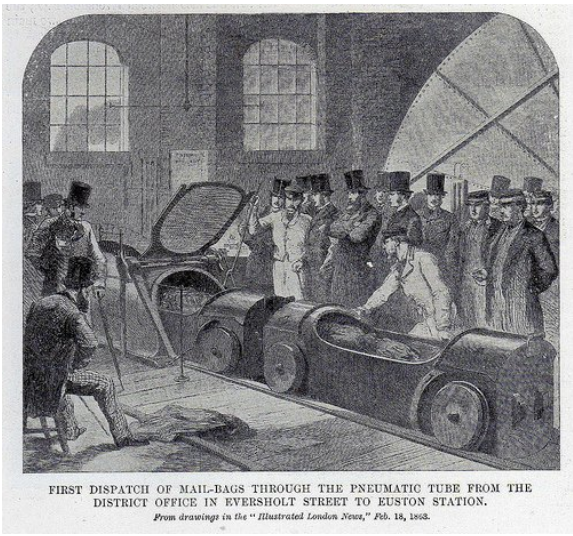
FIRST DISPATCH OF MAIL-BAGS THROUGH THE PNEUMATIC TUBE FROM THE DISTRICT OFFICE IN EVERSHOLT STREET TO EUSTON STATION.
From drawings in the "Illustrated London News," Feb. 18, 1863.

Figure 1.7: First mail dispatch through the pneumatic tube from Eversholt Street to Euston Station. Source: London News, February 28th 1863.

The company wanted to develop other lines within London. An 1130 mm narrow gauge line started to be constructed in September 1863 from Euston to Holborn and entered into service on October 10th 1865. On its inauguration, the chairman, Richard Temple-Grenville, 3rd Duke of Buckingham and Chandos, travelled from Holborn to Euston in one of the capsules. They were the first pneumatic train passengers.

Following the concept, in 1864, the first pneumatic railway was inaugurated, called *Crystal Palace* [24]. Big fans (up to 6.7 meters) actuated by steam machines enforced the movement of the trains. Those 550 meters were discarded at the end without finishing the construction due to financial problems.

Another line from Holborn to St. Martin's le Grand (for the General Post Office) serviced from 1869, with speeds up to 96 km/h.

Finally, the Post Office abandoned this system in 1874, forcing the Dispatch Company to go into liquidation in 1875. The Edinburgh Evening News reported afterwards that the main reason was that the truck containing parcels was stuck continuously in the tunnel.

On the other part of the Atlantic ocean, the success of the pneumatic tubes in England inspired Alfred Ely Beach in the United States [25]. His idea was to put people in carriages and propel them through underground tubes using air pressure generated by fans. An overground model was proven at the 1867 American Institute Fair with success. It was a wooden tube 6 feet in diameter and 30 meters long, capable of moving a ten-passengers vehicle in two ways.

On February 26th, 1870, Beach unveiled a brand new underground route (see the photo in figure 1.8). A single car fitted within the 2.7-meter diameter 95-meter long tube, which ran from Warren Street to Murray Street at 16 km/h, also in both ways. His invention was a popular attraction for the first year; however, while he was trying to get governmental support to expand his invention, a stock market crash made him close his pneumatic company [26].

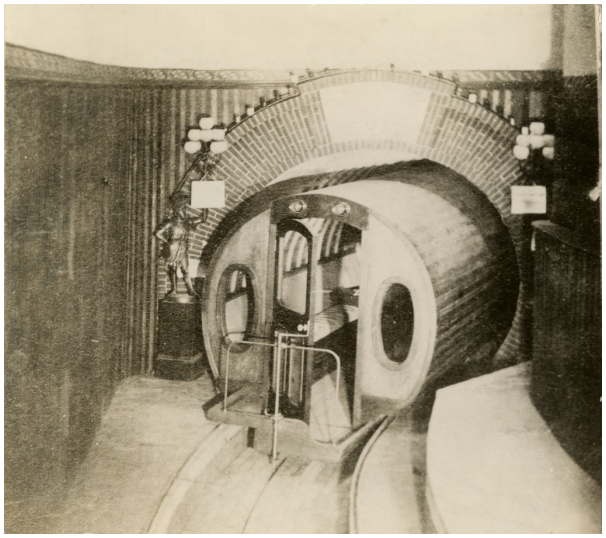

Figure 1.8: Picture of The Beach Pneumatic Subway Tunnel under Broadway, New York City, 1873. Source: New York Historical Society, `https://nyhistory.tumblr.com/post/77917762375/february-26-1870-alfred-ely-beach-debuts-his`, last accessed 21-02-2022.

The subway from Beach was forgotten until 1912, when the old Warren Street station was founded during the construction of a new standard metro line. The passenger car was still on the track.

Vacuum tubes are still used in several applications in the modern world, but not to transport people. They are mainly used to transport material in supermarkets, hospitals, banks... Nevertheless, regarding people transport, the atmospheric railway was eventually discarded in favour of more powerful steam locomotives [19].

The pneumatic railway derived in what is also known as vactrain or ETT, as proposals of the XX century considered to include all the trains inside a vacuum tube. The vactrain was formally invented by Robert Goddard as a freshman at Worcester Polytechnic Institute in the United States in 1904. After that, he published the patent [27]. This invention describes

a system of transportation in which a car containing goods or passengers is moved at high speed through a tube maintained under a low-pressure environment.

1.6 Development of the magnetic train

After the steam locomotive, electric locomotive, and fossil fuel trains, during the XX century, a new concept of magnetic levitation trains arose [28].

The precursor of the magnetic train, or simply *maglev*, was the Russian physicist and mathematician Boris Petrovich Weinberg. In 1913 he created an experimental model of a vacuum train. One year later, he proposed a vacuum transport that used magnetic levitation technologies in Saint Petersburg.

In 1911, Weinberg built an iron prototype that weighed 10 kilograms, able to move through a 20-meter ring road from a copper pipe 32 centimetres in diameter [29]. The pressure inside the pipe was reduced to minimise the aerodynamic drag. The carriage levitated thanks to the attraction from the solenoids placed on top of the pipe. A switching system enabled the current to activate the solenoid in front of the capsule and turn off the current on the solenoid that the carriage just passed. This was the first linear motor working. It took two years for Boris to complete his experiment successfully. The operation of the switches was improved in order to guarantee full levitation and propulsion of the capsule, up to 6 km/h.

In his book "Motion without friction", which he published in 1914 [30], Weinberg described the successful experiments that had already been done and proposed a draft route for passenger traffic at a speed of 800-1000 km/h. The route was in low-pressure conditions, with a cylindrical capsule made of a steel cylinder with a diameter of 0.9 meters and a length of 2.5 meters. The passenger was lying and had a supply of oxygen for breathing. At each station, the carriage was accelerated or braked by linear induction solenoids of about 3 km in length. More electromagnets on the track provided the required levitation force. The World War interrupted the work on this installation.

In 1914, the American inventor Emilie Bachelet (born in France) presented his maglev idea with a physical model. He submitted a report in the Swiss journal "Schwizer Familie" the same year with more information about his model. It is shown in figure 1.9.

He had been granted a patent [31] two years before. He described his invention as a machine to transfer objects at very high speeds from one place to another. The system uses magnets on the vehicle and track to provide levitation and guidance, and a third magnetic field is used to propel the capsules as a linear motor. The patent described how to save electricity by activating the magnets just before the passage of the train and cutting the current after it has passed. Although it was primarily meant to transmit mail and small packages, it could also be used in trains carrying freight or passengers.

Bachelet was quite successful in 1914 with a prototype in an exhibition in London and managed to attract financial support to continue his research until he died in 1946. However, he faced a problem, as at the beginning of the 20th century, the steam locomotive was still the main ground transport; massive electrification of the rail transport had not happened yet. Moreover, the system required, and still requires nowadays, the construction of a specific network.

Figure 1.9: Emile Bachelet with his maglev model, in 1914. Source: "Schwizer Familie" no. 35, June 27, 1914.

After Russia and the United States, the next successful inventor of maglev trains was German. Hermann Kemper [32] was a German engineer considered the maglev railway concept inventor. In 1922 Kember started his research in this field. He resolved a concept in 1933 based on electromagnetic attraction. He received a patent in 1934, the first patent for a magnetic levitation railway. His invention was described as a "monorail vehicle with no wheels attached" that is kept floating through magnetic fields. This was the base of the most successful maglev in history, the German Transrapid.

C. Kerr and C. Lyn [33] proposed in 1961 the use of permanent magnets on track and onboard to levitate through stable repulsion. However, this system was not scalable as the magnets were too heavy and too expensive to cover all the track.

The next evolution of the maglev was the superconductive maglev. Its inventors were Powell, an American physicist, and Gordon Danby in the 1960s. Their inventions included the inductive levitation and stabilisation guideway, null flux geometry, and linear synchronous motor for vehicle propulsion. Those are the basis of the Japanese superconductive maglev Chuo Shinkansen, detailed later in section 1.7.2.2.

In 1963, Power suggested a train suspension based on magnetic repulsion provided by two superconductive coils carrying superconductors on track and onboard [34]. As this proposal was too expensive due to having superconductors on the track, it was soon discarded.

As Powell explained in [35] in 1969, the superconducting magnets are carried by train and interact, through electromagnetic induction, with a track bed formed by a plurality of longitudinally extending arrays of shorted loops. These are composed of non-magnetic metal conductors, such as aluminium. This generates levitation and stabilisation of the attitude and damping of the vehicle. The system was technically and economically feasible since it utilised available materials and required minimal power consumption for operation.

The vehicle should be supported on wheels when at rest or lower speeds, as long as those are below the speeds necessary for the electromagnetic suspension.

This system possesses significant advantages over conventional wheeled or air cushion suspensions, as only a small amount of power is required to levitate the vehicle with a large margin (around 30 centimetres). Also, the need for the fiat and regular roadbed required by ground-effect machines can be eliminated. Furthermore, electromagnetic suspension can be achieved in low-pressure environments, unlike air-cushioned vehicles.

However, magnetic trains require more expensive materials than the ones in standard railways, for instance, permanent magnets, coils or electric steel. Also, the power requirements are typically higher than other propulsion approaches due to the lower efficiency.

1.7 Modern initiatives

1.7.1 Aeromovel

This system is inspired by the atmospheric railway developed during the mid-19th century. It was first patented in 1979 [36] by the Brazilian inventor Oskar Hans Wolfgang Coester in different countries, including the UK. Afterwards, the Brazilian brand Aeromovel was created in 1988.

This concept works as described in figure 1.10. A panel in an enclosed environment is attached to the bottom part of the train. The train is supported by wheels on the top part of the track, like a conventional one. Different pumps are located on the track, and as the train passes, the pressure is increased behind the panel, while in front of it, the tube is vented to evaluate the air displaced. That pressure difference on the panel makes the panel act as a piston, as it transmits the movement to the whole train.

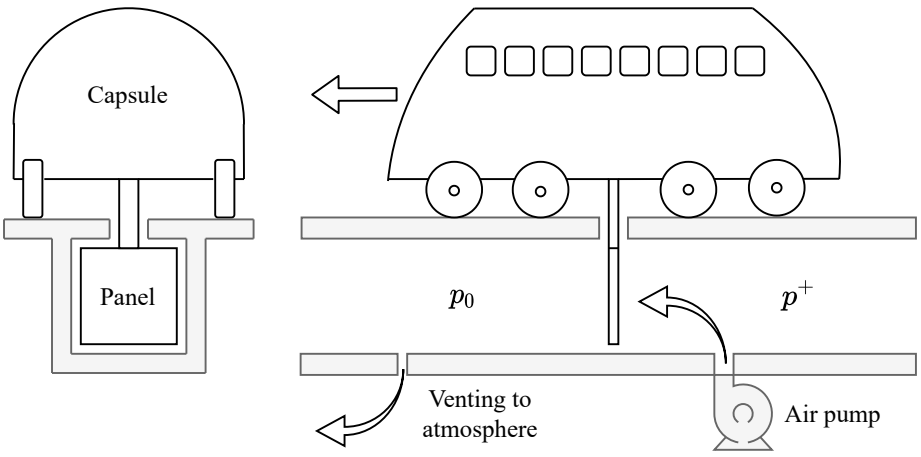

Figure 1.10: Description of the Aeromovel concept.

With his concept, speeds up to 80 km/h have been achieved while maintaining a low energy consumption of 19 Wh/(km pax), which is 30 % lower than the equivalent convention rail system according to Garret in [37]. Similarly, these advantages are reported:

- It can overcome high slopes. Currently, the maximum in service is 10 % in Jakarta.
- The low energy consumption, as exposed previously.
- Small radius in curves, as low as 25 meters.
- The derailment is not possible unless there is a catastrophic situation, as the piston itself prevents the roll of the train.

Apart from the 1 km pilot line developed in 1983 in Porto Alegre (Brazil), there are currently three lines open around the world [37]:

- Jakarta (Indonesia), in 1989. A 3.2 km line with six stations capable of transporting 300 passengers per car.
- Porto Alegre (Brazil), in 2013. A 1 km line as an Automatic People Mover (APM) in the Filho International Airport (POA).
- Canoas (Brazil). Not in service yet, it is already built and can reach speeds up to 120 km/h in a 4.6 km line.

1.7.2 Maglev

Several maglev concepts have operated commercially during the end of XX and beginning of the XXI century. For low to medium speed:

- Birmingham, United Kingdom (1984 - 1995). It was a people mover of short length (600 m) and reached 42 km/h. It was shut down due to electrical system failures [38].
- Berlin, Germany (1989 - 1991). The so-called M-Bahn was a maglev in West Berlin that, for two years, operated at a cruising speed of 80 km/h on a 1,6 km track. It closed due to the fall of the Berlin wall, as the U-Bahn replaced its services [38].
- Aichi Prefecture, Japan (2005 -). An 8.9 km route was opened for the Expo 2005 and reached 100 km/h, named as Linimo system. It was the first autonomous commercial maglev [39].
- Incheon, South Korea (2016 -). A 6.1 km as a people mover on the airport that reaches 80 km/h as cruising speed [40].
- Changsha, China (2019 -). An 18.6 km line between the airport and central station, at a speed of 140 km/h [41].

There are several big projects conducted in China. The most ambitious one is the superconductive maglev at 620 km/h developed in Chengdu by the Southwest Jiaotong University (SWJTU) in collaboration with the CRRC. It uses High-Temperature Superconductors (HTS) at 77 K cooled with liquid nitrogen on the vehicle and permanent magnets on the track. This way, the maglev uses zero energy to levitate and guide magnetically [42]. Even

at low speeds can test its self-centred levitation. That is why the tests were conducted on a 165-meter-long test track, with a levitation gap between 10 and 30 mm.

The propulsion is based on a Linear Synchronous Motor (LSM) with the coils distributed on the track. This system is considered technically sophisticated, so particularly high construction costs are expected for the guideway[3]. A photo of the capsule is seen in 1.11.

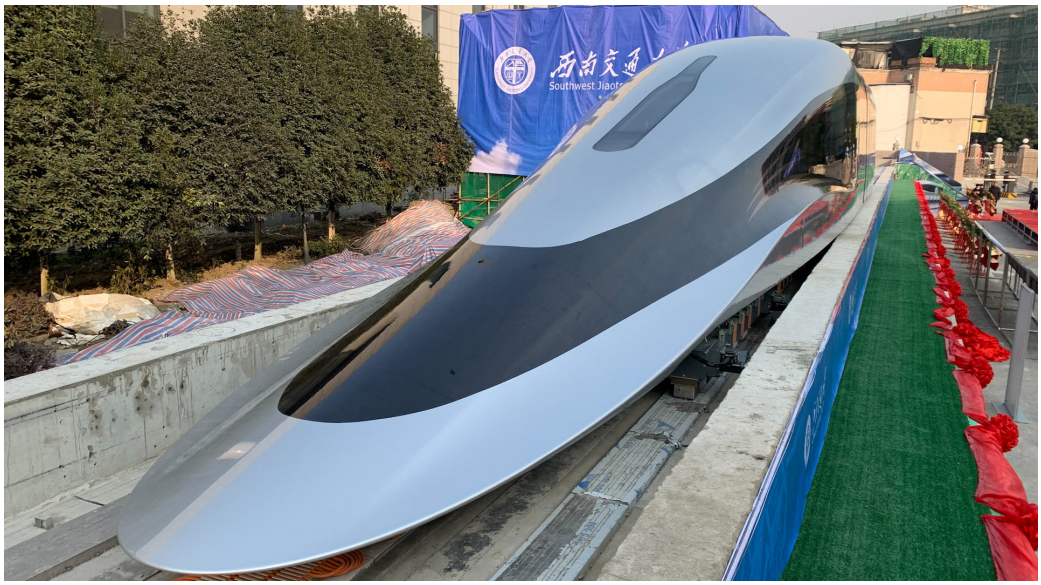

Figure 1.11: Photo of the capsule unveiled Jan. 13 by CRRC in Chengdu. Reference: Chaiwan Ben Post.

Another project developed by China is another maglev, this time without superconductors, with a concept equivalent to the Transrapid[4]. (described in section 1.7.2.1). It is developed by Tongji University in Shanghai, and in 2020 they conducted a successful test at low speed on a 1.5 km test track. China aims to use a 500 km-long high-speed maglev line commercially by 2025. Its target speed is 600 km/h, surpassing the 505 km/h of its predecessor, the German Transrapid.

In the mid-speed field, another initiative from China is found in conjunction with Germany. Chengdu Xinzhu Road & Bridge Machinery Co., Ltd. are building a 4.5 km medium-speed maglev test line in Chengdu. The first part of the test line, with a length of 3.5 km, was already completed in 2020. During that year, speeds of 120 km/h were achieved. The expected commercial speed[5] is up to 200 km/h.

US plans to construct a Maglev line between Washington DC and New York City using the SCMaglev developed by the JRCentral, and in tests during decades in Japan. The environmental study is still in progress in 2022, on Phase I[6].

[3]Reference `https://www.maglevboard.net/en/component/acym/archive/245-maglev-transport-news-january-2021?userid=9433-beewsjVFZ6GqAO&tmpl=raw`, last accessed on 18/01/2021.

[4]Reference link, last accessed on 18/01/2021.

[5]Reference link, last accessed 18/01/2021.

[6]Reference `https://northeastmaglev.com/`, last accessed on 18/01/2021.

For high speed, the singular approaches that have been thoroughly tested are the Japanese Chuo Shinkansen and German Transrapid, described in the following sections.

1.7.2.1 Transrapid

The Transrapid is a maglev train developed by Siemens and ThyssenKrupp firstly for Germany and then installed in China, where it is still operational.

This idea started in 1969 when Germany began developing the maglev [43]. The tests were conducted in the Emsland Maglev-Test facility in Lathen, Germany. The first one was conducted in 1983 with Transrapid 06. In December 1987, the entire test track, with a length of 31.8 km, was completed. It was a loop with a straight line of 12 km. Regular testing started between 1988 and 1993, with Transrapid 07 reaching 450 km/h. The last one tested was the Transrapid 09, which reached 505 km/h in a 75.8 m vehicle.

Despite the successful test, no commercial line was ever built in Germany [44]. In September 2006, a Transrapid train collided with a maintenance vehicle on the track causing several fatalities, the first accident in a maglev system. Finally, the Emsland test track closed down in 2011.

In parallel, the German Transrapid was implemented in Shanghai, China, in 2002. Being the first commercial high-speed maglev line in the world, it is still the only one nowadays. The maglev covers 30.5 km between the Shanghai Pudong International airport to the city. Based on the Transrapid 08, it reaches a commercial cruise speed of 431 km/h.

Regarding the technology [45], the Transrapid uses Electromagnetic Suspension (EMS) for vertical and lateral guidance. The vertical one reacts to the linear motor stator, and the lateral one with a steel plate on the track. The propulsion is provided by a Synchronous Linear Motor (LSM), the long stator on the track. The power for the coils on the vehicle is transmitted with a linear inductor.

The Transrapid levitates during the whole mission. In case of levitation failure, friction skis are placed below the capsule to prevent it from being damaged.

1.7.2.2 SCMaglev

The Superconductive Maglev, abbreviated as SCMaglev or the Chuo Shinkansen, is another maglev train in Japan since 1997 and developed by Mitsubishi Heavy Industries, Nippon Sharyo and Hitachi Rail. Its particularity is that it uses superconductors for levitation and propulsion. Its commercial application is expected in 2027, although the test line is fully operational nowadays.

Japan started the development of high-speed maglev in the 1960s, achieving a top speed of 517 km/h with conventional Electro Dynamic Suspension (EDS) in 1977 on a 7 km long test line [44]. In 1979 they started to apply superconducting technology. In 1997 the Yamanashi maglev test line was finished, which is 42.8 km long and based on commercial standards and with 82 % under tunnels due to the country orography [46]. In 2016 the L0 high-speed maglev train reached on the Yamanashi maglev test line with a seven-car vehicle, a speed of 603 km/h during 10.8 s on the test track in 2016 [47], although it is designed for a commercial speed of 500 km/h. In the 12-car configuration, the train is 299

m long and has a capacity of 728 seats. The manufacturer of the L0 maglev train is a joint venture of Mitsubishi Heavy Industries, Nippon Sharyo and Hitachi Rail.

Thanks to this successful test, the Japanese government approved the construction of the Chuo Shinkansen line in 2014. It will be a 505 km-long maglev line with an operational speed of 500 km/h, connecting Tokyo, Nagoya and Osaka. The first phase of the project to Nagoya is supposed to be finished by 2027 [7]. This will be a 286 km section with 86 % in tunnels. The entire project is supposed to be finished by 2037.

As for the technology, the SCMaglev uses Electrodynamic Suspension (EDS) based on superconductors [48]. The superconductive coils are placed onboard the vehicle. On the last version of the Shinkansen, these are High-Temperature Superconductors (HTS), operating at 77 K. Liquid nitrogen is used to cool down the superconductor to achieve superconducting. Since liquid nitrogen needs to be preserved at a quite low temperature, liquid helium is used to cool down the nitrogen. Thanks to the zero electrical resistance, the superconducting coil can maintain elevation for a while without any power.

On the guideway, two sets of coils are mounted on the track. The null-flux coil for levitation and guidance, is energised when the superconductive coil on the vehicle has a relative speed. The propulsion coil is energised externally on the track that composes the long stator of the LSM.

Also, as the EDS does not work at lower speeds, landing wheels are installed on the vehicle. These are also used in case of emergency.

One of the main advantages of this system is that the guidance system is passive, so there is no need to have a complex active system to control the air gap, which can be higher than 10 mm as opposed to EMS.

1.7.3 Other initiatives

The US government considered the possibility in the 1960s of combining pneumatic tubes with maglev technology between Philadelphia and New York City [25]. However, as the project was too expensive, it was abandoned.

L.K. Edwards, an engineer from Lockheed, tried to rescue also the idea in the 1960s. While Lockheed eventually decided not to continue its research in this area, Edwards formed the Tube Transit, Inc. to exploit "gravity-vacuum transportation". Edwards proposed a Bay Area Gravity-Vacuum Transit (BART) system for San Francisco in 1967 [49], designed to run in tandem with the public transport under construction. He proposed a route from San Jose to Marin, with 23 stations, separated by an average of 4.8 km. Between each one, air would be evacuated upstream of the train, pulling the train on its parabolic course. After the station, the tube sloped downhill until midway between stations. The designed top speed between stops was 336 km/h.

However, the system proposed by Edwards was never built. The same happened with the proposal made by Robert M. Salter a few years later. He proposed in the 1970s an underground Ultra High-Speed Transportation system to run along the Northeast Corridor.

[7] `http://stcsm.sh.gov.cn/xwzx/kjzl/20200623/831c6d0b2a44491eabd25eb025656b7b.`, (last access 2021-12-28)

1.7.3.1 Tubeflight

The Tubeflight involves a vehicle based on an aircraft fuselage, supported by air bearings instead of magnetic levitation, and which has onboard propulsion based on flow induction, for instance, a turbojet engine, inside a tube at atmospheric pressure. Its concept can be seen in figure 1.12.

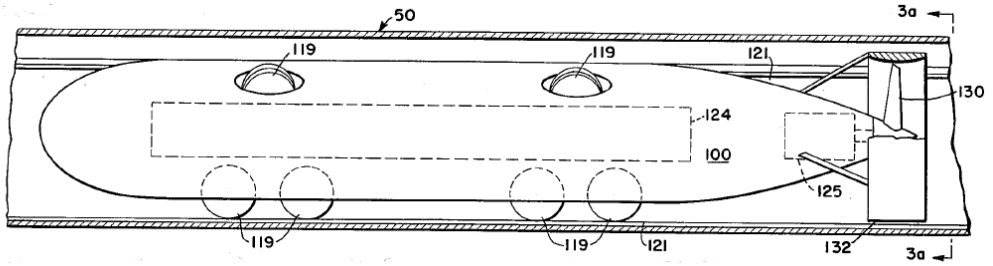

Figure 1.12: Tubeflight concept. Reference: fig 3 from [50].

Tubeflight was invented by J.V. Foa [51] while at Cornell Aeronautical Laboratory in 1947. However, it was not until 1965 that the project received its patent US3213802.

As opposed to other hyperloop-alike proposals, Tubeflight did not want to use a low-pressure environment inside the tube. This would simplify the structure, remove sealing problems, and help the braking due to the piston effect.

The proposed vehicle has a diameter of 2.7 m in a tube between 4.5 m and 5.4 m diameter. The propulsion method considered adding energy to the flow faced by the vehicle, using the pressure and momentum difference as a propulsion method. Two were the proposed solutions: the axial rotatory compressor and the axial-flow cripstosteady pressure exchanger. The latter was a turbine with no blades that takes advantage of the friction forces on a rotatory shaft.

Furthermore, the system used an air bearing system to lift the vehicle and avoid friction with the track. Wings were also included in the vehicle to increase the lift force. The guidance was provided by lateral jets or ground effect.

The initial proposal was to have the propulsion system in pusher mode. In this way, the propeller was placed at the rear part of the vehicle. If the speed had to be increased and blocking problems happened on the passage, another propeller as a puller would have been added.

The target was to transport between 50 and 200 passengers, with an energy consumption of 2155 - 3455 kJ/(km pax) at 320 km/h. Theoretically, the maximum cruise speed was 611 km/h.

The project had budget problems, and finally, only small-scale tests were performed. Some experiments were conducted in 1958 in a 3-meter long tube with electric propulsion and in 1959 using gasoline-powered models in a 6-meter tube. After the success of the first experiments, during the 1960s, they build a 31.37 cm diameter test track of 50 m in

length. Their prototype did not use air bearings. Instead, it used wheels for guidance. The propulsion was a McCulloch Mc-lOO engine providing 15 H.P. at 10000 rpm. To eliminate vehicle rotation arising from engine torque, a counter-rotating gearbox was designed to transmit the power to a pair of 3-bladed, adjustable-pitch propellers. The test started in 1968, and, with a mass of 27 kg, the vehicle reached 120 km/h.

1.7.3.2 Maglifter

Maglifter was a project developed by the NASA at the end of the XX century that consisted of the development of an electromagnetic launcher for spacecraft [52]. The goal was to provide the launching vehicles with 960 km/h to reduce the fuel requirements of the first stage. The target power was between 1 and 3 GW.

The target values were never reached, but a small-scale prototype was successfully tested. For the prototype, the propulsion system was based on a Linear Synchronous Motor (LSM) coreless with permanent magnets on the vehicle.

The guiding system is based on the null flux passive levitation coils. In this way, the magnets for the propulsion are also used for guidance. On the track, passive 8-shaped coils are placed. This propulsion-levitation combination can be seen in figure 1.13.

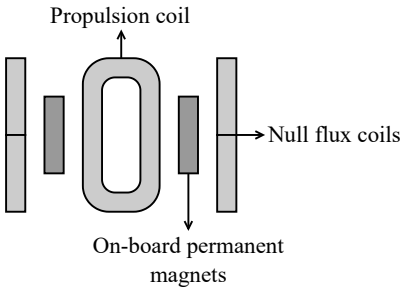

Figure 1.13: Maglifter magnetic propulsion and guidance approach.

The tests were conducted on a 12-meter test track, including 6 meters for braking with passive eddy-current brakes taking advantage of the onboard magnets. 94 km/h, and complete levitation was achieved.

However, several problems prevented the system from being scaled up:

- In terms of propulsion and levitation, the permanent magnets do not scale well with the power. Instead, superconductors should be studied.
- The guidance system is essentially passive. Then, low damping forces appear. This may be unstable for higher speeds, and probably, it should be combined with an active guidance system.
- The energy required for the real-scale launch is around 25 GJ. No existing systems at that time could store that amount of energy. The closest was the Princeton Flywheel Generator with 2.5 GJ.

1.7.3.3 Aerotrain

The Aerotrain was developed in France by Jean Bertin in the 60s to prove the viability of the Tracked Air Cushion Vehicle (TACV) (chapter 4, [53]). It consisted of a capsule in an elevated monorail that used air bearings for guidance, thus avoiding roiling with the ground. A photo of the Aerotrain can be seen in figure 1.14

Figure 1.14: Aerotrain prototype 02 designed by Jean Bertin at an exhibition in Saran, Loiret, France. This file is licensed under the Creative Commons Attribution-Share Alike 3.0 Unported license. Reference: `https://upload.wikimedia.org/wikipedia/commons/0/0e/Exposition_a%C3%A9rotrain_Saran_5.jpg`.

The goal was to build a vehicle for a medium-range distance, for example, the connection as Paris-Lyons (450 km). The vehicle would have had space for 80 seats, 20 meters long, weighing 18 and 20 tons. The average target speed was 400 km/h.

The public funding made it possible to build the first experimental vehicle, called 01, and construct a 6.7 km long trial track between Gometz-la-Ville and Limours (Essonne, south of Paris). The test went successful, as a half-scale vehicle (10 meters long and 2.6 tons) reached 200 km/h.

The Aerotrain 02 tried to prove higher speeds, equipped with a rocket for propulsion and parachutes for braking. On January 22, 1969, the Aerotrain 02 established the world record of TACV flying at 422 km/h at a 5 mm height above the ground. According to the

engineers, the trial proved that higher speeds in a longer track could have been reached with the same prototype. However, no more support from investors was provided, and the project closed in few years after the test.

1.7.3.4 EMALS

The acronym EMALS stands for Electromagnetic Aircraft Launch System [54]. It consists of applying a linear motor to launch aeroplanes in air carriers instead of using the standard hydraulic system. The US Navy had foreseen the utility of an electromagnetic catapult in the 1940s and built a prototype. However, it was not until the recent technical advances in power electronics and storage that this was implemented. The US government has developed the system in partnership with Kaman Electromagnetics (Hudson, MA).

1.7.3.5 Swissmetro

Swissmetro was a project developed in Switzerland at the end of XX and the beginning of the XXI centuries [55]. It is equivalent to a hyperloop, including a maglev in a vacuum tube. The SBB (Schweizerische Bundesbahnen) engineer Rodolphe Nieth started the idea in 1974 due to the difficulty of mobility in his country due to the large number of mountains. This requires many tunnels, especially if one targets at high speeds where obstacles must be avoided. The AlpTransit project in Switzerland covers around 120 km of tunnels [56].

In 1987 the Swiss Department of Transportation commissioned a feasibility study from the German company Dornier, which was released the following year with positive conclusions. Then the government started to be interested and provided the University of Lausanne (EPFL) with credit in the amount of 500 000 Swiss Francs for a preliminary study. The study is co-funded by EPFL and the private sector (35 companies). However, after almost 20 years of studies, in 2006, Ulrich Weidmann of the Federal Institute of Technology in Zurich published a case study for the Swissmetro, concluding that the high investment costs and long construction period made the system non-viable in Europe. Although Siwssmetro did not respond o this study, in 2010, the project was shut down without any built prototype of relevant scale.

However, Swissmetro was an interesting project in the technical part. The levitation system was an Electromagnetic Suspension (EMS) with levitation units on the vehicle, and the linear motor was a hybrid between Reluctance and AC Synchronous [57].

All the interfaces for guidance and propulsion were in the middle of the tube, leaving a large space below the vehicle for emergency purposes.

By his part, the energy was transferred to the vehicle by employing a catenary on top of the tunnel.

Swissmetro project target for speed higher than 360 km/h at a tenth of the atmospheric pressure in tunnels of 0.4 of blockage ratio, which is lower than the ones for HSR. The capsules would have been able to transport 400 passengers, entering into service in 2020.

In response to the Swiss orography, all the lines were planned to be underground, like a large metro network. The most important predicted line was the 89.1 km between Basle and Zurich.

1.8 Development of electric air transportation

During the last decades, different projects have grown trying to make the current air transportation more electric. Here are collected some of them:

Efan-X [58] This project, result of a joint between Rolls-Royce and Airbus, consisted of developing a hybrid aircraft. In the test plane, launched in 2017, one of four jet engines was replaced by a 2 MW electric motor powered by a 3000 VDC battery. The project ended in April 2020, after being the first successful hybrid-electric propulsion system in a demonstrator aircraft.

CityAirbus [59] CityAirbus NextGen is an all-electric, vertical take-off and landing (eVTOL) featuring a wing and eight electric-powered propellers. It has no moving surfaces or tilting elements. It is designed for an 80 km range and a cruise speed of 120 km/h, providing clean urban transportation in major cities. CityAirbus NextGen entered its detailed design phase in 2021, targeting 2023 for the first flight.

Lilium (`lilium.com`) Lilium developed the first electric vertical take-off and landing jet, using technology they named Ducted Electric Vectored Thrust (DEVT). Their prototype has several electric jet engines integrated into the wing flaps, proving advantages in terms of efficiency, noise, and control.

One of the most novel approaches is published by Kshirsagar et al. [60], where they present a hybrid aircraft for 20 MW. Eight fans powered by an electric motor (2.5 MW each) provide the required thrust. The energy comes from two gas turbine generators inside the same aircraft. With a rectifier and a generator, the power produced by the turbines is stored on the plane and feeds the compressor. The fuel used for the generators will be either liquid hydrogen or LNG. They claim that this system can reach efficiencies of at least 93 %.

These projects are highly interesting for hyperloop development, as the power requirements are similar. So, all the research made for electric powertrain for aircraft is applicable for hyperloop propulsion.

1.9 Hyperloop initiatives

1.9.1 Origin

Although the origin of Evacuated Tube Transport is the XIX century, as described during this chapter, it was not until the release of the Hyperloop Alpha [4] that the term *hyperloop* was used for the first time to describe a vacuum transport.

Musk, in his document, proposes that hyperloop should have a compressor in front of the vehicle, which shallows the air in front of the capsule, reducing the aerodynamic drag and using this pressurised air to provide levitation with air bearings and propulsion with the remaining energy.

During the cruise phase, the thrust required to maintain the constant speed is low, however, for the acceleration and braking, the use of a Linear Induction Motor (LIM) with

an aluminium plate on the vehicle and coils on the track is proposed. This way, the large amount of power required for the initial boost is part of the track and does not add weight to the vehicle.

After this first hyperloop proposal, the world started focusing on this new means of transportation. Musk released a university competition (see section 1.9.2.1) and the first private companies appeared in the US: Hyperloop One, now Virgin Hyperloop (see section 1.9.3.1), and Hyperloop Transportation Technologies (see section 1.9.3.2).

1.9.2 Universities

As mentioned, two years after the release of the Hyperloop Alpha, Elon Musk announced the first Hyperloop Pod Competition (HPC) for all universities around the world, to be held in SpaceX (L.A., United States) in 2015.

1.9.2.1 Hyperloop Pod Competition

The HPC had four editions, from 2015 to 2019:

1. The first edition was held in winter 2015 with only presentations in Texas and, in winter 2016, with physical prototypes at SpaceX facilities.

2. The second edition occurred at SpaceX with physical prototypes in the summer of 2017, won by the Technical University of Munich (TUM), reaching 94 km/h with an embedded compressor.

3. The third edition occurred at SpaceX in the summer of 2018, won again by TUM, reaching 324 km/h with rolling wheels.

4. The last edition occurred at SpaceX in the summer of 2019, won again by TUM, reaching 467 km/h with rolling wheels. This year, the first student vehicles with linear motors were able to compete at SpaceX, specifically the Swiss teams EPFLoop and Swissloop with LIMs.

Elon Musk decided not to continue the competition after the fourth edition. Since then, none of his companies has announced anything regarding hyperloop.

1.9.2.2 European Hyperloop Week

In the paradigm that no hyperloop competition was held again, some European teams decided to collaborate and found another competition to be held in Europe, each year in the facilities of one founding team[8]. These teams were:

- Hyperloop UPV, from Universitat Politècnica de València in Spain.
- Swissloop, from ETH Zurich in Switzerland.

[8]Reference: `https://hyperloopweek.com/`, last accessed 31-08-2022.

- Delft Hyperloop, from Delft University in Delft, The Netherlands.
- HYPED from the University of Edinburgh, in Edinburgh, United Kingdom.

To this date, two competitions have been held:

1. The first edition was held in Valencia in 2022. It was won by Swissloop team with a Linear Induction Motor (LIM) able to propel and levitate.
2. The second edition was held in Delft in 2022. It was won by Delft Hyperloop with a prototype able to levitate with Hybrid Electromagnetic Suspension (HEMS) and propel itself with a Linear Synchronous Motor (LSM).

The European Hyperloop Week (EHW) continues its goal to approach hyperloop development to the universities and the rest of the world, promoting its research.

1.9.3 Companies

1.9.3.1 Virgin Hyperloop

Virgin Hyperloop, formerly known as Virgin Hyperloop One and Hyperloop One, is a US company founded in 2013 aiming for hyperloop development. Currently, Virgin Hyperloop is the company with the most success in hyperloop development, as they have been able to perform several successful middle-scale tests of their technology[9]:

- In 2016, they tested the Linear Synchronous Motor (LSM) at more than 100 km/h with permanent magnets onboard.
- In 2017, they tested a vehicle with Electrodynamic Suspension (EDS) with halbach arrays and aluminium. Then, its 4 MW LSM propelled the prototype up to 387 km/h in a 500 m test track (300 m for acceleration), with 100 Pa.
- In 2020, they made the first hyperloop run with passengers inside a capsule. Up to four (two per capsule) people travelled at 173 km/h in a 100 Pa environment.

They found several problems testing their concept. For instance, the magnetic drag of the EDS was higher than expected. Also, they faced difficulties in cooling the active track, apart from the degradation of the systems in vacuum. As a consequence, they decided to move to another concept.

The real-scale proposal from Virgin Hyperloop [61] is a 28 pax vehicle with an energy consumption of 75 Wh/(seat km). To maintain the 100 Pa pressure on the track, they estimate less than 20 Wh/(seat km) energy consumption. On a technological level, they plan on using Electromagnetic Suspension (EMS) for vertical and lateral guidance, whilst a Homopolar Linear Synchronous Motor for the propulsion [62]. With this concept, all the active components will be on the vehicle side, removing them from the track.

[9]Reference: `https://virginhyperloop.com/`, last accessed 31-08-2022.

1.9.3.2 Hyperloop Transportation Technologies

Hyperloop Transportation Technologies, also known as HyperloopTT, is the other US hyperloop company, founded in 2014. They aim to build a hyperloop with passive EDS levitation based on an Inductrack system composed of permanent magnets in a halbach configuration on the vehicle and coils on the track, minimising the magnetic drag. They have provided few details about their propulsion system, although they plan on using a LIM. In terms of pressure, they plan on going at lower than 100 Pa environment[10].

1.9.3.3 Hardt

Hardt was founded in 2016 by former members of the Delft Hyperloop student team competing at the SpaceX Pod Competition, in The Netherlands. They developed a 20 meters middle-scale test track to prove their technology in 2018[11].

Their concept is to use Hybrid Electromagnetic Suspension (HEMS) for levitation and Electromagnetic Suspension (EMS) for lateral guidance. The levitation will be coupled with a Linear Synchronous Motor (LSM) with the coils on the track, using the already installed levitating magnets for the moving part of the motor.

With this system, they plan on reaching a cruise speed of 700 km/h with an energy consumption of 38 Wh/seat/km in a 60 passengers capsule. These figures will mean they will consume 1.5 MW during the cruise phase at a pressure of 100 Pa or lower.

1.9.3.4 Nevomo

Nevomo, formerly known as Hyper Poland, is a company founded in 2017 by the University Team competing at SpaceX Pod Competition. Nevomo has a particular approach for hyperloop development, as they aim to implement the Magrail[12], an intermediate solution to convert the conventional rail lines into maglev lines with magnetic propulsion, without the need of creating a new infrastructure, up to 550 km/h.

In 2019, they built a test track to test their Linear Synchronous Motor (LSM) at low speeds, without levitation.

For their real-scale concept, a passive levitation system with an LSM is proposed. In order to achieve higher speeds up to 1200 km/h, the solution proposed by Nevomo is including the maglev train inside a low-pressure tunnel, this time creating a new infrastructure.

1.9.3.5 Eurotube

Eurotube is a non-profit research organisation based in Switzerland aiming to develop a real-scale test track for hyperloop applications in Switzerland, founded by former members of the SpaceX Pod Competition teams Swissloop[13].

[10]Reference: `https://www.hyperlooptt.com/`, last accessed 31-08-2022.
[11]Reference: `http://hardt.global/`, last accessed 31-08-2022.
[12]Reference: `https://www.nevomo.tech/en/magrail/`, last accessed 31-08-2022.
[13]Reference: `https://eurotube.org/`, last accessed 31-08-2022.

1.9.3.6 Transpod

Transpod is a Canadian company founded in 2015. They were the first to release a technical study about the implementation of hyperloop in 2017 [63]. They proposed a vehicle levitating with Electrodynamic Suspension (EDS) and a combination of propulsion between a Linear Induction Motor (LIM) and a compressor. They planned on using pressures lower than 100 Pa.

The significant difference in the Transpod approach is using a plasma catenary to transfer the energy from the track to the vehicle, removing the active components on the track. This system was recently detailed and named as FluxJet[14]. In this new concept, they removed the aerodynamic propulsion.

1.9.3.7 Swisspod

Swisspod is a Swiss company founded in 2019 in Switzerland by former members of the student team EPFLoop at the SpaceX Pod Competition. They are building a small test track in loop form to test hyperloop technologies in a project called LIMITLESS[15].

1.9.4 Zeleros

Zeleros was founded in 2016 by former members of the Hyperloop UPV student team, which took part in the Hyperloop Pod Competition. Its goal is to develop a commercial application of hyperloop transportation focused on the development of the technologies that the vehicle requires. The concept is shown in figure 1.15.

The approach of *Zeleros* is similar to the one from the Hyperloop Alpha. The vehicle holds a compressor which shallows the air in front of the capsule and compresses it. As the density of this flow increases, it occupies less space and can surpass the cabin leaving space for the payload (passengers or cargo). Then, this air is expanded in a nozzle (after recovering part of the energy in a turbine), providing thrust.

An onboard electric motor powers the compressor. Power electronics and batteries are also in the vehicle. This way, no power has to be transmitted through the track, being totally passive in the cruise phase.

The pressure inside of the tube is a tenth of the atmospheric one, down to 10 kPa. This pressure is based on the lowest certified pressure that a commercial plane has flown: the Concorde [64]. This aircraft was certified at an altitude of 60000 ft, where the pressure is around 7.16 kPa [65]. Not using extremely low pressures helps the certification process of a hyperloop cabin, as one commercial cabin has already served civil passengers. Other hyperloop references have made studies in which the optimal pressure for operation, considering both the track and the vehicle, is around 10 Pa [66, 67]. However, these studies have not taken into consideration the use of a compressor as a propulsion method or the feasibility of the certification process.

[14]Reference: `https://www.transpod.com/press-release/fluxjet-unveiling/`, last accessed 31-08-2022.

[15]Reference: `https://www.swisspod.ch/`, last accessed 31-08-2022.

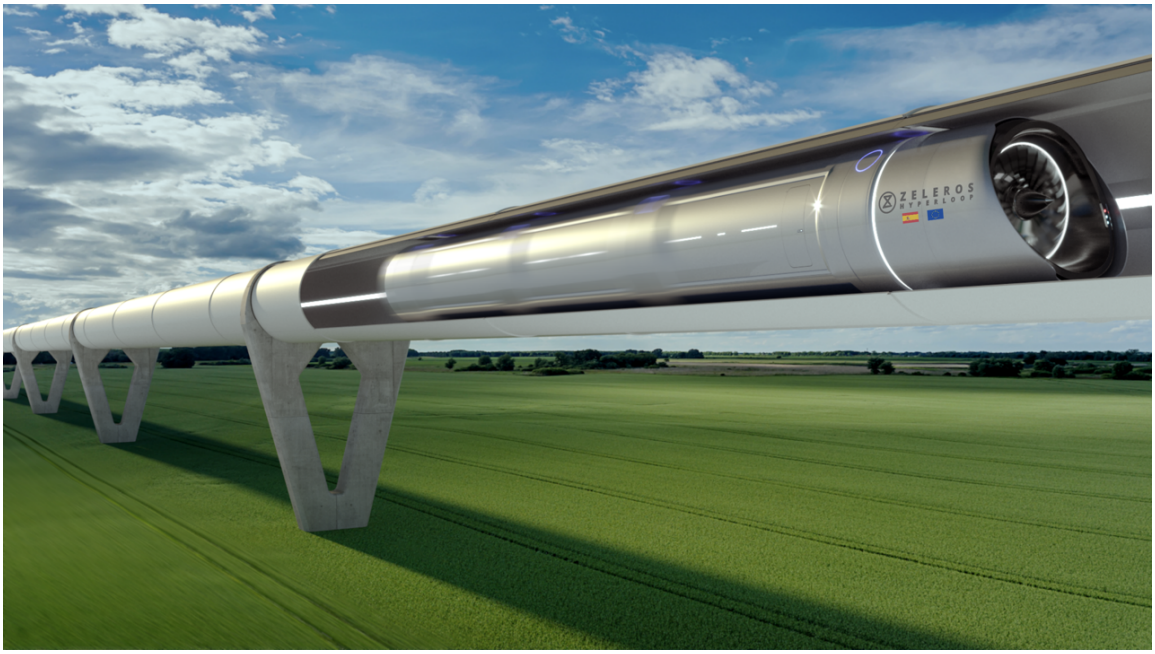

Figure 1.15: Concept of *Zeleros*.

The low-pressure environment inside the tube is obtained thanks to vacuum pumps distributed along the track. These pumps are powered by solar panels on top of the tube. All the described systems are drawn in figure 1.16.

Finally, the levitation system is distributed over the top part of the vehicle and reacts to a levitation interface in the tube. This is shown in figure 1.17.

The levitation concept is based on a Hybrid Electromagnetic Suspension (HEMS). This system includes a levitation unit composed of a permanent magnet and a coil near a ferromagnetic plate. The permanent magnet on the unit is responsible for making the required force to lift the weight of the vehicle, while the coil is the one that corrects the perturbations to maintain the capsule stable. Thus, the vehicle can stably levitate with almost negligible power consumption by controlling the current through the electromagnet. This concept is shown in figure 1.18, although more details about its basis and experiments can be found in [68].

Several units are required in different angles to control the required 5 degrees of freedom: vertical position, lateral position, and the three attitude angles.

Finally, it is important to highlight that a Linear Switched Reluctance Motor (LSRM) is installed for acceleration, braking and slopes. The passive part will be onboard, while the active part will be on track, thus avoiding installing a large amount of power on the capsule. More details of this linear motor are found in [69].

Although the described concept is thought for real-scale transport, *Zeleros* aims to develop a medium-scale prototype beforehand. This way, the different technologies can be tested in a more controlled environment, and the Technology Readiness Level (TRL) can be scaled up more naturally.

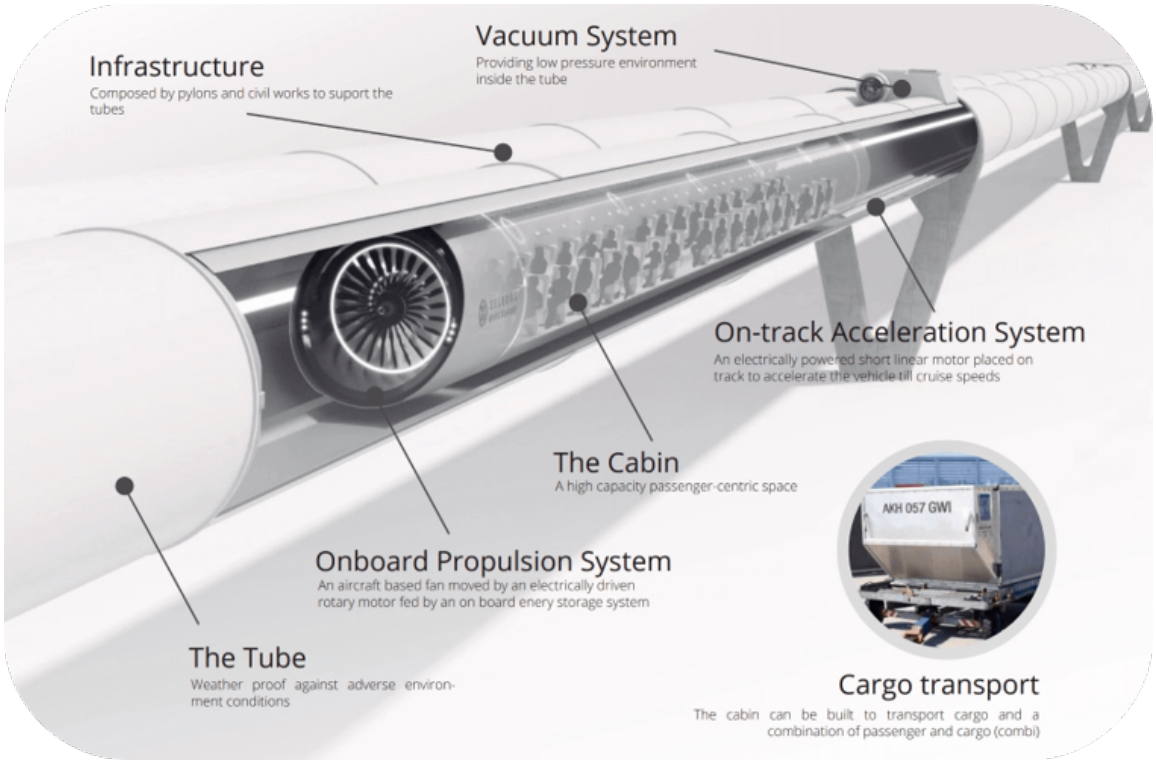

Figure 1.16: Detail of the components of the *Zeleros* vehicle.

1.9.5 Overview

Table 1.1 collects the proposal from each hyperloop and maglev initiative, including the one from *Zeleros*.

Company	Levitation	Cruise propulsion	Pressure level
Transrapid	EMS	LSM	Atmospheric
Chuo Shinkansen	HTS-EDS	HTS-LSM	Atmospheric
Swissmetro	EMS	LSRM - LSM	10 kPa
Virgin Hyperloop	EMS	Homopolar LSM	< 100 Pa
HyperloopTT	EDS (Inductrack)	-	< 100 Pa
Hardt	HEMS	LSM	< 100 Pa
Transpod	EDS	LIM	< 100 Pa
Zeleros	**HEMS**	**Compressor**	**10 kPa**

Table 1.1: Technological approach from each hyperloop-alike initiative.

This thesis does not aim to describe the working of each magnetic levitation and propulsion system deeply, as their model on the simulator will be simplified. However, more information about each linear motor approach can be found in [70], and about the levitation

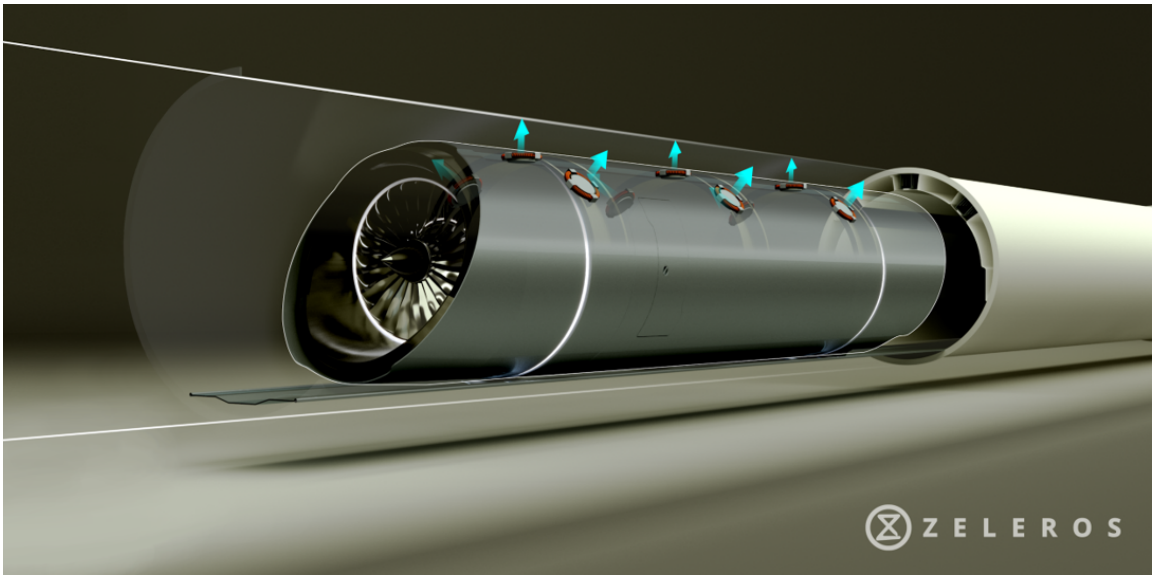

Figure 1.17: Levitation of the *Zeleros* concept.

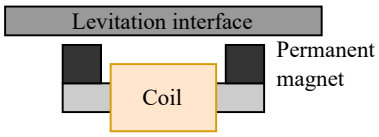

Figure 1.18: Detail of the levitation unit.

systems in [66].

Note that most approaches use EMS or HEMS for levitation, including the *Zeleros* one. As for the propulsion, only *Zeleros* uses aerodynamic propulsion. The rest employ linear motors, being the Synchronous the most common typology. This explains why all the concepts aim to operate at very low-pressures (100 Pa or less), while *Zeleros* can use 10 kPa.

1.10 Dynamic models

The modelling of maglev dynamics is explained in [71, 72]. These sources describe the equations used to model the dynamic behaviour of these vehicles in cruise operation. Even references about the Transrapid model have been found [73], which have been really useful in developing the *Zeleros* simulator.

Moreover, some hyperloop models have been found in the literature:

- Independent study from a PhD student of Swiss Federal Institute of Technology of Lausanne, Lausanne, Switzerland [74].
- TransPod model explanation [63].

- The optimisation of a Hyperloop generic model based on different magnetic propulsive approaches [70].
- The optimisation in the model of Virgin Hyperloop [75].

1.11 Thesis organization

In the **first chapter**, an introduction to the historical and most modern hyperloop-alike approaches has been done. The *Zeleros* concept was also described, which will be the central pillar for the rest of the thesis.

With the goals and the concept in mind, the **second chapter** describes the aerodynamics of the capsule, comparing it to a potential concept without a compressor. As hyperloop travels at a very high-speed in a closed environment, and *Zeleros* uses a compressor for the propulsion, the aerodynamics of the capsules are of significant importance for the model.

As there is a small gap between the vehicle and the tube during the capsule length, the friction effects on this domain are the object of study in the **third chapter**. This is known as Fanno flow and is highly important for the model described in the following chapter.

The dynamic model for the *Zeleros* concept is explained in detail in the **fourth chapter**. It includes information from the previous two chapters. Regarding the middle-scale system, another model similar to the previous one is explained in the **fifth chapter**. For both, several results using the models are conducted in their respective parts.

Finally, the main conclusions of all the studies are drawn in the **sixth chapter**.

Chapter 2

Aerodynamic study of the capsule

One of the main purposes of the thesis is to perform an aerodynamic study of the capsule as, due to the nature of its propulsion system, it is the most relevant force in the cruise phase of the hyperloop vehicle from *Zeleros*.

Part of this chapter has been published in the *Results in engineering* journal under the title "CFD simulation of a hyperloop capsule inside a closed environment", and in the *MDPI Applied sciences* journal under the title"CFD Simulation of a Hyperloop Capsule Inside a Low-Pressure Environment Using an Aerodynamic Compressor as Propulsion and Drag Reduction Method"; both papers with Temoatzin González and Sergio Hoyas as co-authors.

Nomenclature

β	Blockage ratio
L	Capsule length
h	Capsule height
r_c	Compressor radius
r_n	Nozzle radius
c_D	Drag coefficient
$\dot{m}_{ref}$	Tube mass flow
$\dot{m}_c$	Compressor mass flow
V_{ref}	Speed in the infinite
p_{ref}	Static pressure in the infinite
T_{ref}	Static temperature in the infinite
M_{ref}	Mach number in the infinite
$T_{t,ref}$	Total temperature in the infinite
$T_{t,c}$	Total temperature in the compressor
$T_{t,n}$	Total temperature in the nozzle
$p_{t,ref}$	Total pressure in the infinite
R	Ideal gas constant (287.55 kJ/kg/K)
γ	Perfect gas adiabatic ratio (1.4)

c_p	Specific heat at constant pressure (1006.43 kJ/kg/K)
N_T	Net thrust
$\dot{W}$	Power
y^+	Heigh of the first mesh layer in wall units

2.1 Introduction

Electric propulsion is the future in transportation [76]. This is why research in trains to overcome current speeds is widely conducted nowadays. In that sense, aerodynamics is not a minor issue if higher velocity wants to be achieved. Apart from other limits, such as the catenary contact [77] or the wheel-rail contact [78], aerodynamics is present in the ground transportation systems as a strong limitation, especially when focusing on tunnels.

Specific issues are peculiar to the movement of trains inside tunnels, and they do not appear in open air [56]. One of these problems is the compression and expansion waves generated when the train enters the tunnel. This scenario must be considered during the design process of a standard HSR. Also, other authors have researched this topic. Ehrendorfer et al. [79] analysed this particular entrance effect. Kwon et al. [80] used the response surface methodology and axisymmetric compressible Euler equations to optimise the nose shape of a train and minimise the tunnel compression wave. More work about nose optimisation was conducted by Choi and Kim in [81] and by Zhang in [82].

Conventional trains in tunnels, ETTs, and hyperloops have in common that are moving objects at high speeds inside a confined space. In this environment, two primary sources provoke drag [83, 84]. One of them is the choking of the flow when the local Mach number reaches its critical level. The second one is the presence of shock waves at transonic and supersonic speeds that travel through the tube. When critical Mach is reached, a high-pressure blockage is generated in front of the capsule, endangering the operability of this system.

In that sense, the Hyperloop Alpha [4] proposes two approaches to delay both effects in hyperloop. One way consists of increasing the tube size to reduce the blockage ratio of the capsule, which directly affects the cost of the infrastructure. The other is to add a compressor to the vehicle, which will increase the pressure of the shallowed air, preventing its acceleration and choking. The addition of a compressor will allow the use of smaller tunnels before reaching transonic speeds, reducing the cost of the infrastructure. In any case, the tube pressure can be lowered to reduce the impact of transonic patterns.

Taking into consideration the pressure as a variable, the ratio between the cross-sectional area of the capsule and the tunnel (known as Blockage Ratio or BR), and the speed or Mach number of the vehicle, several studies varying these parameters arise [81, 85, 86, 87]. Chen et al. [88] added the effect of the levitating gaps in their confined simulations. Liu et al. [89] provided significant conclusions, as he reported that the friction drag is far smaller than the pressure drag. They also noticed that the aerodynamic and pressure drag coefficients do not vary with the tube pressure but change considerably with the BR. The drag itself varied linearly with the pressure and almost squarely with the train speed.

A similar study was performed by Zhang [82], who varied the nose length to reduce the

aerodynamic drag more than a 2 % at 0.2 atm[1] and 800 km/h, with a BR equal to 0.2. Oh et al. [87] analysed a wide range of pressures, concluding that the pressure drag was significantly affected by the increase in the BR. Yang et al. [90] also reported that different operating speeds and working vacuum pressures significantly affected the resistance of the capsule and investigated the head and tail of the train to minimise this force.

The connection between the vacuum tubes has also been the object of study by other authors. Jia et al. [91] studied the Pressure Recycle Ducts (PRD) and the influence of the interval length and opening width of PRD on the differential pressure. Similar work was conducted in [56] for the Swissmetro project, which is equivalent to the hyperloop concept.

The effect of the temperature in the tube train was studied by Bao et al. [92] at 0.1 atm, from 243 K to 393 K. They reported that supersonic phenomena are more severe when decreasing the temperature, as the Mach number increases at a certain speed, 1000 km/h. High tube temperatures increase the speed of sound, reducing the Mach number for the same pod speed, delaying the onset of choking and reducing the aerodynamic drag. However, Oh et al. [87] reported that increasing the tube temperature to minimise drag is relatively inefficient.

Another field of study was more focused on the wave propagation itself, not only the drag of the vehicle. Chu et al. [93] used a three-dimensional compressible turbulence model to investigate the pressure waves generated while two trains were passing each other in a tunnel. Kim and Rho [94] reported that the pressure waves of a high-speed train in a tunnel show complicated variations due to their propagation and superposition. Zhou et al. [95] researched the wave phenomena produced by evacuated-tube maglev trains running at a super high speed. Finally, Niu et al. [96] analysed the formation and evolution mechanism of aerodynamic heating in the tube.

Other studies were performed for the Hyperloop Pod Competition [97] held by SpaceX and The Boring Company from 2016 to 2019 in Los Angeles, California. For the competition, several university teams studied the effects of the shape of the capsule inside a low-pressure environment.

One of the most relevant studies from these teams is the one from Braun et al. [98] for Purdue University. They designed a kind of hyperloop capsule that could generate lower drag and effective lift forces inside the evacuated tube. They conducted three-dimensional computational simulations of a hyperloop system with varying capsule shapes. They found that drag could be reduced by a maximum of 69 % compared with the optimised lift design.

Another important study was conducted by Opgenoord et al. [99] for the MIT, who predicted flow separation and transition on the capsule.

However, none of the previous studies, apart from the Hyperloop Alpha, considered using a compressor inside the evacuated tube, which is one of the main purposes of the present work. Chin et al. [100] presented in 2015 an overall system of the hyperloop concept and quantified the choking risk, which is determined by the minimum section between the capsule and the inner tube wall. Furthermore, the low-pressure operation leads to low Reynolds numbers, which enhances the risk of early separation of a laminar boundary layer in the rear part of the vehicle. They proposed adding a compressor to the

[1]To facilitate the discussion in this chapter, all the pressures are given in standard atmosphere units, or atm.

vehicle to overcome the choking problem, known as the Kantrowitz limit. Then, part of the mass flow passes through the capsule, increasing the maximum achievable speed.

This was the first time a study of an ETT performance with aerodynamic propulsion was conducted. However, no CFD was performed; only a 0D analysis was done to compute the energy consumption. They reported a difference of 0.16 on the Mach number just by adding a compressor. It is important to remark that Musk in [4] considered the compressor only for levitating purposes.

This study aims to compare the performance of a hyperloop that uses aerodynamic propulsion operating at a certain pressure level and one that does not. This comparison is conducted at different blockage ratios and train speeds, mainly focused on evaluating the power required to maintain the speed in both cases.

Moreover, from the parametric study for the blockage ratio, the equivalent tunnel size that matches the same performance for both cases is obtained. The aim is to quantify the tunnel size reduction when having aerodynamic propulsion on the vehicle, as proposed by Musk [4] and Chin et al. [100].

For this analysis, a simplified geometric model is employed. As it has been assumed axisymmetry on the case to reduce the computational cost, the model does not reproduce the actual geometry of a maglev train. Purely cylindrical shapes are used for the tube and the vehicle, the latter perfectly placed in the middle of the former. For research purposes, this simplification is still useful to compare cases in which the capsule has or has not installed the compressor, especially when using the blockage ratio as an independent variable instead of absolute areas. In any case, the model is based on the Transrapid Maglev train used in [85], whose maximum speed is 505 km/h [101].

This chapter is divided as follows. In the second section, the geometry, mesh, and set-up are exposed. Later, in the third section, the solver type is detailed, as well as the flow behaviour of the case without aerodynamic propulsion. Finally, the fourth section discusses the differences in the performance of the capsule and flow patterns when installing a compressor.

2.2 Materials and Methods

2.2.1 Geometry

Two different geometries are used for this study. The first geometry, shown in figure 2.1, does not include the compressor. The model had a total length of $L = 51.7$ m and a height of $h = 3.7$ m. From now on, this case is named *base*. The nose and tail of the geometry are equivalent ellipses of 4.6 m long, and the intersection angle with the horizontal axis is 70 degrees. Both ellipses are tangent to the straight part of the vehicle, which measures 42.5 m long.

Based on this geometry, a modified one is developed by adding a compressor on the front face of radius r_c, and a nozzle on the rear face of the capsule of radius r_n. The total length and height of the train are not modified. The nose and tail of the vehicle are still ellipses of the same length as the previous model, 4.6 m. Now, they are tangent to the compressor or nozzle lines and to the straight part of the vehicle.

From now on, this geometry, shown in figure 2.2, is named as *compressor*, or abbreviated *comp*.

All the cases for this paper have fixed the area of compressor and nozzle through their respective radius:

$$r_c = r_n = 3.2\,\text{m}. \tag{2.1}$$

This model is prepared to be axially swept. This geometric operation does not reproduce the actual geometry of a maglev train. However, as already mentioned, this process simplifies the simulation and still allows the performance comparison of both cases.

2.2.2 Numerical domain

The capsule is embedded into a cylindrical fluid domain. An axial plane can be seen in figures 2.1 and 2.2. To avoid the influence of the boundary conditions, the inlet and outlet of the tunnel are placed $10L$ away from the train, both upstream and downstream. This corresponds to 140 times the height h of the capsule, which is considered enough for this case. Other authors used smaller domains, such as Zhang et al. [82] who used $27h$ upstream and $50h$ downstream, Oh et al. [87] who used $1.76L$ upstream and $5.65L$ downstream, Bao et al. [92] who used $31.25h$ and $69h$, and Li et al. [86] who used $34h$ and $78h$ respectively.

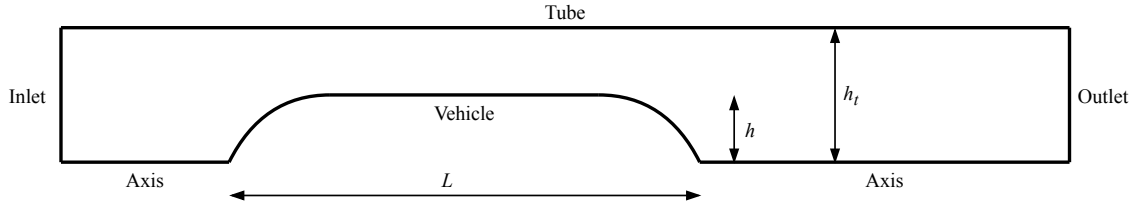

Figure 2.1: Drawing of the geometry for the *base* case. Not to scale.

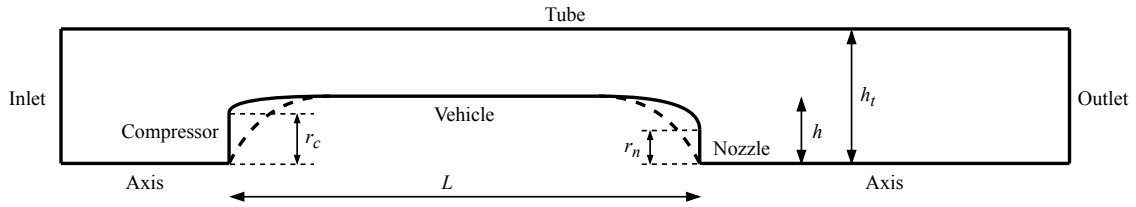

Figure 2.2: Drawing of the geometry for the *compressor* case. Not to scale.

Another input parameter is required to define the tunnel height. This is the blockage ratio β defined as the quotient between the cross-sectional area and the tunnel:

$$\beta = \left(\frac{h}{h_t}\right)^2. \tag{2.2}$$

Once β is fixed, the height of the tunnel, h_t, can be derived from equation (2.2).

2.2.3 Mesh

The mesh employed is a hybrid mesh formed using the blocks shown in figure 2.3. All the blocks are structured, apart from the two unstructured, marked with an u. These blocks are used to adapt the boundary layer mesh to the near field domain avoiding bad quality elements, as later discussed in figure 2.6. These unstructured regions use mainly quadrilateral elements.

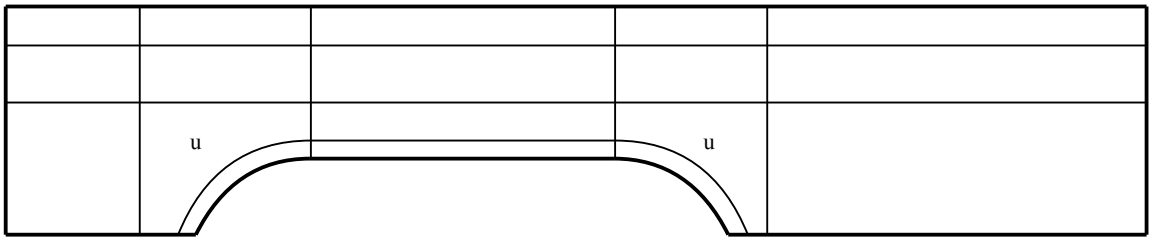

(a) Blocking of the *base* case.

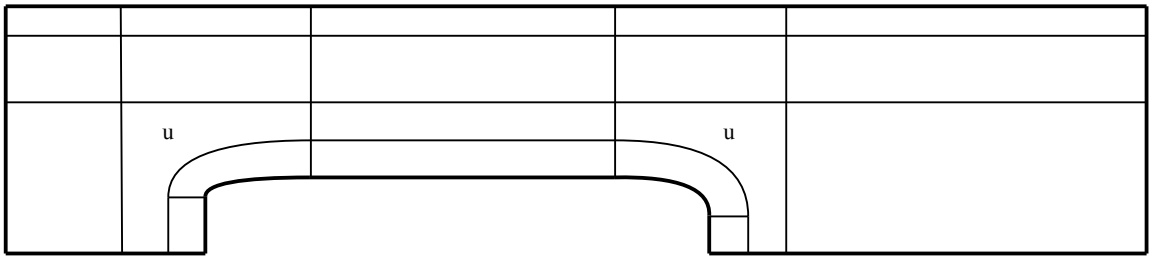

(b) Blocking of the *compressor* case.

Figure 2.3: Blocking chosen for the mesh.

Three meshes have been proposed to perform the mesh sensibility study (see table 2.2), using the drag coefficient c_D. The set-up chosen for this study is the most restrictive one, having the highest speed (700 km/h), pressure (1 atm) and β (0.75). This is the case where waves are stronger due to the larger energy on the inlet flow.

Mesh	**# Elements**	**y^+ tunnel**	**y^+ capsule**	**Drag**	**c_D**	**Error** [%]
Coarse	96045	3.14	4.63	16472904	16.539	-
Medium	171947	1.74	0.83	16407199	16.473	−0.40
Fine	366079	0.78	0.41	16410542	16.477	0.02

Table 2.2: Meshes used in the sensibility study.
More details about the mesh sensitivity study are provided in section 2.3.1.

The final mesh chosen is the medium-size one, which has 171,947 elements. The reason is that the difference in the drag with respect to the fine mesh is less than 1 %, which is also lower than the difference concerning the coarse one. Also, it is the first mesh that gets an y^+ lower than 1 in the capsule, as recommended by Bao et al. [92] in their ETT

simulations.

The mesh employed in [85] for the same geometry and speed had 77,000 elements. As the mesh parameters are equal on the *base* and *compressor* cases, the sensibility study is considered valid for both set-ups.

Regarding these parameters, the boundary layer on the tube wall has been set as a geometric progression using a first element height of 5×10^{-6} m, a progression ratio of 1.25, and 38 layers. For the boundary layer on the capsule, the resolution is increased, using a first layer height of 10^{-6} m, a geometric ratio of 1.2, and 58 layers. These prism layers allow obtaining a $y^+ = 0.83$ on the vehicle wall and $y^+ = 1.74$ on the tube wall.

The capsule boundary layer geometric progression is maintained until the normal distance to the wall (horizontal or vertical) is 0.37 m, which implies that the largest element in the unstructured region is 1.75 times larger than the last element height on the boundary layer. Then, the space between the two boundary layers has used a linear progression that ensures the same spacing on the border elements between blocks.

The mesh size on the compressor, turbine, and front and rear faces of the vehicle have a uniform spacing equal to the last boundary layer height (0.0326 m). On the channel, a bigeometric progression is imposed, using a geometric ratio of 1.05 for both ends.

A large element size is imposed near inlet and outlet boundaries to avoid wave reflection. These elements result from setting a geometric progression from the end of the unstructured block to the inlet and outlet boundaries. The growth ratio is 1.012 with 400 layers upstream and 1.006 with 700 layers downstream.

By using the mesh parameters already described, the meshes for the different blockage ratios are obtained. They are shown in figure 2.5 for the *base* case, and in figure 2.4 for the *compressor*. Note that both cases are equivalent in terms of element size and distribution. The captures are taken for the case of $\beta = 0.75$, which is considered the most restrictive due to the proximity of both boundary layers. For the first case, a capture for $\beta = 0.20$ is also provided to show better how the channel between the vehicle and the tube has been discretised.

The quality and number of elements for each mesh are collected in table 2.3. The quality is always above 0.37 for the *base* case, and above 0.33 for the *compressor* case. Moreover, only one element has a quality below 0.4 for the first case and only 20 (around 0.01 %) for the second case. To better understand what this implies to the actual mesh, figure 2.6 represents the worse quality elements for the *compressor* case, whose quality is slightly lower. These elements are mainly near the border between the structured and unstructured blocks, as the mesh has to transition from the boundary layer to the near-field size.

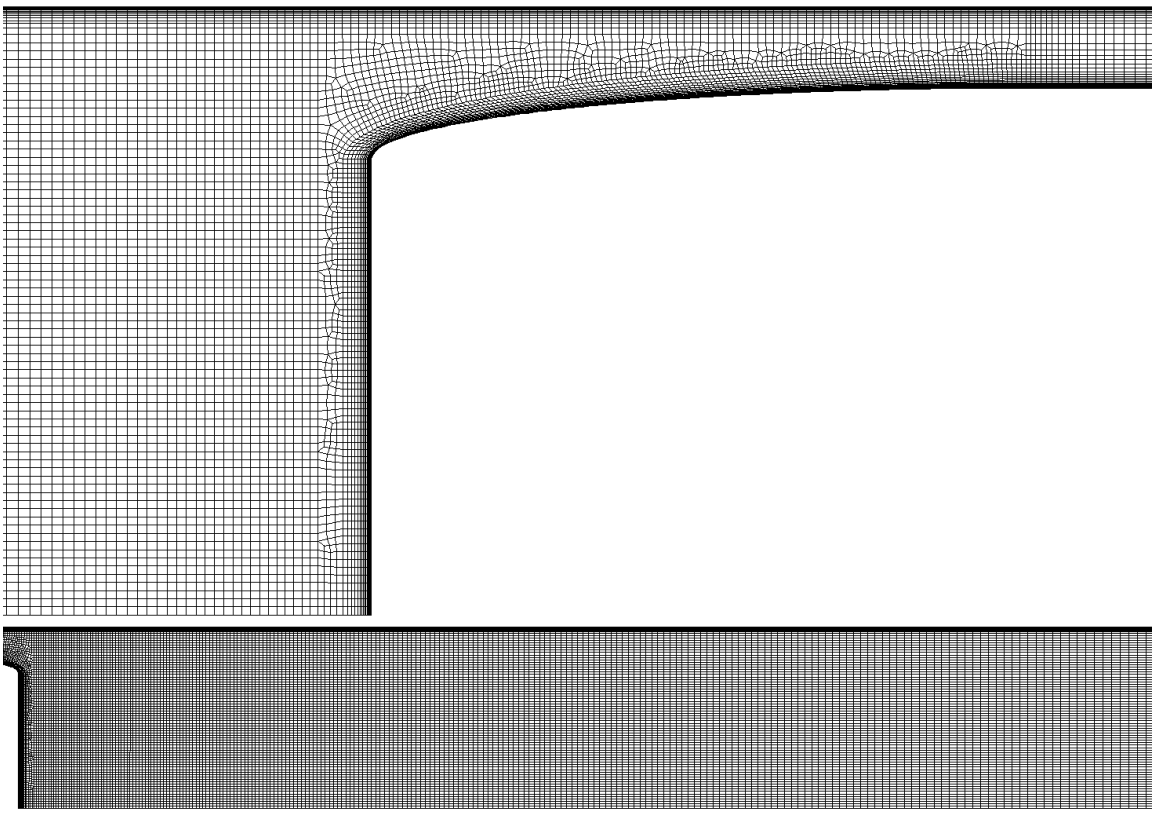

Figure 2.4: Captures for the mesh used in the *compressor* case and $\beta = 0.75$. The top figure is for the upstream domain, and the bottom is for the wake.

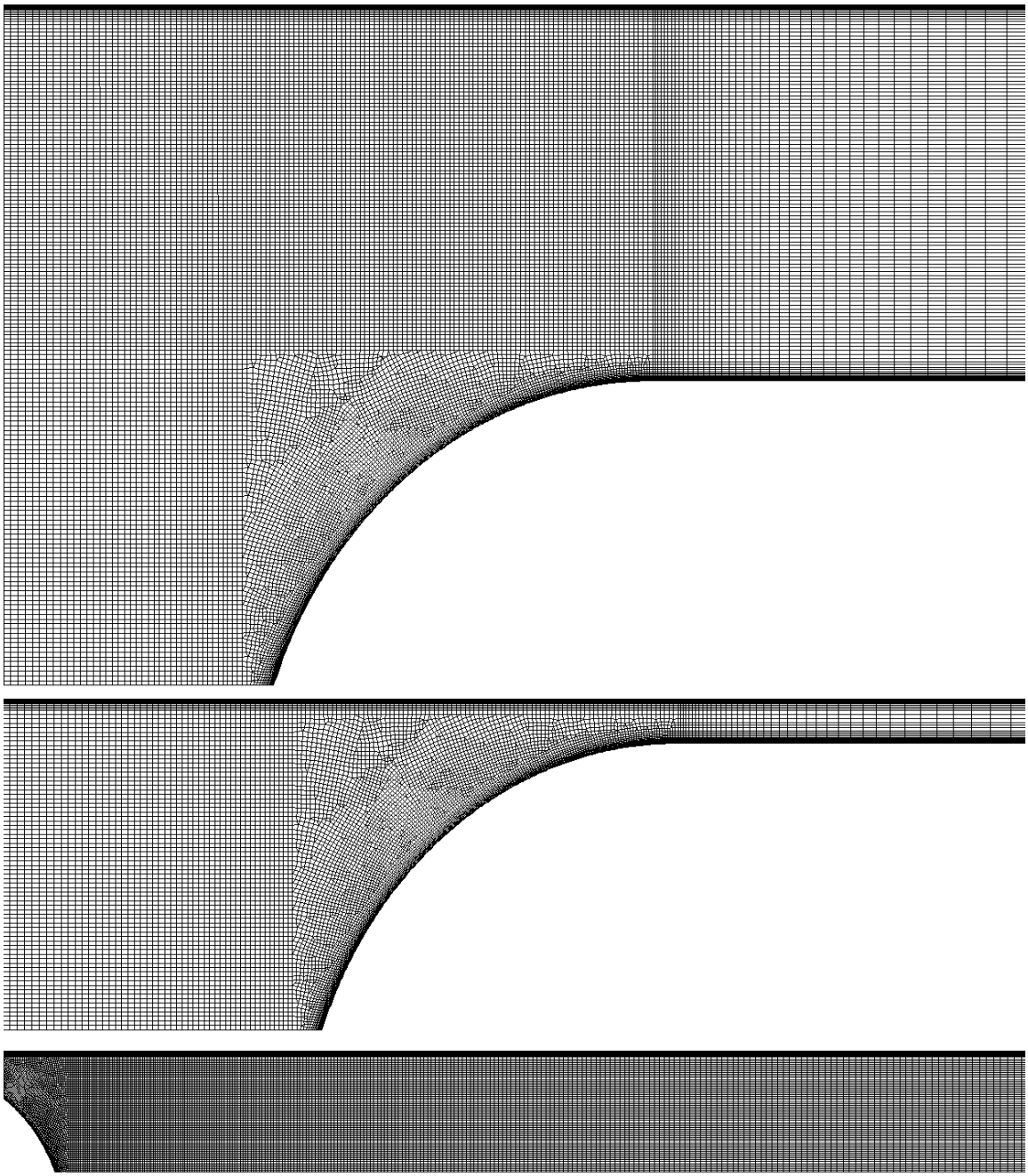

Figure 2.5: Captures for the mesh used in the *base* case. Except the upper one, which is for $\beta = 0.2$, the rest of the images are for $\beta = 0.75$. The top figures show the upstream domain, and the bottom shows the wake.

Case	BR	Min. quality	Mean quality	Elements
Base	0.20	0.3727	0.9975	297971
Base	0.35	0.3727	0.9968	234251
Base	0.50	0.3727	0.9963	201683
Base	0.60	0.3727	0.9960	187523
Base	0.70	0.3727	0.9958	176195
Base	0.75	0.3727	0.9957	171947
Comp	0.20	0.3372	0.9982	298121
Comp	0.35	0.3372	0.9977	234446
Comp	0.50	0.3372	0.9973	201901
Comp	0.60	0.3372	0.9971	187751
Comp	0.70	0.3372	0.9969	176431
Comp	0.75	0.3372	0.9968	172186

Table 2.3: Quality and mesh size for the different cases.

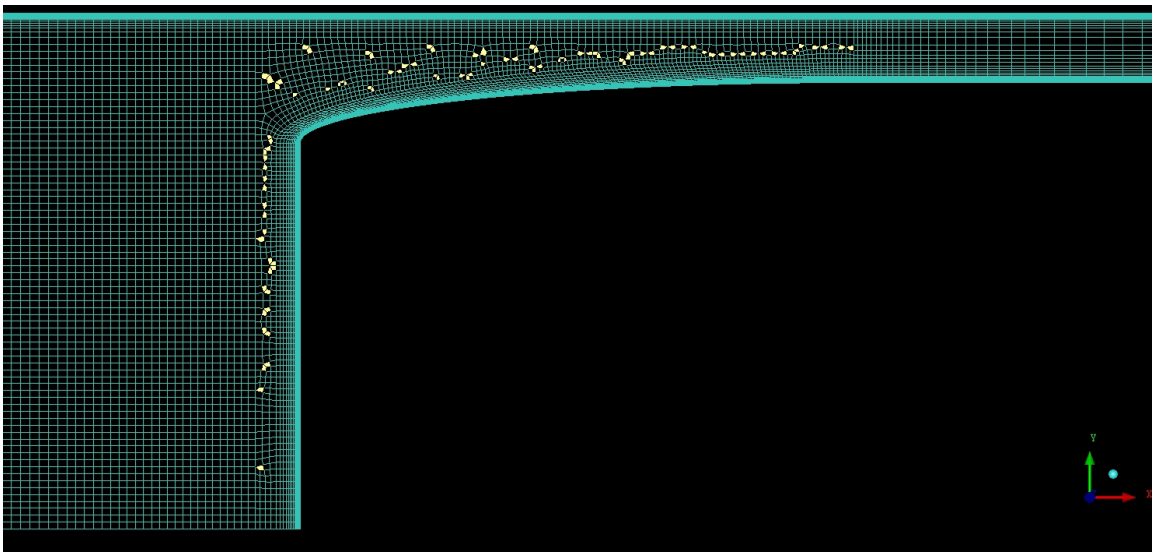

Figure 2.6: Contours of lowest quality (< 0.5) elements on the *compressor* case for $\beta = 0.75$.

2.2.4 Set up

The simulation has been conducted using a 2D axisymmetric model to reduce the computational cost, maintaining the accuracy of the results. The rotation axis is the *axis* line shown in figure 2.1 and figure 2.2. Previous studies also used this hypothesis for both trains at atmospheric pressure [80] and at low-pressure [85, 89, 95].

Some authors also compared the accuracy of their results using a 3D and a 2D axisymmetric model. Ehrendorfer et al. [79] compared the 2D model with experimental results at

real-scale and atmospheric pressure, concluding that the wave problems were reproduced correctly. Li and Yuangui [102] performed a similar experiment in 2017, focusing on the transonic entrance of a train in a tunnel with the 2D model. For lower pressures, Oh et al. [87] compared simulations for a sphere, concluding that, at transonic speeds, the maximum error on the drag was about 4 %.

Regarding the thermodynamic parameters, the specific heat ratio γ and ideal gas constant for the air R, are considered invariant with the pressure. Regarding the viscosity, the Sutherland model has been used as in [87, 82, 85].

The scheme employed is a second-order spatial discretisation, using $k-\omega$ SST model as turbulence model [87]. Kim et al. in [85] compared the results for different turbulence models, including $k-\omega$ SST, $k-\epsilon$, Spalart-Allmaras, and a laminar case for the same *base* scenario presented in this work. They reported less than a 4 % of difference among all the models simulated.

Furthermore, Morden et al. in [103] compared the different turbulence models concerning experimental results of train aerodynamics. They concluded that the $k-\omega$ SST model provided the best surface pressure among the available RANS models.

The solver is compressible pressure-based. A Riemann solver has also been tested, whose results are shown in section 2.3.2.

Regarding the steadiness of the case, a steady solver has been selected to reduce the computational cost, as only time-averaged values are to be obtained. An unsteady simulation has also been performed to check the validity of this hypothesis, whose results are shown in section 2.3.2. The use of a steady solver is valid since wave propagation is not studied, which is a time-dependent effect. Only steady-state values for the drag and thrust want to be computed.

The different boundaries conditions on the domain, marked in figure 2.1 and figure 2.2, are:

- Inlet: it is imposed the mass flow $\dot{m}_{ref}$ and the total temperature $T_{t,ref}$. Both are based on the capsule speed V_{ref}, reference pressure p_{ref}, static temperature T_{ref}, and the tunnel area $\pi h^2/\beta$:

$$\dot{m}_{ref} = \frac{p_{ref}}{RT_{ref}} \frac{\pi h^2}{\beta} V_{ref}, \tag{2.3}$$

$$T_{t,ref} = T_{ref} + \frac{V_{ref}^2}{2c_p}. \tag{2.4}$$

- Tube: moving and adiabatic wall. The speed on the wall is equal to the speed of the capsule, V_{ref}, in a ground reference frame.
- Outlet: pressure outlet, set to the same pressure as the reference pressure of the tube p_{ref}.
- Vehicle: static and adiabatic wall.
- Axis: rotation axis to convert the 2D domain into an axisymmetric one.

- Nozzle: mass flow inlet. It is imposed the mass flow that the turbomachinery can shallow $\dot{m}_c$, and the total temperature at the nozzle exit $T_{t,n}$. The value chosen for both variables is discussed in section 2.2.6.
- Compressor: pressure outlet, modifying the pressure until the mass flow set on the nozzle is obtained.

Zhang et al. in [82] used pressure-far-field for the inlet and the outlet to describe free compressible flow at the infinite boundary. However, this condition implies providing the pressure, temperature, and Mach number at both boundaries, imposing the mass flow as a consequence. This condition may cause several problems if it is not placed very far away is not realistic to set the far field Mach and pressure. Also, as the thermal transfer to the tube is not modelled, the infinite temperature and pressure cannot be reached at the outlet. This is because friction effects on the vehicle, and the inefficiencies of the compressor add energy to the flow. Finally, if some boundary layer remains on the tube, the pressure-far-field will dissipate. All these issues may even lead to convergence problems in the case.

The values taken by the different variables are listed below:

- Reference speed V_{ref}: 505 km/h (current limit for Transrapid) and 700 km/h (higher speed considered for hyperloop).
- Reference pressure p_{ref}: 0.1 atm.
- Blockage ratio β: from 0.2 to 0.75.
- Reference temperature T_{ref}: 288.15 K, same as in [85].
- Turbulence intensity: 5 %.

The tunnel size is computed using a range for the blockage ratio. The lower limit is based on current HSR tunnels, 0.23 [104, 105]. Other studies used similar values such as 0.2 in [82] and 0.28 in [92]. The upper limit of the blockage ratio has been chosen as 0.75 because, at this value, the boundary layer of the tunnel and the capsule nearly collapse.

Regarding the selected pressure, for the *base* case, 0.01 atm, 0.1 atm, and 1 atm are studied; while for the *compressor* case, only 0.1 atm is simulated. This is the expected pressure that a hyperloop installing a compressor could work. It is also the value used by other authors in their ETT studies, such as Bao et al. [92] and Swissmetro [56]. Zhang et al. [82] used a similar figure, 0.2 atm.

The solver used for this case is ANSYS Fluent. 8 cores were used during 56 hours to compute the 168 cases.

2.2.5 Inlet boundary condition

Concerns about the choice of the boundary condition at the inlet exist due to the simplification of the problem. As will be discussed in section 2.3.3, the drag value is highly dependent on the upstream boundary condition. Two different boundary conditions are analysed, total pressure inlet and mass flow inlet.

In the real case, the upstream thermodynamic conditions vary continuously due to the wave propagation inside a tube. The consequence is that the drag is not only a function of the actual speed of the capsule V_{ref}, but also of the position of the train inside the tunnel, how fast this speed has been reached, and where the boundary conditions are placed (i. e. tube walls, another vehicle, changes on the tube size...). This effect cannot be reproduced with the current simplification of the problem and makes it not possible to set a constant value for the inlet boundary.

As a representative average result, the boundary condition chosen at the inlet imposes the mass flow. This condition is the most restrictive and represents the case in which all the mass flow passes through the channel between the tunnel and the train. This is considered the design point of hyperloop, as it avoids air compression in front of the capsules, which would considerably increase the drag on a route. If the total pressure is imposed, the mass flow that should pass through the vehicle may not be guaranteed.

The behaviour of the boundary conditions is a relevant difference with respect to an open tunnel. While in a closed tube, if the required air does not pass around the vehicle, it ends up being compressed in the front; with open ends, this displaced air can exit the domain without being compressed.

However, the inlet boundary condition is not the only factor affecting upstream flow behaviour. If too much mass flow is imposed on the inlet, the Kantrowitz limit [106] is reached. This limit occurs when the flow reaches sonic conditions (Mach equal to 1) on the smaller cross-sectional area, which is the passage between the tunnel and the capsule. Using an isentropic 1D simplification, the Kantrowitz limit leaves a 2D space in the plane (β,M_{ref}) in which the flow is not blocked, and all the mass flow can pass around the capsule without increasing its far-field pressure. This solution space is shown in figure 2.7.

The Mach number where the Kantrowitz limit is achieved is the critical Mach number. Beyond this value, if the physical mass flow is imposed, the pressure has to increase over p_{ref} and speed has to decrease under V_{ref} to maintain the inlet corrected mass flow, as it will be seen in figure 2.16.

2.2.6 Specific set up for the compressor and nozzle

This case has two additional degrees of freedom: the internal mass flow $\dot{m}_c$, directly imposed on the compressor and nozzle boundary conditions; and the specific power transmitted to the flow, imposed on the nozzle through the total temperature $T_{t,n}$. Both are varied to meet the following specifications:

- Net thrust (N_T) equal to 0. This ensures that the case is comparable to the *base* one. The net thrust is computed as follows:

$$N_T = \dot{m}_c \left(V_n - V_c\right) + p_n A_n - p_c A_c - D_{wall}. \tag{2.5}$$

- Same isentropic efficiency η throughout all cases, equal to 0.07.

The fact that the value for the isentropic efficiency is so low can be explained due to its definition. This parameter tries to collect in one number all the processes that occur inside the hyperloop capsule and, for simplicity, are not modelled in the CFD. These are the flow

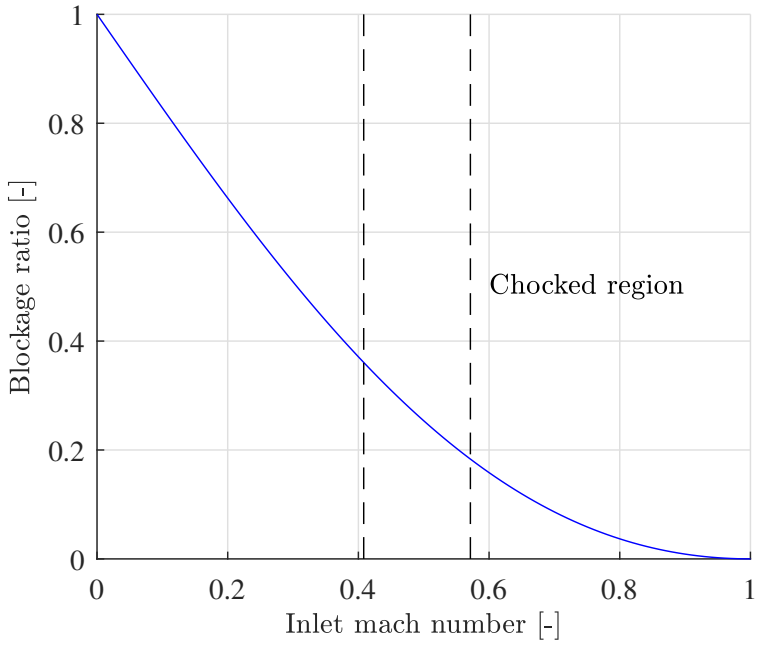

Figure 2.7: Kantrowitz limit as a function of the inlet Mach of the domain M_{ref} or the blockage ratio β. Speeds of 500 km/h and 700 km/h, computed using a static temperature of 288.15 K, are marked with dashed lines.

compression on the turbomachinery, internal duct, and flow expansion on a turbine and a nozzle. All the inefficiencies of these three processes are included in η.

The $T-s$ diagram shown in figure 2.8 represents thermodynamically what is occurring to the non-modelled flow and helps to understand the definition of the efficiency. In this figure, the three evolutions shown are:

- Intake and compressor (c): from 2 to 3.
- Internal ducting (f): from 3 to 4.
- Turbine and nozzle (t): from 4 to 5.

With these values in mind, the isentropic efficiency is defined as follows:

$$\eta = \frac{T_{25ts} - T_{2t}}{T_{5t} - T_{2t}} = \frac{\pi^{\frac{\gamma-1}{\gamma}} - 1}{\frac{T_{5t}}{T_{2t}} - 1} = \frac{\pi^{\frac{\gamma-1}{\gamma}} - 1}{\frac{T_{t,n}}{T_{t,c}} - 1}, \tag{2.6}$$

where π is the total pressure ratio on the compressor and the nozzle.

Further details about what occurs to the internal flow are provided in chapter 4. For this study, the purpose of this definition is to have a way to measure the non-modelled flow and ensure equality among the different cases.

The values obtained for the compressor and nozzle boundary conditions that match the prescribed net thrust and efficiency are collected in table 2.4.

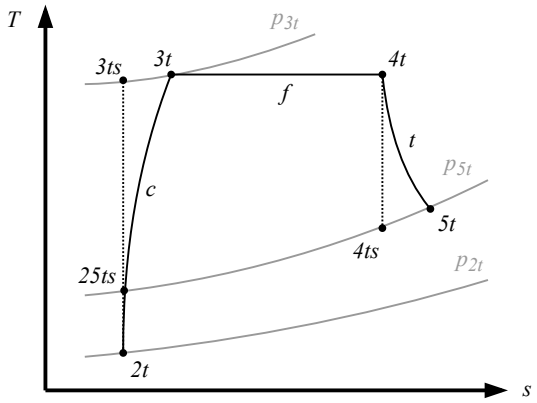

Figure 2.8: $T - s$ diagram showing the thermodynamic evolution of the internal flow of the capsule. In this diagram, the intake is station 2, and the nozzle exhaust is station 5.

BR	$\dot{\mathbf{m}}_\mathbf{c}$ **@ 500 km/h**	$\dot{\mathbf{m}}_\mathbf{c}$ **@ 700 km/h**	$\mathbf{T_{t,n}}$ **@ 500 km/h**	$\mathbf{T_{t,n}}$ **@ 700 km/h**
0.20	540.3 kg/s	750.5 kg/s	310.8 K	327.1 K
0.35	558.9 kg/s	780.1 kg/s	313.8 K	333.7 K
0.50	584.2 kg/s	828.1 kg/s	319.0 K	348.5 K
0.60	607.9 kg/s	883.4 kg/s	324.9 K	369.7 K
0.70	639.2 kg/s	931.9 kg/s	333.7 K	394.3 K
0.75	657.4 kg/s	950.9 kg/s	339.4 K	411.3 K

Table 2.4: Internal mass flow and nozzle total temperature for the different cases considered.

2.2.7 Knudsen number

It is important to check that the continuum medium hypothesis is still valid for the most restrictive case, 0.01 atm, otherwise, the Navier-Stokes equations cannot be used. For that purpose, the Knudsen number Kn is computed to ensure that it is lower than 0.01 [89]. This number is defined as:

$$Kn = \frac{k_b T}{\sqrt{2}\pi d^2 P L}, \tag{2.7}$$

where:

- L: characteristic length, based on capsule length $L = 51.7$ m, as in [98].
- P: operating pressure, using $p_{Ref} = 0.1$ atm.
- T: operating temperature, using $T_{ref} = 288.15$ K.
- k_b: Boltzmann constant.
- d: characteristic particle length, which is taken as the hard diameter of O_2 molecule, which is 4.07×10^{-10} m [107].

For the present case, this value is 1.03×10^{-8}, which means the continuous medium hypothesis is valid. In fact, it would still be valid for pressure values as low as 10^{-7} atm, which are out of scope for this application.

2.3 Results

Before exposing the results, it is important to explain how the drag coefficient c_D is obtained. It is based on the wall speed, the tunnel reference pressure, and the cross-sectional area of the capsule:

$$c_D = \frac{2D}{\rho_{ref} A_{ref} V_{ref}^2}. \tag{2.8}$$

The reference area A_{ref} is obtained as follows:

$$A_{ref} = \pi h^2. \tag{2.9}$$

2.3.1 Mesh sensibility

As previously commented in section 2.2.3, three meshes have been proposed to perform the mesh sensibility study, choosing as the final mesh the medium size one.

The contours of Mach number for the three meshes are plotted in Figure 2.9. There, the difference between the different cases is almost unnoticeable.

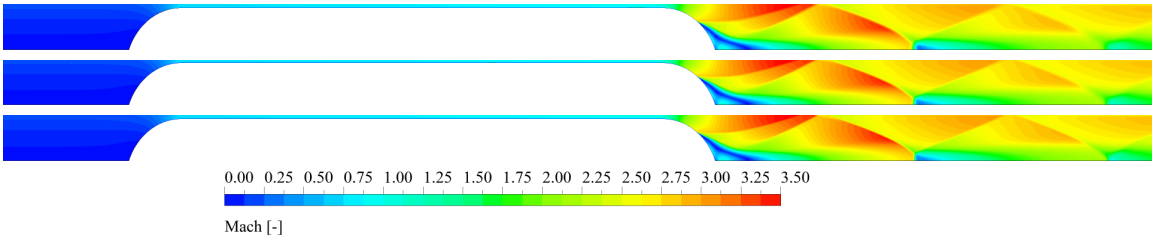

Figure 2.9: Mach contours for the cases of the mesh sensibility study. The top contour is the coarse mesh, and the bottom is the fine one.

2.3.2 Solver type

Due to wave propagation, the flow is unsteady. However, to reduce the computational cost of the simulation, a comparison between a steady and an unsteady case (with time step equal to 10^{-6} s) has been performed.

An unsteady Riemann solver was also tested. A priori, this solver is the one recommended for highly compressible cases, where compression waves appear. This result and the ones from the steady comparison are collected in table 2.5. The set-up for the case is the same as the mesh sensibility one.

Solver	Drag [kN]	Error [%]
Riemann	16423	-
Pressure based transient	16408	-0.088
Pressure based steady	16502	-0.095

Table 2.5: Different solvers used.

Pressure-based steady solver is used for the rest of the cases, according to the results shown in table 2.5. Note that the difference between this solver and the theoretically preferred (Riemann) is less than 1 %, while the former is significantly faster.

It is important to remember that the goal of the present work is to obtain steady-state values for the drag, not to reproduce the wave propagation on the domain.

However, even in a steady scenario, the effect of the waves regarding the variation of the pressure and speed upstream of the domain can still be reproduced as an average induced value, as seen in section 2.3.3.

2.3.3 Inlet boundary condition

As discussed in section 2.2.5, one of the uncertainties of this case is the boundary condition on the inlet. For this reason, two different conditions on the *base* scenario have been tested:

- Impose mass flow (case 1), computed using the reference values and the area of the tunnel:

$$\dot{m}_{ref} = \rho_{ref} \pi h_t^2 V_{ref}. \tag{2.10}$$

- Impose total pressure (case 2), computed using the reference pressure and speed:

$$p_{t,ref} = p_{ref} \left(1 + \frac{\gamma - 1}{\gamma} \frac{V_{ref}^2}{\gamma R T_{ref}} \right)^{\frac{g}{\gamma - 1}}. \tag{2.11}$$

Results are shown in table 2.6. The values are obtained for a reference pressure of 0.022 atm and 0.021 atm, as in [85].

Note that case 1 provides higher drag than the reference value, while case 2 is the opposite. The main reason is the larger upstream pressure (p_{inlet}) when imposing the mass flow, which also implies a reduction in the speed V_{inlet} in all the cases. The difference concerning the reference speed is known as *induced speed*.

This means that the actual value of drag is highly dependent on the upstream boundary condition. In the real case, due to wave propagation in a closed environment where more than one train is circulating, this upstream pressure varies continuously. The consequence is that the drag is not only a matter of the actual speed of the capsule V_{ref} but also of the position of the train inside the tunnel and what has happened previously, which cannot be reproduced with the presented simplification of the problem.

As a representative average result, the boundary condition chosen is mass flow, as explained in section 2.2.4. This condition is the most restrictive, and it represents the case

Imposed	$\mathbf{V_{ref}}$	$\mathbf{p_{ref}}$	$\mathbf{V_{inlet}}$	$\mathbf{p_{inlet}}$	**Drag [kN]**	**Drag** [85] **[kN]**
Mass flow (1)	700	0.022	374	0.043	148.43	83.08
Pressure (2)	700	0.022	373	0.026	36.77	
Mass flow (1)	500	0.021	358	0.030	63.45	44.69
Pressure (2)	500	0.021	325	0.022	13.56	

Table 2.6: Drag for different boundary conditions and $\beta = 0.5$. Speed in km/h and pressure in atm.

in which all the mass flow goes through the channel between the tunnel and the train, which is more realistic in a tunnel with closed walls. Otherwise, the train will accumulate mass in front of it, increasing the pressure continuously until the drag reduces the train speed or the air can pass through the passage.

Note that, almost independently of the train speed V_{ref}, the actual flow speed upstream V_{inlet} is similar in all cases, and always lower than the reference one. This is a consequence of the channel blockage between the train and the tunnel. Regarding the pressure, imposing mass flow increases the upstream pressure considerably, 50 % at 500 km/h and 100 % at 700 km/h. When pressure is imposed, this effect also appears, but is less effective.

In any case, this increase in the inlet pressure leads to the drag differences seen in the table.

The fact that the pressure increases to maintain the flow through the passage is related to the Kantrowitz limit [106]. This limit occurs when the flow reaches sonic conditions (Mach equal to 1) on the smaller cross-sectional area, which is the passage between the tunnel and the capsule. Using an isentropic 1D simplification, the Kantrowitz limit leaves a 2D space in the plane (β,M_{ref}) in which the flow is not blocked, and all the mass flow can pass around the capsule without increasing the pressure intentionally. This solution space was shown in figure 2.7.

The Mach number where the Kantrowitz limit is achieved is known as the critical Mach number. Beyond this value, if the physical mass flow is imposed, the pressure has to increase to maintain the reduced mass flow, as seen in table 2.6.

To further detail what occurs with the pressure, the pressure coefficient along the tunnel is represented in figure 2.10. Its definition is:

$$C_p = \frac{p - p_{ref}}{p_{t,ref} - p_{ref}}, \tag{2.12}$$

where $p_{t,ref}$ is the total reference pressure.

As previously seen, there is a considerable increase in pressure on the front face of the capsule, larger as the tunnel gets smaller (larger β). For $\beta = 0.2$, note that the pressure coefficient variation on the inlet is almost negligible, which means this case is below the Kantrowitz limit seen previously. Once this limit is overcome, the pressure on the inlet increases as already exposed.

It is important to notice that there is a strong depression downstream of the capsule, followed by oscillatory behaviour due to the oblique shock waves still present in the tunnel.

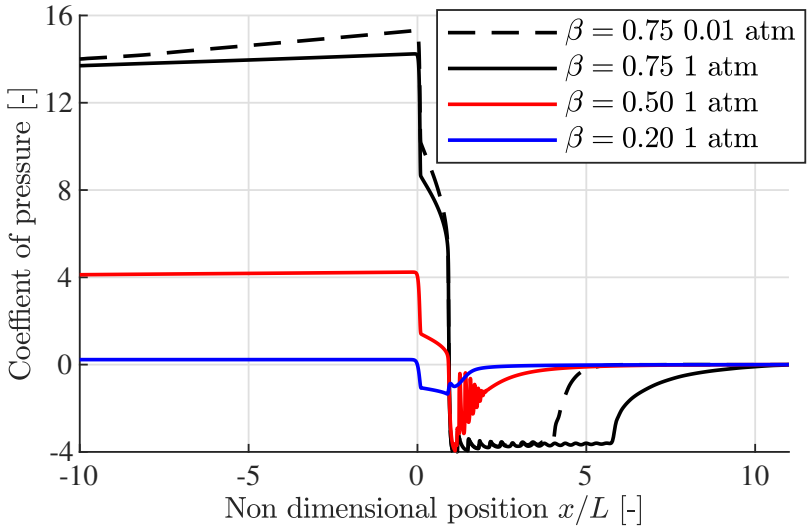

Figure 2.10: Coefficient of pressure along the tube for different cases (700 km/h).

Finally, there is a sudden compression of the flow to accommodate the outlet pressure. However, the difference with the reference pressure is not remarkable. For the largest tunnel ($\beta = 0.20$), there are no waves downstream, as the flow is not choked when passing through the small gap between the train and the tunnel.

Another remarkable effect is that the shape of the C_p evolution is more dependent on the BR than on the reference pressure, as seen when comparing the two black lines in figure 2.10.

These flow patterns are better seen when representing the contours of the Mach number in figure 2.12. There, the presence of shock waves due to the high-speed flow on the gap is evident. These waves explain the oscillatory behaviour of the pressure seen in figure 2.10, occurring at high BR but not at $\beta = 0.2$, where these supersonic patterns do not appear.

2.3.4 Flow behaviour for the *base* model

A parametric study using different values for the velocity (500 and 700 km/h), pressure (0.01, 0.1 and 1 atm) and blockage ratio (from 0.2 to 0.75) has been performed. The results are shown in figure 2.11, where the drag coefficient is plotted for the different parameters analysed.

There is a low dependency of the drag coefficient with the pressure, which means that the drag scales linearly with that parameter, as previously reported in [89]. In the figure, the significant dependency on the blockage ratio is also shown. If the tunnel has $\beta > 0.2$, the drag grows exponentially. Remember that the common value for HSR is 0.23, making it evident why the size of the tunnels is not smaller. It is important to remark that for 700 km/h, all the curve is above the Kantrowitz limit ($\beta = 0.18$), and for 500 km/h, the limit is $\beta = 0.36$. This explains why the slope is increasing considerably from those values, also stated in [87].

Focusing on an example, if taken the drag of the capsule at 700 km/h in a common

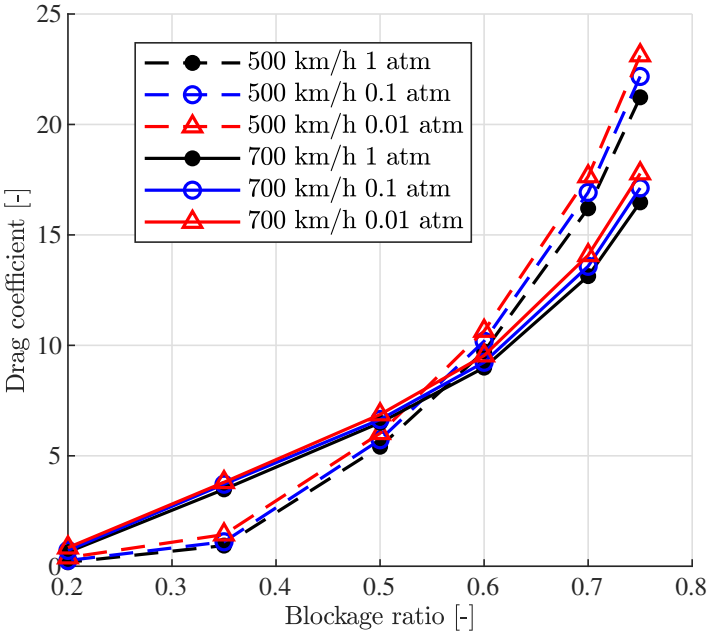

Figure 2.11: Drag coefficient for the parametric study.

tunnel ($\beta = 0.2$), the c_D is 0.64 at atmospheric pressure. This blockage ratio means that the tunnel has a radius 124 % higher than the one from the train. The same drag can be achieved when reducing the pressure to 0.1 atmospheres and using $\beta = 0.5$ ($c_D = 6.50$), which means that the tunnel is only required to be 41 % larger in terms of the radius with respect to the vehicle.

Finally, the speed affects values on the c_D curve, as all the simulated region is chocked. This is why the drag coefficient is far from being considered constant with speed on this range, although this parameter should be constant for purely subsonic flow as reported in [89]. The trend is highly dependent on the BR, as for lower BRs, the c_D is higher at 500 km/h, while at higher BRs, it happens the opposite.

Having said that, the Mach number contours of the flow for the *base* case are shown in figure 2.12 for three different blockage ratios: $\beta = 0.2, 0.5, 0.75$. Figure 2.12a represents the flow at 500 km/h and figure 2.12b at 700 km/h for 0.1 atm, and figure 2.12c for 0.01 atm.

Firstly, for $\beta = 0.2$, the flow is not sonic at any point, and there is a strong detachment downstream of the train. This detachment is larger at 700 km/h.

For the intermediate case, $\beta = 0.5$, the pattern is entirely different. While at 700 km/h, the flow holds oblique shock waves downstream the train, at 500 km/h, the Fanno flow is accelerated up to supersonic, but then this high-speed flow enlarges the downstream detachment.

Finally, at $\beta = 0.75$, the oblique shock waves are stronger than fro 700 km/h. However, for 500 km/h, the waves are starting to be developed, but they are rapidly diffused.

Then, figure 2.12b and figure 2.12c show the effect of the pressure at 700 km/h. For the first case, $\beta = 0.2$, the flow behaves similarly. Equivalent detachment occurs downstream

of the train without any sonic points. For the intermediate β, the obliques shock waves have been completely developed for 0.1 atm and not for 0.01 atm, in which, after the first reflection, the subsonic flow separates. Finally, for $\beta = 0.75$, there is a remarkable shock wave pattern downstream the train for both cases. Qualitatively, the flow behaves in the same way, independently of the pressure.

Once the flow reaches the critical Mach number, the cases start to behave as a converging-diverging nozzle. There, the passage acts as the throat; upstream of the capsule, there is subsonic flow, and downstream, a supersonic region appears.

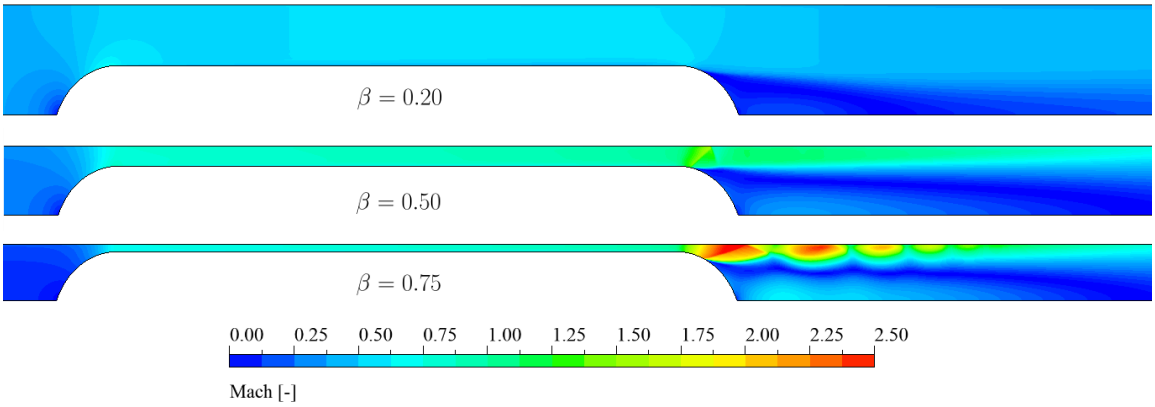

(a) 500 km/h and 0.1 atm.

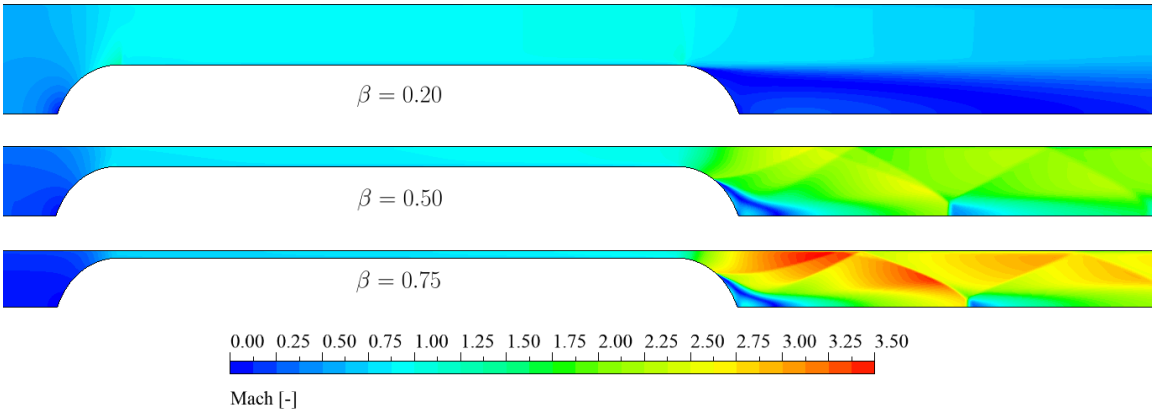

(b) 700 km/h and 0.1 atm.

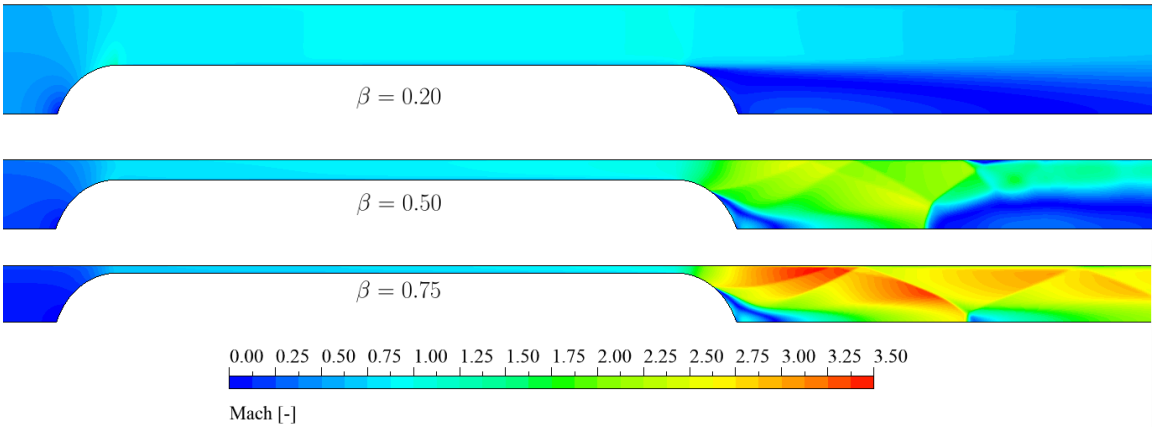

(c) 700 km/h and 0.01 atm.

Figure 2.12: Mach contours for $\beta = 0.2$, $\beta = 0.5$, and $\beta = 0.75$ and different pressures and speeds.

2.4 Discussion

The discussion section is based on comparing the performance of the *base* and *compressor* cases. The drag cannot be used for that purpose, as by definition is null for the *compressor* case, so, a new variable needs to be employed: the input power.

When the compressor is not installed, and the train is a completely closed body, the aerodynamic resistance is a variable representative of the performance of the vehicle. However, in the *compressor* case, the capsule is not a closed body, and part of the flow is allowed to go through it, increasing its energy internally thanks to the turbomachinery. In this scenario, the drag and the thrust have no physical meaning if computed separately; only the net thrust can be obtained. The net thrust is not a variable comparable to the drag of the first case. Note that the former has to be equal to zero for the comparison, as discussed in section 2.2.6.

The definition of the power takes into account the required energy per time unit that maintains the vehicle speed; in the *base* case to overcome the drag and in the *compressor* case to reach a zero net thrust level. Thus, the power is computed differently depending on the case:

- *Base* case: the mechanical power transmitted to the vehicle: $\dot{W}_{base} = DragV_{ref}$.
- *Compressor* case: the aerodynamic power the compressor transmits to the fluid: $\dot{W}_{comp} = \dot{m}_c c_p \left(T_{t,n} - T_{t,c}\right)$.

Note that none of the cases considers the efficiency, which means that the electric machine that drives the system must have higher power. This is a strong simplification, as the *base* case is typically driven by a linear motor, whose electromechanical efficiency is considerably lower than that of a rotatory motor driving the compressor.

Once it is clear how the power has been defined, in figure 2.13 the required power for the *base* and *compressor* cases is compared. The main conclusion is that, while the difference is not important for low blockage ratios, for higher ones, it is beneficial to use a compressor to minimise the required energy for both 500 km/h and 700 km/h.

From the same figure, note that, for the *base* case, the slope of the curve at 700 km/h increases exponentially for all the BR, as the Kantrowitz limit has been surpassed from $\beta = 0.18$. When the reference speed decreases to 500 km/h, this exponential growth also starts from the same limit, set at $\beta = 0.36$. In case of installing the compressor, the slope of both curves is considerably lower, especially at 500 km/h when the Kantrowitz limit is never reached.

The actual percentage that the *compressor* case improves is represented in figure 2.14. Note that for low blockage ratios, the compressor does not work properly (even worse for 500 km/h), but for high blockage ratios, the power consumption is around 70 % lower than for the *base* case. Both curves decrease asymptotically to a certain value, from which the relative improvement of the compressor is constant.

The compressor bases its improvement on delaying the transonic effects. Thus, the shock waves present in figure 2.12 occur at higher speeds, as will be discussed in figure 2.15, and the induced pressure and speed upstream of the capsule are mitigated, as it will

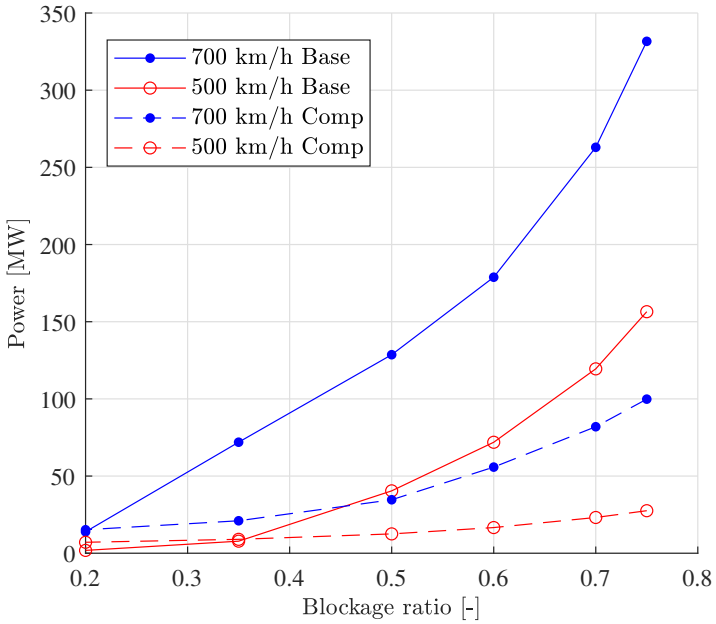

Figure 2.13: Required power comparison for the different blockage ratios and speeds, at 0.1 atm.

be seen in figure 2.16. These effects, as they appear at high blockage ratios, explain why the improvement of the compressor is more significant in this region.

Thus, the power reduction can be better explained by analysing the flow patterns. This is why in figure 2.15 the Mach contours for the *base* and *compressor* cases are compared for different blockage ratios at the largest simulated speed, 700 km/h.

For $\beta = 0.20$, figure 2.15a shows no shock waves in none of the cases. However, the acceleration of the flow on the passage is more significant for the *base* case. Here, the improvement in the case is not due to the avoidance of transonic effects but a consequence of the mitigation of the downstream subsonic separation.

For $\beta = 0.50$ and $\beta = 0.75$ in figures 2.15b and 2.15c respectively, the flow behaviour is equivalent. For the *base* case, the flow is so accelerated on the channel that obliques shock waves appear. These waves disappear when the compressor is installed, explaining why the required power is considerably reduced.

Actually, for $\beta = 0.20$ and $\beta = 0.50$ the flow on the *compressor* case is subsonic everywhere, as these cases are operating under the Kantrowitz limit (see figure 2.17). For $\beta = 0.75$, figure 2.15c shows that Mach numbers greater than 1 are locally reached, but shock waves are still avoided.

It is important to remark that the flow patterns with the compressor are more uniform among the cases. Qualitatively, they are not affected by the size of the tunnel.

On the other hand, the effect on the induced speed is shown in figure 2.16, where the actual inlet speed from the simulation is plotted against the blockage ratio for different reference speeds. Note that the *compressor* case, especially at 500 km/h, can maintain the capsule speed at the inlet. However, for the *base* case, the upstream pressure increase does

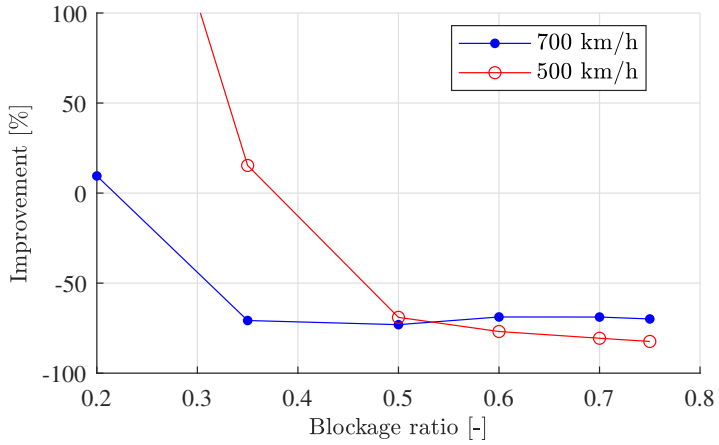

Figure 2.14: Power improvement of the compressor case concerning the *base* case for different blockage ratios and speeds.

not allow maintaining the inlet speed, which decreases linearly with the blockage ratio.

Also, note that induced speed is nearly the same for the *base* case for both reference speeds, as this effect mainly depends on the geometry.

Not only the mitigation of the shock waves, but the fact that the induced speed for the *compressor* case is considerably lower is also an indicator of the improvement in this case.

Then, it is analysed how far each case is from reaching the Kantrowitz limit. This is evaluated by computing the Mach number at the end of the passage between the capsule and the tunnel, which is the throat for these cases. Thus, it is the location where sonic speeds are firstly reached. The Mach number is represented in figure 2.17 for each reference speed and BR. Not only from CFD but it is also obtained the isentropic Mach number M computed using the compressible mass flow equation, comparable to the *base* case:

$$(1-\beta)\,M\left[1+\frac{\gamma-1}{2}M^2\right]^{-\frac{\gamma+1}{2(\gamma-1)}} = M_{ref}\left[1+\frac{\gamma-1}{2}M_{ref}^2\right]^{-\frac{\gamma+1}{2(\gamma-1)}}. \tag{2.13}$$

For 700 km/h and no compressor, the capsule always operates above the Kantrowitz limit, which is what the operator wants to avoid. As previously mentioned, the limit is 0.18 according to the analytic approximation. In this scenario, quite big tunnels (BR less than 0.2) have to be used, which is a BR even lower than for HSR (0.23). For 500 km/h, the Kantrowitz limit occurs at 0.36, which is not an exceptionally high value.

The use of a compressor increases these limits considerably, allowing full BR operation at 500 km/h and limiting the operation to tunnels of $\beta = 0.5$ or lower blockage ratios for 700 km/h.

The analytical approximation closely follows the trend of the *base* case. However, it is required to have more CFD points to reproduce the exact BR accurately where sonic conditions are reached. Also, note that, although the analytical approximation outputs a Mach equal to 1 on the throat, the CFD value is slightly higher than 1. This was also reported by Lijo et al. in [108] after conducting some experiments for a Poiseuille flow in a pipe.

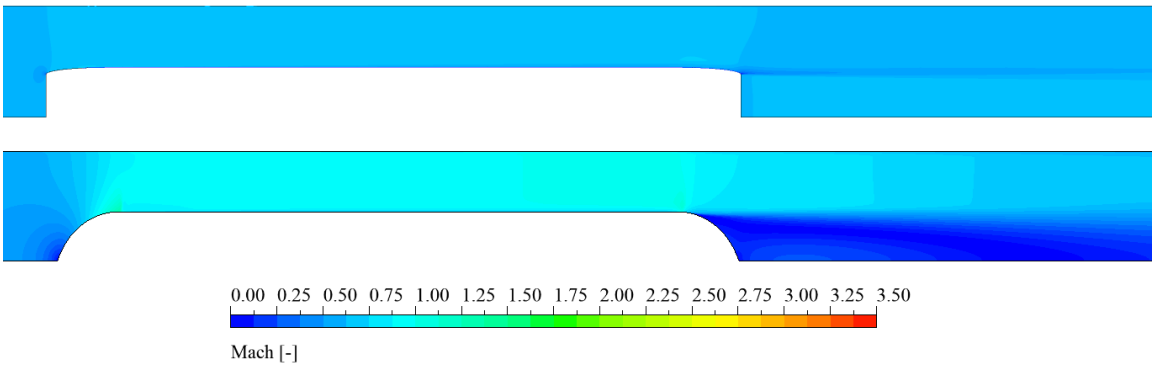

(a) $\beta = 0.20$.

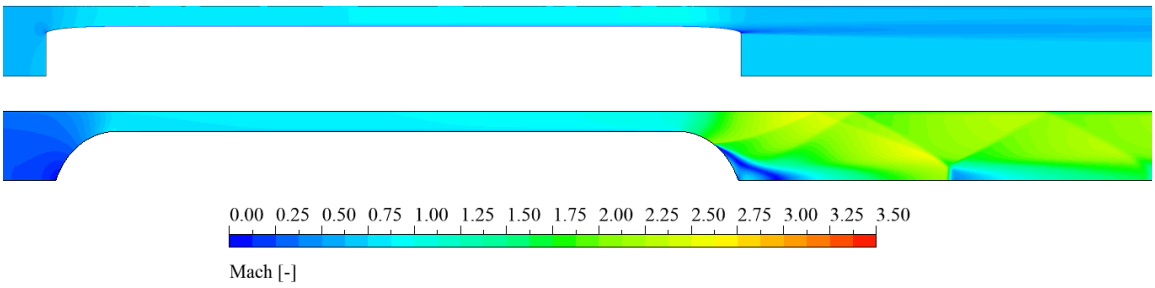

(b) $\beta = 0.50$.

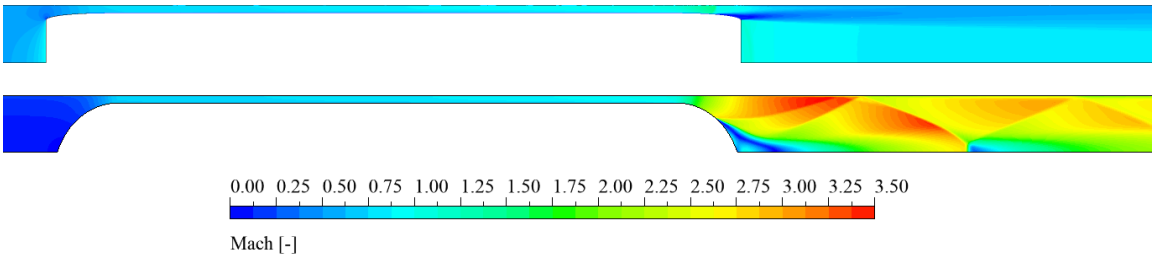

(c) $\beta = 0.75$.

Figure 2.15: Mach contour for the *compressor* case (upper figure) and the *base* case (lower figure), for 700 km/h and different blockage ratios.

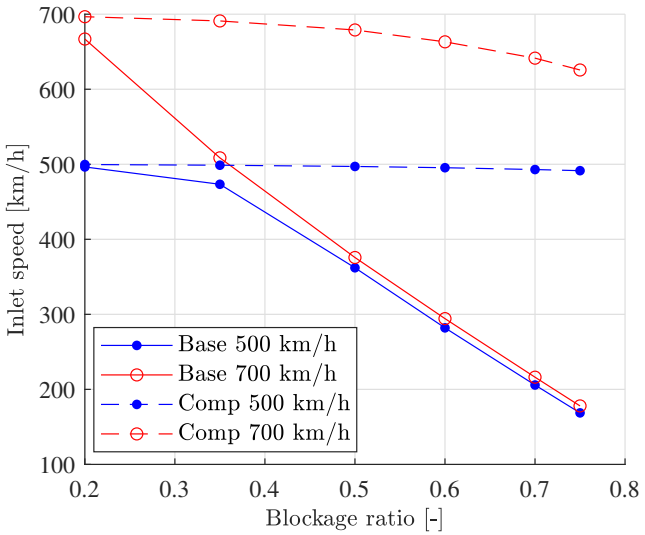

Figure 2.16: Inlet speed for the different blockage ratios and speeds.

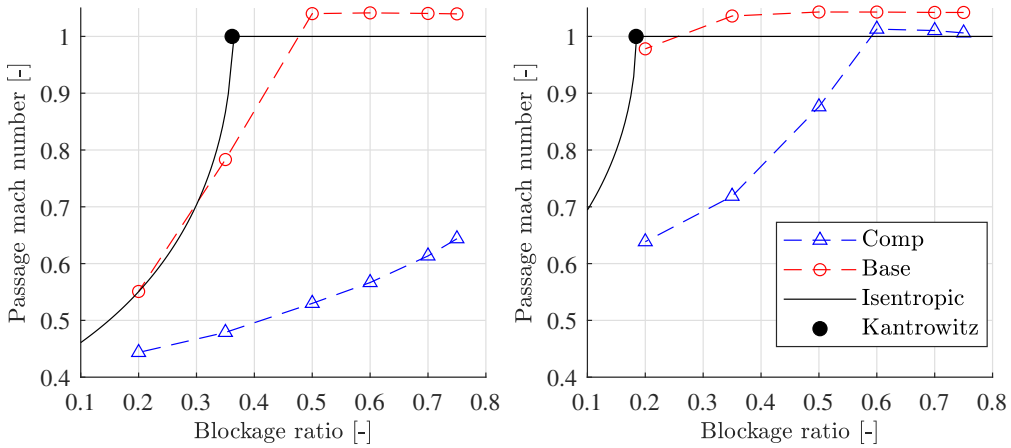

Figure 2.17: Mach number at the end of the passage for 500 km/h or Mach 0.408 (left) and 700 km/h or Mach 0.571 (right).

To better analyse how the addition of a compressor improves the performance of the capsule in terms of transonic effects, the equivalent blockage ratio among the two cases is represented in figure 2.18. This value was obtained from the CFD curves shown in figure 2.17, making both passage Mach numbers equal.

From the plotted data, one can conclude again that the installation of a compressor allows the use of smaller tunnels if the same blockage wants to be achieved, which implies higher BR when using turbomachinery. Also, note that the trend is linear for 500 km/h and 700 km/h until the Kantrowitz limit is achieved for the *compressor* case (BR between 0.5 and 0.6).

Due to this linearity until the choke of the flow occurs, the following regression, inde-

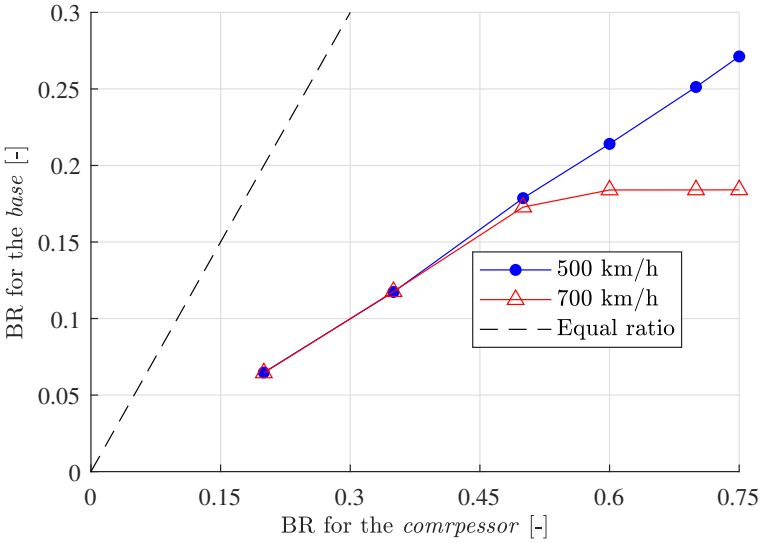

Figure 2.18: Blockage ratio comparison for the case with and without compressor.

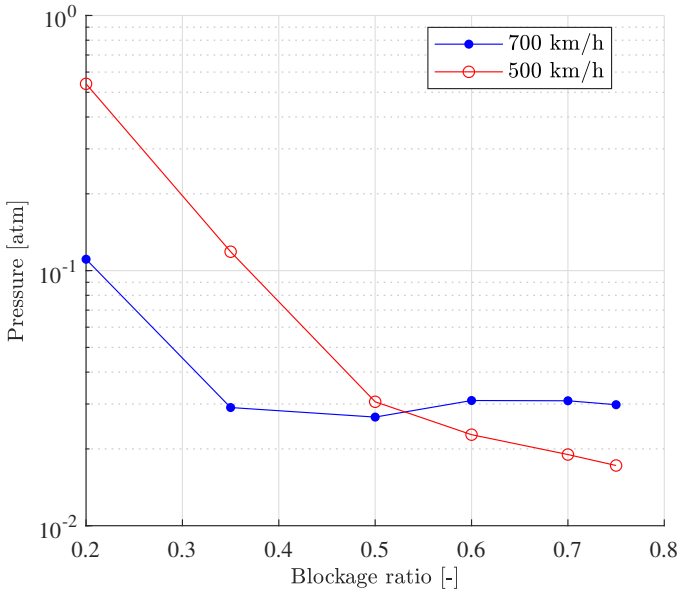

Figure 2.19: Equivalent pressure for the *base* case that requires the same power than the *compressor* case at 0.1 atm for the different blockage ratios and speeds.

pendent of the speed, can be assumed:

$$\beta_{Comp} = 2.82\beta_{magelv}. \tag{2.14}$$

This relation indicates that the BR of the tunnel can be 2.8 times higher when installing a compressor on the vehicle. In terms of physical parameters, this means that, for the same vehicle cross-section, the area of the tube can be 2.8 lower with aerodynamic propulsion.

The final study conducted is to obtain the pressure for the *base* case that matches the same power consumption as the *compressor* one. To do this, a linear relation of the drag with the pressure has been assumed. This trend is not only reported here (see figure 2.11) but also by Liu et al. in [89].

Having said that, the results of this study are shown in figure 2.19. For medium or high blockage ratios, 0.02 atm at 500 km/h and 0.03 atm at 700 km/h are required to perform similarly. Considering the real system, this implies an increase in the complexity and hazardousness of the case without a compressor.

Chapter 3

Fanno model

As commented in the first chapter, Fanno flow is essential for the hyperloop model explained in the fourth and fifth chapters. This is why the mathematical approach used for this flow is detailed in this chapter.

Nomenclature

R	Ideal gas constant (287.55 kJ/kg/K)
γ	Perfect gas adiabatic ratio (1.4)
c_p	Specific heat at constant pressure (1006.43 kJ/kg/K)
u_w	Wall speed
x	Longitudinal coordinate
L	Channel length
A	Cross-sectional area
C_{int}	Interior perimeter
C_{ext}	Exterior perimeter
f	Fanning or friction factor
f_{int}	Internal friction factor
f_{ext}	External friction factor
C_f	Friction coefficient
$C_{f,int}$	Internal friction coefficient
$C_{f,ext}$	External friction coefficient
D_h	Hydraulic diameter
$D_{h,int}$	Internal hydraulic diameter
$D_{h,ext}$	External hydraulic diameter
D_{eq}	Equivalent diameter
M_1	Mach number at the inlet
M_2	Mach number at the outlet
p_{1t}	Total pressure at the inlet
p_{2t}	Total pressure at the outlet
ρ_1	Density at the inlet

ρ_2	Density at the outlet
u_1	Speed at the inlet
u_2	Speed at the outlet
p_1	Static pressure at the inlet
p_2	Static pressure at the outlet
T_t	Total temperature
$F_{friction}$	Total friction force
$F_{f,int}$	Internal friction force
$F_{f,ext}$	External friction force
τ	Wall shear stress
$\tau_{w,int}$	Internal wall shear stress
$\tau_{w,ext}$	External wall shear stress
K	Ratio between internal and external shear stress
Re	Reynolds number
PR	Pressure Ratio
β	Blockage ratio
ε	Surface roughness
L_{crit}	Critical length

3.1 Introduction

In hyperloop application, as sketched in figure 3.1, a capsule for cargo or passenger transport moves while levitating inside a tube, where pressure conditions can be adapted. As the capsule levitates, free space around it is left. Then, a fluid domain with an interior wall (the capsule) and an exterior wall (the tube) is created. In a first approximation, this space can be considered axisymmetric. The movement of the capsule generates a movement in the surrounding flow, which leads to several types of fluid mechanics problems.

Accurate and fast modelling is necessary to get a practical simulation tool. For this purpose, the complex problem of the moving object inside a confined space is split into different simpler ones. One of these problems is the flow in the gap between the capsule and the tube, named as the passage.

The accurate modelling of this flow is essential to know the pressure drop of the capsule, so friction effects have to be considered. As the width of this domain (small passage) is

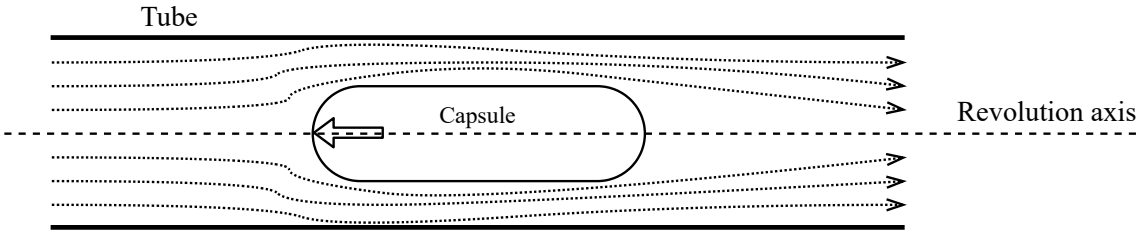

Figure 3.1: Qualitative representation of the flow around a hyperloop capsule.

considerably lower than the length (corresponding to the capsule length), this model can be referred to as Fanno flow. The flow must also be considered adiabatic for this hypothesis to be valid. Otherwise, one would have Rayleigh effects [109].

In pure Fanno flow [108], the air density and temperature decrease, whereas the mean velocity and Mach number increase along the axis of the duct. These changes are more important as the pressure drop grows until the duct chocks and the flow becomes sonic for a certain pressure ratio. These non-negligible thermodynamic variations make this particular flow relevant to the overall hyperloop performance.

The problem of the flow through a channel or a duct has been widely studied, both, experimentally and numerically. Typically, these flows are driven by two effects: the movement of the wall or Couette flow [110], or the pressure drop between the inlet and the outlet, or Poiseuille flow [111]. Even, the combination of both effects can appear in one case, leading to Couette-Poiseuille flows [109, 112].

In the hyperloop case, Couette effects are present as the capsule wall moves with respect to the tube wall. Also, Poiseuille is part of the problem due to the pressure drop between the inlet and the outlet of the domain, which always appears when an object is moving inside a confined space. This pressure loss was estimated in chapter 2.

Several other works have addressed the flow on a channel, which can be 2D or, at least, 3D with periodicity on the lateral walls. An example is the work by [113], who performed experiments on low to moderate Reynolds numbers on Couette-Poisuille fully developed turbulent plane.

However, the vast majority of the channel Couette-Poiseuille flow studies are focused on the laminar to turbulent transition, with Reynolds number relatively low. Hains [114] studied the stability of the Couette-Poioseuille flow numerically. Klotz et al. [115, 116] analysed experimentally the transitional Reynolds number at low speeds for plane Couette-Poiseuille flow with zero mean advection velocity. They also performed an extensive review of previous experimental, theoretical, and numerical studies of this flow.

Hu and Zhong [117] took one step forward from the stability analysis performed previously for incompressible flows. They studied numerically the linear stability of supersonic Couette flows for a perfect gas governed by the Sutherland law.

However, these previous studies were conducted for planar domains, which is not the actual hyperloop application described in figure 3.1. Regarding flow in ducts, Zhu and Reitz [118] developed a 1D code for subsonic and supersonic Poiseuille flows with Fanno and Rayleigh conditions, applied to EGR in internal combustion engines. Durst et al. [119] studied the development length in a Poiseuille flow for a wide variety of Reynold numbers.

An experiment for compressible flow was conducted by Lijo et al. [108]. Mach number slightly greater than one at the outlet of a Poiseuille flow was reported, as opposed to what the Fanno theory predicts. Also, supersonic experiments were performed by Miyazato et al. [120] in long constant-area ducts with friction. They also reported differences with respect to the one-dimensional theory in terms of the critical length in a Fanno flow. For a given inlet Mach number and friction coefficient, the maximum possible length of the duct was shorter than that predicted by the theory. Later, Mullin [121] performed experimental studies for the turbulent transition stability on duct flows.

Even though duct flows consider the curvature of the walls, geometrically, a circle

cannot reproduce the real case present on the passage flow studied (see figure 3.1). As already mentioned, these domains are composed of two concentric cylinders.

So, in annular domains, Ishida et al. [122] used DNS to study the transitional regimen for incompressible Poiseuille flows at low friction Reynolds numbers. One recent study, from Kunii et al. [123] added the Couette effect to the annular flow, but only to study the turbulent to laminar transition. One year later, [124] added the Rayleigh effect to the Couette-Poiseuille annular flow, looking for an analytical solution for a power-law fluid.

None of these studies in annular domains can be directly applied to the present scenario, as neither the Reynolds nor the Mach number matches the values for a hyperloop application. Thus, particular modelling is required. This is why the authors have developed a new approximation to the Fanno flow equation, using several hypotheses discussed in the second section.

So, this paper aims to obtain a simplified expression for the compressible Fanno flow inside an annular duct under the movement of one of the walls. This simplified expression can be solved with the same computation effort as the original Fanno equation. Then, it is avoided to use more advanced techniques, such as CFD, with a reasonable deviation in the results.

It is important to highlight that the standard Fanno flow is applied to a compressible Poiseuille flow in a duct. For the present case, the formulation has varied to consider both the annular-shaped domain and the speed of one of the walls in the longitudinal direction (Couette effect).

3.2 Numerical method

3.2.1 Numerical domain

The flow is assumed to be 1D, steady and compressible, as the aim is to reproduce the flow in the gap between the vehicle and the tube. This domain is considerably longer than wider, ensuring the validity of this hypothesis. Actually, the CFD validation (see section 3.3.2) has been conducted for cases in which the length of the domain is, at least, 50 times the hydraulic diameter.

Although the solution varies only in one dimension, the curvature of the interior and exterior walls that compose the annular domain have been considered through a correction on the hydraulic diameter, discussed below.

It is also important to highlight that, although the original Fanno differential equation can be solved analytically, this particular case requires a numerical approach. To overcome this problem, the ratio between the shear stress on the interior and exterior walls must be uniform in the longitudinal coordinate. The results shown in section 3.3.2.2 will prove the validity of this hypothesis.

To analyse this problem, a moving reference frame is assumed. The case is detailed in figure 3.2. The tube (exterior wall) moves at the speed of the pod ($u_w = u_{pod}$), and the interior wall is stopped. So, a Couette-Poisuille flow is obtained. The radial-azimuthal averaged flow on the channel depends on the x position and is named $u(x)$.

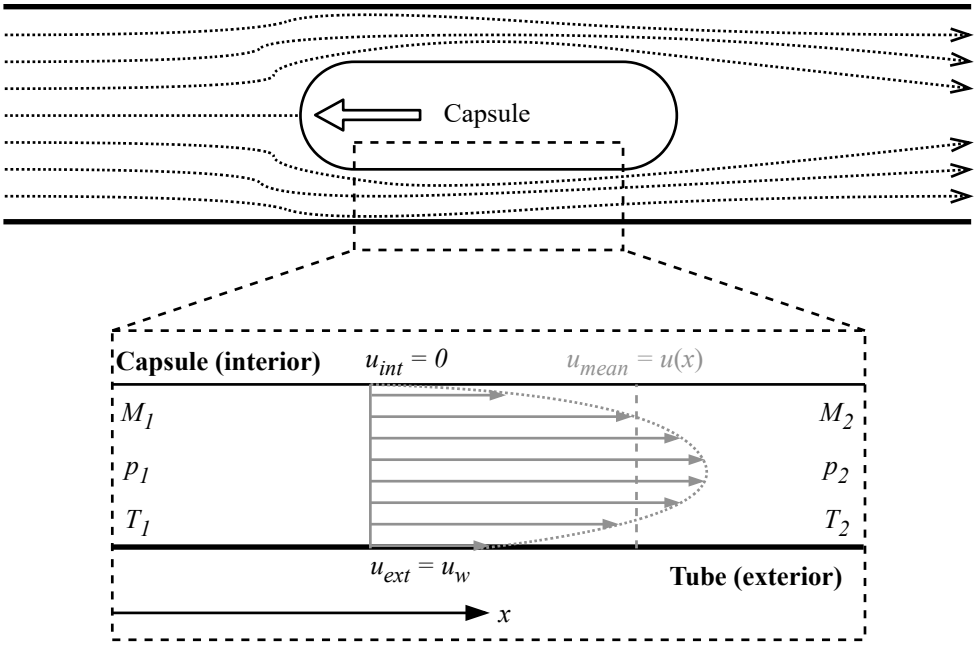

Figure 3.2: Detail of the Fanno flow for this problem.

The longitudinal coordinate x ranges from 0 to the channel length L.

The friction with the walls, characterised by a friction factor f, provokes a difference between the Mach number at the inlet M_1 and the one at the outlet M_2. The same happens for the total pressure (p_{1t}, p_{2t}). The Mach number increases due to friction, while the total pressure decreases.

On the other hand, the channel is characterised by a cross-section named A, while the interior wall has a wet perimeter of C_{int} and the exterior wall has a wet perimeter of C_{ext}.

3.2.2 Generic equations

The starting point to obtain the relevant equations for this problem is the momentum conservation in one dimension [109]. The transient and gravitational terms are neglected, while the viscosity is included in the term F_{friction}. The equation is presented in integral form:

$$\rho_1 u_1^2 A + p_1 A = \rho_2 u_2^2 A + p_2 A + F_{friction}. \tag{3.1}$$

There is a momentum loss between stages 1 and 2 due to the friction force $F_{friction}$. Assuming that there is an interior and exterior wall, this force can be modelled as follows:

$$F_{friction} = C_{int} \int_0^L \tau_{w,int}\, \mathrm{d}x + C_{ext} \int_0^L \tau_{w,ext}\, \mathrm{d}x. \tag{3.2}$$

Then, back to equation (3.1):

$$\rho_1 u_1^2 + p_1 = \rho_2 u_2^2 + p_2 + \frac{1}{A}\left(C_{int} \int_0^L \tau_{w,int}\, \mathrm{d}x + C_{ext} \int_0^L \tau_{w,ext}\, \mathrm{d}x \right). \tag{3.3}$$

And, in differential form:

$$\mathrm{d}p + \mathrm{d}\left(\rho u^2\right) = -\frac{1}{A}\left(C_{int}\tau_{w,int} + C_{ext}\tau_{w,ext}\right)\mathrm{d}x. \tag{3.4}$$

The following expression for the surface stresses is used:

$$\tau_{w,int} = \frac{1}{2}\rho u^2 C_{f,int}, \tag{3.5}$$

$$\tau_{w,ext} = \frac{1}{2}\rho\left(u - u_w\right)^2 C_{f,ext}. \tag{3.6}$$

Then, the differential equation can be re-expressed as:

$$\mathrm{d}p + \mathrm{d}\left(\rho u^2\right) = -\frac{\rho}{2}\left(\frac{C_{int}}{A}u^2 C_{f,int} + \frac{C_{ext}}{A}\left(u - u_w\right)^2 C_{f,ext}\right)\mathrm{d}x. \tag{3.7}$$

In this case, as appendix A.3 will explain, it is more practical to use the friction factor f instead of the friction coefficient C_f. Assuming that $C_{f,i} = f_i/4$ and dividing everything by the dynamic pressure:

$$\frac{\mathrm{d}p}{\frac{\gamma}{2}pM^2} + 2u\frac{\mathrm{d}u}{u^2} = -\frac{f_{int}}{D_{h,int}}\mathrm{d}x - \left(1 - \frac{u_w}{u}\right)^2\frac{f_{ext}}{D_{h,ext}}\mathrm{d}x, \tag{3.8}$$

where:

$$D_{h,int} \equiv \frac{4A}{C_{int}}, \tag{3.9}$$

$$D_{h,ext} \equiv \frac{4A}{C_{ext}}. \tag{3.10}$$

Now, equation (3.8) is going to be reformulated to obtain the standard Fanno expression (section 3.2.2.1) and a simplified expression (section 3.2.2.2) that is solved analytically in section 3.2.3.1. Equation (3.8) will be numerically solved in section 3.2.3.2 without further hypotheses.

3.2.2.1 Standard Fanno equation

To reach the *standard* Fanno flow equation the following hypotheses have to be taken:

- Wall is still: $u_w = 0$.
- Both friction factors are equal: $f_{int} = f_{ext} = f$. The friction factor f is also assumed to be constant, corresponding to an average value of the stream-wise skin friction, as done by the Fanno theory [108]
- Hydraulic diameter is defined as follows: $D_h^{-1} \equiv D_{h,int}^{-1} + D_{h_ext}^{-1} = \frac{C_{int}+C_{ext}}{4A}$.

The following equation for *standard* Fanno flow is reached:

$$\frac{\mathrm{d}p}{\frac{\gamma}{2}pM^2} + 2u\frac{\mathrm{d}u}{u^2} = -\frac{f}{D_h}\mathrm{d}x. \tag{3.11}$$

3.2.2.2 Modified Fanno equation

When the previous hypothesis is not considered, the following constant is defined to simplify the solution:

$$K \equiv \frac{C_{ext}\tau_{w,ext}}{C_{int}\tau_{w,int}} = \left(1 - \frac{u_w}{u}\right)^2 \frac{C_{ext}}{C_{int}}. \tag{3.12}$$

This is a strong hypothesis, as K is not a constant due to its dependence on $u\,(x)$. However, this assumption must be made to obtain the analytic solution. If the friction factor is also assumed to be equal in both walls (f), the differential equation (3.8) can be expressed as:

$$\frac{\mathrm{d}p}{\frac{\gamma}{2}pM^2} + 2u\frac{\mathrm{d}u}{u^2} = -\frac{f}{D_{h,int}}\left[1 + \left(1 - \frac{u_w}{u}\right)^2 \frac{D_{h,int}}{D_{h,ext}}\right]\mathrm{d}x, \tag{3.13}$$

$$\frac{\mathrm{d}p}{\frac{\gamma}{2}pM^2} + 2u\frac{\mathrm{d}u}{u^2} = -\frac{f}{D_{h,int}}\left(1 + K\right)\mathrm{d}x. \tag{3.14}$$

Then, the equivalent diameter can be defined:

$$D_{eq} \equiv \frac{D_{h,int}}{1+K} = \frac{4A}{C_{int}\left(1+K\right)} = \frac{4A}{C_{int} + C_{ext}\left(1 - \frac{u_w}{u}\right)^2}. \tag{3.15}$$

And so, the differential equation is now the Fanno one:

$$\frac{\mathrm{d}p}{\frac{\gamma}{2}pM^2} + 2u\frac{\mathrm{d}u}{u^2} = -\frac{f}{D_{eq}}\mathrm{d}x. \tag{3.16}$$

3.2.3 Solution to Fanno equation

In this section it is obtained the analytical solution of the original Fanno equation (3.11) and Fanno modified equation (3.16) in section 3.2.3.1.

Also, the numerical solution of the differential Fanno equation (3.8) without any additional hypothesis is obtained in section 3.2.3.2.

3.2.3.1 Analytical solution

The solution to the equations (3.11) and (3.16) is the following [125]:

$$f\frac{L}{D} = \left[\frac{1-M^2}{\gamma M^2} + \frac{\gamma+1}{2\gamma}\log\left(\frac{\left(\gamma+1\right)M^2}{2+\left(\gamma-1\right)M^2}\right)\right]_1^2. \tag{3.17}$$

In this case, the diameter D is equal to the hydraulic diameter D_h as defined in section 3.2.2.1 for the *standard* Fanno solution, or the equivalent diameter D_{eq} as defined in (3.15).

From equation (3.17), the Mach number at the outlet M_2 can be computed. Then, the total pressure ratio between the inlet and the outlet can be computed using the following expression:

$$\pi_{21} = \frac{p_{2t}}{p_{1t}} = \frac{M_1}{M_2}\left(\frac{1 + \frac{\gamma-1}{2}M_2^2}{1 + \frac{\gamma-1}{2}M_1^2}\right)^{\frac{\gamma+1}{2(\gamma-1)}}, \tag{3.18}$$

where adiabatic flow ($T_{1t} = T_{2t}$) has been assumed.

Also, it can be demonstrated that the Reynolds number is equal at the inlet and the outlet, so $Re_1 = Re_2$.

By his part, the ratio between the equivalent diameter and the hydraulic diameter is the following:

$$\frac{D_{eq}}{D_h} = \frac{4A}{C_{int}\left(1+K\right)}\frac{C_{int}+C_{ext}}{4A} = \frac{C_{int}+C_{ext}}{C_{int}+\left(1-\frac{u_w}{u}\right)^2 C_{ext}}. \tag{3.19}$$

The friction force can be computed as:

$$F_{friction} = C_{int}\int_0^L \tau_{w,int}\,\mathrm{d}x + C_{ext}\int_0^L \tau_{w,ext}\,\mathrm{d}x. \tag{3.20}$$

Using the previous approximation (3.12):

$$F_{friction} = C_{int}\int_0^L \tau_{w,int}\,\mathrm{d}x + KC_{int}\int_0^L \tau_{w,int}\,\mathrm{d}x = F_{f,int}\left(1+K\right), \tag{3.21}$$

where $F_{f,int}$ is the friction force on the inner face:

$$F_{f,int} \equiv C_{int}\int_0^L \tau_{w,int}\,\mathrm{d}x. \tag{3.22}$$

And so:

$$F_{f,int} = \frac{F_{friction}}{1+K}. \tag{3.23}$$

The total friction force can also be computed using the integral form:

$$F_{friction} = A\left(p_1 - p_2 + \rho_1 u_1^2 - \rho_2 u_2^2\right). \tag{3.24}$$

These expressions are valid even for the standard Fanno approach if $u_w = 0$ or $K = C_{ext}/C_{int}$.

The friction force can be non-dimensionalised by dividing by the inlet dynamic pressure and the total wet area:

$$\frac{F_{friction}}{A} = \rho_1 u_1^2\left[\frac{1}{\gamma M_1^2}\left(1-\frac{p_2}{p_1}\right) + 1 - \frac{p_2}{p_1}\frac{M_2^2}{M_1^2}\right]. \tag{3.25}$$

3.2.3.2 Numerical solution

For the numerical solution, a transformation of (3.8) has to be conducted to obtain the ODE system. Firstly, the RHS is going to be simplified using the following assignment:

$$g\left(u\right) \equiv -\frac{f_{int}}{D_{h,int}} - \left(1-\frac{u_w}{u}\right)^2\frac{f_{ext}}{D_{h,ext}}. \tag{3.26}$$

So, equation (3.8) can be reexpressed as:

$$\frac{\mathrm{d}p}{\frac{\gamma}{2}pM^2} + 2u\frac{\mathrm{d}u}{u^2} = g\left(u\right)\mathrm{d}x. \tag{3.27}$$

In appendix A.1 equation (3.27) is developed to obtain the ODE system. This case cannot be simplified to only one ODE but two solving for the speed (or Mach number) and the temperature.

Two different formulations are obtained. One is used to compute the outlet Mach number according to a certain length, so the independent variable is x. The dependant variables are $\left(u^2, T\right)$. This is equation (A.10) from appendix A.1.

$$\begin{Bmatrix} \frac{\mathrm{d}u^2}{\mathrm{d}x} \\ \frac{\mathrm{d}T}{\mathrm{d}x} \end{Bmatrix} = \begin{Bmatrix} 1 \\ \frac{-1}{2c_p} \end{Bmatrix} \frac{\gamma}{1 - \frac{\gamma RT}{u^2}} u^2 g\left(u\right). \tag{3.28}$$

The other is useful for the critical length, as the independent variable is the Mach number M. The dependant variables are (x, T). This is equation (A.20) from appendix A.1.

$$\begin{Bmatrix} \frac{\mathrm{d}x}{\mathrm{d}M} \\ \frac{\mathrm{d}T}{\mathrm{d}M} \end{Bmatrix} = \begin{Bmatrix} \frac{2\left(M^2-1\right)}{\gamma M^3 g(u)} \\ \left(1-\gamma\right) MT \end{Bmatrix} \left(1 + \frac{\gamma - 1}{2} M^2\right)^{-1}. \tag{3.29}$$

This system can output the critical length when solved from M_1 to $M_2 = 1$.

Thanks to having the Fanno equation in differential form, the hypothesis that the friction factor remains constant throughout the passage as the Reynolds is constant, can be avoided. Now, variations in the Reynolds and friction factor can be considered.

Other important considerations are the following:

- The dynamic viscosity is computed using the Sutherland equation.
- The ODE system is resolved using Euler explicit.
- The Reynolds used to compute the moving wall takes into consideration the relative speed and the annular hydraulic diameter:

$$Re_{int}\left(x\right) = \frac{D_h u\left(x\right)\rho}{\mu\left(T\right)}, \tag{3.30}$$

$$Re_{ext}\left(x\right) = \frac{D_h \left|u\left(x\right) - u_w\right|\rho}{\mu\left(T\right)}. \tag{3.31}$$

It can be demonstrated that the pressure ratio between the inlet and the outlet can be computed in the same way as exposed for the analytical solution in equation (3.18).

3.3 Results

3.3.1 Mesh independence

As an ODE is solved, a mesh sensibility study is required. In figure 3.3 the error in the critical length for different ΔM solving the system (3.29) and the error in the PR for the critical length for different Δx solving the system (3.28) is plotted. Note that, instead of the space step for the PR plot, the ratio between Δx and L_{crit} is considered to be more representative.

The data for this study is the following:

- $M_1 = 0.5$.
- $p_1 = 10$ kPa.
- $T_1 = 300$ K.
- $\varepsilon = 0$.
- $\beta = 0.6267$.
- $D_h = 1.0$.
- $u_w/u_1 = 0.98$.
- Re constant.

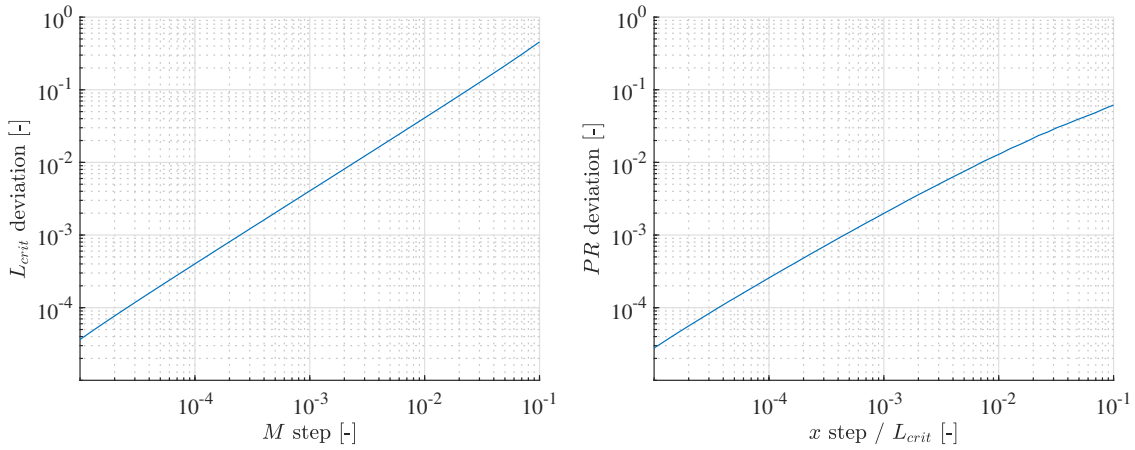

Figure 3.3: Error in the critical length (left figure) and PR for these lengths using different integration variables.

For an error of 0.5 %, a Mach resolution of 0.0011 is required; and for the space resolution (with respect to the critical length) of 0.0023.

3.3.2 Validation with CFD

In this section, the solution of the different Fanno approaches of this study is contrasted with a solution obtained from a commercial CFD solver: Fluent. The set-up for the solver is the following:

- Total length of 50 m, removing 15 m at the beginning and 5 m at the end to avoid the intake and outtake effects.
- Compressible pressure-based solver.
- $k - \omega$ SST turbulence model.

- Steady solution.
- 2D axisymmetrical annular domain.
- Outlet pressure of 10 kPa, and inlet total temperature of 300 K.

3.3.2.1 Pressure ratio

Once the step is clear, the results of the PR are computed for different friction factors, β, and wall speeds u_w/u_1. Three different solvers for the Fanno flow are used:

- Standard Fanno solution with the hydraulic diameter for annular flow (*standard*).
- Modified Fanno solution with analytic solution (*modified*).
- Numeric solution of the Fanno equation (*numeric*).

This is done in figure 3.4. Compared to the Fluent solution, the two closer are the *modified* and *numeric*. Note that the original Fanno overestimates the pressure loss and has a different trend. This is a consequence of not considering the movement of the wall in this approach.

Note that the *modified* approach and the *numeric* are quite close to each other and the Fluent solution. Theoretically, *numeric* should be more accurate, although this is not always this way. However, for higher β and lengths the *numeric* approach is closer to the reference solution. The solution is less accurate for larger f.

It is important to remark that the PR decreases in the *standard* Fanno approach instead of being constant due to the increase in the M_1 through the different u_w/u_1 points.

3.3.2.2 Shear stress

In this section, the C_f is used as a comparison with Fluent, only for the *numeric*. The *original* or *modified* approaches are not compared because they do not integrate throughout the channel, so they do not predict any evolution.

The plots for $u_w/u_1 = 0.35$ are represented in figure 3.5 and for $u_w/u_1 = 0.35$ in figure 3.6.

Note that, regardless of the wall speed, the interior friction coefficient is underpredicted, but the exterior one is overpredicted. However, both of them are close to the Fluent solution.

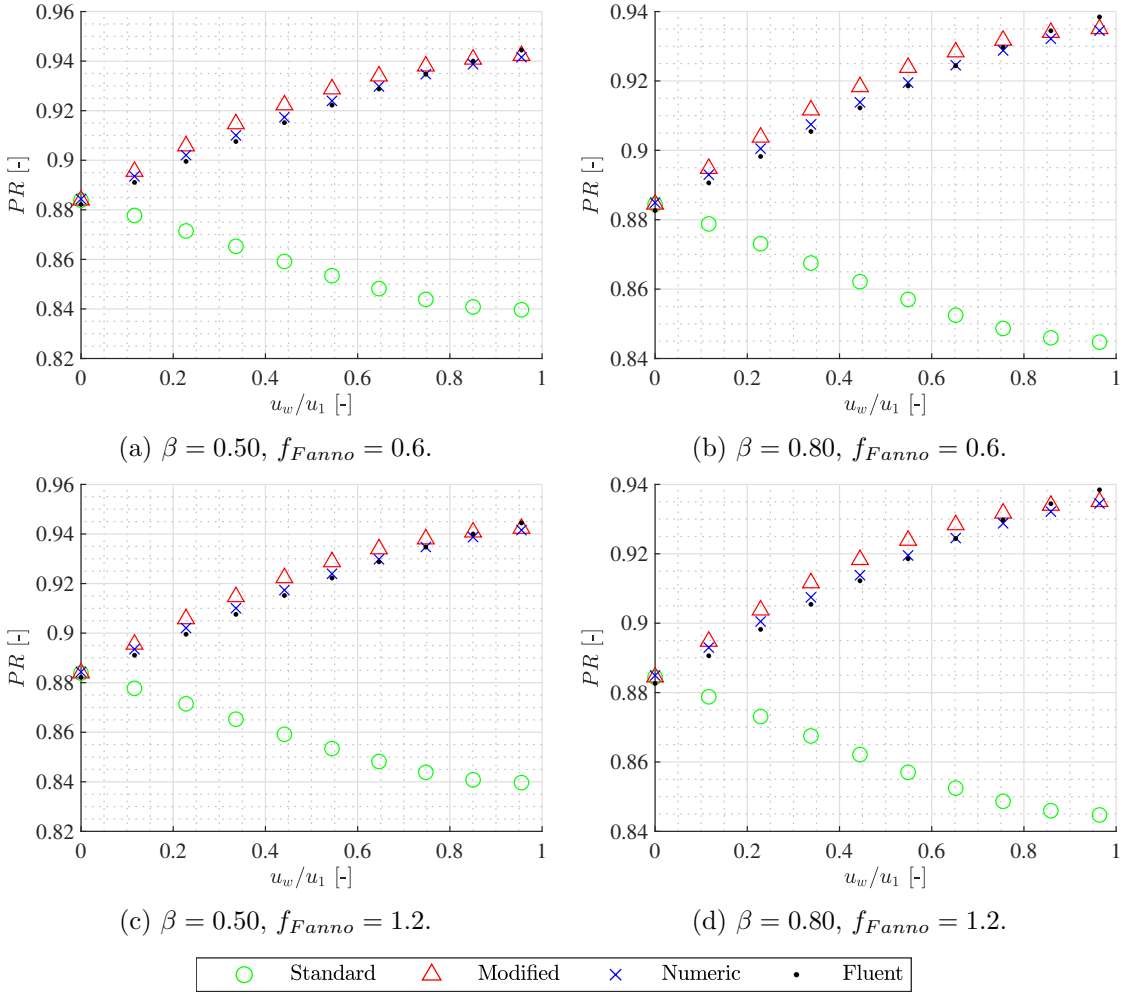

(a) $\beta = 0.50$, $f_{Fanno} = 0.6$.

(b) $\beta = 0.80$, $f_{Fanno} = 0.6$.

(c) $\beta = 0.50$, $f_{Fanno} = 1.2$.

(d) $\beta = 0.80$, $f_{Fanno} = 1.2$.

Figure 3.4: Pressure ratio comparison between the different Fanno approaches.

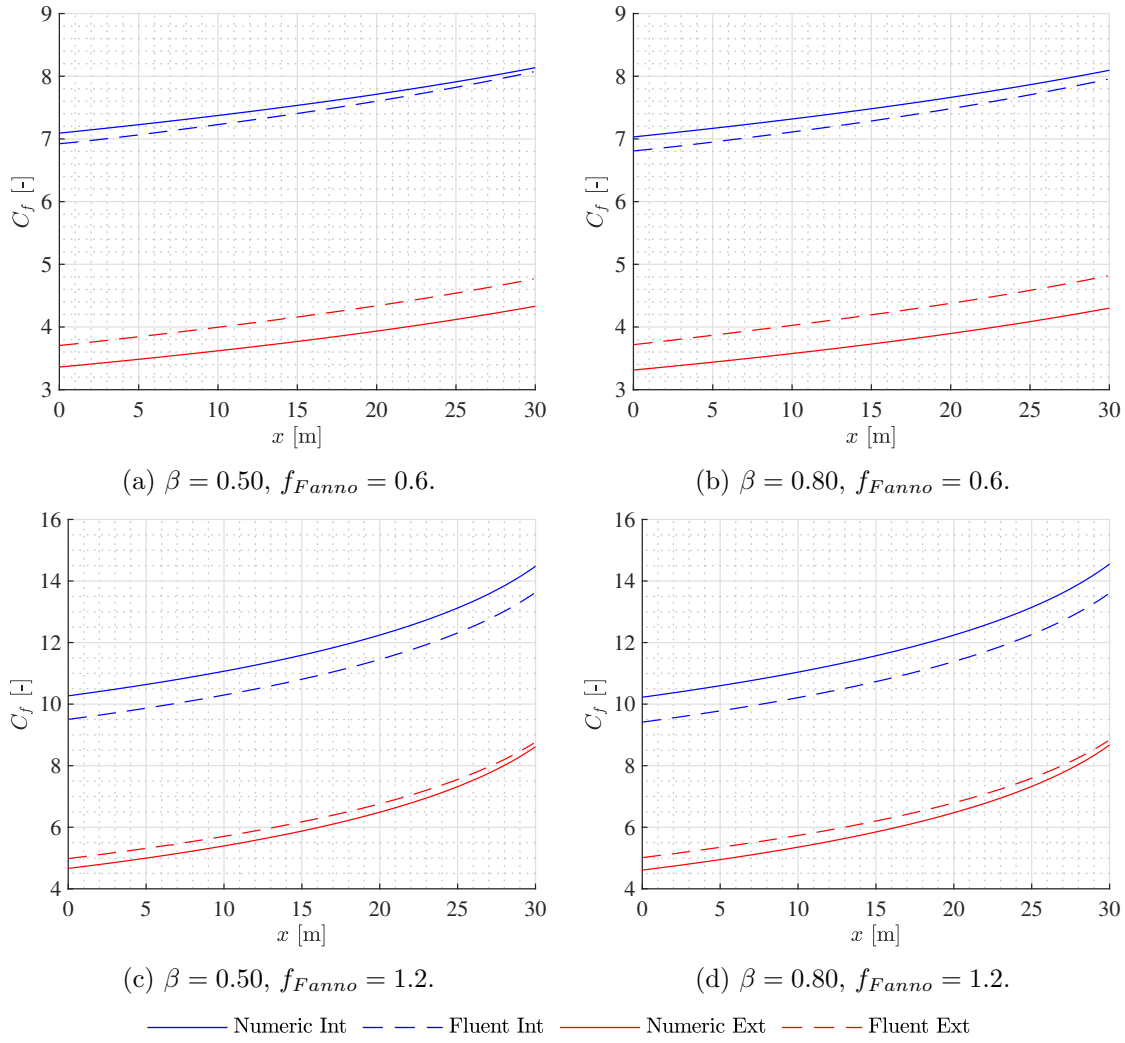

(a) $\beta = 0.50$, $f_{Fanno} = 0.6$.

(b) $\beta = 0.80$, $f_{Fanno} = 0.6$.

(c) $\beta = 0.50$, $f_{Fanno} = 1.2$.

(d) $\beta = 0.80$, $f_{Fanno} = 1.2$.

Figure 3.5: Friction coefficient comparison between the 1D and CFD numeric solutions for $u_w/u_1 = 0.35$.

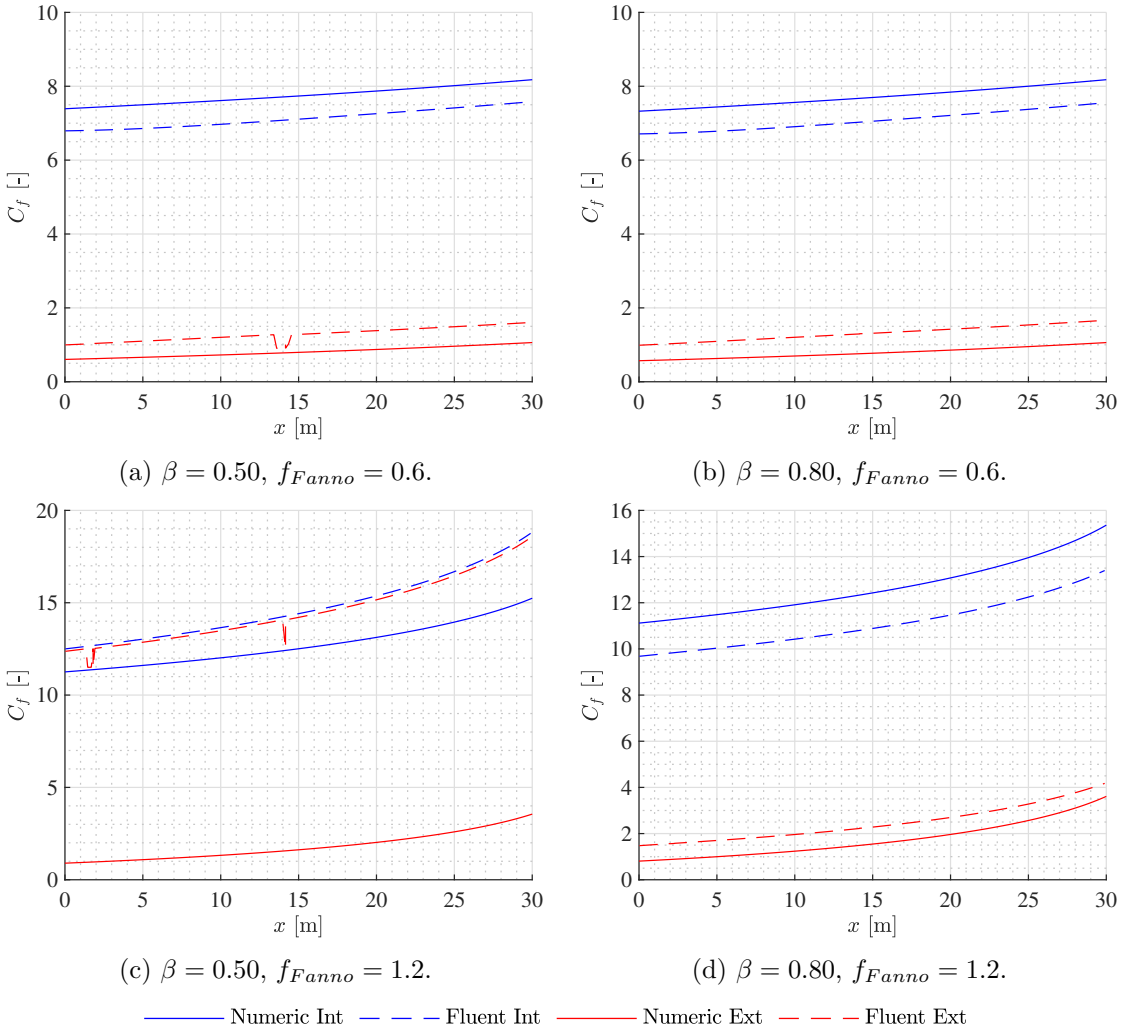

(a) $\beta = 0.50$, $f_{Fanno} = 0.6$.

(b) $\beta = 0.80$, $f_{Fanno} = 0.6$.

(c) $\beta = 0.50$, $f_{Fanno} = 1.2$.

(d) $\beta = 0.80$, $f_{Fanno} = 1.2$.

Figure 3.6: Friction coefficient comparison between the 1D and CFD numeric solutions for $u_w/u_1 = 0.75$.

3.3.3 Critical length

First, using the *numeric* approach, the critical length for different Reynolds, β, and u_w is compared. As the u_w increases, the critical length increases due to the reduction in friction of one of the walls. Also, as β decreases, the critical length increases due to the larger area. By his part, the variation with Reynolds is negligible as long as the flow is turbulent. The transition to laminar flow is seen in $Re = 10^4$.

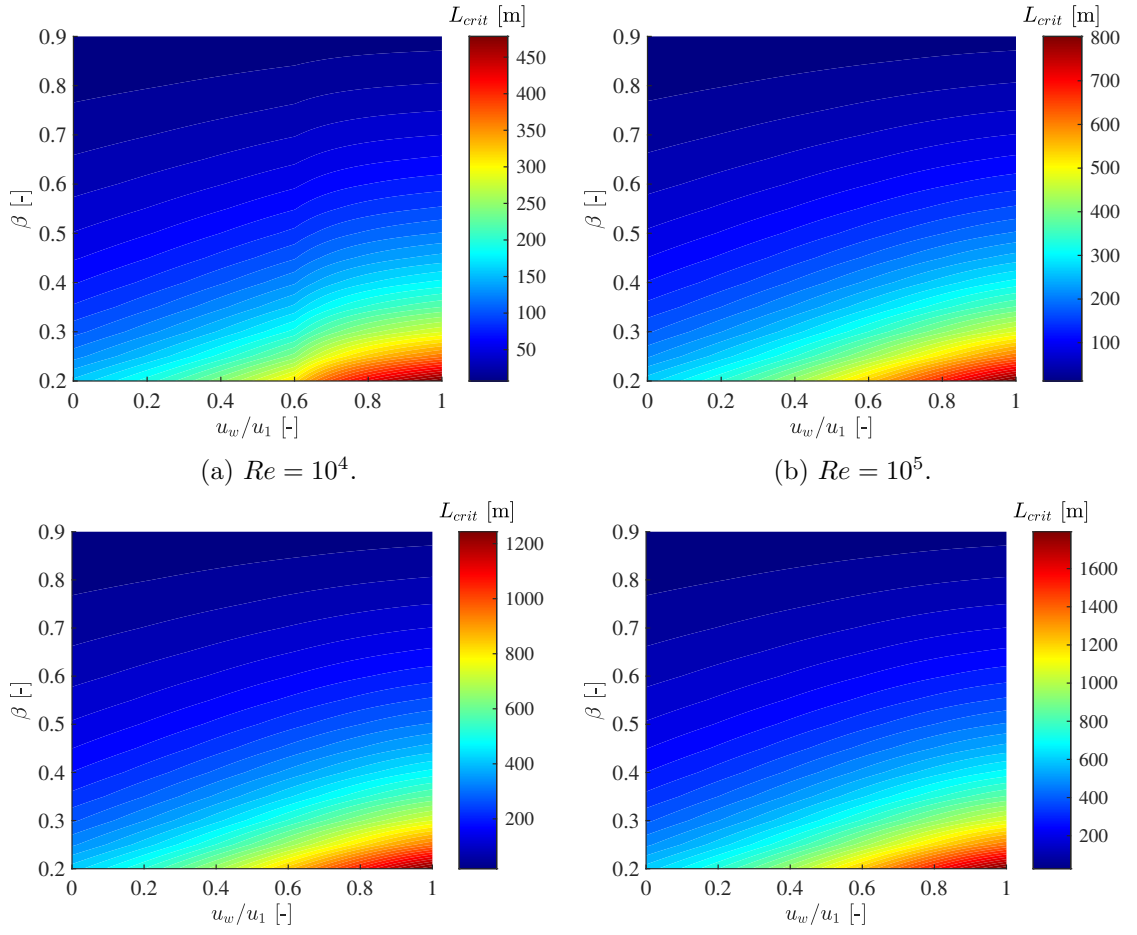

(a) $Re = 10^4$. (b) $Re = 10^5$.

(c) $Re = 10^6$. (d) $Re = 10^7$.

Figure 3.7: Critical length contours for different Reynolds, β, and u_w/u_1.

Figure 3.8 compares the critical length for the three different Fanno solutions. Note that *original* does not predict any variation (as it does not consider the wall speed), but the *modified* and *numeric* do predict a evolution. Note that the *numeric* approach under-predicts the critical length. Note that, for the lowest Reynolds, there is a change in the trend due to the appearance of laminar flow. Then, the slope increases due to the increase in the friction factor.

These results and the ones analysing the PR in figure 3.4 lead to consider that, taking

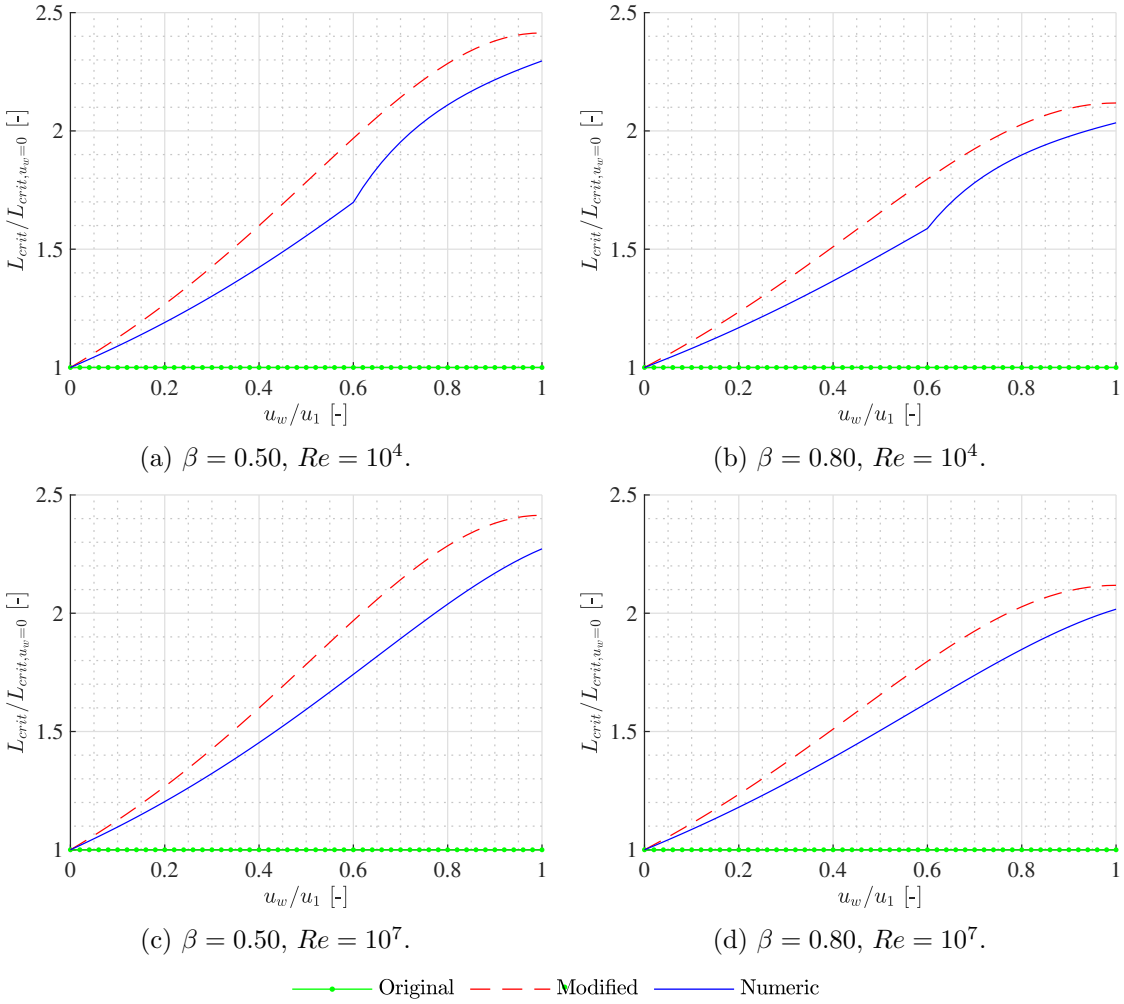

(a) $\beta = 0.50$, $Re = 10^4$.

(b) $\beta = 0.80$, $Re = 10^4$.

(c) $\beta = 0.50$, $Re = 10^7$.

(d) $\beta = 0.80$, $Re = 10^7$.

Figure 3.8: Critical length comparison for the different approximations.

into consideration the computational cost, the *modified* is the best approach.

3.3.4 Analysis of the equivalent diameter

This section analyses the parameter D_{eq}/D_h and its dependencies with the blockage ratio β and the wall speed u_w/u. The equation that describes this relation for concentric circles is (see appendix A.2, equation (A.31)):

$$\frac{D_{eq}}{D_h} = \frac{1+\sqrt{\beta}}{\left(1-\frac{u_w}{u}\right)^2+\sqrt{\beta}}. \tag{3.32}$$

It is important to state that the physical meaning of the parameter D_{eq}/D_h is how much easier it is for the flow to cross the channel when the wall is moving with respect to a pure Poiseuille flow.

Firstly, in table 3.2, the most relevant values are collected, for $\beta = 0, 1$. The full representation is shown in figure 3.9. It can be seen that the curve starts at 1, leading to a maximum at $u_w/u = 1$, crossing again 1 at $u_w/u = 2$ and reducing to 0 when u_w/u tends to infinity.

$\mathbf{u_w/u}$	$\mathbf{D_{eq}/D_h}$ $(\beta = \mathbf{0})$	$\mathbf{D_{eq}/D_h}$ $(\beta = \mathbf{1})$
0	1	1
1	∞	2
2	1	1
∞	0	0

Table 3.2: Values for the D_{eq}/D_h parameter for different β and u_w/u.

The larger the β the smaller D_{eq}/D_h on the range $u_w/u = [0, 1]$. This means the more constrained the channel, the less improvement concerning the pure Poiseuille flow is obtained.

In figure 3.10, the maximum value of D_{eq}/D_h is plotted with respect to β. This maximum occurs always at $u_w/u = 1$. It is shown that it tends to infinity as β tends to 0, but for the range [0.25,1], the variation is reduced to be between 2 and 3. This means that, for the common range of values of β, the ratio for the diameter is between 1 and 3. For the typical range of the blockage ratio [0.25,0.75] [126] the maximum value of the ratio is 3.

However, in practice, u_w/u is always in between the range [0,1). The main reason is that when a hyperloop capsule moves forward, the air that passes through the gap between itself and the tube goes faster than the air upstream of the capsule. As u_w equals the capsule speed, it means that $u > u_w$ for any case. So, the values shown for $u_w/u > 1$ have no physical meaning.

This means that, as proved in figure 3.9, the equivalent diameter will always be larger than the hydraulic diameter, with the maximum value at $u_w/u = 1$, leading to fewer losses as the wall speed increases. Remember that, as seen in figure 3.8, the critical length increases as u_w/u increases due to this reduction in friction losses.

By his part, the β value has no physical meaning over 1 and under 0 (included).

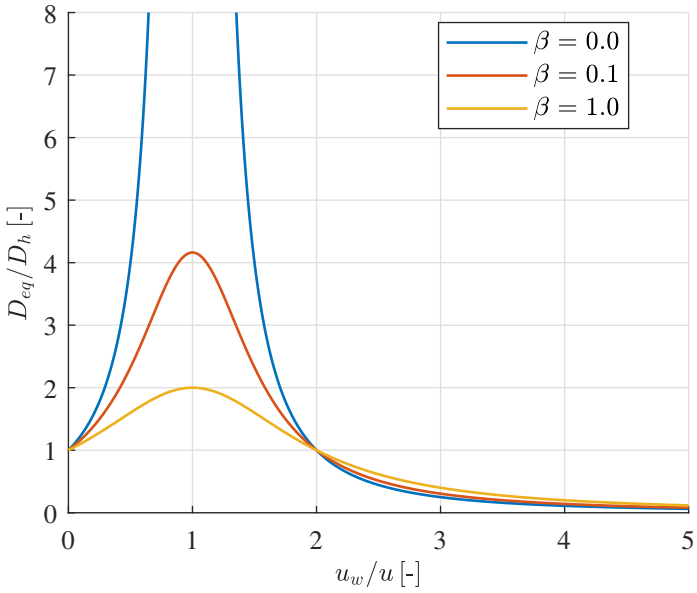

Figure 3.9: Parameter D_{eq}/D_h with respect to u_w/u for different β.

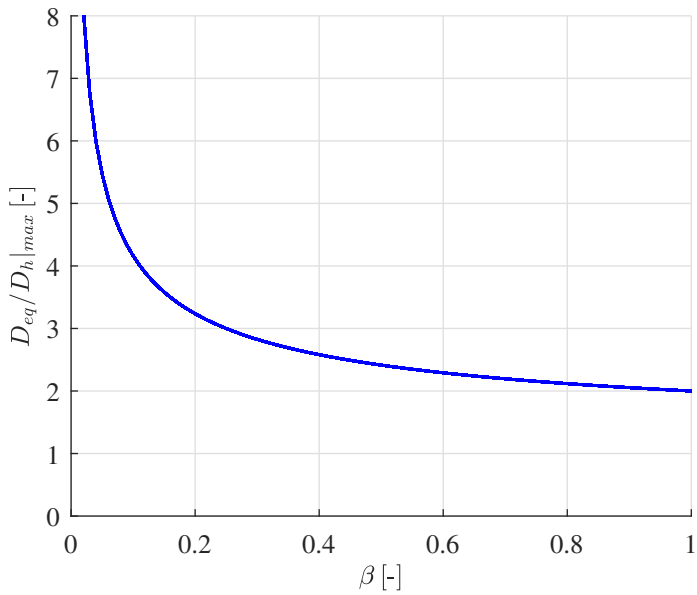

Figure 3.10: Maximum value of the parameter D_{eq}/D_h with respect to β.

3.3.5 No constant Reynolds analysis

In this section, the critical length using the *numeric* approach considers the Reynolds variation. It is important to remark that for the *original* or *modified* approaches, Fanno hypothesises that the friction factor is uniform and ensures that the Reynolds is constant throughout the channel.

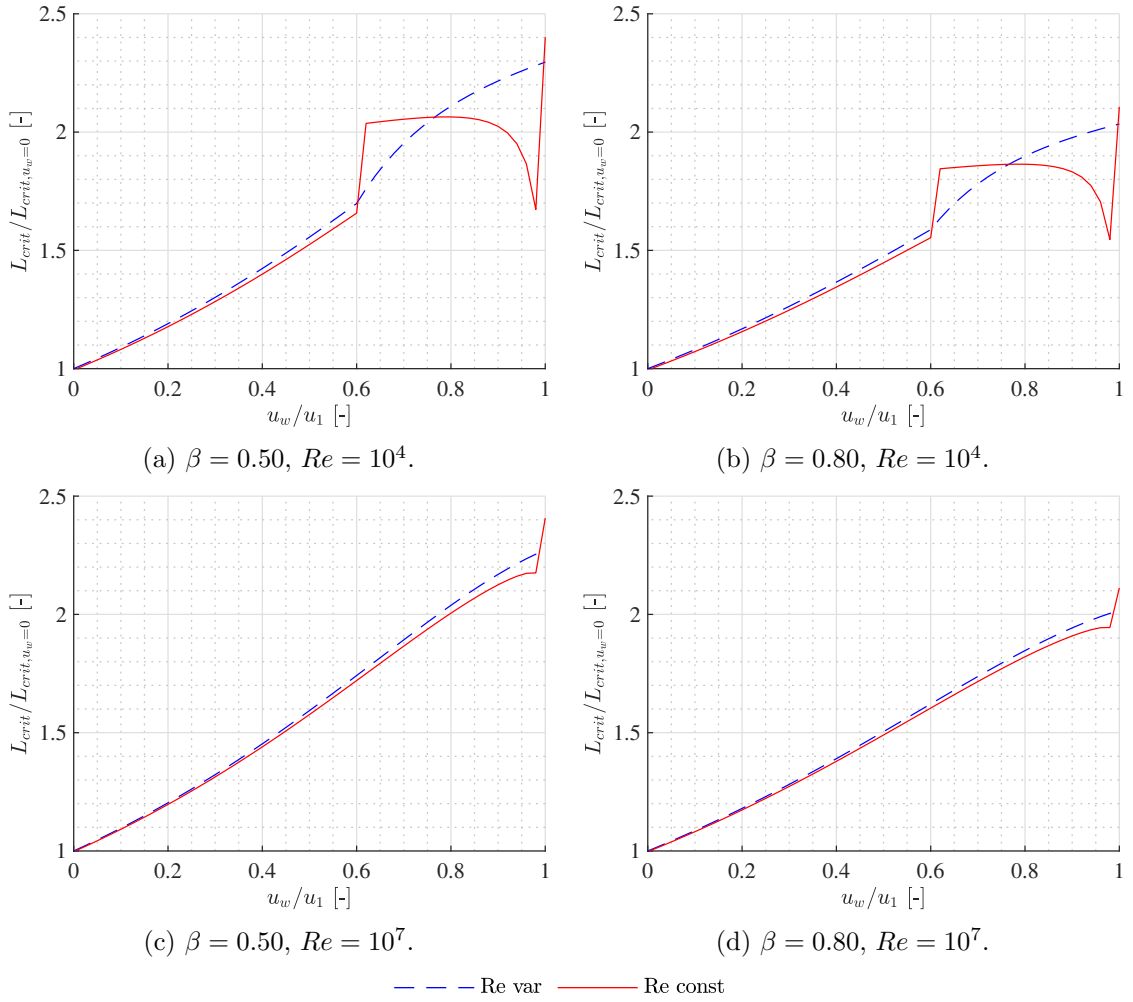

(a) $\beta = 0.50$, $Re = 10^4$.

(b) $\beta = 0.80$, $Re = 10^4$.

(c) $\beta = 0.50$, $Re = 10^7$.

(d) $\beta = 0.80$, $Re = 10^7$.

Figure 3.11: Critical length comparison for the *numeric* approach assuming Reynolds constant or variable.

In figure 3.11 it is demonstrated that the variation of critical length is low as long as the flow is turbulent. Once the flow is laminar, the variation of the Reynolds is significant. Note the jump of the curve for $Re = 10^4$ when the critical value is reached. After that, the critical length decreases until values close to $u_w = u_1$ as the friction factor tends to be infinite, which is non-physical.

Chapter 4

Real-scale model

Nomenclature

β	Blockage ratio ($= A_{pod}/A_0$)
P_i	Perimeter at station i
$D_{h,i}$	Hydraulic diameter at station i
$D_{eq,i}$	Equivalent diameter at station i
A_i	Cross area of component i
L_i	Length of component i
D_i	Diameter of component i
ε_{ch}	Surface roughness of the channel
ε_{duct}	Surface roughness of the duct
R	Ideal gas constant (287.55 kJ/kg/K)
γ	Perfect gas adiabatic ratio (1.4)
c_p	Specific heat at constant pressure (1006.43 kJ/kg/K)
g	Earth's gravity
m	Vehicle mass
m_i	Mass of component i
λ_{mag}	Ratio of magnetic drag to weight
u_w	Wall speed
a	Wall acceleration
N_T	Net thrust
$N_{T,trg}$	Target net thrust
$\dot{W}_c$	Power consumed by the compressor
$\dot{W}_t$	Power consumed by the turbine
$F_{w,i}$	Force at station i
$F_{w,i}$	Force at the wall at station i
u_i	Thermodynamic speed at station i
M_i	Mach number at station i
T_i	Static temperature at station i
p_i	Static pressure at station i

ρ_i	Static density at station i
p_{it}	Total pressure at station i
T_{it}	Total temperature at station i
p_{its}	Total pressure at station i with isentropic evolution
ρ_{it}	Total density at station i
Re	Reynolds number
$\dot{W}_i$	Power consumed or provided by component i
E_{bat}	Energy required on the batteries
E_{spc}	Specific energy (measured in kJ/(km pax)
$\dot{W}_{tot}$	Total power installed in the capsule
$\dot{W}_{net}$	Net power
$IMFR$	Inlet Mass Flow Ratio
π_c	Pressure Ratio of the compressor
π_{ij}	Total pressure ratio between station i and j
η_i	Efficiency of the component i
$\dot{m}_\pi$	Mass flow shallowed by the compressor
$\dot{m}_\beta$	Mass flow around the capsule
$\dot{m}_i$	Mass flow at station i
$\dot{m}_{i,crit}$	Critical mass flow at station i
α_t	Ratio of the enthalpy on the turbine with respect to the one on the compressor
n_{row}	Number of passengers in each row in the cabin
m_{pod}	Vehicle mass
L_{pod}	Vehicle length
L_{duct}	Duct length
L_{ch}	Channel length
d_{cru}	Distance to be covered during the cruise phase
n_{pax}	Number of passengers
ρ_i	Volumetric density of the component i
λ_i	Mass density of the component i

4.1 Introduction

This section describes the dynamic model developed for the real-scale system of the hyperloop proposed by *Zeleros*. This design tool allows the analysis of different scenarios according to different proposed missions of the vehicle. Its goals are:

- Estimate the mass and overall dimensions of the system.
- Estimate the mass and volume of the main components.
- Estimate the requirements in terms of mass, volume and energy of the battery.
- Define the thermodynamic cycle on the propulsive system.
- Establish the requirements of the propulsive system, for instance, pressure ratio of the fan, ducting area, nozzle area...

- Estimate the energy consumption and power requirements.

As the performance of the system is obtained, it is possible to compare this system with other means of transportation.

To solve this proposed problem, several hypotheses had to be taken to simplify the physics involved in the problem:

- Only the cruise phase is analysed, as the goal is to obtain a design point.
- This is a 0D model; no space or time integration is conducted.
- Only what happens around the vehicle is modelled, as the tube is considered infinite. This means that the design point is a representative point of the whole mission, but not to a certain point on the track.
- Only longitudinal dynamics are considered.
- The interference of other capsules is neither considered.
- The exchange of mass and energy from the tube to the exterior is not considered.

The model has been developed in Matlab.

4.2 Dynamic model

The model developed for the real-scale system of *Zeleros* is a dynamic model in one degree of freedom (dof), the longitudinal or axial one. Due to the mostly unknown geometry of the vehicle and the tube of a real-scale hyperloop, a more complex model could not be developed.

The first step is to consider the forces acting on the vehicle. A schematic is shown in figure 4.1. These forces are the following:

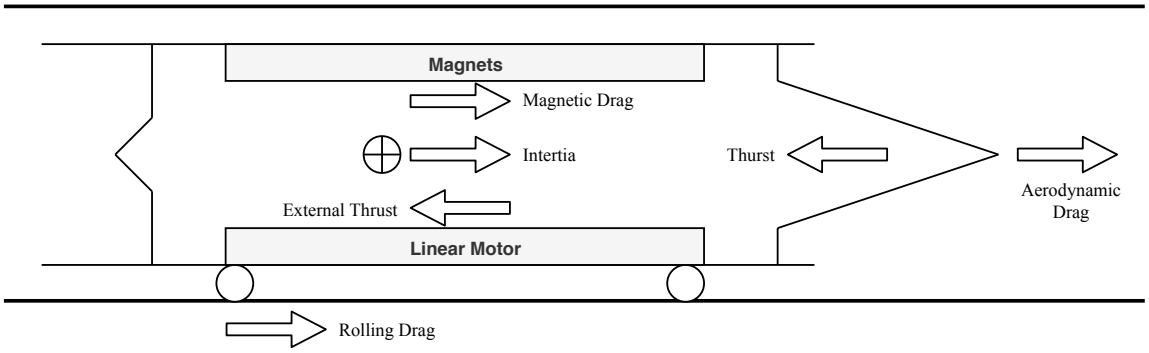

Figure 4.1: Overview of the forces around the capsule in a generic position on the tube.

- **Thrust**: this is the propulsive force in cruise, provided by the turbomachinery included in the vehicle.

- **External thrust**: this is the acceleration provided by the linear motor during acceleration or braking phases.
- **Aerodynamic drag**: resultant of the aerodynamic force over the walls of the prototype.
- **Magnetic drag**: drag resulting from the magnets. It is modelled as a constant parameter named as drag-to-lift ratio λ_{mag}: $D_{mag} = \lambda_{mag} mg$.
- **Rolling friction**: this takes into account the momentum losses due to the wheels in contact with the ground in phases where the capsule is not levitating.
- **Inertia**: in order to consider a quasi-steady case, the inertial force due to the acceleration of the mass of the vehicle is included as an additional force opposing the movement. Its value is $F_I = ma$.

Due to modelling exclusively the cruise phase on the simulator, the capsule is assumed to be levitating, and, as a consequence, no rolling friction forces are considered. Also, the same hypothesis makes that the external thrust has not to be modelled either.

Then, the remaining forces are the magnetic drag, the aerodynamic drag and the thrust. As the magnetic resistance is simplified with a constant coefficient proportional to the vehicle mass, the rest of the section will be focused on the aeropropulsion of the vehicle. Also, to simplify the problem, the aerodynamic drag and thrust will be joined in one unique force: the net thrust. Splitting these two aerodynamic forces does not have physical meaning, as the thrust level largely affects the pressure and momentum field around the capsule and the drag.

So, the sum of forces on the vehicle is the following, according to the second law of Newton:

$$N_T - D_{mag} - F_I = 0 \rightarrow N_T = m\left(a + \lambda_{mag} g\right). \tag{4.1}$$

So, to maintain a constant speed during the cruise phase, the net thrust must be equal to the magnetic drag. Furthermore, if any extra acceleration is required, N_T must also overcome the inertial term. The computation of the net thrust is described in section 4.3.

4.3 Aeropropulsive model

The aeropropulsive model must solve the concept shown in figure 4.2, where a simplification of the vehicle is represented, focused on the propulsive system. There, a capsule inside a *tube* or tunnel travels at a certain speed. Part of the air goes around the object, flowing through the gap between the vehicle and the tube, named as *channel*, while another part is absorbed by the *compressor*. For the latter, the turbomachinery increases its energy and density, so it can go through the vehicle, leaving space for the rest of the components and the payload, included on the *cabin*. From the inner flow, part of its energy is recovered on a *turbine* before exhausting it through the *nozzle*, mixing with the exterior flow.

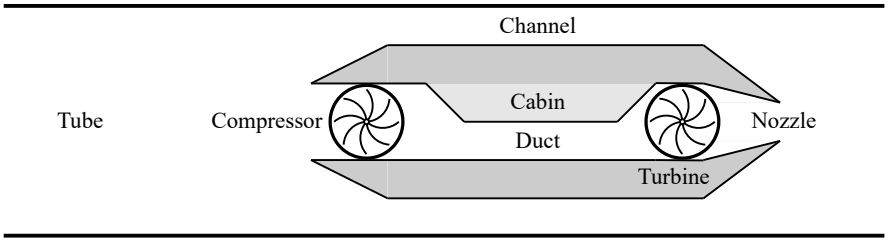

Figure 4.2: Simplification of the concept of hyperloop.

Note that an important distinction between *duct*, *channel*, and *tube* is made. The *duct* is the geometry able to transfer the flow from the compressor to the turbine and the nozzle within the capsule, while the *channel* is the free area between the capsule and the tube wall. The *tube* refers to the whole structure where the capsules move. If not otherwise stated, the *tube* area or diameter refers to the inner one.

Before deeply analysing the equations used on the model, a high-level vision of the code is described and shown in figure 4.3. The overall inputs for the code are the following:

- λ_{mag}: ratio between the weight and the magnetic drag.
- a_{cr}: acceleration allowed for the cruise. This can help, for instance, to reach higher speeds than the cruise one, surpass slopes, or overcome non-modelled drag.
- D_{tube}: tube diameter.
- D_{pod}: capsule diameter.
- n_{row}: number of passengers in each row in the cabin.
- Cabin par: parameters to define the geometry of the cabin. These will be detailed in section 4.5.1.
- u_0: capsule speed.
- p_0: static pressure on the tube.
- T_0: static temperature on the tube.
- $\dot{m}_c$: mass flow shallowed by the compressor.
- $IMFR$: Inlet Mass Flow Ratio. From this parameter compressor mass flow can be computed as: $\dot{m}_c = IMFR\, A_{pod} u_0 \rho_0$.
- π_c: pressure ratio of the compressor.
- M_4: Mach at the end of the ducts. This parameter is often more useful than the pressure ratio of the compressor as the turbomachine is not designed. The actual restriction is that the internal duct must not be blocked.

- α_t: ratio of the enthalpy on the turbine with respect to the one on the compressor.
- A_9: area of the nozzle.
- η_{th}: different efficiencies of the thermodynamic cycle. These will be explained in section 4.4.
- η_{sys}: different system efficiencies. These will be explained in section 4.5.2.
- d_{cru}: distance to be covered during the cruise phase.
- n_{pax}: number of passengers.
- Pod par: parameters that define the mass and length of the vehicle. These will be defined in section 4.5.3.

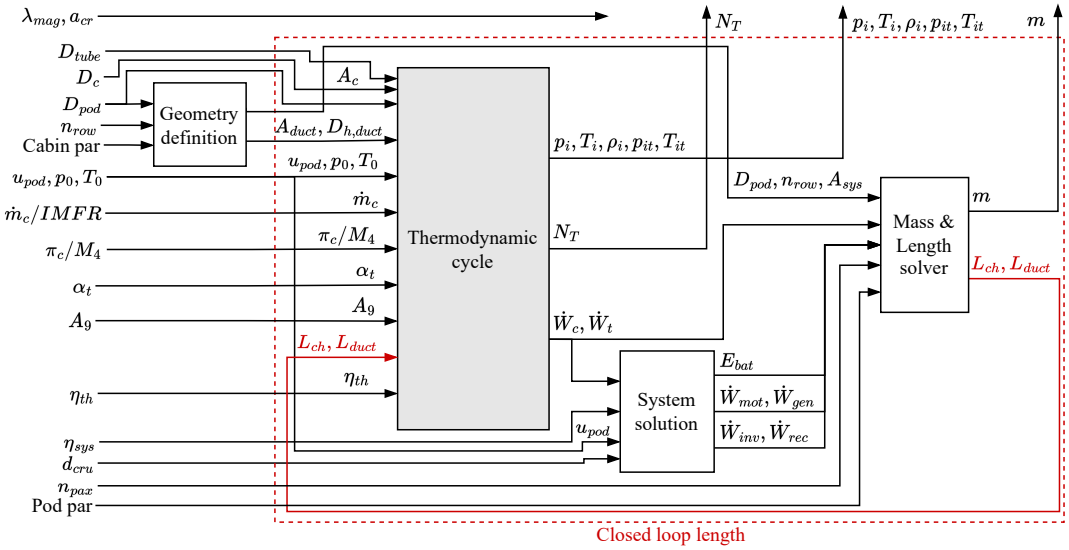

Figure 4.3: Top level architecture of the code.

- N_T, m: net thrust and mass of the capsule.
- ρ_i, T_i, p_i, p_{it}, T_{it}: thermodynamic variables in each station.
- $\dot{W}_{mot}$, $\dot{W}_{gen}$, $\dot{W}_{inv}$, $\dot{W}_{rec}$: power consumed by each component, in particular, the motor, generator, inverter and rectifier.
- $\dot{W}_c$, $\dot{W}_t$: power consumed by the compressor and the turbine.
- E_{bat}: energy required on the batteries.
- A_{comp}: cross-sectional area occupied by each component.

- L_{ch}: channel length.
- L_{duct}: length of the duct.

The different modules are the following:

- *Geometry definition*: this module computes the transversal areas of the vehicle, including the cabin. It is explained in section 4.5.1.
- *Thermodynamic cycle*: this is the actual propulsive model which solves the 0D model of the system. It is explained in section 4.4.
- *System solution*: according to the power required by the compressor and the turbine, and the efficiency of the different components, it computes the power and energy consumed by the vehicle. It is explained in section 4.5.2.
- *Mass & Length solver*: according to the space allowed from the geometry definition and the requirements of the components computed in the *System solution*, this module computes the mass and length of the vehicle. It is explained in section 4.5.3.

4.4 Thermodynamic cycle

To obtain the net thrust, the flow around the capsule must be solved, which is the aim of this thermodynamic model. A moving reference frame placed on the vehicle is used on the approach. For that reason, the tube moves at the wall speed u_w, as the unperturbed flow, and the capsule remains still.

As the aerodynamic forces are the most relevant to the solution of the problem, a propulsive 0D discretisation of the problem based on the standard of the aero-engines industry [127] is used. These are shown in figure 4.4, where two different control volumes are represented: the one around the vehicle $V_{f,ext}$ and the one going through it $V_{f,int}$. Note also that there is a compression wave in front of the capsule to model the cases in which not all the flow displaced by the capsule can surpass it.

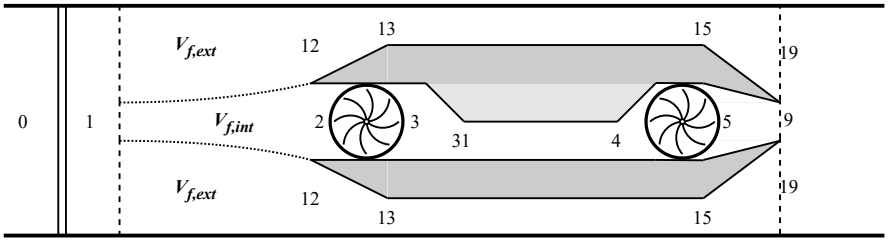

Figure 4.4: Nomenclature used to solve the thermodynamic cycle.

In more detail, the description of each station is the following:

- Upstream:

  - Stage 0: far field. The flow is not perturbed at all by the vehicle.
  - Stage 1: after the compression wave. This wave propagates the information of the choked channel between the capsule and the tube, rapidly modifying the upstream conditions from 0.

- Interior control volume:
  - Stage 2: on the compressor face. The current tube goes from 1 to 2.
  - Stage 3: just after the compression phase. The energy of the flow is maximum at this stage.
  - Stage 31: after the transition of the ducts.
  - Stage 4: at the end of the ducts and before the turbine (if any). Between 31 and 4 there is a Fanno flow.
  - Stage 5: after the turbine. If there is no turbine, 4 and 5 are the same station.
  - Stage 8: on the nozzle throat.
  - Stage 9: on the nozzle exit.

- Exterior control volume:
  - Stage 12: on the starting of the nacelle. The difference with 1 is the area, reduced by the capsule.
  - Stage 13: when the capsule starts its cylindrical shape. Between 1 and 13 there is a pressure loss.
  - Stage 15: when the capsule starts to decrease its cross-section to adapt to the nozzle. Typically, this is the external throat. Afterwards, the area should increase again.
  - Stage 19: equivalent to the nozzle exit, but on the exterior part. There is again a pressure loss between 15 and 19.

As seen in figure 4.3, the inputs of this module are the following:

- D_{tube}: tube diameter.
- D_{pod}: capsule diameter.
- A_{duct}: duct cross-section.
- $D_{h,duct}$: hydraulic diameter of the duct, as it may not be annular.
- u_{pod}: capsule speed, or in this case also wall speed or V_w.
- p_0: static pressure on the tube.
- T_0: static temperature on the tube.
- $\dot{m}_c$: mass flow shallowed by the compressor.

- π_c or M_4: pressure ratio of the compressor or Mach number at station 4. This affects how the internal cycle is computed, as explained in section 4.4.3.
- α_t: ratio of the enthalpy on the turbine with respect to the one on the compressor.
- A_9: area of the nozzle.
- L_{ch}: the length of the channel.
- L_{duct}: the length of the duct.
- η_{th}: different efficiencies of the thermodynamic cycle. These are:
  - Diffuser total pressure ratio: π_d.
  - Compressor isentropic efficiency: η_c.
  - Turbine isentropic efficiency: η_t.
  - Ducting total pressure ratio on the transition: π_{tr}.
  - Nozzle total pressure ratio: π_n.
  - Front isentropic efficiency on the bypass flow: η_f. Its obtention is detailed in appendix B.4.
  - Rear isentropic efficiency on the bypass flow: η_r. Its obtention is detailed in appendix B.4.

The outputs of this module are the following:

- ρ_i, T_i, p_i, p_{it}, T_{it}: thermodynamic variables in each station.
- N_T: net thrust.
- $\dot{W}_c$, $\dot{W}_t$: power consumed by the compressor and the turbine.

The boundary conditions for this problem are the following:

- Inlet mass flow imposed, based on the unperturbed conditions as remarked in equation (4.4). This condition ensures that no flow is accumulated and all the mass displaced by the control volume of the capsule goes through it, which is a consequence of the hypothesis of infinite tube.
- Inlet total temperature imposed, as in equation (4.2).
- Inlet total pressure imposed, as in equation (4.3).

With this boundary conditions, the downstream pressure cannot be fixed. Generally, it will be lower than the one on the tube, which is the same effect as seen in [128].

As this is an internal flow, blocking problems may arise, as already discussed in section 2.2.5. This discontinuity of the problem implies different ways of solving the problem depending on the blocking state of the flow. Table 4.2 collects all these cases.

This, leads to considering different modifications to the equations applied to meet the specifications of the case in particular:

Case	Interior	Exterior	Compression wave
1	0	0	0
2	0	1	1
3	1	0	0
4	1	1	1

Table 4.2: Different procedures for the blocking of the different domains.

- Case 1: there is no compression wave, so stations 0 and 1 have the same values.
- Case 2 (exterior blocked): the compression wave appears, and p_{1t} and T_{1t} are recomputed to allow all the mass flow to go through the channel.
- Case 3 (interior blocked): the turbomachinery cannot absorb that mass flow, and $\dot{m}_\pi$ is decreased to the critical value. On its own, the upstream conditions are not modified, but the decrease in $\dot{m}_\pi$ leads to an increase in the mass through the channel $\dot{m}_\beta$.
- Case 4 (interior and exterior blocked): the compression wave appears again, and the mass flow through the compressor decreases to its critical value. Then, the external mass flow increases accordingly.

Cases 3 and 4 cannot occur when imposing M_4 as this Mach is always lower than 1, and the internal duct cannot be blocked. The code fails if π_c is imposed instead of M_4. So, cases 1 and 2 are the only ones described in this document. The solution process between them is considerably modified.

There are several modules on the code accounting for the different cases. The solving process is shown in figure 4.5. As for the modules, these are:

- Interior (normal): solves the interior flow, from station 1 to station 5 (see section 4.4.3.1 when imposing π_c and section 4.4.3.2 when imposing M_4).
- Exterior (normal): solves the external flow if it is not blocked, from station 1 to station 15 (see section 4.4.2.1).
- Exterior (blocked): solves the external flow if it is blocked, from station 1 to station 15 (see section 4.4.2.2. It can also solve 19 blocked as explained in appendix B.2.
- Discharge: solves the nozzle (station 9) and rear part of the capsule, station 19 iteratively (see section 4.4.4).

In the following points, the equations to solve the cycle are explained. It is important to remark that several times the continuity equation is said to be solved in a specific station. The algorithm is detailed in appendix B.1.

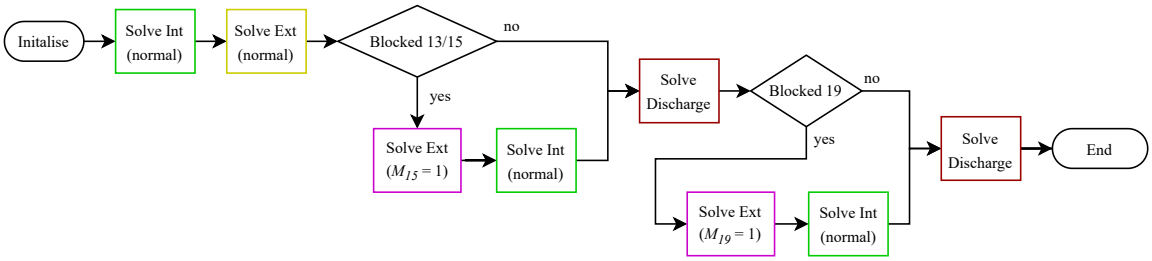

Figure 4.5: Flow chart describing the solving process conducted on the model.

4.4.1 Initial station

Firstly, the total conditions in station 0 are computed:

$$T_{0t} = T_0 \left(1 + \frac{\gamma - 1}{2} M_0^2\right), \tag{4.2}$$

$$p_{0t} = p_0 \left(1 + \frac{\gamma - 1}{2} M_0^2\right)^{\frac{\gamma}{\gamma - 1}}. \tag{4.3}$$

The mass flow in 0 is also computed:

$$\dot{m}_0 = \frac{p_0}{RT_0} u_0 A_0, \tag{4.4}$$

where u_0 is equal to the body speed u_w as the station 0 is the unperturbed flow.

Then, the speed and density at 0:

$$u_0 = M_0 \sqrt{\gamma R T_0}, \qquad \rho_0 = \frac{p_0}{RT_0}. \tag{4.5}$$

The mass flow on the channel $\dot{m}_\beta$:

$$\dot{m}_\beta = \dot{m}_0 - \dot{m}_\pi. \tag{4.6}$$

The rest of the process is explained in the following sections.

4.4.2 External channel solution

In this section, the computation of the conditions until 15 is explained, according to the values at station 1. This process is shown in figure 4.6.

4.4.2.1 No chocked external channel

If the channel is not blocked, the conditions in 1 are the same as in 0, as no compression wave appears:

$$T_{1t} = T_{0t}, \qquad p_{1t} = p_{0t}, \qquad M_1 = M_0. \tag{4.7}$$

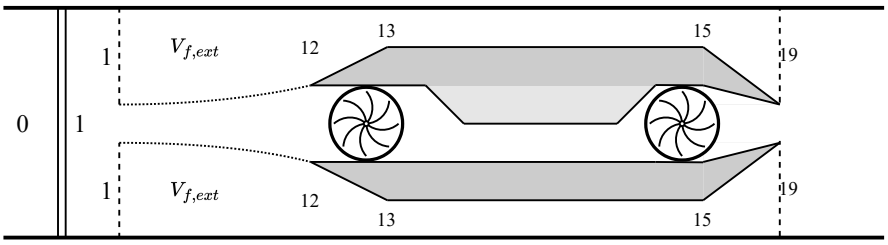

Figure 4.6: Stages modelled for the external flow.

Now, the internal cycle is solved up to station 5, as explained in section 4.4.3.1. It allows to determine:

$$[T_{5t}, p_{5t}, M_5] = \text{internal}\left(\dot{m}_\pi, T_{1t}, p_{1t}, L_{duct}, A_{duct}, D_{h,duct}\right). \tag{4.8}$$

Between stations 1 and 12, there is an isentropic flow, as the losses on the current tube are neglected:

$$T_{12t} = T_{1t}, \qquad p_{12t} = p_{1t}. \tag{4.9}$$

The Mach in 12 (M_{12}) is computed using the compressible continuity equation:

$$M_{12} = \frac{\dot{m}_\beta}{A_{12}} \frac{\sqrt{T_{12t}}}{p_{12t}} \sqrt{\frac{R}{\gamma}} \left(1 + \frac{\gamma - 1}{2} M_{12}^2\right)^{\frac{\gamma+1}{2(\gamma-1)}}. \tag{4.10}$$

To compute equation 13, station 12 is omitted, and the following isentropic efficiency is defined, equivalent to the one from a diffuser:

$$\eta_f = \frac{h_{13ts} - h_1}{h_{13t} - h_1} = \frac{\frac{T_{13ts}}{T_1} - 1}{\frac{T_{13t}}{T_1} - 1} = \frac{\left(\frac{p_{13ts}}{p_1}\right)^{\frac{\gamma-1}{\gamma}} - 1}{\frac{T_{13t}}{T_1} - 1}. \tag{4.11}$$

This implies that the total pressure in 13 ($p_{13ts} = p_{13t}$) is computed as:

$$p_{13t} = p_1 \left(1 + \eta_f \frac{\gamma - 1}{2} M_1^2\right)^{\frac{\gamma}{\gamma-1}}. \tag{4.12}$$

Moreover, as the flow is adiabatic:

$$T_{13} = T_{1t}. \tag{4.13}$$

Now, in station 13, the critical mass flow $\dot{m}_{13,crit}$ can be computed:

$$\dot{m}_{13,crit} = A_{th} \frac{p_{13t}}{\sqrt{T_{13t}}} \sqrt{\frac{\gamma}{R}} \left(\frac{\gamma + 1}{2}\right)^{-\frac{\gamma+1}{2(\gamma-1)}}. \tag{4.14}$$

If $\dot{m}_\beta < \dot{m}_{13,crit}$ the following equations are used. If not, section 4.4.2.2 explains the process.

Also, note the definition of the throat area:

$$A_{th} \equiv A_{13} = A_{15}. \tag{4.15}$$

The Mach at station 13 can be computed using, again, the compressible continuity equation:

$$M_{13} = \frac{\dot{m}_\beta}{A_{th}} \frac{\sqrt{T_{13t}}}{p_{13t}} \sqrt{\frac{R}{\gamma}} \left(1 + \frac{\gamma - 1}{2} M_{13}^2\right)^{\frac{\gamma+1}{2(\gamma-1)}}. \tag{4.16}$$

Using p_{13t}, T_{13t}, $A_{13} = A_{th}$, M_{13}, $\dot{m}_{13} = \dot{m}_b$, and the geometric parameters (length and diameter) the Fanno flow can be solved as explained in appendix A.4. With those equations, π_{1315} and M_{15} are computed. At a high level, the Fanno solver is the following:

$$[M_{15}, \pi_{1315}] = \text{Fanno}\left(M_{13}, u_w, u_{13}, \varepsilon_{ch}, Re_{13}, D_{pod}, D_{tube}, L_{ch}\right). \tag{4.17}$$

The rest of the parameters at 15 are:

$$p_{15t} = \pi_{1315} p_{13t}, \tag{4.18}$$

$$T_{15t} = T_{13t}. \tag{4.19}$$

If the Fanno flow was blocked, section 4.4.2.2 reformulates all the processes of this section.

4.4.2.2 Chocked external channel

If the external channel is chocked, M_{15} is set to 1. Then, the rest of the parameters are unknown, and the process is not explicit, from station 1 to station 15 on the external channel.

Now, stations 0 and 1 are not equivalent due to the compression shock wave. As the channel is blocked and all the mass flow wants to go through the fluid domain, the upstream pressure must be increased, leading to this difference.

The equation system used for the iteration of this process is the following:

- Total pressure ratio on the diffusion process between stations 1 and 13. From equation (4.11):

$$\pi_{0113} = \left[\frac{1 + \eta_f \frac{\gamma-1}{2} M_1^2}{1 + \frac{\gamma-1}{2} M_1^2}\right]^{\frac{\gamma}{\gamma-1}}. \tag{4.20}$$

- Adiabatic compression between 1 and 0:

$$p_{0t}^{1-\gamma} T_{0t}^{\gamma} = p_{1t}^{1-\gamma} T_{1t}^{\gamma}. \tag{4.21}$$

- Compressible continuity at 15 (chocked). Adiabatic flow, i. e. $T_{1t} = T_{15t}$, has been used:

$$\dot{m}_\beta = A_{th}\frac{p_{15t}}{\sqrt{T_{15t}}}\sqrt{\frac{\gamma}{R}}\left(\frac{\gamma-1}{2}\right)^{-\frac{\gamma+1}{2(\gamma-1)}} = A_{th}\frac{p_{1t}}{\sqrt{T_{1t}}}\pi_{0113}\pi_{1315}\sqrt{\frac{\gamma}{R}}\left(\frac{\gamma-1}{2}\right)^{-\frac{\gamma+1}{2(\gamma-1)}}. \quad (4.22)$$

- Compressible continuity at 1:

$$M_1 = \frac{\dot{m}_0}{A_0}\frac{\sqrt{T_{1t}}}{p_{1t}}\sqrt{\frac{R}{\gamma}}\left(1+\frac{\gamma-1}{2}M_1^2\right)^{\frac{\gamma+1}{2(\gamma-1)}}. \quad (4.23)$$

- Once the conditions at 1 are solved, station 13 can be solved again assuming adiabatic flow:

$$p_{13t} = \pi_{0113}p_{1t}, \quad (4.24)$$
$$T_{13t} = T_{1t}. \quad (4.25)$$

- With the conditions in 13, Fanno flow can be recomputed as explained in appendix A.4. Then, it is obtained again M_{13} and π_{1315}. It does not matter if the mass flow is higher than the critical on the Fanno because the pressure upstream will increase to allow all the mass to pass. At a high level, the Fanno solver is the following:

$$[M_{13}, \pi_{1315}] = \text{Fanno}\left(M_{15}, u_w, u_{13}, \varepsilon_{ch}, Re_{13}, D_{pod}, D_{tube}, L_{ch}\right). \quad (4.26)$$

The system is solved with two nested loops, the outer iterating over M_{13} and the inner iterating over M_1.

1. Guess π_{1315}. For the first step, a blocked Fanno channel is solved as explained in appendix A.4. The conditions in 12 for the Reynolds and flow speed are used. This allows to estimate M_{13}.
   (a) Guess M_1. For the first step, it is equal to M_0.
   (b) Compute π_{0113} from equation (4.20).
   (c) Solve equations (4.21) and (4.22) analytically for T_{1t} and p_{1t} as explained in appendix B.2.
   (d) Obtain M_1 from equation (4.23), and compare it with the initial guess.
2. Compute station 13 using equations (4.24) and (4.25).
3. Obtain u_{13} and Re_{13} from conditions in 13.

4. Solve Fanno from 13 to 15 as a blocked channel, using the conditions in 13 for the flow speed and the Reynolds, obtaining M_{13} and π_{1315}, as indicated in equation (4.26).

5. Compare with initial M_{13} guess.

The outer loop can be removed if enough confidence is given to the initial guess of M_{13} using the conditions in 12 for the flow speed and the Reynolds. These parameters only slightly affect the friction factor. This means that, as the length does not vary, the effects on the final result are almost negligible.

Between stations 1 and 12, there is an isentropic flow, as the losses on the current tube are neglected:

$$T_{12t} = T_{0t}, \qquad p_{12t} = p_{0t}. \tag{4.27}$$

The Mach in 12 (M_{12}) is computed using the compressible continuity equation:

$$M_{12} = \frac{\dot{m}_b}{A_b}\frac{\sqrt{T_{12t}}}{p_{12t}}\sqrt{\frac{R}{\gamma}}\left(1+\frac{\gamma-1}{2}M_{12}^2\right)^{\frac{\gamma+1}{2(\gamma-1)}}. \tag{4.28}$$

Regarding station 15:

$$p_{15t} = \pi_{1315}p_{13t}, \tag{4.29}$$

$$T_{15t} = T_{13t}. \tag{4.30}$$

Finally, station 19 cannot be computed until the area at 9 is obtained in section 4.4.4. There, the iterative process to obtain 9 and 19 simultaneously is explained.

4.4.3 Internal flow solution

In this section, the computation of the conditions at the entry of the nozzle (5) is explained according to the values at station 1. This process is shown in figure 4.7. Firstly, all the main components are explained here.

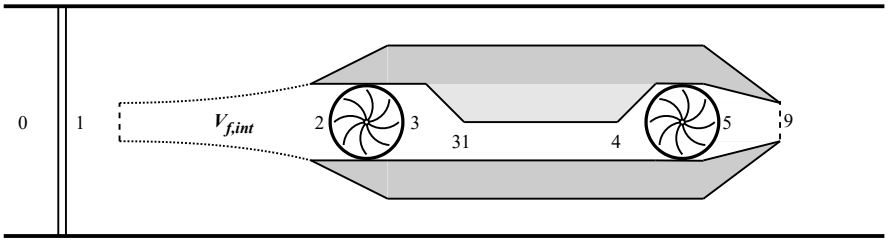

Figure 4.7: Stages modelled for the internal flow.

The diffuser is computed using a constant pressure loss between stations 1 and 2 (π_d):

$$p_{2t} = \pi_d p_{1t}. \tag{4.31}$$

As the flow is adiabatic:

$$T_{2t} = T_{1t}. \tag{4.32}$$

At this point, if the area of the compressor is provided A_c, the Mach at the inlet of the compressor can be computed using the continuity equation:

$$M_2 = \frac{\dot{m}_\pi}{A_c} \frac{\sqrt{T_{2t}}}{p_{2t}} \sqrt{\frac{R}{\gamma}} \left(1 + \frac{\gamma - 1}{2} M_2^2\right)^{\frac{\gamma+1}{2(\gamma-1)}}. \tag{4.33}$$

The compressor is solved with the following equations:

$$p_{3t} = \pi_c p_{2t}, \tag{4.34}$$

$$T_{3t} = T_{2t} \left[1 + \frac{1}{\eta_c} \left(\pi_c^{\frac{\gamma-1}{\gamma}} - 1\right)\right]. \tag{4.35}$$

Then, the duct transition, between 3 and 31:

$$p_{31t} = \pi_{tr} p_{3t}, \tag{4.36}$$

$$T_{31t} = T_{3t}. \tag{4.37}$$

Then, Mach in 31 is computed using the compressibility continuity equation:

$$M_{31} = \frac{\dot{m}_\pi}{A_{duct}} \frac{\sqrt{T_{31t}}}{p_{31t}} \sqrt{\frac{R}{\gamma}} \left(1 + \frac{\gamma - 1}{2} M_{31}^2\right)^{\frac{\gamma+1}{2(\gamma-1)}}. \tag{4.38}$$

Next, the pressure ratio between 31 and 4, π_{34} solving the Fanno flow is obtained, as explained in appendix A.4. At a high level, the solver does the following:

$$[M_4, \pi_{34}] = \text{Fanno}\left(M_{31}, \varepsilon_{duct}, Re_{31}, D_{h,duct}, A_{duct}, L_{duct}\right). \tag{4.39}$$

Then, conditions in 4 are computed:

$$p_{4t} = \pi_{34} p_{3t}, \tag{4.40}$$

$$T_{4t} = T_{3t}. \tag{4.41}$$

Finally, the turbine is solved from the compressor using the ratio between enthalpies α_t:

$$T_{5t} = T_{4t} - \alpha_t \left(T_{3t} - T_{2t}\right), \tag{4.42}$$

$$p_{5t} = p_{4t} \left[1 - \frac{1}{\eta_t} \left(1 - \frac{T_{5t}}{T_{4t}}\right)\right]^{\frac{\gamma}{\gamma-1}}. \tag{4.43}$$

The nozzle is solved in section 4.4.4, as it is coupled with the external flow.

The definition of the isentropic efficiencies for the compressor and the turbine are the following:

$$\eta_c = \frac{h_{3ts} - h_{2t}}{h_{3t} - h_{2t}} = \frac{\frac{T_{3ts}}{T_{2t}} - 1}{\frac{T_{3t}}{T_{2t}} - 1} = \frac{\pi_c^{\frac{\gamma-1}{\gamma}} - 1}{\frac{T_{3t}}{T_{2t}} - 1}, \tag{4.44}$$

$$\eta_t = \frac{h_{4t} - h_{5t}}{h_{4t} - h_{5ts}} = \frac{1 - \frac{T_{5t}}{T_{4t}}}{1 - \frac{T_{5ts}}{T_{4t}}} = \frac{1 - \frac{T_{5t}}{T_{4t}}}{1 - \left(\frac{p_{5t}}{p_{4t}}\right)^{\frac{\gamma-1}{\gamma}}}. \tag{4.45}$$

4.4.3.1 Internal flow imposing PR

In this section, the value of π_c is known, so the diffuser, compressor and transition can be solved straightforward as exposed in equations (4.31) to (4.37). Mach in 31 is obtained by solving equation (4.38) and then is followed the process described in appendix A.4 using the parameters in 31 to determine π_{34} and M_4 from the Fanno on the ducts. Next, the total pressure p_{4t} and temperature T_{4t} are computed using equations (4.40) and (4.41) respectively. The turbine is also solve as equations (4.42) and (4.43).

If M_4 was larger than the $M_{4,max}$ established by the user, M_4 is fixed to that value, and the problem is solved iteratively as detailed in section 4.4.3.2.

4.4.3.2 Internal flow imposing Mach

In this section, the value of M_4 is known. Firstly the diffuser, compressor and transition are solved straightforward as exposed in equations (4.31) to (4.37) assuming that $\pi_c = 1$.

Then, Mach in 31 is obtained by solving equations (4.38). After that, the process described in appendix A.4 is used to determine π_{35} and $M_{4,lim}$. This is the maximum value of M_4 as $\pi_c = 1$ is the lowest the fan can compress. If $M_{4,lim}$ is lower than the imposed one, M_4 is changed to $M_{4,lim}$, and the solution has already been obtained.

Otherwise, if $M_{4,lim} > M_4$ the process is iterative, using the following system:

1. Guess π_c. For the first iteration, $\pi_c = 1$ is used.
2. Compressor is solved using equations (4.34) and (4.35), obtaining p_{3t} and T_{3t}.
3. Transition is solved using equations (4.36) and (4.37), obtaining p_{31t} and T_{31t}.
4. M_{31} is computed using equations (4.38).
5. Fanno flow is solved by setting the Mach at the exit M_4, and using the conditions at the entrance 31 for the Fanno parameter, as described in appendix A.4. π_{34} and M_{31} are determined.
6. p_{31t} is computed directly from the continuity equation (4.38), taking T_{31t} and M_{31} from the previous steps.

7. The application again of equation (4.36) allows to recompute p_{3t} from p_{31t}.
8. The application again of equation (4.34), as p_{2t} is fixed, allows to recompute π_c.
9. π_c is compared with the initial guess.

4.4.4 Rear expansion solution

The code can compute the closure of the nozzle and the external channel in two different ways, one assuming that the areas are known, as described in section 4.4.4.1, or when the areas are unknown, as described in section 4.4.4.2.

Firstly, the isentropic efficiencies between 15 and 19 and between 5 and 9 are defined:

$$\eta_n = \frac{h_{5t} - h_9}{h_{5t} - h_{9s}}, \qquad \eta_r = \frac{h_{15t} - h_{19}}{h_{15t} - h_{19s}}. \tag{4.46}$$

Assuming that the flow is adiabatic ($T_{15t} = T_{19t}$) and ($T_{5t} = T_{9t}$), the previous equations can be reformulated as:

$$\eta_n = \frac{1 - \frac{T_9}{T_{5t}}}{1 - \left(\frac{p_9}{p_{5t}}\right)^{\frac{\gamma-1}{\gamma}}}, \tag{4.47}$$

$$\eta_r = \frac{1 - \frac{1}{1+\frac{\gamma-1}{2}M_{19}^2}}{1 - \left(\frac{p_{19}}{p_{15t}}\right)^{\frac{\gamma-1}{\gamma}}}. \tag{4.48}$$

4.4.4.1 Discharge with known areas

The internal and external flow are independent with known areas. Then, no match between static pressure at 9 and 19 is forced as they are just an output.

Firstly, the external channel is solved following this iterative process:

1. Guess M_{19}.
2. Compute p_{19} from equation (4.48): $p_{19} = p_{15t}\left[1 - \frac{1}{\eta_r}\left(1 - \frac{1}{1+\frac{\gamma-1}{2}M_{19}^2}\right)\right]^{\frac{\gamma}{\gamma-1}}$.
3. Obtain M_{19} from the continuity equation at 19 (solved as in section B.1.1):

$$M_{19} = \sqrt{\frac{\sqrt{1 + 2(\gamma-1)\left(\frac{\dot{m}_\beta}{A_{19}p_{19}}\right)^2 T_{19t}\frac{R}{\gamma}} - 1}{\gamma - 1}}.$$

In general, this problem has two different real roots: the subsonic and the supersonic. The solution is chosen based on whether 15 was blocked or not:

- If 15 was blocked:

  - The supersonic solution is taken if exists. Now the external channel is a convergent-divergent supersonic nozzle, in which station 15 is the throat.
  - If the supersonic solution does not exist, the subsonic one is taken, as the flow does not have enough energy to overcome the sonic point.

- If 15 was not blocked:
  - The subsonic solution is taken if exists. Now the external channel is a convergent-divergent full subsonic nozzle, in which station 15 is the throat.
  - If the subsonic solution does not exist, M_{19} is set to one, which means that the nozzle is blocked at the outlet, in 19. In this case, stations 1-19 must be solved simultaneously, as described in appendix B.2.

It is important to highlight that if one wants to find the supersonic solution, instead of the iterative process already mentioned, a mid-point method is used to solve the system. The iterative process always finds the subsonic solutions if two of them exist.

For the internal flow, the process is equivalent to the one described before:

1. Guess M_9.
2. Compute p_9 from equation (4.47): $p_9 = p_{5t}\left[1 - \frac{1}{\eta_n}\left(1 - \frac{1}{1+\frac{\gamma-1}{2}M_9^2}\right)\right]^{\frac{\gamma}{\gamma-1}}$.
3. Obtain M_9 from the continuity equation at 9:

$$M_9 = \sqrt{\frac{\sqrt{1 + 2\left(\gamma - 1\right)\left(\frac{\dot{m}_\pi}{A_9 p_9}\right)^2 T_{9t}\frac{R}{\gamma}} - 1}{\gamma - 1}}.$$

Also, in this case, the iterative process always finds the subsonic solution. However, in case of a convergent-divergent nozzle, the mid-point algorithm is used to find the supersonic solution.

4.4.4.2 Discharge with unknown areas

Now, the exhaust area for 9 and 19 are unknown, so a new closure has to be included to solve the system. Although two variables are introduced, only one degree of freedom is included as the following relation can be directly obtained from a mechanical restriction:

$$A_{19} = A_0 - A_9, \tag{4.49}$$

which means that it is not important if the solution for 9 or 19 is obtained; the other is easily inferred.

The other degree of freedom is restricted by trying to match the static pressure at 9 and 19. For this, the plot in figure 4.8 shows a qualitative relation between A_9 and the pressures p_9 and p_{19}, for three different cases depending on the location of the solution $p_9 = p_{19}$. On the whole, the pressure on the nozzle increases when its area increases. As a result, as A_9

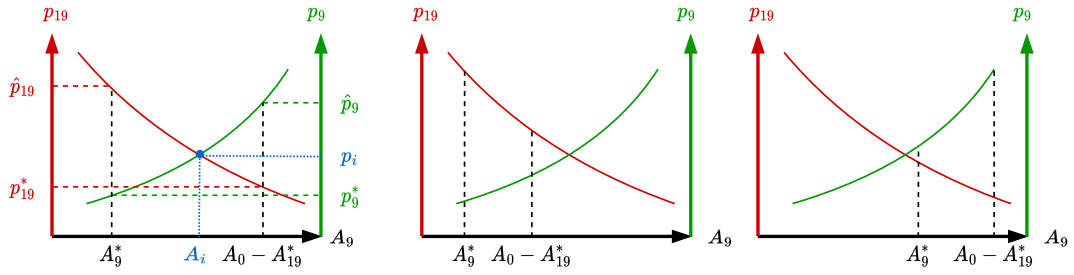

Figure 4.8: Relation between area and pressure at stations 9 and 19.

increases, A_{19} decreases and then p_{19} decreases too. So, p_9 and p_{19} have opposite trends. Real results of these functions are represented in figures 4.18 and 4.17.

The solution is to find the same static pressure for both stations, corresponding to the point i in the graph, where $p_9 = p_{19}$. This area and pressure are named A_i and p_i, respectively.

To find that point, the critical conditions have to be checked first, as they mark the limits of curves and if the solution is in a physical range or not. Firstly, neither of the areas can be lower than its critical, so these are computed:

$$A^*_9, p^*_9 = f\left(T_{5t}, p_{5t}, \eta_n, \dot{m}_\pi\right), \tag{4.50}$$
$$A^*_{19}, p^*_{19} = f\left(T_{15t}, p_{15t}, \eta_r, \dot{m}_\beta\right). \tag{4.51}$$

This function follows the following procedure (for station 9):

$$p^*_9 = p_{5t}\left(1 - \frac{1}{\eta_n}\frac{\gamma-1}{\gamma+1}\right)^{\frac{\gamma}{\gamma-1}}, \tag{4.52}$$
$$p^*_{9t} = p^*_9\left(\frac{\gamma+1}{2}\right)^{\frac{\gamma}{\gamma-1}}, \tag{4.53}$$
$$T_{9t} = T_{5t}, \tag{4.54}$$
$$A^*_9 = \frac{\dot{m}_\pi\sqrt{T_{9t}}}{p_{9t}}\sqrt{\frac{R}{\gamma}}\left(\frac{\gamma+1}{2}\right)^{\frac{\gamma+1}{2(\gamma-1)}}. \tag{4.55}$$

And for station 19:

$$p_{19}^* = p_{15t}\left(1 - \frac{1}{\eta_r}\frac{\gamma-1}{\gamma+1}\right)^{\frac{\gamma}{\gamma-1}}, \tag{4.56}$$

$$p_{19t}^* = p_{19}^*\left(\frac{\gamma+1}{2}\right)^{\frac{\gamma}{\gamma-1}}, \tag{4.57}$$

$$T_{19t} = T_{15t}, \tag{4.58}$$

$$A_{19}^* = \frac{\dot{m}_\beta\sqrt{T_{19t}}}{p_{19t}}\sqrt{\frac{R}{\gamma}}\left(\frac{\gamma+1}{2}\right)^{\frac{\gamma+1}{2(\gamma-1)}}. \tag{4.59}$$

Then, it is known that:

$$A_9 \in [A_9^*, A_0 - A_{19}^*], \tag{4.60}$$

to avoid primary areas lower than the critical ones. In other words, there is no solution if $A_0 - A_{19}^* < A_9^*$. In those cases, the solution can be obtained by setting $A_9 = A_9^*$ and iterating with the procedure explained in section 4.4.4.1.

In any case, when the problem can be solved with the standard procedure, still $\hat{p}_9$ and $\hat{p}_{19}$ have to be determined. $\hat{p}_9$ is the pressure in 9 when 19 is blocked, and $\hat{p}_{19}$ is the pressure in 19 when 9 is blocked. These functions are:

$$\hat{p}_9, \hat{M}_9 = f\left(T_{5t}, p_{5t}, \eta_n, \dot{m}_\pi, A_0 - A_{19}^*\right), \tag{4.61}$$

$$\hat{p}_{19}, \hat{M}_{19} = f\left(T_{15t}, p_{15t}, \eta_r, \dot{m}_\beta, A_{19}^*\right). \tag{4.62}$$

Equations (4.61) and (4.62) are the result of the iterative process described in section 4.4.4.1, as they define an expansion with known area.

Once the pressures at the boundaries are known, three cases arise:

1. $\hat{p}_{19} < p_9^*$ (right graph in figure 4.8). In this case, p_{19} is too low, and the solution is set to critical A_9^*, as expressed in equation (4.50). Conditions in 19 are computed as in equation (4.62).

2. $\hat{p}_{19} > p_9^*$ and $p_{19}^* > \hat{p}_9$ (middle graph in figure 4.8). In this case, p_9 is too low, and the solution is set to critical A_{19}^*, as expressed in equation (4.51). Conditions in 9 are computed as in equation (4.61).

3. There is a solution because the curves intersect within the range of solution to A_9 (left graph in figure 4.8). If assumed there is a linear relationship between the area and the pressure, the first approximation to the non-linear solution is made as:

$$A_i = \frac{A_0\left(\hat{p}_{19} - p_9^*\right) + A_9^*\left(\hat{p}_9 - p_{19}^*\right) + A_{19}^*\left(p_9^* - \hat{p}_{19}\right)}{\hat{p}_9 - p_9^* + \hat{p}_{19} - p_{19}^*}. \tag{4.63}$$

A numerical method is used to solve for A_i and p_i.

4.4.5 Outputs

One of the most important parameters to compute after solving the entire cycle is the total net thrust (N_T). For that, the fluid domain shown in figure 4.9 is used, whose boundaries are the following:

- 1, 9, 19: Pressure and momentum are considered.
- 1-13, 15-19: All the terms are neglected, as no force over the walls has been simulated.
- 13-15: Due to Fanno flow, a force over the wall and the capsule has been computed.

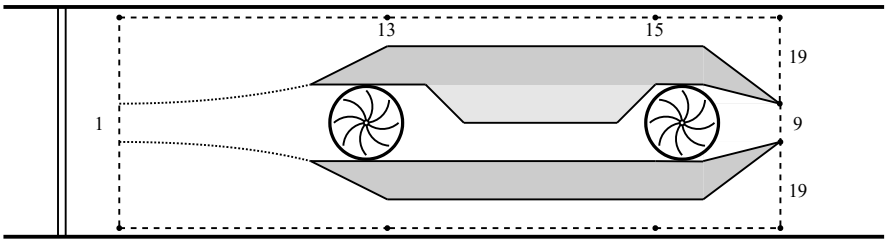

Figure 4.9: Control volume used to compute the net thrust.

So, using the momentum conservation, the net thrust is computed as follows:

$$N_T = p_9 A_9 + p_{19} A_{19} - p_1 A_0 + \dot{m}_\pi u_9 + \dot{m}_\beta u_{19} - \dot{m} u_1 - F_{w,13-15}. \tag{4.64}$$

To compute $F_{w,13-15}$ a control volume from 13 to 15 is used. In that volume, the total drag over the walls is:

$$F_{13-15} = F_{w,13-15} + F_{pod,13-15} = (p_{13} - p_{15})\, A_{ch} + \dot{m}_\beta\, (u_{13} - u_{15})\,. \tag{4.65}$$

From the Fanno flow in chapter 3 equation (3.12), it is known that:

$$K_{Fanno} = \frac{F_{w,13-15}}{F_{pod,13-15}}. \tag{4.66}$$

So, equation (4.65) can be reformulated as:

$$F_{w,13-15} = \frac{F_{13-15}}{1 + K_{Fanno}} = \frac{(p_{13} - p_{15})\, A_{ch} + \dot{m}_\beta\, (u_{13} - u_{15})}{1 + K_{Fanno}}, \tag{4.67}$$

which can be plugged into equation (4.64) to obtain the net thrust finally.

Another relevant parameter is the power consumed by the compressor:

$$\dot{W}_c = \dot{m}_\pi c_p\, (T_{3t} - T_{2t}) = \dot{m} c_p T_{2t} \left\{ \left[1 + \frac{1}{\eta_c} \left(\pi_c^{\frac{\gamma-1}{\gamma}} - 1 \right) \right] - 1 \right\}, \tag{4.68}$$

and by the turbine:

$$\dot{W}_t = \alpha_t \dot{W}_c. \tag{4.69}$$

4.5 Non-thermodynamic modules

4.5.1 Geometry definition

In this section, the cross-section distribution of the capsule is described. This is done to know the space left for the duct and other components.

The inputs of this module are the following:

- D_{pod}: external diameter of the capsule.
- n_{row}: number of passenger per row.
- Cabin par: parameters of the cabin. These are described in section 4.5.1.3 or 4.5.1.4, depending on the type of cabin chosen, described in section 4.5.1.1.

The outputs are the following:

- A_{duct}: cross-section of the duct.
- $D_{h,duct}$: hydraulic diameter of the duct.
- A_{sys}: cross-section area left for the electric components: motor, generator, batteries, inverter and rectifier.

4.5.1.1 Cabin dimensions

Firstly, two different cabin configurations are considered, as seen in figure 4.10. The configuration where the duct is placed below the cabin, named *D-duct*, is shown on the left. Then, the auxiliary systems can be placed on both sides of the cabin. By his part, the right configuration shows that the duct can enclose the cabin, named *A-duct*, leaving space for other systems just below the cabin. In both configurations, the levitation system is placed on the top part of the vehicle.

Another important input parameter is the passengers per row n_{row} that defines the width of the cabin. Thus, three different configurations for seating have been considered (all of them with one corridor), collected in table 4.3[1]. These are based on commercial aircraft.

With the chosen configuration, the following parameters are automatically defined:

- $d_{cab,int}$: interior diameter of the cabin.
- $d_{cab,ext}$: exterior diameter of the cabin.
- h_{cab}: interior height of the cabin.

[1]Reference: `https://www.fairchild-dornier.com/3.html` for the Farchild, `https://web.archive.org/web/20101011091936/http://www.crj.bombardier.com/CRJ/en/specifications.jsp?langId=en&crjId=900` for the Bombardier and `https://www.fokkerservices.com/aircraft/fokker` for the Fokker, last accessed 04-09-2022.

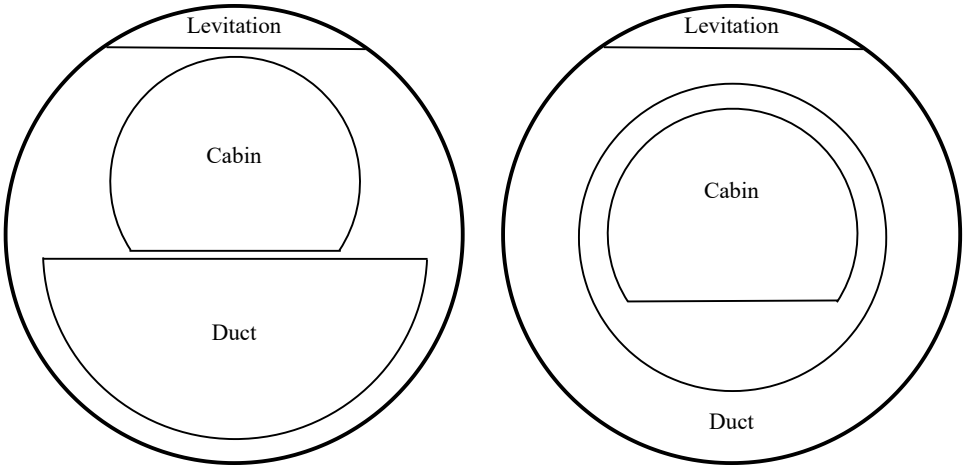

Figure 4.10: Two different distributions of the cabin.

Configuration	Reference plane	Cab diam	Cab diam (ext)	Height
2+1	Fairchild Dornier 328JET	2.18 m	2.41 m	1.89 m
2+2	Bombardier CRJ900	2.50 m	2.71 m	1.89 m
2+3	Fokker 100	3.10 m	3.26 m	2.11 m

Table 4.3: Dimension of the cabin for the reference commercial aircraft.

The space left for batteries is the same as the interior of the cabin. Upstream and downstream of the cabin, there is space for these systems instead of space for passengers or payload. This area is named A_{sys}.

Furthermore, to define the position of the duct and the cabin, the following parameters are also defined as input:

- δ_{lev}: the gap between the vehicle wall and the top part of the cabin. This is space left for the levitation system.
- δ_{floor}: the gap between the cabin and the duct. Only for *D-duct*.
- δ_{bottom}: the gap between the bottom part of the duct and the vehicle wall. Only for *D-duct*.
- $w_{cab,duct}$: space between the exterior of the cabin and the ducts Only for *A-duct*.
- w_{wall}: with of the vehicle wall.

With these parameters, another important one is defined, which is the radius of the capsule on the interior $R_{pod,int}$:

$$R_{pod,int} = D_{pod} - w_{wall}. \tag{4.70}$$

4.5.1.2 Area for levitation and the cabin

The area occupied by the levitation A_{lev} is the following:

$$A_{lev} = R_{pod,int}^2 \left(\arccos \Lambda - \Lambda \sqrt{1 - \Lambda^2} \right), \tag{4.71}$$

where:

$$\Lambda = 1 - \frac{\delta_{lev}}{R_{pod,int}}. \tag{4.72}$$

Another important item to compute is the cabin area A_{cab}, which is equivalent to the area of the systems on the vehicle A_{sys}. This is computed as:

$$A_{cab} = R_{pod,int}^2 \left[(\pi - \arccos \Lambda) - \Lambda \sqrt{1 - \Lambda^2} \right], \tag{4.73}$$

where:

$$\Lambda = \frac{2h_{cab}}{d_{cab,int}} - 1. \tag{4.74}$$

4.5.1.3 Method for *A-duct*

The duct area corresponds to the annular section around the cabin minus a certain space left for levitation. This is seen in figure 4.11. The equation used to compute the area is:

$$A_{duct} = \pi \frac{d_{pod,int}^2}{4} - \pi \frac{\left(d_{cab,ext} + 2w_{cab,duct}\right)^2}{4} - A_{lev}. \tag{4.75}$$

By his part, the perimeter is computed as:

$$P_{duct} = \pi \left(d_{pod,int} + d_{cab,ext} + 2w_{cab,duct} \right). \tag{4.76}$$

And finally, the hydraulic diameter:

$$D_{h,duct} = \frac{4A_{duct}}{P_{duct}}. \tag{4.77}$$

4.5.1.4 Method for *D-duct*

The basic cabin is presented in figure 4.12. It consists of an external circumference, defined by the internal diameter of the vehicle and two sections: the duct (bottom) and the cabin (top). The section for the passengers has an internal and external perimeter due to the width of the wall as the cabin is pressurised.

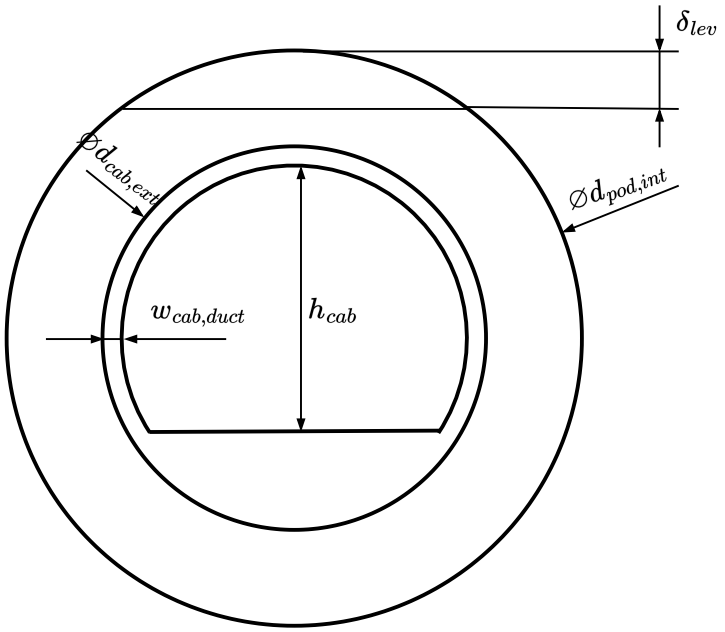

Figure 4.11: Dimensions used to define the cabin with *A-duct*.

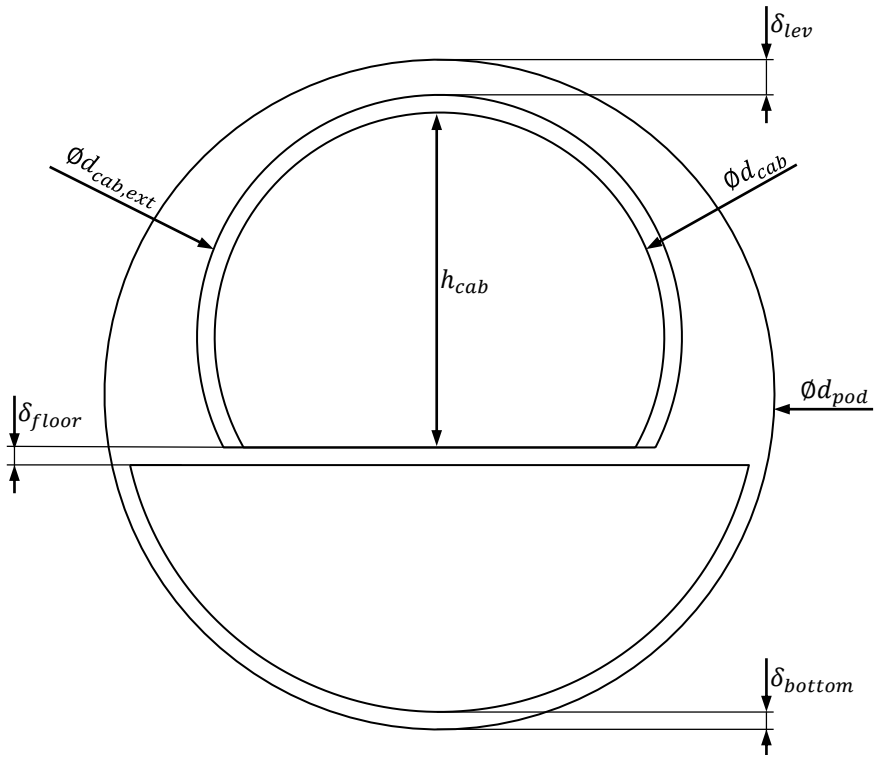

Figure 4.12: Dimensions used to define the cabin with *D-duct*.

The detail of A_{duct} and $D_{h,duct}$ computation is described in appendix B.3.

4.5.1.5 Results

The values used to obtain the results of the present section are the following:

- $\delta_{lev} = 0.15$ m.
- $\delta_{floor} = 0.1$ m.
- $\delta_{bottom} = 0.1$ m.
- $w_{wall} = 0.025$ m.
- $w_{cab,duct} = 0.1$ m.
- D_{pod} part of the parametric swept.
- n_{row} part of the parametric swept.

The results are plotted in figure 4.13. Note that the area of the duct is larger for the *A-duct*, although its hydraulic diameter is higher. Depending on the case, the best configuration is one or the other.

4.5.2 System solver

Once the thermodynamic cycle is solved, the energy balance of the whole vehicle has to be done. The input parameters of this module are the following:

- $\dot{W}_c$: power consumed by the compressor. This is an output of the *Thermodynamic cycle*.
- $\dot{W}_t$: power consumed by the turbine. This is an output of the *Thermodynamic cycle*.
- η_{sys}: efficiency of the different systems and auxiliary power. This is an input of the whole code. The individual values are the following:
  - Efficiency of the system:
    - η_m: batteries.
    - η_{em}: motor.
    - η_{eg}: generator.
    - η_{ei}: inverter.
    - η_{er}: rectifier.
    - η_{ew}: wires and protections.
    - η_{mc}: mechanical transmission.
  - Auxiliary power:
    - η_l: power to the levitation system with respect to the propulsion power.

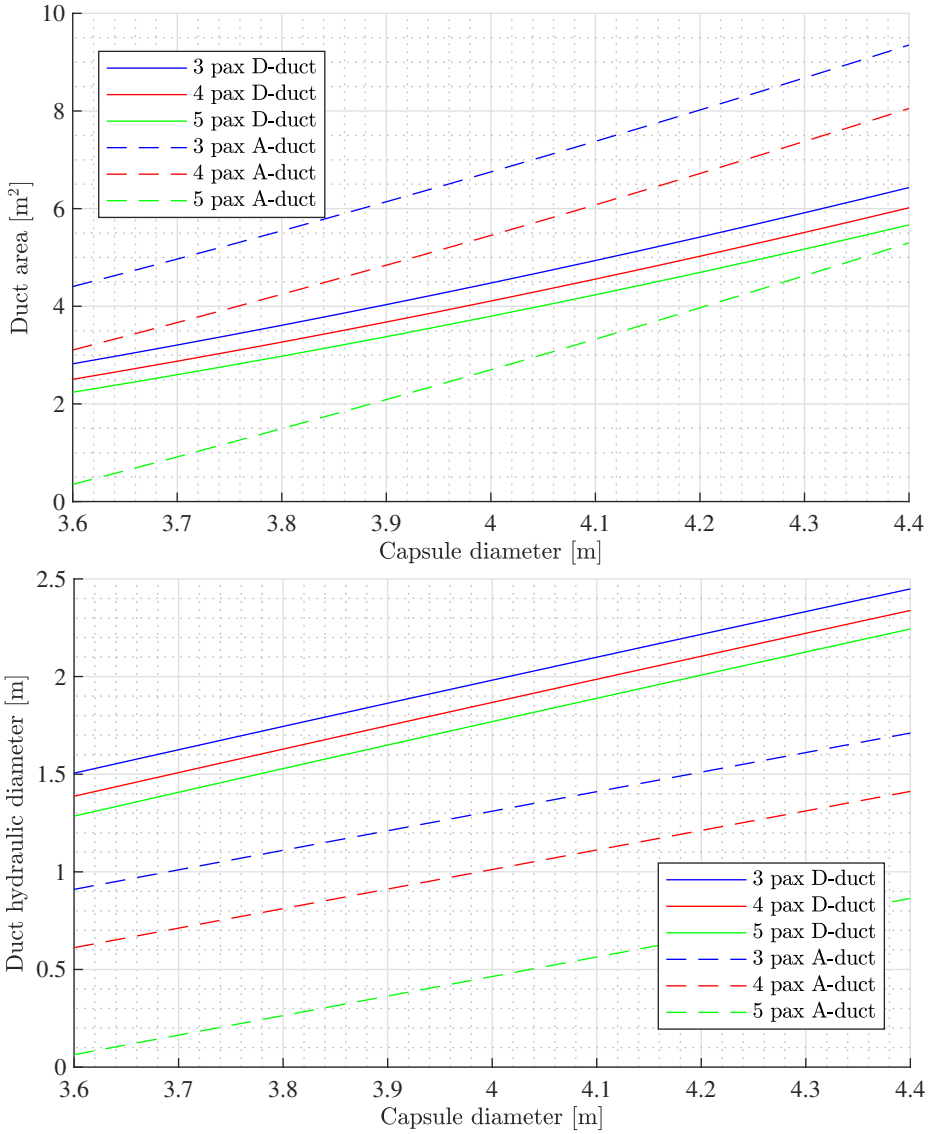

Figure 4.13: Area and hydraulic diameter for the duct in A and D configurations.

  - η_a: power to the auxiliary systems with respect to the propulsion power.
  - η_b: extra energy on the batteries.

- u_{pod}: capsule speed. This is an input of the whole code.
- d_{cru}: cruise distance. This is an input of the whole code.

The outputs are:

- E_{bat}: energy stored by the batteries.
- $\dot{W}_{mot}$: power consumed by the motor.

- $\dot{W}_{gen}$: power recovered by the generator.
- $\dot{W}_{inv}$: power consumed by the inverter.
- $\dot{W}_{rec}$: power recovered by the rectifier.

To complete the energy balance, knowing how much power has to be drawn from the batteries is important. In equation (4.68), the mechanical power from the compressor was defined. The electrical one required by the motor:

$$\dot{W}_{mot} = \frac{\dot{W}_c}{\eta_{mc}\eta_{em}}. \tag{4.78}$$

By his part, the electrical power captured on the generator is:

$$\dot{W}_{gen} = \dot{W}_t \eta_{mc}\eta_{eg}. \tag{4.79}$$

Then, the power on the inverter and rectifier:

$$\dot{W}_{inv} = \dot{W}_{mot}\eta_{ei}^{-1}, \tag{4.80}$$

$$\dot{W}_{rec} = \dot{W}_{gen}\eta_{er}. \tag{4.81}$$

And the power drawn from the batteries $\dot{W}_{c,elec}$, or provided to them $\dot{W}_{t,elec}$:

$$\dot{W}_{c,elec} = \dot{W}_{mot}\left(\eta_{ei}\eta_{ew}\right)^{-1}, \tag{4.82}$$

$$\dot{W}_{t,elec} = \dot{W}_{gen}\left(\eta_{er}\eta_{ew}\right). \tag{4.83}$$

Then, the total power has to add the power to levitation and auxiliary systems:

$$\dot{W}_{tot} = W_{c,elec}\left(1 + \eta_l + \eta_a\right). \tag{4.84}$$

The net power takes into account the difference between the total power:

$$\dot{W}_{net} = \dot{W}_{tot} - \dot{W}_{t,elec}. \tag{4.85}$$

Then, the energy required for the route of d_{cru} length is the following:

$$E_{req} = \frac{\dot{W}_{net} d_{cru}}{u_{pod}\eta_m}. \tag{4.86}$$

This is the energy used to compute the efficiency of the system. However, the total energy carried on the vehicle is higher due to safety reasons:

$$E_{bat} = E_{req}\left(1 + \eta_b\right). \tag{4.87}$$

The diagram plotting the energy flow is shown in figure 4.14.

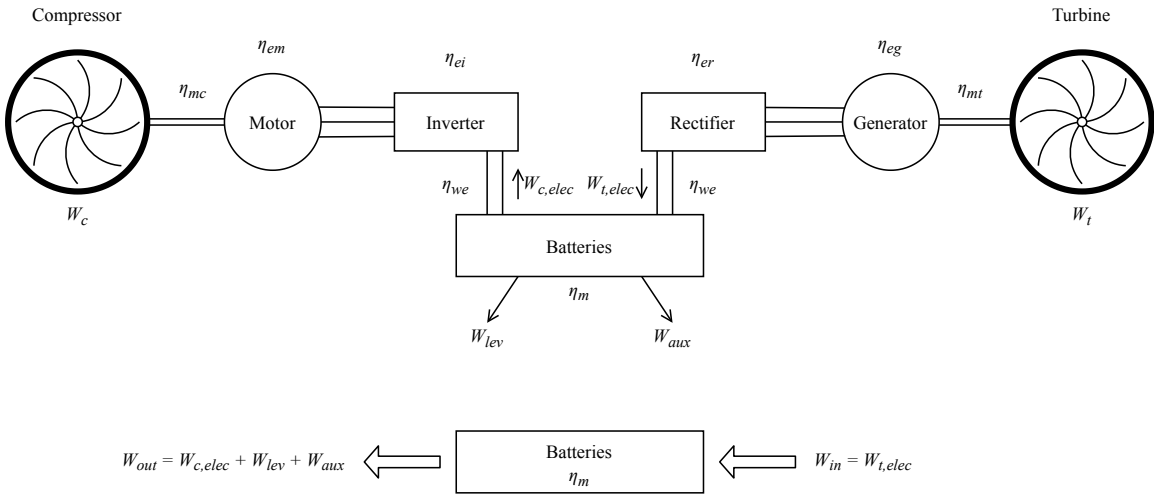

Figure 4.14: Power transmission from the compressor to the turbine.

From the above magnitudes, the parameters that define the efficiency of the system are the following, which are usually outputs to the user:

- Electric motor power: $\dot{W}_{mot}$. Refer to equation (4.78).
- Total energy to store: E_{bat}. Refer to equation (4.87).
- Specific energy: $E_{spc} = E_{req}/\left(d_{cru} n_{pax}\right)$.

4.5.3 Mass and Length solver

The primary goal of this module is to compute the capsule length, the duct, and the total mass. For that purpose, the following inputs are used:

- A_{sys}: cross area of the systems, which include the motor, generator, inverter, rectifier and batteries. Coming from the *geoemtry definition* module.
- E_{bat}: energy stored on the battery. Coming from the *system solution* module.
- $\dot{W}_{mot}, \dot{W}_{gen}$: power consumed by the motor and generator. Coming from the *system solution* module.
- $\dot{W}_{inv}, \dot{W}_{rec}$: power consumed by the inverter and rectifier. Coming from the *system solution* module.
- n_{pax}: number of passengers, coming from the user input.
- n_{row}: number of passengers per row, coming from the user input.
- D_{pod}: diameter of the vehicle, coming from the user input.
- Pod parameters: these include different values that define the mass and volume density of the components, detailed in the following subsections.

4.5.3.1 Vehicle length

The *Pod parameters* required as input to this sub-module are the following:

- ρ_{mot}: volumetric power density of the motor. The same value is used for the generator.
- ρ_{inv}: volumetric power density of the inverter. The same value is used for the rectifier.
- ρ_{bat}: volumetric energy density of the batteries.
- n_{sec}: number of passengers per cabin.
- d_{pitch}: space between seats.
- Duct configuration, whether it is *D-duct* or *A-duct*.

To know the length of the vehicle its longitudinal distribution has to be defined. A top view of a vehicle section is shown in figure 4.15.

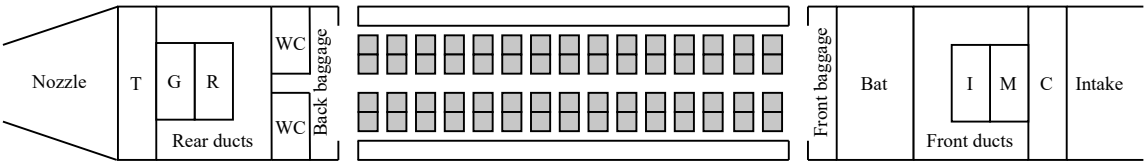

Figure 4.15: Overview of distribution of the capsule. The flow goes from right to left.

As the flow enters, it goes through the intake and the compressor. Then, it flows through the transition of the duct that has two different parts, one in parallel with the motor and the inverter and another to adapt the flow to the *D-duct* or *A-duct* shape. Then, it goes around the space for batteries and the cabin (with seats, baggage space, WC, and front and rear doors). Finally, another transition occurs at the end of the vehicle to adapt the flow to the turbine (if it exists) or the nozzle. For the former, the transition leaves inner space for the rectifier and the generator.

The calculation of the length of each one of the zones is the following:

- Intake: 1 m.
- Compressor: 1 m.
- Motor: $L_{mot} = \dot{W}_{mot} / (\rho_{mot} A_{sys})$.
- Inverter: $L_{inv} = \dot{W}_{inv} / (\rho_{inv} A_{sys})$.
- Front ducts: 4 m for the *D-duct*, or 1 m for the *A-duct*.
- Batteries: $L_{bat} = E_{bat} / (\rho_{bat} A_{sys})$.
- Cabin. It has space for the passengers, the baggage, toilets and doors. More than one cabin can be in the vehicle, each with its own facilities. The number of cabins is computed as the closer integer to $n_{cab} = n_{pax}/n_{sec}$. The length left for each part of the cabin is the following:

  - Front baggage: 0.7 m.
  - Front door: 0.6 m.
  - Passengers: considering a pitch between seats of d_{pitch} m and the number of seats per row as n_{row}, the passengers length is $L_{pax} = \frac{n_{pax}}{n_{row}} d_{pitch}$. The pitch value chosen is 0.76 m[2].
  - Rear door: 0.6 m.
  - Rear baggage: 0.7 m.
  - Toilets: 1 m.

- Rear ducts: 4 m for the *D-duct*, or 1 m for the *A-duct*.
- Rectifier: $L_{rec} = \dot{W}_{rec} / (\rho_{inv} A_{sys})$.
- Generator: $L_{gen} = \dot{W}_{gen} / (\rho_{mot} A_{sys})$.
- Turbine: if the turbine is present, its length is $L_t = 1.5$ m.
- Nozzle: 2 m.

Then, the total length is:

$$L_{pod} = L_{min} + n_{cab} \left(\frac{n_{pax}}{n_{row}} d_{pitch} + L_{min,cab} \right) + \frac{E_{bat}}{\rho_{bat} A_{bat}} + \frac{\dot{W}_{mot} + \dot{W}_{gen}}{\rho_{mot} A_{sys}} + \frac{\dot{W}_{inv} + \dot{W}_{rec}}{\rho_{inv} A_{sys}} + L_T, \tag{4.88}$$

where $L_{min,cab} = 3.6$ m, and $L_{min} = 13$ m for the *D-duct* or $L_{min} = 7$ for the *A-duct*, including one extra meter.

By his part, the duct length is also important to compute for the Fanno flow. Only the length between turbine and compressor is considered, removing the length of the ducts, as they have their own pressure ratio loss:

$$L_{duct} = L_{pod} - L_{duct,pod}. \tag{4.89}$$

$L_{duct,pod}$ takes the value:

- For *A-duct* 6 m without turbine, and 7.5 m with turbine.
- For *D-duct* 12 m without turbine, and 13.5 m with turbine.

4.5.3.2 Weight estimation

The vehicle parameters required as input to this sub-module are the following:

- λ_{mot}: power density of the motor. The same value is used for the generator.
- λ_{inv}: power density of the inverter. The same value is used for the rectifier.

[2]Reference: `https://www.iberia.com/es/a-bordo/tipos-de-asientos/`, last accessed 29-08-2022.

- λ_{bat}: energy density of the batteries.
- λ_{com}: power density of the compressor.
- λ_{tur}: power density of the turbine.
- λ_{lev}: ratio between the mass of the levitation and the vehicle.
- λ_{bra}: ratio between the mass of the brakes and the vehicle.
- λ_{msc}: ratio between the mass of the miscellaneous and the vehicle.
- λ_{str}: mass per unit length of the structure.
- D_{ref}: reference diameter for which the parameter λ_{str} is defined.
- λ_{pax}: mass per passenger.

The mass of the batteries is determined by the expected technology:

$$m_{bat} = E_{bat}/\lambda_{bat}. \tag{4.90}$$

The mass of the turbomachinery is determined by the expected technology:

$$m_{com} = \lambda_{com}\dot{W}_c, \tag{4.91}$$
$$m_{tur} = \lambda_{tur}\dot{W}_t. \tag{4.92}$$

The mass of the motor and generator is determined by the expected technology:

$$m_{mot} = \lambda_{mot}\dot{W}_{mot}, \tag{4.93}$$
$$m_{gen} = \lambda_{mot}\dot{W}_{gen}. \tag{4.94}$$

The mass of the power electronics is also defined by the expected technology:

$$m_{inv} = \lambda_{inv}\dot{W}_{inv}, \tag{4.95}$$
$$m_{rec} = \lambda_{inv}\dot{W}_{rec}. \tag{4.96}$$

For the structure:

$$m_{str} = \lambda_{str}L_{pod}\frac{D_{pod}}{D_{ref}}. \tag{4.97}$$

For the total of passengers, the mass estimated is:

$$m_{pax} = \lambda_{pax}n_{pax}. \tag{4.98}$$

The mass of the levitation, brakes and miscellaneous is defined as a fraction of the vehicle mass:

$$m_{lev} = \lambda_{lev} m_{pod}, \tag{4.99}$$
$$m_{bra} = \lambda_{bra} m_{pod}, \tag{4.100}$$
$$m_{msc} = \lambda_{msc} m_{pod}. \tag{4.101}$$

Finally, the formula that computes the total weight is the following:

$$m_{pod} = \frac{m_{bat} + m_{com} + m_{tur} + m_{mot} + m_{gen} + m_{inv} + m_{rec} + m_{str} + m_{pax}}{1 - (\lambda_{lev} + \lambda_{bra} + \lambda_{msc})}. \tag{4.102}$$

4.6 Loop closure

This section explains how the problem is closed to add the required restrictions in the dof left on the problem.

4.6.1 Inner loop definition

As seen in figure 4.3, once the *Thermodynamic cycle*, *System solver*, and *Mass and Length Solver* modules are solved, the system is iterated with the feedback of the length of the vehicle L_{pod} as in equation (4.88), and the duct L_{duct} as in equation (4.89):

$$L_{new} = L_{old} + \lambda_L \left(L_{new} - L_{old} \right). \tag{4.103}$$

where λ_L is the relaxation factor.

Once the error is below a certain tolerance, a vehicle is computed, not only thermodynamically, but its mass is also obtained.

4.6.2 Optimisation and closure of net thrust

The inner loop of the code aims to obtain the net thrust of a defined design point, but some parameters can vary to obtain the required net thrust according to the mission. The target net thrust is defined in equation (4.1), $N_{T,trg}T$ from now on, which implies that the value depends on the mass and not necessarily is equal to the value computed for a certain vehicle as in the length loop described in section 4.6.1.

Figure 4.16 shows the process used to match the net thrust with its target.

Note that there is a new module called *Solver* N_T that is able to modify the parameters $\dot{m}_\pi$, π_c or M_4, α_t, and A_9 to complete the restriction.

Four different modes have been implemented in this outer loop:

1. $N_T \geq N_{T,trg}$ varying A_9 doing a parametric sweep.
2. $N_T \geq N_{T,trg}$ varying α_t doing a parametric sweep.

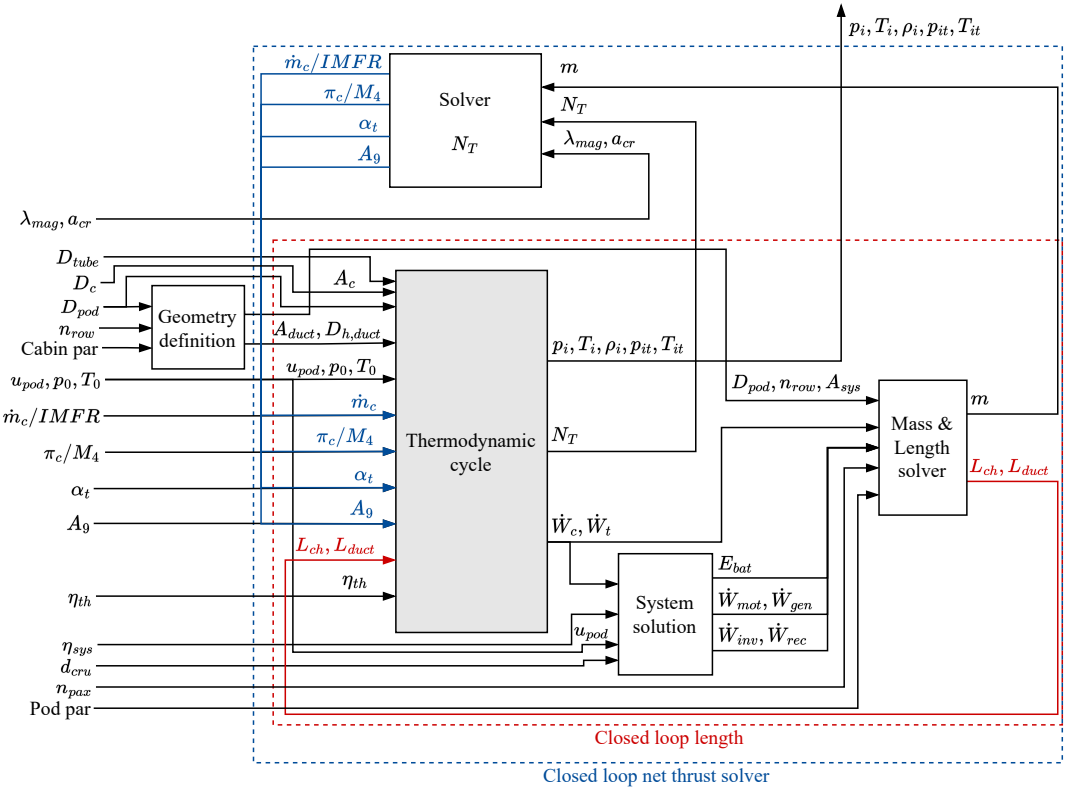

Figure 4.16: Top level architecture of the code including the N_T solver.

3. $N_T \geq N_{T,trg}$ and optimisation varying A_9 and α_t doing a parametric sweep.

4. $N_T \geq N_{T,trg}$ and optimisation varying A_9 and α_t doing a parametric sweep, and M_4 using the interior-point algorithm [129].

5. $N_T \geq N_{T,trg}$ and optimisation varying A_9 and α_t doing a parametric sweep; and M_4 and $\dot{m}_c$ using the interior-point algorithm [129].

The software allows to optimise three different variables: the net power energy $\dot{W}_{net}$, the installed power $\dot{W}_{tot}$ or the pressure difference in the discharge $|p_9 - p_{19}|$.

4.7 Results

In the results section, the simulator is used to obtain results from the real-scale system, aiming for a design point. The input parameters for the simulation are collected in table 4.4.

Variable	Description	Value
u_{pod}	Capsule speed	615 km/h
d_{cru}	Cruise distance	700 km
-	Duct configuration	*D-duct*
λ_{mag}	Ratio between magnetic drag and weight	0.02
a_{cr}	Cruise in acceleration	0
T_0	Tube air temperature	300 K
p_0	Tube air pressure	10 kPa
η_b	Extra energy stored on the batteries	0.25
η_l	Ratio of power to the levitation	0.02
η_a	Ratio of power to the auxiliary systems	0.03
λ_{lev}	Levitation mass ratio	0.1
λ_{bra}	Brakes mass ratio	0.05
λ_{msc}	Miscellaneous mass ratio	0.025
λ_{str}	Mass per unit length of the structure	166.67 kg/m
D_{ref}	Reference diameter for the structure mass	3.2 m
λ_{pax}	Mass per passenger	100 kg/pax
λ_{mot}	Power density of the motor/generator	16 kW/kg
λ_{inv}	Power density of the inverter/rectifier	18 kW/kg
λ_{bat}	Energy density of the batteries	500 Wh/kg
λ_{com}	Power density of the compressor	15 kW/kg
λ_{tur}	Power density of the turbine	15 kW/kg
ρ_{mot}	Volumetric power density of the motor/generator	64 kW/L
ρ_{inv}	Volumetric power density of the inverter/rectifier	36 kW/L
ρ_{bat}	Volumetric energy density of the batteries	1000 Wh/L
n_{sec}	Number of passengers per cabin	100
d_{pitch}	Space between seats	0.76 m
π_d	Diffuser pressure ratio	0.98
η_c	Compressor efficiency	0.85
η_t	Turbine efficiency	0.90
η_n	Nozzle efficiency	0.98
π_{tr}	Duct transition pressure ratio	0.96
η_m	Batteries efficiency	0.98
η_{em}	Motor efficiency	0.96
η_{eg}	Generator efficiency	0.98
η_{ei}	Inverter efficiency	0.98
η_{er}	Rectifier efficiency	0.98
η_{ew}	Wires and protections efficiency	0.985
η_{mc}	Mechanical transmission efficiency	0.995

Table 4.4: Value for all the parameters required for the simulator. The performance values for battery, motor and power electronics are a prediction for 2035 [130].

4.7.1 Validation of the model with CFD

Validation of the present code is performed concerning the parameters obtained with CFD in one of the cases from chapter 2. The simulation, in particular, has the following inputs:

- $D_{cab} = 3.2$ m.
- $L_{pod} = 50$ m.
- $\beta = 0.75$.
- $T_{0t} = 310$ K.
- $u_{pod} = 700$ km/h.
- $IMFR = 0.9$.
- $\eta_f = 1.061$.
- $\eta_r = 0.870$.
- $\alpha_t = 0$.
- $A_9 = 32.17$ m^2.

Moreover, to get the same operation point in the compressor, the conditions in 5 have to be directly imposed in the code. As explained in chapter 2, the CFD model did not include the compressor or the duct:

- $p_{5t} = 14.56$ kPa.
- $T_{5t} = 420$ K.

The comparison between the results from the code and CFD is collected in table 4.5. All the variables extracted from the simulator are within an acceptable range with respect to CFD. The largest difference (23 %) appears in the friction force prediction on the wall. However, this is still valid if one considers the strong hypothesis taken during the development of the simplified Fanno solution in chapter 3. Also, as this case was deeply blocked, the Fanno approximation itself may not be as accurate.

The remaining variables are below a 10 % deviation. The pressures are, in general, more accurate than the Mach numbers. The formers have a maximum deviation of 5 % in the external discharge static pressure p_{19}, which is a challenging value to reproduce. This pressure is a consequence of the rear expansion over the capsule wall and must model possible detachments in the rear part of the vehicle (see chapter 2, figure 2.15c). This cannot be easily reproduced in a 0D model.

With these results, the simulator gets validated, and further outputs can be trusted.

Variable	Fluent	Code	Error
M_1	0.467	0.458	-2.0%
M_2	0.685	0.632	-7.7%
M_{12}	0.355	0.318	-10.3%
M_{12}	0.355	0.318	-10.3%
M_{13}	0.707	0.680	-3.8%
M_{15}	1.006	1.000	-0.6%
M_{19}	0.838	0.861	2.7%
M_9	0.957	0.954	-0.3%
p_{1t} [kPa]	14.54	14.76	1.5%
p_{12t} [kPa]	14.74	14.76	0.2%
p_{13t} [kPa]	14.67	14.89	1.5%
p_{15t} [kPa]	13.58	13.42	-1.2%
p_{19t} [kPa]	12.54	13.10	4.5%
p_{2t} [kPa]	14.54	14.76	1.5%
p_{9t} [kPa]	14.56	14.56	0.0%
p_1 [kPa]	12.52	12.79	2.1%
p_9 [kPa]	8.083	8.109	0.3%
p_{19} [kPa]	7.643	8.073	5.6%
u_1 [m/s]	160.6	157.5	-1.9%
D_{wall} [kN]	11.16	13.73	23.1%

Table 4.5: Comparison between the results from CFD and the simulator for validation.

4.7.2 Parametric study

Before proceeding with the optimisation of the vehicle in section 4.7.3, this section focuses on analysing the trends of essential variables. This parametric study discusses the effect of design parameters such as the nozzle area A_9 and the recovery factor α_t. The capsule diameter is fixed to 3.8 m, $M_4 = 0.9$, $n_{pax} = 50$, $n_{row} = 3$ and $\dot{m}_\pi = 165$ kg/s.

Figure 4.18 shows the evolution of different output variables for a tube diameter of 6 meters. The first plot represents the Mach number in stations 9, 19 and 15. This case is subsonic for the whole range.

The Mach in 15 is not affected by the nozzle area because the geometry in this station (space between capsule and tube wall) is not affected by A_9. Moreover, M_{15} is neither a function of the turbine recovery factor as α_t affects the internal flow, not the external one.

As opposed to M_{15}, M_9 and M_{19} are a function of the nozzle area. As A_9 increases (and A_{19} decreases), M_9 decreases and M_{19} increases. Note that only M_9 varies with α_t. As more energy is recovered in the turbine, the flow expands less in the nozzle, increasing its outlet pressure and decreasing its speed.

Similar trends are observed with the pressures in 9 and 19. For the same reason, only p_9 is affected by the recovery factor, which makes the pressure decrease as more energy is drawn from the turbine. Moreover, as opposed to the Mach numbers trends, p_9 increases

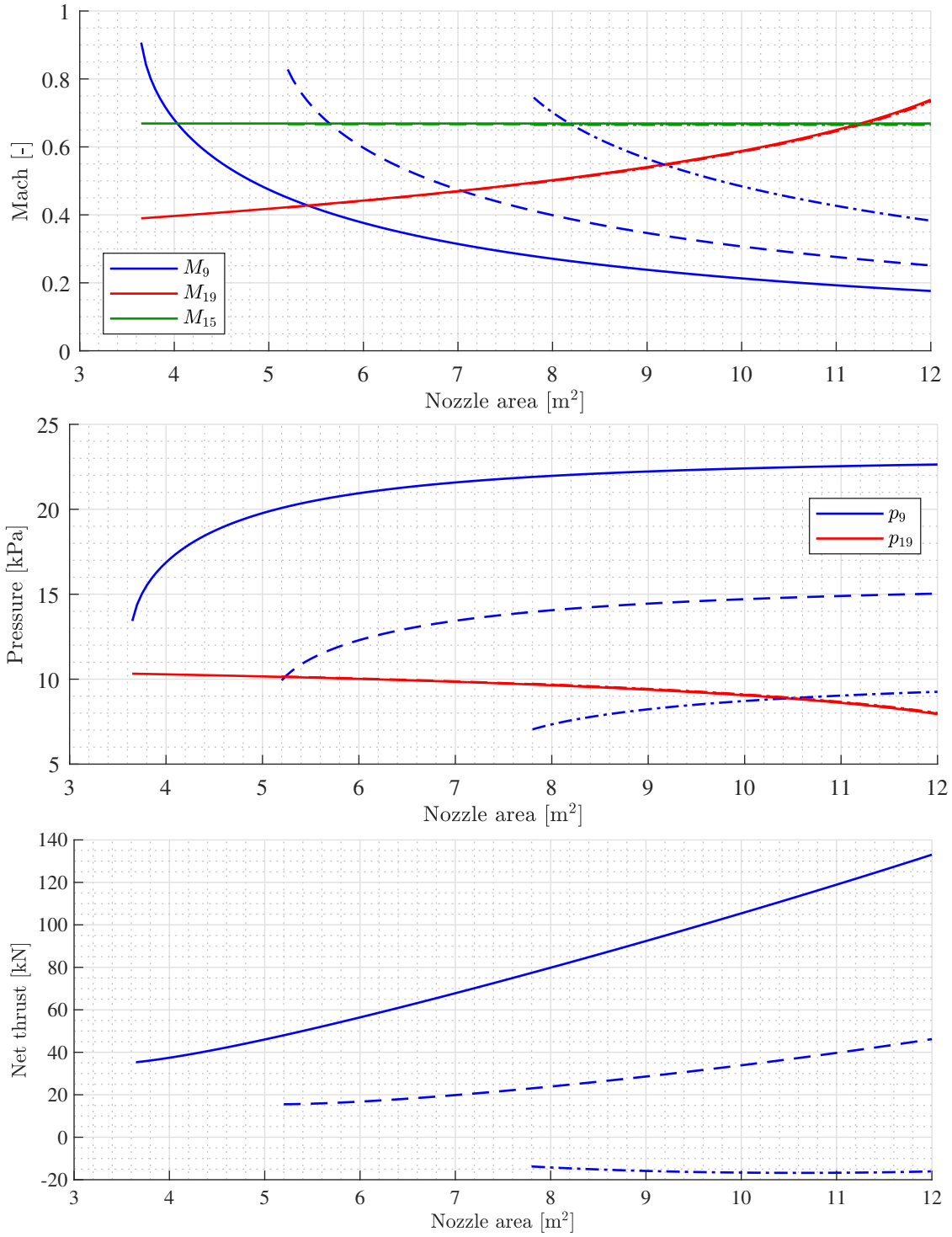

Figure 4.17: Different output variables varying α_t and A_9, for $D_{tube} = 6$ m. Continuous line (–) for $\alpha_t = 0$, dashed line (– –) for $\alpha_t = 0.4$ and dotted-dashed line (–.–) for $\alpha_t = 0.8$.

when its area increases, and the same for p_{19}.

The fact that p_9 increases and p_{19} decreases when A_9 increases make it possible to find the solution where both pressures are matched at the outlet. This is the ideal case, but the intersection of both curves in the physical range is only possible for $\alpha_t = 0.8$. Note that, for $\alpha_t = 0$, both pressures differ up to 14 kPa, which implies a very low mixing efficiency. As this mixing process is not modelled in this simulator, the optimisation process (section 4.7.3) avoids points where both pressures differ more than 500 Pa.

The net thrust is also represented. This variable increases as the A_9 does. This is because the thrust in this problem is dominated by the pressure term, not the momentum one. Remember that p_9 increased while M_9 decreased with the nozzle area variation. Moreover, when recovering more energy in the turbine, the net thrust decreases as more electrical energy is recovered from the flow, not transferred to the fluid. Notice that in areas with flat pressure evolution, the N_T variation is also low.

When using a 5-meter tube (see figure 4.18), all the trends are preserved, except for the M_{15} and M_{19} due to the transition to sonic or supersonic conditions. In this case, the channel is blocked for all the points. From the largest A_9 until $A_9 = 11$ m^2 the throat is 19, as $M_{19} = 1$ and M_{15} is subsonic. As the nozzle area decreases (or A_{19} increases), the geometry behaves as a naval nozzle. There, M_{15} is the throat for the incoming subsonic flow, and supersonic conditions are reached from 15 to 19. This transition is not affected by α_t. Furthermore, the point at which the throat starts to be 15 implies an increase in the slope of p_{19} and N_T evolutions.

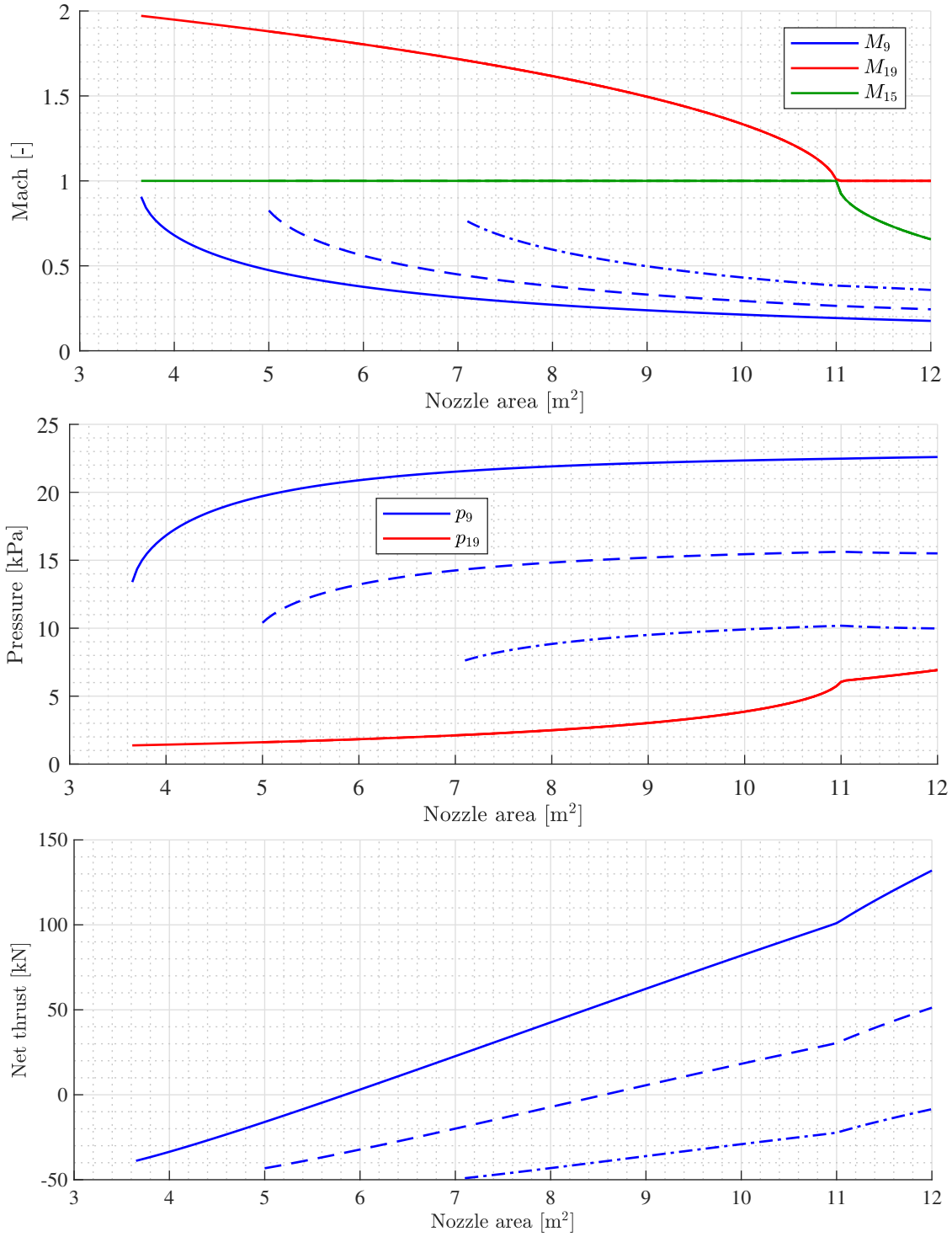

Figure 4.18: Different output variables varying α_t and A_9, for $D_{tube} = 5$ m. Continuous line (–) for $\alpha_t = 0$, dashed line (– –) for $\alpha_t = 0.4$ and dotted-dashed line (–.–) for $\alpha_t = 0.8$.

Finally, the total pressure and temperature evolutions with A_9 are represented in figure 4.19 for a 5-meter and 6-meter tube. For the latter, the pressure and temperature values at the inlet remain constant as the channel is blocked. So, no pressure increase is required upstream to force the mass flow transfer. These values correspond exactly with the tube infinite conditions p_{0t} and T_{0t}.

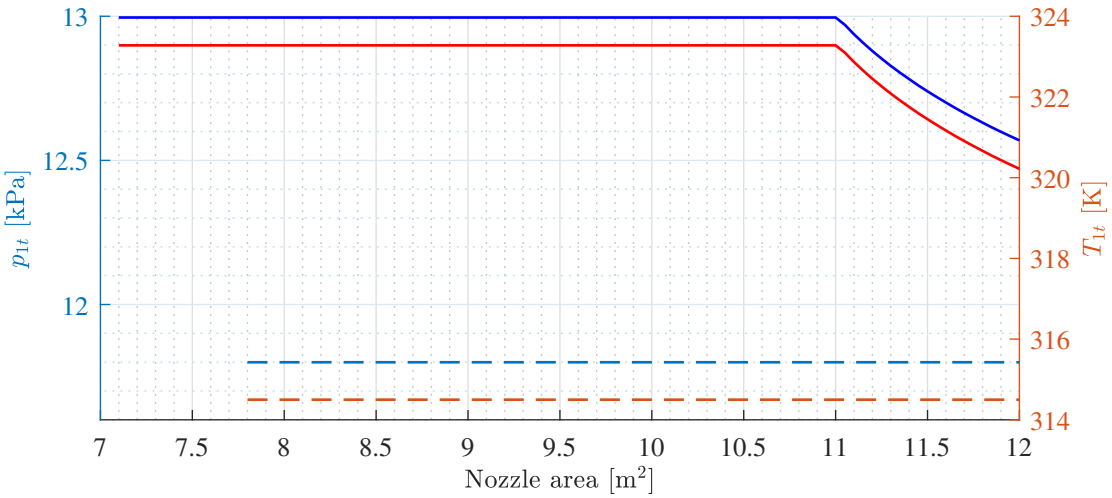

Figure 4.19: p_{1t} and T_{1t} varying nozzle exit area for $\alpha_t = 0$. Continuous line (–) for $D_{tube} = 5$ m and dashed line (– –) for $D_{tube} = 6$ m.

However, for the 5-meter tube, all the solutions are blocked. Then, p_{1t} and T_{1t} are higher to force the mass flow transfer. When the throat is 19, and 15 is subsonic, pressure and temperature increase exponentially until 15 also reaches sonic conditions. From there, when $M_{15} = 1$, p_{1t} and T_{1t} no longer increase and remain constant.

4.7.3 Optimisation

An optimisation process is conducted to obtain a design point for the vehicle. As commented in section 4.6.2 the optimiser (number 4) acts over the design parameters A_9, α_t and M_4, searching for points where $N_T \geq N_{T,trg}$. Optimiser 5 also uses the compressor mass flow, although this algorithm has not been used.

Two different vehicles have been considered for the optimisation. One is the so-called "Z50", the vehicle that has 50 seats. The other is the "Z150", with space for 150 passengers.

For the Z50 and Z150, the optimisation process takes into consideration the following input parameters:

- $D_{tube} = 5,6$ m.
- $n_{row} = 3,4$.
- $\dot{m}_\pi = 130, 165, 200, 230, 255$ kg/s.
- $D_{pod} = 3.6, 4.6$ m (spacing 0.1 m).

The parameter D_{tube} is out of the optimisation process. So, a different solution will be defined for each tube diameter value.

The restrictions used for the solution are the following:

- The absolute difference between p_{19} and p_9 must be lower than 500 Pa. As seen in figures 4.18 and 4.18, if this difference is not considered, p_9 can be significantly different than p_{19}. This leads to non-physical results as the mixing process has not been modelled.
- $N_T > N_{T,trg}$. The net thrust must be higher than the target net thrust to ensure the cruise speed.
- The channel must not be blocked, so $M_{19} < 1$ and $M_{15} < 1$. Although the chocked flow is modelled and may seem locally beneficial as the N_T increases (see figure 4.18), in a real case this scenario should be avoided. If one capsule blocks the channel, the upstream pressure and temperature increase (see figure 4.19) and negatively affect the performance of the rest of the vehicles on the route.

The target optimisation variable is the net power $\dot{W}_{net}$. This parameter was defined in equation (4.85). It is the difference between the total power and the one recovered from the turbine. This parameter defines the energy consumption in a route, which is highly important to evaluate the performance of the system.

4.7.3.1 Z50 vehicle

The first step is to differentiate the use of 3 or 4 passengers per row (n_{row}). This is a balance between having a larger cross-section in a 4-row configuration or having a longer vehicle in a 3-row cabin. The diameter reduction or the length increase negatively affects the Fanno losses so that an optimum can be reached.

Figure 4.20 represents the total and net powers for a 5-meter tube and a 6-meter tube. The two configurations are close to each other. The optimum for each tube diameter occurs for a 4-row configuration, regardless of the total or net power taken. From now on, all the cases use $n_{row} = 4$ as input.

From the plot $\dot{W}_{tot} = \dot{W}_{tot}\left(\dot{W}_{net}\right)$ more conclusions can be drawn. This graph has a limited solution space, as $\dot{W}_{tot}$ must be higher than $\dot{W}_{net}$. The lower limit is the line $\dot{W}_{tot} = \dot{W}_{net}$, with no turbine. The upper limit is the vertical axis, where the turbine recovery is maximum. Furthermore, note that the optimum in terms of net power may not be the same as the total power optimum, although they are close. This means installing more power is more efficient if part of it can be recovered.

The total and net power are represented in figure 4.21 with respect to the compressor pressure ratio. For a 5-meter tube the plot is in figure 4.21a, and for a 6-meter tube in figure 4.21b. Note that, while the net power has a larger dispersion due to variations in A_9 and α_t, the total power follows a more deterministic function. The reason is that the total power (proportional to the compressor power) is only a function of the pressure ratio and the mass flow for a constant efficiency (see equation (4.68)). This explains why each

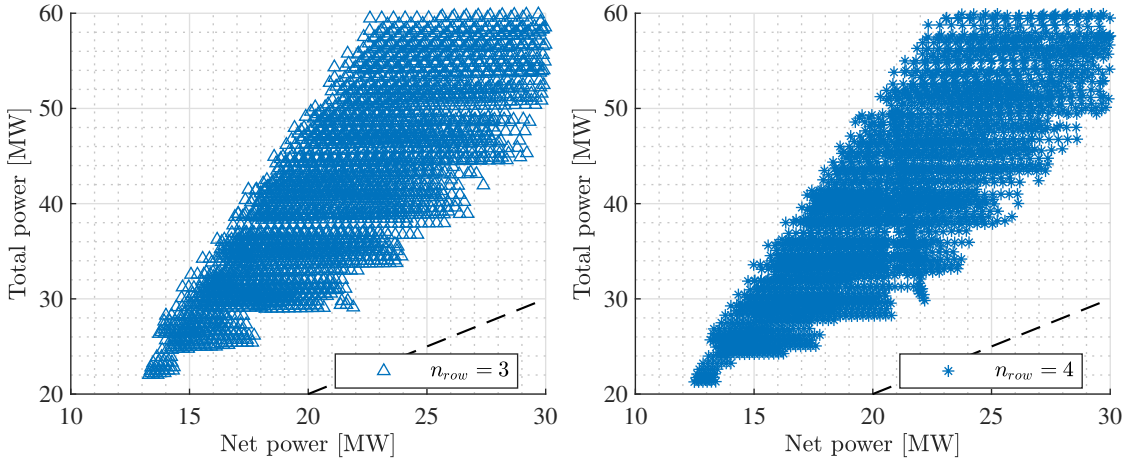

(a) $D_{tube} = 5$ m. $n_{row} = 3$ left and $n_{row} = 4$ right.

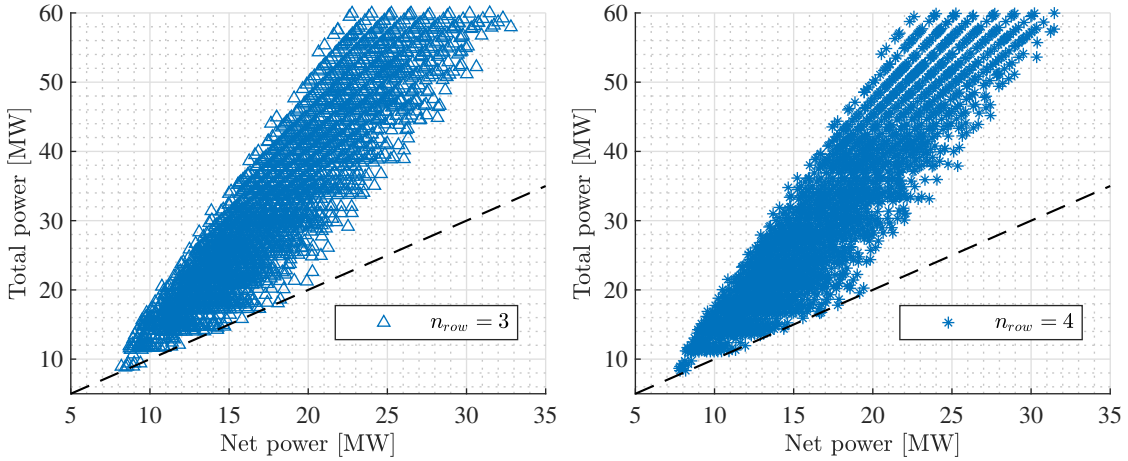

(b) $D_{tube} = 5$ m. $n_{row} = 3$ left and $n_{row} = 4$ right.

Figure 4.20: Total versus net power for different cabin row configurations for the Z50. Dashed line (−−) indicates where $\dot{W}_{net} = \dot{W}_{tot}$.

mass flow follows a unique line. The variation in the input parameter M_4 (equivalent to the pressure ratio) determine the location in the mass flow isoline.

In all cases, the lower the mass flow, the lower the total and net powers. In general, the minimum pressure ratio is not a function of the mass flow. However, for the smaller tube, larger mass flows reach slightly lower π_c.

Note that the lowest $\dot{m}_\pi$ has only solutions for the largest diameter. For smaller tubes, less mass can go around the capsule, and more mass is required for the compressor. Then, the pressure ratio must increase, as more energy must be transferred to the internal flow.

Now, the optimum is going to be found. To do this, several plots are included in appendix B.5.1 for $D_{tube} = 5$ m, and in appendix B.5.2 for $D_{tube} = 6$ m. These represent the total versus the net power, highlighting different capsule diameters and compressor mass flows.

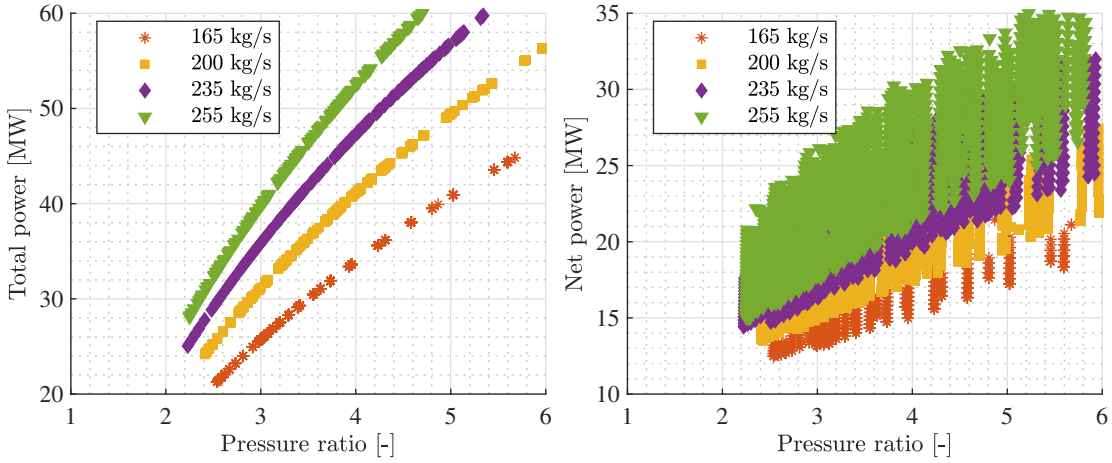

(a) $D_{tube} = 5$ m

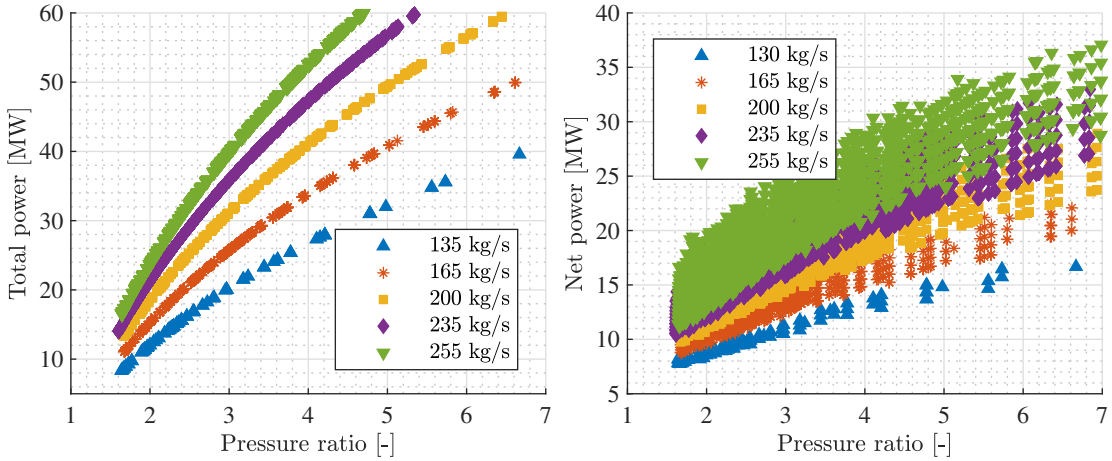

(b) $D_{tube} = 6$ m

Figure 4.21: Total (left figure) and net (right figure) power versus pressure ratio for the Z50.

In this section, only the envelope of the optimums is represented in figure 4.22. These curves follow a parabolic trend, although the ascending part of the curves is not represented because this part does not match the physical restriction. The $\dot{W}_{net}$ optimum occurs for larger capsule diameter when the mass flow is higher.

Moreover, in both tube sizes, the lowest consumption occurs for the lowest compressor mass flow. The physical meaning is that the compressor should shallow the lowest mass flow possible because the energy required to increase its pressure is larger than the external friction losses.

On the whole, the range of the solution for a 6-meter tube is more extensive. Not only because of the appearance of the $\dot{m}_\pi = 130$ kg/s line but also because larger capsule diameters do not have a solution for $D_{tube} = 5$ m. At these points, the flow has less space and chocks, not complying with the restrictions.

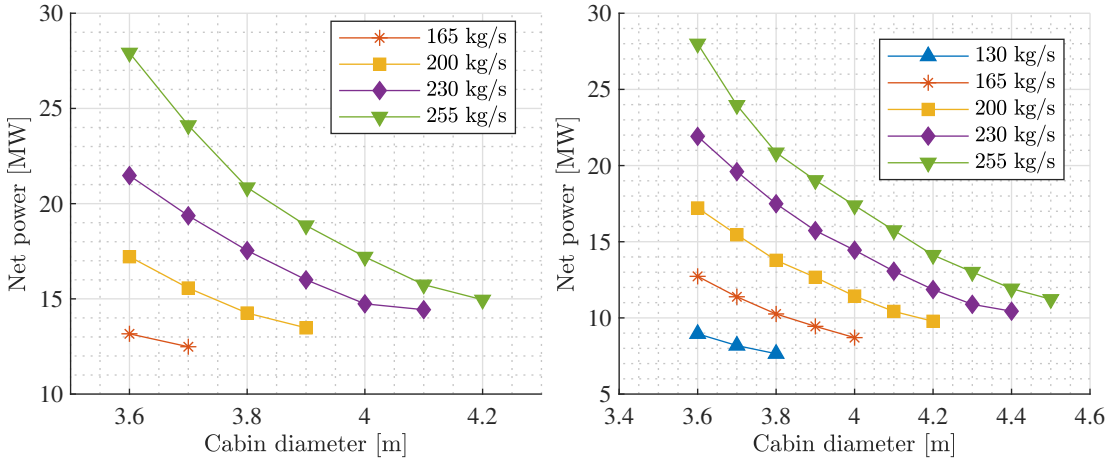

Figure 4.22: Optimums net powers for each capsule diameter and compressor mass flow for the Z50. $D_{tube} = 5$ m (left) and $D_{tube} = 6$ m (right).

4.7.3.2 Z150 vehicle

For the Z150 vehicle, the optimum cabin configuration was, again, the 4-row configuration. This time, the plots have not been included for convenience. The graphs for the total and net powers with respect to the pressure ratio are represented in figure 4.23a for the 5-meter tube, and in figure 4.23b for the 6-meter tube. The same conclusions are drawn from these plots as those extracted for the Z50 (figure 4.21). Now the minimum pressure ratio is larger than the one for Z50, as more energy is required to overcome the duct friction losses.

Moreover, as opposed to the Z50, there is no solution for $\dot{m}_\pi = 130$ kg/s. As the channel length is larger, less mass flow can go around the vehicle without blocking.

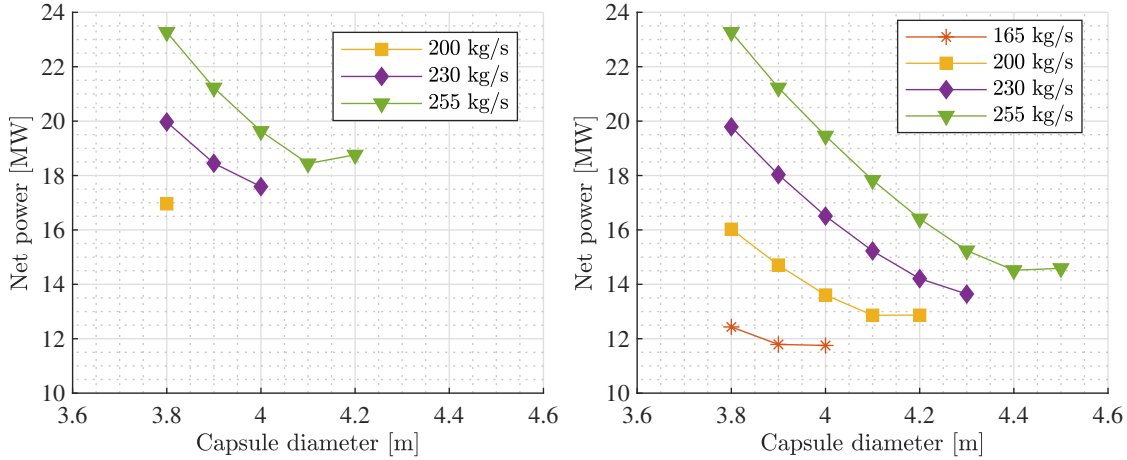

Figure 4.24: Optimums net powers for each capsule diameter and compressor mass flow for the Z150. $D_{tube} = 5$ m (left) and $D_{tube} = 6$ m (right).

Several plots are included in appendix B.5.3 for $D_{tube} = 5$ m, and in appendix B.5.4 for

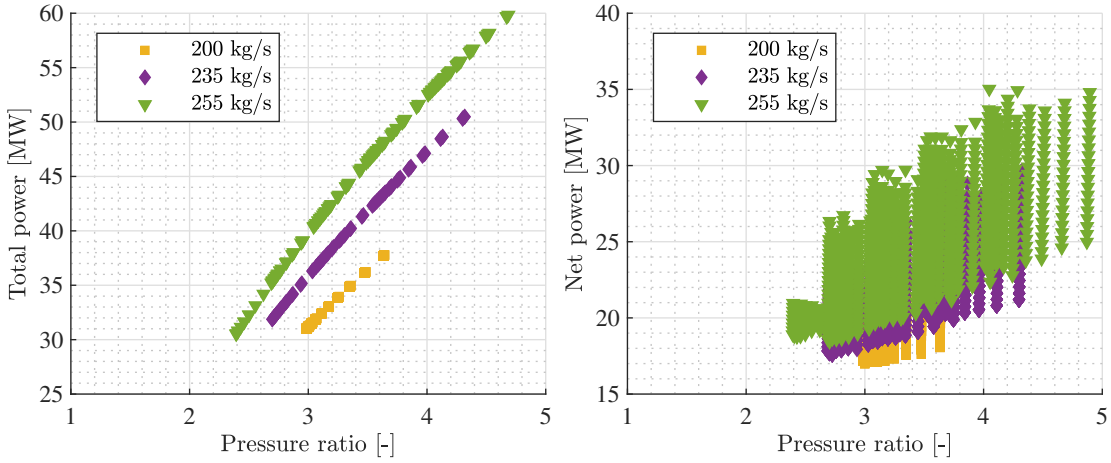

(a) $D_{tube} = 5$ m

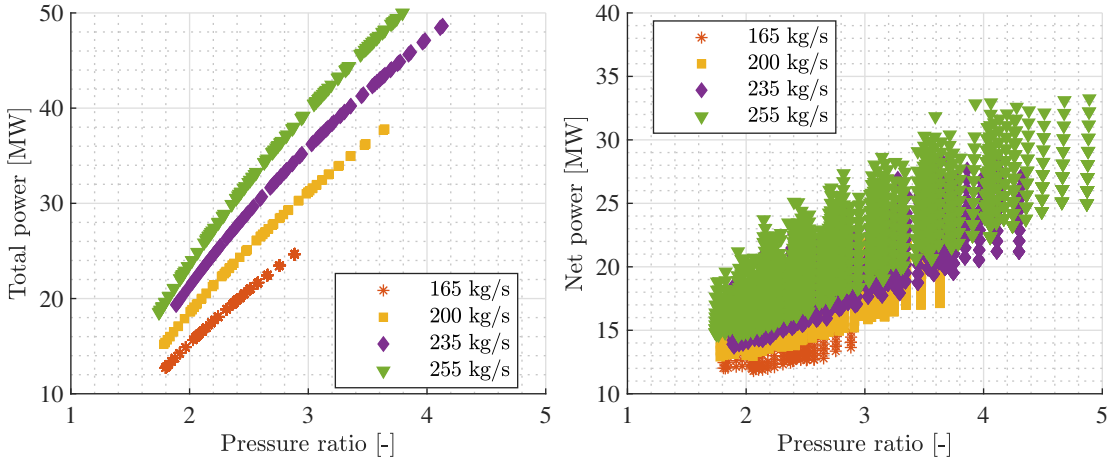

(b) $D_{tube} = 6$ m

Figure 4.23: Total and net power versus pressure ratio for the Z150.

$D_{tube} = 6$ m. They represent the total versus the net power for different capsule diameters and compressor mass flows.

The plot of the optimums for the Z150 is done in figure 4.24. Fewer solutions are encountered than for the Z50. Even, for $\dot{m}_\pi = 200$ kg/s, only one point exists for the smaller tube. For the rest, the same trends are observed as in the Z50. Although the optimum for each mass flow was lower for the Z50, in small capsule diameters and large mass flows, the Z150 is more efficient.

4.7.4 Reference vehicle

Table 4.6 collects the optimum design for each tube diameter and cabin capacity analysed. These are the optimums of figures 4.22 and 4.24.

As the tube is larger, the energy requirements (E_{bat}) are lower. As previously mentioned,

Vehicle	**Z50**	**Z50**	**Z150**	**Z150**
D_{tube} [m]	5	6	5	6
n_{pax} [-]	50	50	150	150
n_{row} [-]	4	4	4	4
u_{pod} [km/h]	615	615	615	615
d_{cru} [km]	700	700	700	700
D_{pod} [m]	3.7	3.8	3.8	4
$\dot{m}_{\pi}$ [kg/s]	165	130	200	165
M_4	0.90	0.90	0.78	0.86
α_t [-]	0.50	0.10	0.57	0.11
A_9 [m^2]	5.452	3.925	7.026	4.821
p_{19} [kPa]	9.830	9.968	9.786	9.677
p_9 [kPa]	9.739	9.962	9.334	9.677
$p_{19} - p_9$ [kPa]	-0.091	-0.006	-0.451	0.000
N_T [kN]	9.869	9.815	9.841	9.817
$N_{T,trg}$ [kN]	9.807	9.807	9.807	9.807
$N_T - N_{T,trg}$ [kN]	0.062	0.008	0.034	0.010
M_9 [-]	0.806	0.850	0.814	0.937
M_{19} [-]	0.408	0.444	0.392	0.438
M_{15} [-]	0.867	0.805	0.689	0.881
π_c [-]	2.539	1.639	3.058	1.808
W_{net} [MW]	12.49	7.647	16.96	11.75
W_{tot} [MW]	21.28	8.337	31.82	12.87
m_{pod} [tn]	64.02	42.14	101.5	76.21
L_{pod} [m]	31.87	30.13	56.05	54.08
E_{bat} [MWh]	17.76	10.88	24.13	16.72
E_{spc} [kJ/(km pax)]	1462	895	662	459

Table 4.6: Variables from the different optimum points in terms of $\dot{W}_{net}$.

the more space is left for the flow, the less Fanno losses in the channel. However, the infrastructure cost will increase, which has not been modelled in the simulator. The specific energy (E_{spc}) is lower when more seats are included, as the energy is divided by a higher value.

Moreover, the capsule diameter (D_{pod}) is higher for wider tubes, enabling more Fanno losses in the channel, reducing the ones in the duct. Note also that the compressor mass flow is more significant for smaller tubes. As the space left around the vehicle is smaller, the compressor must shallow more flow. Then, the pressure ratio must also increase to overcome the pressure losses with the more mass flow in the duct. Moreover, the recovery factor has to be higher, as there is an excess of energy in the internal flow to surpass the cabin. Instead of converting all the internal flow energy to thrust on the nozzle, recover part in the turbine is more efficient.

Comparing the Z50 and Z150, as the former is smaller, it has fewer losses and requires

less pressure ratio, compressor mass flow, power and energy.

In all cases, the nozzle is adapted, although it is almost blocked for the 6-meter tube and the Z150 vehicle. The lowest M_9 is reached for the Z50 vehicle and the smallest tube.

Furthermore, the M_4 resulting from each optimisation is equal to the maximum value (0.9) or close to it. This means that the optimum corresponds to compressing the flow as low as possible.

The chosen design to proceed with the following results is the Z50 with a 6-meter tube. For this system, the $T - s$ diagram is shown in figure 4.25. This plot is similar to the ones from the Bryton cycle, removing the energy addition from 3 to 4, as now there is no combustion chamber.

Another difference is that the compressor enthalpy jump (from 2 to 3) and the turbine jump (from 4 to 5) do not have to be equal. Now, the system is not mechanically coupled, and the energy is provided by a battery. This means that the recovery on the turbine is free from the pressure ratio on the compressor. Note that, in this case, the recovery is only 10 %.

Finally, the nozzle pressure does not have to match in inlet pressure in 1 (if adapted), as there is a pressure loss around the vehicle that reduces the downstream static pressure ($p_{19} < 10$ kPa). However, this particular case has both pressures so close that they overlap on the diagram.

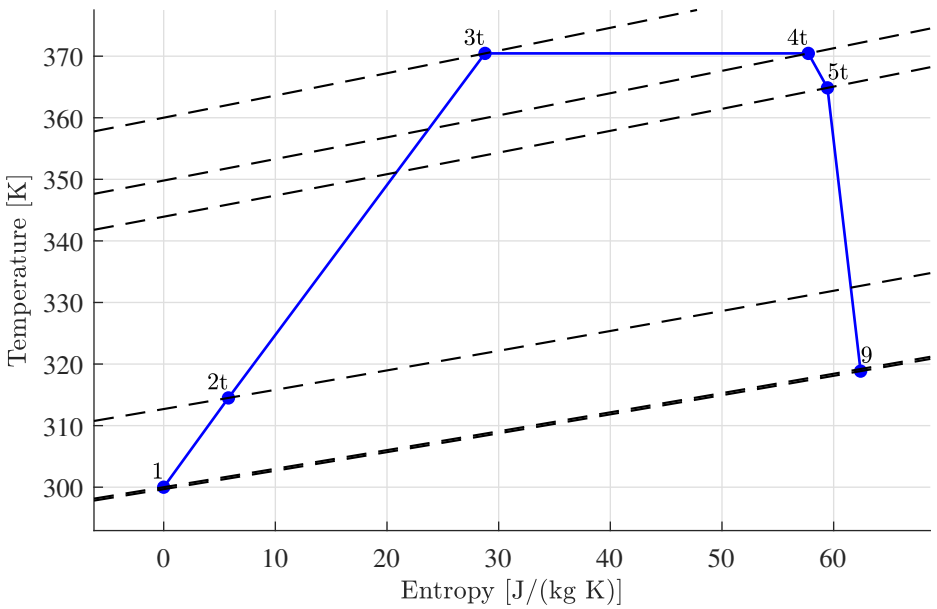

Figure 4.25: $T - s$ diagram for the internal cycle of the selected design.

The pressure and temperature in each thermodynamic station are represented in figure 4.26. For the internal flow, the compressor increases the pressure and temperature of the flow from 2t to 3t. After that, there is a Fanno pressure loss in the duct, but the total temperature remains constant as this process is assumed adiabatic. After 4t, the turbine recovers part of the total pressure, decreasing the total temperature. Finally, the nozzle

has a slight total pressure loss (from 5t to 9t) and recovers flow momentum (from 9t to 9) to provide the thrust. Note that p_9 reaches the value in 19, which is the ambient value for the expansion. The static temperature is also recovered but stays higher than the inlet value.

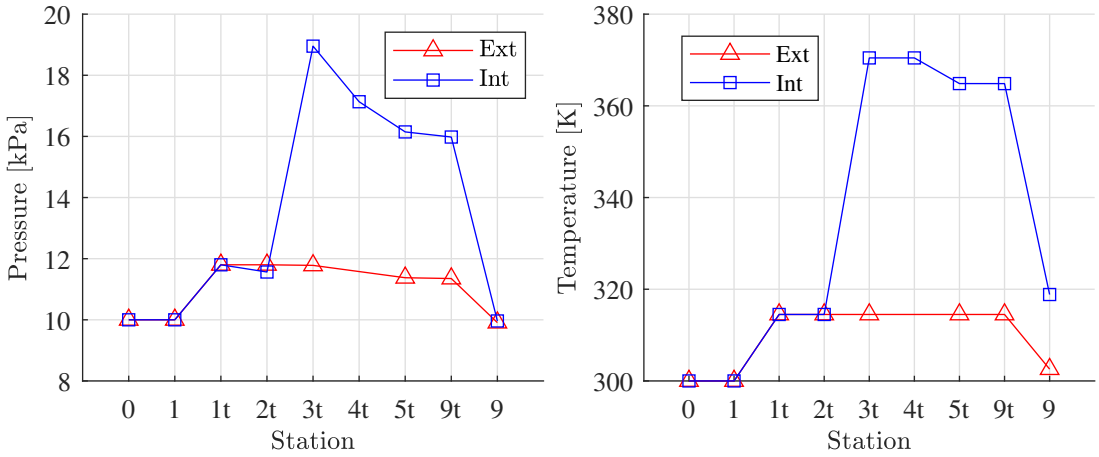

Figure 4.26: Pressure (left) and temperature (right) in different stations of the selected design. The external stations have a "1" before the name that appears on the axis.

The external flow has a simpler variation. It suffers a pressure loss from 13t to 15t due to the Fanno on the channel. As in this case the tube is not small, η_r is close to one, and, consequently, the pressure loss between 5t and 9t is negligible. Finally, in 19, the pressure is recovered.

Lastly, the mass distribution of the vehicle is plotted in figure 4.27. Note that the battery holds 50 % of the total mass. The rest of the systems are in the same order, being the second largest the structure with 6 tn (15 %). The brakes and powertrain represent only 5 % of the total mass each.

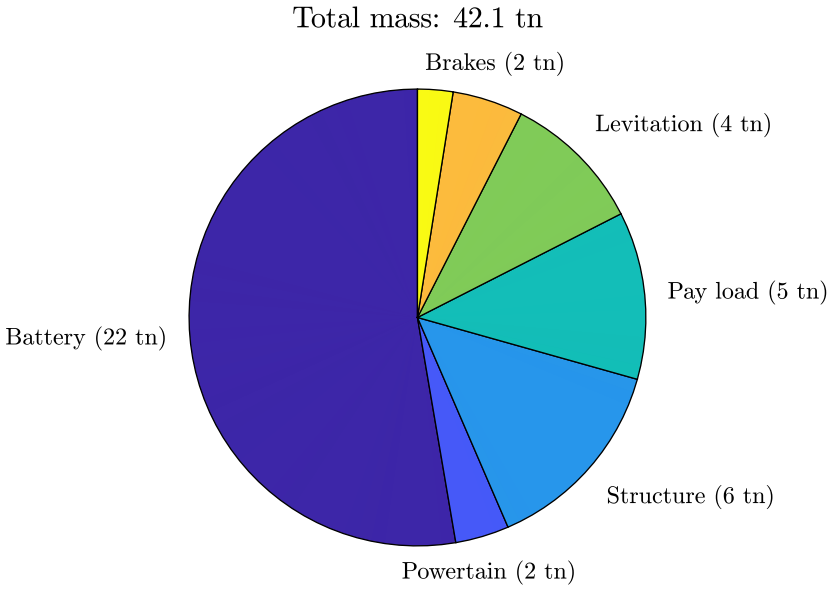

Figure 4.27: Mass distribution of the selected vehicle design.

4.7.5 Comparison with other means of transportation

Once a vehicle is chosen, its performance can be compared with other means of transportation. Table 4.7 collects data from the High-Speed Rail, maglev and aeroplanes, apart from *Zeleros*' hyperloop.

Mode	**Railway** [131]		**Maglev** [131]		**Aeroplane** [132]		**HL**
Vehicle	ICE3	TGV Duplex	TR08	SCMaglev	E190	A321	**Z150**
Distance [km]	255	140	255	400	363	1287	**700**
Speed (cru) [km/h]	330	320	430	500	785	865	**615**
Speed (avg) [km/h]	196	-	-	-	439	706	**565**
E_{spc} [kJ/(km pax)]	180	155	291	435	2377	1293	**459**

Table 4.7: Energy consumption for different means of transportation. TR08 is the Transrapid model operated in Germany (section 1.7.2.1).

The railway holds the lowest consumption, although it travels at the lowest speed in the comparison (200 km/h on average). The maglev train reaches 430 km/h with more than 60 % more consumption than the HSR. Its mean speed has not been found. Using the superconductive maglev (SCMaglev), the cruise speed reaches 500 km/h with more than double the HSR consumption.

The performance of the aeroplanes is highly dependent on the route. For short routes, around 363 km, the aeroplane is highly inefficient. With an average speed lower than 430 km/h, its energy consumption is an order of magnitude higher than the one of the train. Regarding longer routes, 1287 km for this example, the aeroplane is more competitive. Its

energy consumption is reduced by half, and the average speed surpasses 700 km/h.

Hyperloop remains in between the aeroplane and the maglev. Its average speed is 565 km/h, higher than the maglev and the plane on short routes. Moreover, its energy consumption is between a fifth and a third of the aeroplane, slightly higher than the SCMaglev.

Further analysis has been conducted comparing the aeroplane average speed and the hyperloop one. For the latter, an acceleration and deceleration phase of 0.25 Gs is considered, plus a 5 minutes extra time to reduce the tube pressure. The results are represented in figure 4.28. Note that, for the plane, there is a significant difference between considering or not the taxi time. Due to the congestion in some airports, this difference can be higher than 150 km/h. Even, the mean speed is as low as 300 km/h for the shortest routes. Thanks to these low speeds, hyperloop is competitive in the whole range analysed, always faster than the plane with taxi.

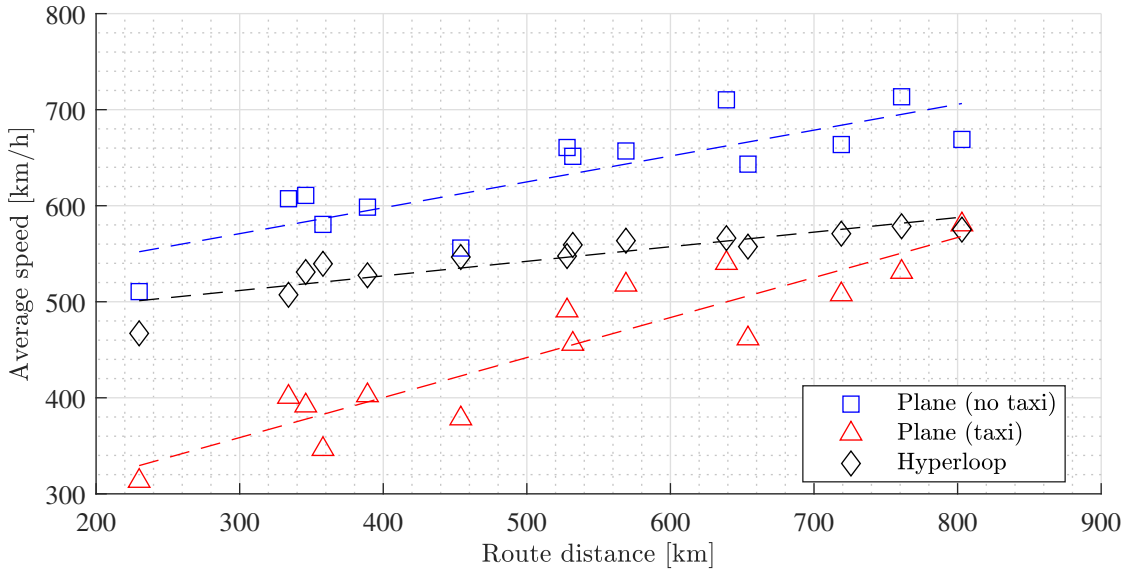

Figure 4.28: Aeroplane average speed function of the route distance. Reference: 14 routes and 280 flights analysed from `flightaware.com`.

4.8 Future work

The thermodynamic model implemented in this section is quite complete as it considers a broad scope of boundary conditions. However, the algorithm that computes the area to match the internal and external downstream static pressures may fail with the external channel blocked. Even, for subsonic flow, this solver is not used as no physical solution is in range in most cases.

The map of the rear expansion efficiency η_f can be more detailed, as now it only considers the blockage ratio and speed. Similarly, the rear expansion closure may consider the losses when mixing flows with different pressure and temperature levels.

Regarding the optimisation process, the geometry should be included in the optimisation loop, not only cycle parameters. The effects of the tube and capsule size are significant on the performance of the vehicle, and it is not evident which trend is the most efficient.

The economic cost must also be included. Apart from being a critical output parameter, it can affect the loop. Currently, the optimum is the largest tube possible in diameter. However, this is because the cost has not been included, and only the thermodynamics affect the solution. If the cost is included, an actual optimum in terms of operation can be obtained.

Other mission phases can also be implemented in the model, at least to estimate the acceleration energy cost. Even some example routes may be included, considering velocity variations in the middle of the route to accommodate curves. In this sense, the computation of the off-design performance of the capsule should be included to obtain a complete operation map.

Finally, a more detailed product may improve the estimations of cabin dimensions, areas, lengths, masses and energy consumption.

Chapter 5

Middle-scale system

Nomenclature

β	Blockage ratio ($= A_{pod}/A_0$)
g	Earth's gravity
v_{cru}	Cruise speed
m_{pod}	Mass of the vehicle
L_{track}	Length of the track
L_{pod}	Length of the capsule
v_{tr}	Braking transition speed
Δt	Time step
n	Step
N_T	Net thrust
T_{aero}	Aerodynamic torque
F_{aero}	Aerodynamic force
λ_{mag}	Magnetic drag ratio
F_{mag}	Magnetic drag force
F_N	Normal wheel force
μ_r	Rolling friction coefficient
F_{rol}	Rolling friction force
μ_{FB}	Friction coefficient of the friction brake
N_{FB}	Normal force by each friction brake module
n_{FB}	Number of FB modules
F_{FB}	Friction brake force
x_{LM}	Linear Motor length
a_{LM}	Maximum acceleration of the LM
P_{LM}	Maximum power of the LM
F_{LM}	Linear Motor force
n_{MB}	Number of MB modules
$F_{MB,x}$	Magnetic brake x force
$F_{MB,y}$	Magnetic Brake y force

F_{brake}	Braking force
v_{tr}	Maximum speed for the FB
$\dot{W}_i$	Power by component i
t	Time
x	Position
v	Capsule speed
a	Acceleration
M	Mach number
x_f	Front capsule position
x_r	Rear capsule position
p_f	Front static pressure in the tube
p_r	Rear static pressure in the tube
p_f	Front static temperature in the tube
T_r	Rear static temperature in the tube
ρ_f	Front static density in the tube
ρ_r	Rear static density in the tube
N	Compressor real speed
$\dot{m}$	Tube mass flow
$\dot{m}_\pi$	Internal mass flow
$\dot{m}_\beta$	External mass flow
T_n	Nozzle exit temperature
u_n	Nozzle exit speed
T_p	Passage or channel temperature
u_p	Passage or channel speed
u_i	Thermodynamic speed at station i
p_i	Thermodynamic pressure at station i
T_i	Thermodynamic temperature at station i
ρ_i	Thermodynamic density at station i
p_{it}	Total pressure at station i
T_{it}	Total temperature at station i
$T\cdot$	Motor or fan torque
V	Voltage
I	Current
p_{ref}	Reference pressure for compressor map definition (101325 Pa)
T_{ref}	Reference temperature for compressor map definition (288.15 K)
R	Ideal gas constant (287.55 kJ/kg/K)
γ	Perfect gas adiabatic ratio (1.4)
c_p	Specific heat at constant pressure (1006.43 kJ/kg/K)

5.1 Introduction

As mentioned in section 1.9.4, *Zeleros* is developing a middle-scale prototype to reduce the uncertainty and cost of the project. This prototype also requires a dynamic simulator. So,

the current chapter aims to describe this model, which holds the following hypotheses:

- Only longitudinal dynamics are solved.
- Transient effects are simplified using a quasi-steady solver.
- The simulator includes all the phases of the mission, not only cruise as in the real-scale simulator.
- The model of several subsystems is included and simplified with their hypotheses.

The model has been developed in Python.

5.2 Mission

This vehicle will perform a mission, which has to be modelled on the simulator, as opposed to the real-scale system where only the cruise in an infinite tube was modelled.

The mission consists of the capsule being accelerated externally to a certain speed. Then the compressor thrust is used exclusively to maintain the speed while levitating. Finally, the prototype brakes safely before the end of the track. Everything happens inside a tube under low-pressure conditions. No payload is required to complete this mission. The mission is represented in figure 5.1. Three different phases are identified:

1. Acceleration: the linear motor propels the vehicle from 0 to v_{cru}, and it does not levitate. The compressor provides thrust progressively.
2. Cruise: the compressor provides the required net thrust to maintain the cruise speed v_{cru}. The vehicle also levitates.
3. Braking: the compressor performs as a windmill, and the magnetic brakes actuate at the beginning, while at the end, the friction brakes. The transition is defined by a speed named v_{tr}. During this whole phase, the vehicle does not levitate.

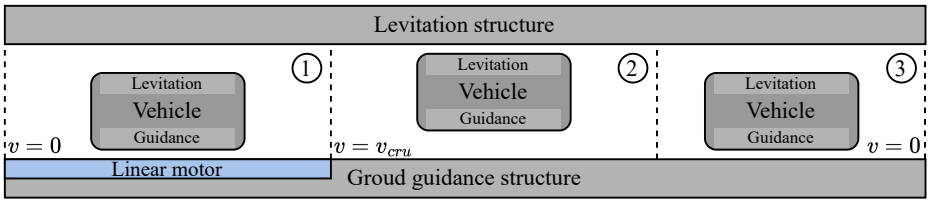

Figure 5.1: Mission of the prototype.

The parameters that define the mission are:

- Cruise speed: v_{cru}.
- Mass of the vehicle: m_{pod}.

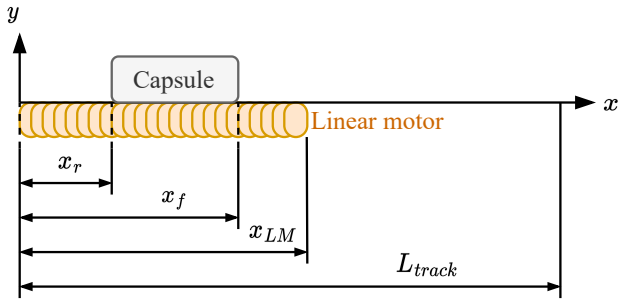

Figure 5.2: Reference system used in the code.

- Length of the track: L_{track}.
- Braking transition speed: v_{tr}.

To complete that mission, the vehicle has the following systems integrated:

- Aerodynamic propulsion: based on the turbofan, the duct and the nozzle. No turbine is included. This system provides the required thrust for the cruise phase.
- Magnetic propulsion: a linear motor able to propel the vehicle to the cruise speed v_{cru}.
- Levitation system: magnetic levitation system which lifts and guides the vehicle during the cruise phase.
- Energy system: the onboard energy storage system is based on batteries that feed the levitation, aerodynamic and magnetic brake systems.
- Guidance system: this system guides the vehicle while it is not levitation. It is composed of wheels.
- Magnetic brake: the brake is composed of coils that, when energised, create a force that reduces the momentum of the vehicle. This brake is used at high speeds to prevent contact.
- Friction brake: a friction brake is used to stop the vehicle at lower speeds when the magnetic brake is not as useful.

The reference system is shown in figure 5.2. The x axis is the longitudinal one, while the y is the vertical one. The vehicle starts in $x = 0$ and moves towards the positive x axis. The front of the vehicle is placed each time in x_f, while the rear part is in x_r. The length of the linear motor on the track is x_{LM}, while the total length of the tube is L_{tube}.

5.3 Dynamic model

5.3.1 Physic problem

The problem to be solved is shown in figure 5.3. It consists of a hyperloop vehicle travelling inside an enclosed tube at a certain speed u_{pod}, which is time-dependent.

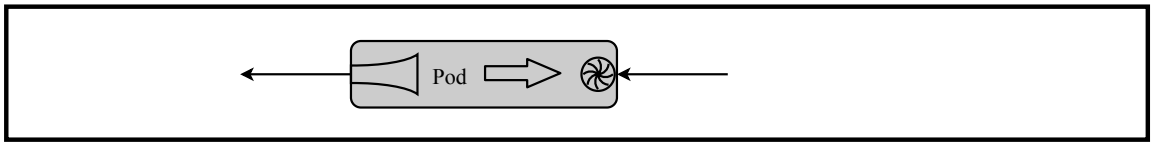

Figure 5.3: Schematic view of the problem to be solved. Capsule moves from left to right.

The present code is aimed to solve only the longitudinal degree of freedom of the vehicle. For that, the different forces (see figure 5.4) are the following:

- F_{LM}: linear motor force.
- F_{aero}: aerodynamic net force, including thrust and drag.
- F_N: normal force on the wheels, used to compute the rolling friction force.
- F_{rol}: rolling friction force.
- F_{FB}: friction brake force.
- $F_{MB,x}$: magnetic brake horizontal force.
- $F_{MB,y}$: magnetic brake vertical force.

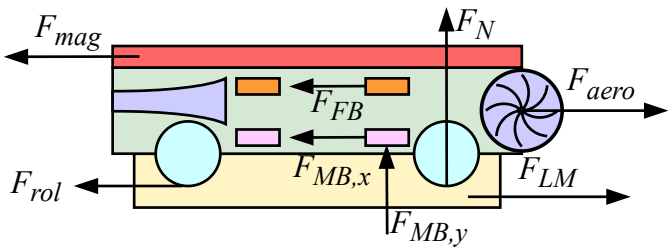

Figure 5.4: Forces actuating on the vehicle.

The mission phase in which each force actuates is collected in table 5.2.

Force	Phase 1	Phase 2	Phase 3
Linear motor	x		
Compressor thrust	x	x	x (windmill)
Ground resistance	x		x
Levitation magnetic drag		x	
Friction brake			x
Magnetic brake			x

Table 5.2: Forces appearing in each mission phase.

As in the real-scale model, the thermodynamic effects are the most relevant for this problem. This is why the problem is focused on separately solving the effects on the tube and around the vehicle. So, there are two steps, one in which the forces acting on the capsule are integrated and one in which the effects on the tube thermodynamics are computed.

5.3.2 Integration scheme

This section details the overall integration scheme used in the code. The top-level functionality of the code is shown in figure 5.5.

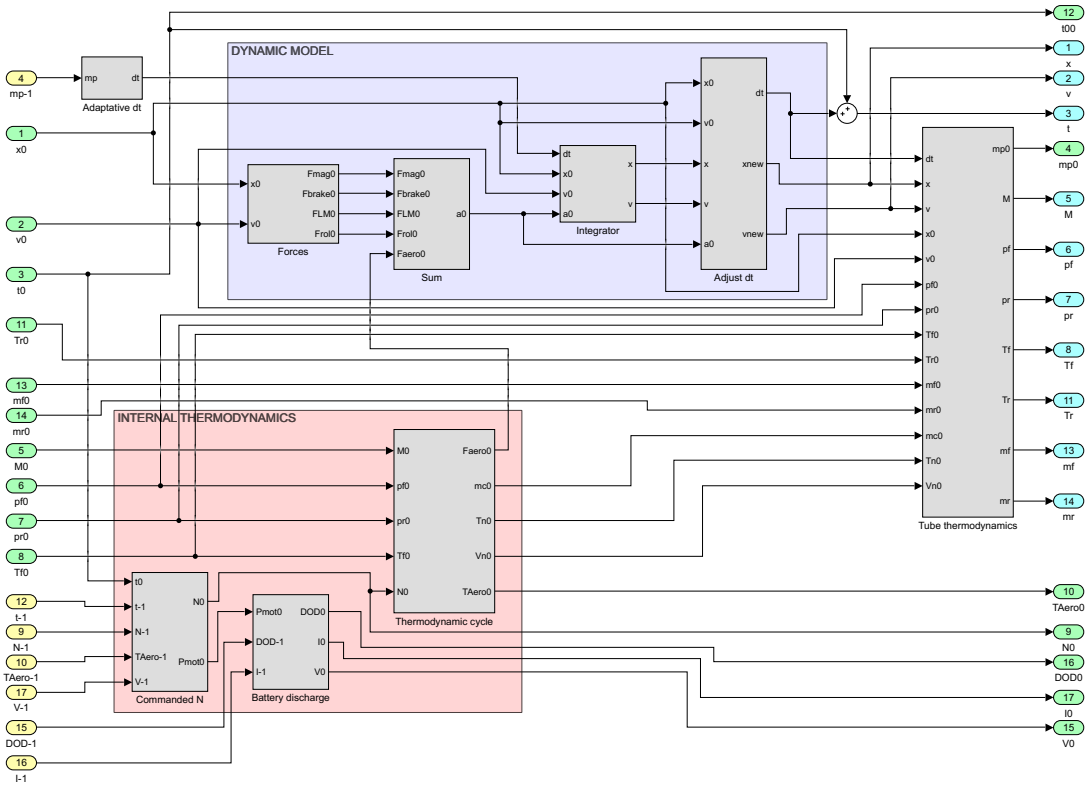

Figure 5.5: Top level functionality of the model.

To avoid some algebraic loops, some models are solved in current time instant (n) and others in future step ($n+1$). Even some information from the previous step ($n-1$) is used:

- Step $n-1$: the variables that end with "-1". Coloured in yellow.
- Step n: the variables that end with "0" Coloured in green.
- Step $n+1$: the variables coloured in blue.

An exception is the time step Δt, which does not correspond to any step but to the transition. So, it is defined as:

$$\Delta t_n \equiv t_n - t_{n-1}. \tag{5.1}$$

Each time step, the following modules are solved:

1. Time integration (section 5.3.2.1): the adaptive time step is computed, and the main data structure is reallocated if necessary.
2. Internal thermodynamics (section 5.3.2.2): the internal model, from intake to nozzle, is solved.
3. Dynamic model (section 5.3.2.3): all the forces over the vehicle are computed. Then, their sum can be computed, and, consequently, the acceleration.
4. Tube thermodynamics (section 5.3.2.4): the thermodynamic variables on the tube are computed, including pressures, temperatures, induced speeds...

The variables involved in the present study are collected in table 5.3.
The system is solved each time step until a stopping criterion is reached, which can be:

- The vehicle has reached the end of the tube, so $x_f = L_{tube}$.
- The vehicle has accelerated and stopped, so $v_{pod} \leq 0$.
- Any module has given an error.

5.3.2.1 Step 1: Time step

In each iteration, the time step can be modified if high gradients of a certain variable are detected. The stretching function is the following:

$$\Delta t_n = \begin{cases} \Delta t_n \lambda^n & \text{if refining,} \\ \Delta t_n \lambda^{-(c-b)} & \text{if increasing,} \end{cases} \tag{5.2}$$

where the parameters mean the following:

- b: number of steps before increasing the time step again.
- c: number of time steps that no refinement was performed.

Symbol	Description	Symbol	Description
Δt	Time step	t	Time
x	Position	v	Capsule speed
a	Acceleration	M	Mach number
x_f	Front position	x_r	Rear position
p_f	Front static pressure	p_r	Rear static pressure
p_f	Front static temperature	T_r	Rear static temperature
ρ_f	Front static density	ρ_r	Rear static density
$\dot{m}_\pi$	Internal mass flow	$\dot{m}_\beta$	External mass flow
T_n	Nozzle exit temperature	u	Thermodynamic speed
N	Compressor speed	T_{aero}	Aerodynamic torque
F_{aero}	Aerodynamic force	F_{mag}	Magnetic drag force
F_{rol}	Rolling friction force	F_N	Normal wheel force
F_{FB}	Friction brake force	F_{LM}	Linear Motor force
$F_{MB,x}$	Magnetic brake x force	$F_{MB,y}$	Magnetic Brake y force

Table 5.3: Variables involved in the overall model.

- n: number of refinement levels.
- Δt_{max}: maximum allowed time step.
- Δt_{min}: minimum allowed time step.
- Δt_{ini}: initial time step.
- λ: refinement factor $\lambda \in (0, 1)$.

The process decided for the refinement is the following (see figure 5.6):

- The system at time n is advanced to $n + 1$ using Δt_n.
- **if** gradient criteria is met:
  - c is increased by 1.
  - The number of refinement levels n is set to 0.
  - Until $c > b$, the time step is conserved.
  - Since $c > b$ the time step is $\Delta t_n = \Delta t_{n-1} \lambda^{-(c-b)}$.
- **if** gradient criteria is **not** met:
  - The number of steps before refining, c is set to 0.
  - If on the first refinement level, save $\overline{\Delta t} = \Delta t_n$.
  - Increase n by 1.
  - Repeat time step n with time step $\Delta t_n = \overline{\Delta t} \lambda^n$.

The gradient criteria are the following:

- External mass flow: $\left(\dot{m}_{\beta,n+1} - \dot{m}_{\beta,n}\right)/\Delta t_n \geq \ddot{m}_{\beta}$.
- Front static temperature: $\left(T_{f,n+1} - T_{f,n}\right)/\Delta t_n \geq \dot{T}_f$.
- Rear static temperature: $\left(T_{r,n+1} - T_{r,n}\right)/\Delta t_n \geq \dot{T}_r$.

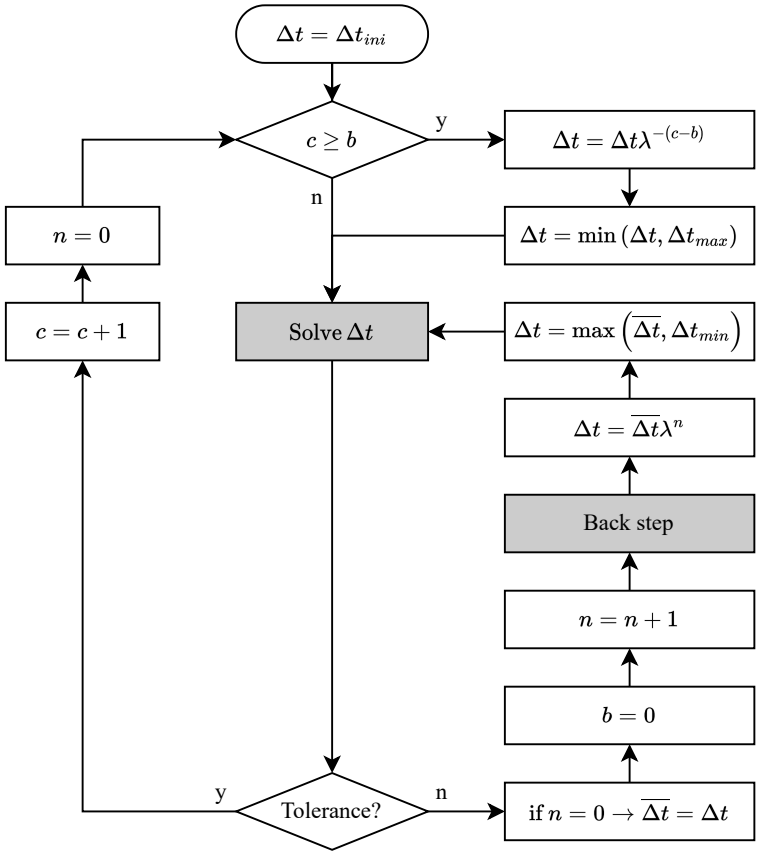

Figure 5.6: Adaptive time step algorithm.

5.3.2.2 Step 2: Thermodynamic model

The thermodynamic model is divided into three different submodels:

- Commanded N: outputs the current compressor speed required on the shaft. It is detailed in 5.6.3.
- Battery discharge: with the required power, computes the voltage, current and DOD of the battery. It is detailed in 5.6.2.

- Thermodynamic cycle: knowing the thermodynamics of the tube (which are the boundary conditions) and the speed of the compressor solves the thermodynamics around the vehicle, internally and externally. It is detailed in 5.4.

The cycle is solved based on the following inputs:

- Vehicle Mach number: $M_{f,n}$.
- Front static pressure: $p_{f,n}$.
- Rear static pressure: $p_{r,n}$.
- Front static temperature: $T_{f,n}$.
- Compressor real speed: N_n.

Once the cycle is solved, all its variables can be accessed for the current time step.

5.3.2.3 Step 3: Dynamic problem

In this step, Newton's second law over the vehicle is applied. Five different forces are computed for the acceleration; all evaluated at the current time step n:

- F_{aero}: the aerodynamic force, named net thrust (thrust minus drag).
- F_{mag}: magnetic drag.
- F_{LM}: linear Motor thrust.
- F_{MB}: magnetic brake force.
- F_{FB}: friction brake force.

The computation of each of them is detailed in section 5.6.1.
Once each force is computed, the acceleration can be obtained as follows:

$$a_n = \frac{1}{m}\sum F_i = \frac{F_{aero} + F_{mag} + F_{LM} + F_{MB} + F_{FB}}{m}. \tag{5.3}$$

Then, the speed and position can be integrated, assuming the acceleration is constant during the time step:

$$v_{n+1} = v_n + a_n \Delta t, \tag{5.4}$$

$$x_{n+1} = x_n + v_n \Delta t + \frac{1}{2} a_n \Delta t^2. \tag{5.5}$$

The position is divided into two different magnitudes, the front and rear positions:

$$x_{f,n+1} = x_{n+1}, \tag{5.6}$$
$$x_{r,n+1} = x_{n+1} - L_{pod}. \tag{5.7}$$

In case the capsule is in the cruise phase and reaches the braking position (x_{brake}), the time step is adapted to capture this point accurately. This happens when $x_{f,n+1} > L_{tube} - x_{brake}$. At that moment, the acceleration is assumed to be the same (a_n), and the position, time and speed are recomputed:

$$x_{f,n+1} = L_{tube} - x_{brake}, \tag{5.8}$$
$$v_{n+1} = \sqrt{v_n^2 + 2a_n\left(x_{f,n+1} - x_{f,n}\right)}, \tag{5.9}$$
$$\Delta t_n = \begin{cases} \frac{x_{f,n+1}-x_{f,n}}{v_n} & \text{if} \quad a_n = 0, \\ \frac{v_n}{a_n}\left[\sqrt{1 + 2a_n\frac{x_{f,n+1}-x_{f,n}}{v_n^2}} - 1\right] & \text{if} \quad a_n \neq 0. \end{cases} \tag{5.10}$$

By his part, if the speed detected on the next time step v_{n+1} is lower than 0, the prototype has already stopped, and the mission is finished. In that case, the time step is also recomputed to match $v_{n+1} = 0$ at the last time step. For that, the acceleration is assumed to be the same, a_n, and:

$$v_{n+1} = 0, \tag{5.11}$$
$$x_{f,n+1} = x_{f,n} - \frac{v_n^2}{2a_n}, \tag{5.12}$$
$$\Delta t_n = \frac{-v_n}{a_n}. \tag{5.13}$$

In both cases, the rear position is again computed:

$$x_{r,n+1} = x_{f,n+1} - L_{pod}. \tag{5.14}$$

5.3.2.4 Step 4: Thermodynamic tube model

This point solves the thermodynamics of the tube. To model them, the domain is divided into two control volumes, one on the front and one on the rear. Within those volumes, the thermodynamic variables are assumed to be constant, which means that no wave propagation happens, and the speed of sound is infinite. This separation can be seen in figure 5.7.

In this division, the vehicle is modelled as an entity that can shallow a certain amount of mass flow $\dot{m}_\pi$ and exhaust it at a certain energy level T_n, computed in the thermodynamic cycle. There is also another mass exchange between the volumes, assumed adiabatic, which is the flow that goes through the gap between the vehicle and the tube, $\dot{m}_\beta$. Note that these control volumes are not fixed in time; their size depends on the capsule position. The

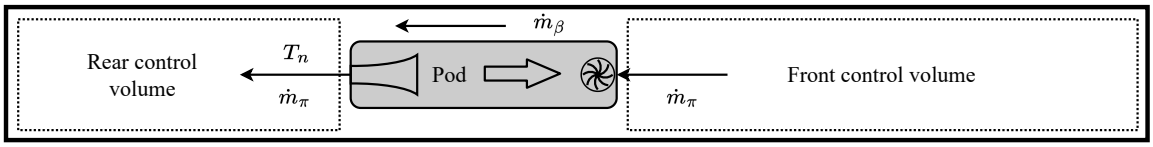

Figure 5.7: Domain division on the physic problem.

system to solve uses the information in the current step n to solve the next $n+1$. The derivation of the equations is detailed in section 5.5.

$$\dot{T}_r = -\left(\frac{\gamma-1}{V_r}Au + \frac{\dot{m}}{m_r} - \gamma\frac{\dot{m}_\beta}{m_r}\lambda_r\right)T_r + \gamma\frac{\dot{m}_\beta}{m_r}\lambda_f T_f + \gamma\left(\frac{\dot{m}_\beta}{m_r}\frac{v_{if}^2\lambda_f + v_{ir}^2\lambda_r}{2c_p} + \frac{\dot{m}_\pi}{m_r}T_{nt}\right) - \frac{\dot{m}}{m_r}\frac{v_{ir}^2}{2c_v}, \tag{5.15}$$

$$\dot{T}_f = \left(\frac{\gamma-1}{V_f}Au + \frac{\dot{m}}{m_f} - \gamma\frac{\dot{m}_\beta\lambda_f + \dot{m}_\pi}{m_f}\right)T_f - \gamma\frac{\dot{m}_\beta}{m_f}\lambda_r T_r - \gamma\left(\frac{\dot{m}_\beta}{m_f}\frac{v_{if}^2\lambda_f + v_{ir}^2\lambda_r}{2c_p} + \frac{\dot{m}_\pi}{m_f}\frac{v_{if}^2}{2c_p}\right) + \frac{\dot{m}}{m_f}\frac{v_{if}^2}{2c_v}. \tag{5.16}$$

To discretise the system, the equations are rewritten as follows:

$$\begin{aligned}\dot{T}_r &= A_{rr}(t)\,T_r + A_{rf}(t)\,T_f + B_r(t)\,,\\ \dot{T}_f &= A_{fr}(t)\,T_r + A_{ff}(t)\,T_f + B_f(t)\,.\end{aligned} \tag{5.17}$$

The following equivalences are required:

$$A_{rr} \equiv -\left(\frac{\gamma-1}{V_r}Au + \frac{\dot{m}}{m_r} - \gamma\frac{\dot{m}_\beta}{m_r}\lambda_r\right), \tag{5.18}$$

$$A_{ff} \equiv +\left(\frac{\gamma-1}{V_f}Au + \frac{\dot{m}}{m_f} - \gamma\frac{\dot{m}_\beta}{m_f}\lambda_f\right) - \gamma\frac{\dot{m}_\pi}{m_f}, \tag{5.19}$$

$$A_{rf} \equiv +\gamma\frac{\dot{m}_\beta}{m_r}\lambda_f, \tag{5.20}$$

$$A_{fr} \equiv -\gamma\frac{\dot{m}_\beta}{m_f}\lambda_r, \tag{5.21}$$

$$B_r \equiv +\gamma\left(\frac{\dot{m}_\beta}{m_r}\frac{v_{if}^2\lambda_f + v_{ir}^2\lambda_r}{2c_p} + \frac{\dot{m}_\pi}{m_r}T_{nt}\right) - \frac{\dot{m}}{m_r}\frac{v_{ir}^2}{2c_v}, \tag{5.22}$$

$$B_f \equiv -\gamma\left(\frac{\dot{m}_\beta}{m_f}\frac{v_{if}^2\lambda_f + v_{ir}^2\lambda_r}{2c_p} + \frac{\dot{m}_\pi}{m_f}\frac{v_{if}^2}{2c_p}\right) + \frac{\dot{m}}{m_f}\frac{v_{if}^2}{2c_v}. \tag{5.23}$$

To solve this system, equations (5.17) are expressed in a matrix form:

$$\left\{\dot{T}\right\} = [A]\,\{T\} + \{B\}\,, \tag{5.24}$$

where:

$$[A] \equiv \begin{bmatrix} A_{rr} & A_{rf} \\ A_{fr} & A_{ff} \end{bmatrix}, \; \{B\} \equiv \begin{Bmatrix} B_r \\ B_f \end{Bmatrix}, \; \{T\} \equiv \begin{Bmatrix} T_r \\ T_f \end{Bmatrix}, \; \left\{\dot{T}\right\} \equiv \begin{Bmatrix} \dot{T}_r \\ \dot{T}_f \end{Bmatrix}. \tag{5.25}$$

Now the equations are discretised in time. Applying the Crank-Nicholson method to equation (5.24), the following system is achieved:

$$\frac{\{T\}_{n+1} - \{T\}_n}{\Delta t_n} = \frac{1}{2}\left([A]_{n+1}\{T\}_{n+1} + \{B\}_{n+1} + [A]_n\{T\}_n + \{B\}_n\right). \tag{5.26}$$

That equation can be reordered as follows:

$$\left([I] - \frac{\Delta t_n}{2}[A]_{n+1}\right)\{T\}_{n+1} = \left([I] + \frac{\Delta t_n}{2}[A]_n\right)\{T\}_n + \frac{1}{2}\left(\{B\}_{n+1} + \{B\}_n\right). \tag{5.27}$$

This system can be solved each time step if values for $[A]_n$, $[A]_{n+1}$, $\{B\}_n$, and $\{B\}_{n+1}$ are provided. That means evaluating in current time (n) and in future time ($n+1$) the following variables: V_r, V_f, m_r, m_f, u, λ_r, λ_f, $\dot{m}_\pi$, $\dot{m}_\beta$, T_{nt}, v_{ir}, and v_{if}.

However, not all the variables can be evaluated in future time because they are still unknown. For such cases, those variable are assumed constant during the integration: $\dot{m}_\beta$, $\dot{m}_\pi$, T_{nt}, λ_r, and λ_f.

5.4 Thermodynamic cycle

The nomenclature used for this thermodynamic solver is shown in figure 5.8. These are:

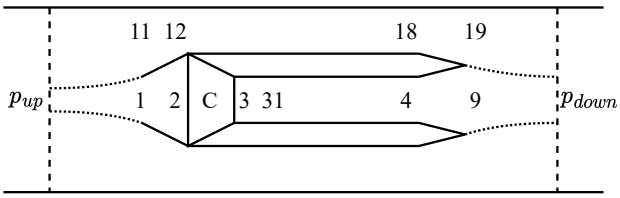

Figure 5.8: Thermodynamic stations map.

- Upstream: inlet of the domain, marked as *up*. Until 1 there is a current duct.
- Intake: between 1 and 2.
- Compressor: between 2 and 3.
- Transition: between 3 and 31. This adapts the axial flow of the compressor to the main shape.
- Duct: between 31 and 4.

- Nozzle: between 4 and 9.
- External intake: adapts the flow between 11 and 12.
- External channel: the channel between 12 and 18.
- External nozzle: pressure recovery from 18 to 19.
- Downstream: uniform flow after the mixing at *down*.

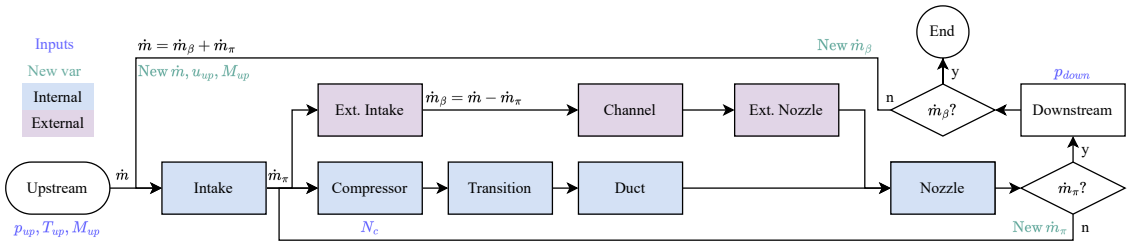

Figure 5.9: Flow of the solver.

The inputs for the solver are the following:

- Inlet static pressure: p_{up}.
- Inlet static temperature: T_{up}.
- Inlet Mach: M_{up}.
- Downstream static pressure: p_{down}.
- Compressor speed: N.

5.4.1 Upstream

From *up*, two current ducts go until 1 and 11 stations. In *up*, the flow is assumed to be perfectly mixed and uniform. The inputs of this module are:

- Inlet static pressure: p_{up}.
- Inlet static temperature: T_{up}.
- Inlet Mach: M_{up}.

The outputs of this module are:

- Total pressure at 1: p_{1t}.
- Total temperature at 1: p_{1t}.

- Total pressure at 11: p_{11t}.
- Total temperature at 11: p_{11t}.
- Total mass flow: $\dot{m}$.

There is an isentropic flow to 1 and 11 stations:

$$p_{1t} = p_{up}\left(1 + \frac{\gamma - 1}{2} M_{up}^2\right)^{\frac{\gamma}{\gamma - 1}}, \tag{5.28}$$

$$T_{1t} = T_{up}\left(1 + \frac{\gamma - 1}{2} M_{up}^2\right). \tag{5.29}$$

$$p_{11t} = p_{up}\left(1 + \frac{\gamma - 1}{2} M_{up}^2\right)^{\frac{\gamma}{\gamma - 1}}, \tag{5.30}$$

$$T_{11t} = T_{up}\left(1 + \frac{\gamma - 1}{2} M_{up}^2\right). \tag{5.31}$$

The total mass flow is computed as follows:

$$\dot{m} = \frac{p_{up} A_{tube} u_{up}}{R T_{up}} \tag{5.32}$$

The total mass flow and inlet speed are recomputed if there is accumulation (as explained in section 5.4.10:

$$\dot{m} = \dot{m}_\pi + \dot{m}_\beta, \tag{5.33}$$

so, the induced speed appears:

$$u_{up} = \frac{R T_{up} \dot{m}}{p_{up} A_{tube}}. \tag{5.34}$$

5.4.2 Intake

This solves the flow between 1 and 2, where the intake of the compression system is placed. The inputs of this module are:

- Inlet total pressure: p_{1t}.
- Inlet total temperature: T_{1t}.
- Diffuser total pressure ratio: π_d.

The outputs of this module are:

- Total pressure at 2: p_{2t}.

- Total temperature at 2: T_{2t}.
- Internal mass flow: $\dot{m}_\pi$.

The diffuser adiabatic pressure loss is applied:

$$T_{2t} = T_{1t}, \tag{5.35}$$
$$p_{2t} = \pi_d p_{1t}. \tag{5.36}$$

The internal mass flow $\dot{m}_\pi$ is imposed. At the end of the cycle, this mass flow is compared with the one computed at the nozzle to close the iterative loop.

5.4.3 External intake

This solves the flow between 11 and 12, where there is a convergent geometry. The inputs of this module are:

- Inlet total pressure: p_{11t}.
- Inlet total temperature: T_{11t}.

The outputs of this module are:

- Inlet total pressure: p_{12t}.
- Inlet total temperature: T_{12t}.
- External mass flow: $\dot{m}_\beta$.

Assuming an adiabatic flow:

$$p_{12t} = p_{11t}, \tag{5.37}$$
$$T_{12t} = T_{11t}. \tag{5.38}$$

Finally, the external mass flow is computed as follows:

$$\dot{m}_\beta = \dot{m} - \dot{m}_\pi. \tag{5.39}$$

5.4.4 Channel

This process solves the flow between 12 and 18. This is an annular Fanno flow as the one solved in appendix A.4. The inputs of this module are:

- Mach number in 12: M_{12}.
- Wall speed: u_{pod}.

- Inner diameter: D_{pod}.
- Outer diameter: D_{tube}.
- Length of the channel: L_{ch}.
- Total pressure in 12: p_{12t}.
- Total temperature in 12: T_{12t}.
- Surface roughness: ε.

The outputs of this module are:

- Mach number in 18: M_{12}.
- Total pressure in 18: p_{18t}.
- Total temperature in 18: T_{18t}.

Using p_{12t}, T_{12t}, $A_{12} = A_{th}$, M_{12}, $\dot{m}_{12} = \dot{m}_{\beta}$, and the geometric parameters (length and diameter) the Fanno flow can be solved as explained in appendix A.4. With those equations, π_{1218} and M_{18} are computed. The rest of the parameters at 18 are:

$$p_{18t} = \pi_{1218} p_{18t}, \tag{5.40}$$

$$T_{18t} = T_{18t}. \tag{5.41}$$

5.4.5 External nozzle

This is the expansion between 18 and 19 on the external flow. The inputs of this module are:

- Mach number in 18: M_{18}.
- Total pressure in 18: p_{12t}.
- Total temperature in 18: T_{12t}.
- Rear expansion isentropic efficiency: η_r.

The outputs of this module are:

- Mach number in 19: M_{19}.
- Static pressure in 19: p_{19}.
- Total pressure in 19: p_{19t}.
- Total temperature in 19: T_{19t}.

Firstly, the definition of η_r is equivalent to the one performed in section 4.4.4:

$$\eta_r = \frac{1 - \frac{1}{1+\frac{\gamma-1}{2}M_{19}^2}}{1 - \left(\frac{p_{19}}{p_{15t}}\right)^{\frac{\gamma-1}{\gamma}}}, \tag{5.42}$$

which is obtained from CFD simulations.

The process to solve the station is also equivalent to the one described in section 4.4.4.1:

1. Guess M_{19}.
2. Compute p_{19} from equation (5.42): $p_{19} = p_{15t}\left[1 - \frac{1}{\eta_r}\left(1 - \frac{1}{1+\frac{\gamma-1}{2}M_{19}^2}\right)\right]^{\frac{\gamma}{\gamma-1}}$.
3. Obtain M_{19} from the continuity equation at 19 (solved as in appendix B.1.1):

$$M_{19} = \sqrt{\frac{\sqrt{1 + 2\left(\gamma - 1\right)\left(\frac{\dot{m}_\beta}{A_{19}p_{19}}\right)^2 T_{19t}\frac{R}{\gamma}} - 1}{\gamma - 1}}.$$

Both M_{19} are compared and iterated until their absolute difference is below a certain tolerance. After the convergence, the total pressure is obtained:

$$p_{19t} = p_{19}\left(1 + \frac{\gamma+1}{2}M_{19}^2\right)^{\frac{\gamma}{\gamma-1}}, \tag{5.43}$$

and the total temperature is conserved: $T_{15t} = T_{19t}$.

5.4.6 Compressor

The compressor increases the pressure from station 2 to 3. The inputs of this module are:

- Total pressure at 2: p_{2t}.
- Total temperature at 2: T_{2t}.
- Internal mass flow: $\dot{m}_\pi$.
- Compressor speed: N.
- Compressor map, shown in figure 5.10.

The outputs of this module are:

- Total pressure at 3: p_{2t}.
- Total temperature at 3: p_{2t}.

The compressor map is a function that follows these functions:

$$(\pi_c, \eta_c) = f\left(\dot{m}_\pi^*, N^*\right), \tag{5.44}$$

where $\dot{m}_\pi^*$ is the corrected mass flow:

$$\dot{m}_\pi^* = \frac{\dot{m}_\pi \sqrt{T_{2t}/T_{ref}}}{p_{2t}/p_{ref}}, \tag{5.45}$$

and N^* is the corrected speed:

$$N^* = \frac{N}{T_{2t}/T_{ref}}. \tag{5.46}$$

As all the data is known, the conditions at the outlet can be computed following these relations:

$$p_{3t} = \pi_c p_{2t}, \tag{5.47}$$

$$T_{3t} = T_{2t}\left(1 + \frac{\pi_c^{\frac{\gamma-1}{\gamma}} - 1}{\eta_c}\right). \tag{5.48}$$

5.4.7 Transition

The transition is between stations 3 and 31 and refers to the geometrical adaption from the compressor outlet to the regular part of the duct. In this transition, there is a pressure loss characterised by CFD:

$$p_{31t} = \pi_{tr} p_{3t}, \tag{5.49}$$

$$T_{31t} = T_{3t}. \tag{5.50}$$

5.4.8 Duct

This is the process to solve between 31 and 4. This is an annular Fanno flow as the one solved in appendix A.4. The inputs of this module are:

- Mach number in 31: M_{31}.
- Cross area: A_{duct}.
- Hydraulic diameter: $D_{n,duct}$.
- Length of the duct: L_{duct}.
- Total pressure in 31: p_{31t}.
- Total temperature in 31: T_{31t}.

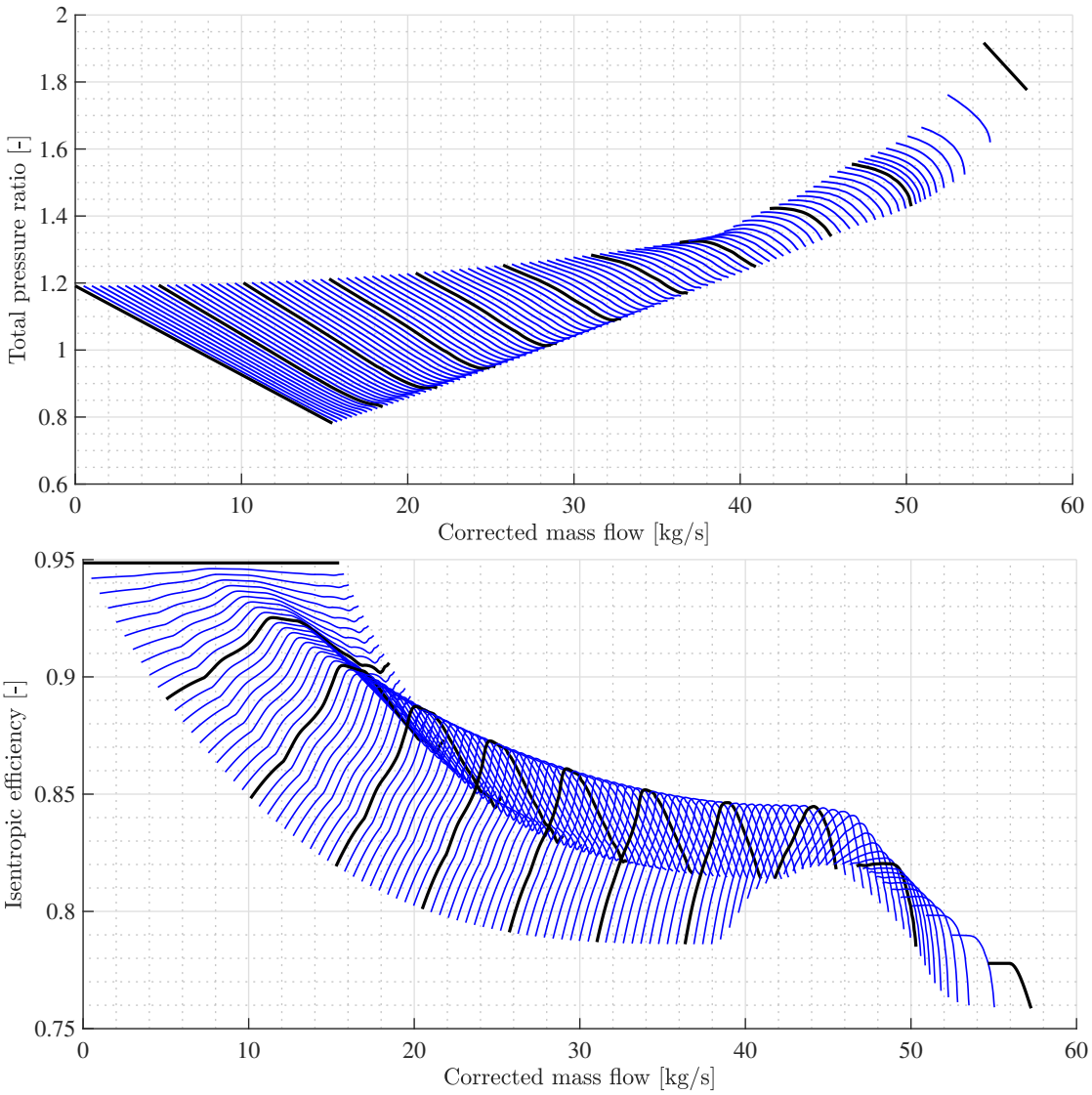

Figure 5.10: Compressor map. Black lines are separated a 10 %, from 0 % to 100 % in corrected speed. Obtained by *Zeleros* from CFD simulations.

- Surface roughness: ε.

The outputs of this module are:

- Mach number in 4: M_4.
- Total pressure in 4: p_{4t}.
- Total temperature in 4: T_{4t}.

Using p_{4t}, T_{4t}, $A_4 = A_{duct}$, M_4, $\dot{m}_4 = \dot{m}_\pi$, and the geometric parameters (length and diameter) the Fanno flow can be solved as explained in appendix A.4. With those equations, π_{34} and M_4 are computed. The rest of the parameters at 4 are:

$$p_{4t} = \pi_{34} p_{31t}, \tag{5.51}$$
$$T_{4t} = T_{31t}. \tag{5.52}$$

5.4.9 Nozzle

The nozzle expands the flow from 4 to 9, trying to match p_{19} as much as possible. The inputs of this module are:

- Pressure at 5: p_{5t}.
- Temperature at 5: T_{5t}.
- Exit area: A_9.
- Static pressure at 19: p_{19}.
- Nozzle efficiency: η_n.

The outputs of this module are:

- Pressure at 9: p_9, p_{9t}.
- Temperature at 9: T_9, T_{9t}.
- Density at 9: ρ_9.
- Internal mass flow: $\dot{m}_\pi$.
- Mach at 9: M_9.
- Velocity at 9: u_9.

As the nozzle is assumed to be adiabatic, the output total temperature is directly obtained $T_{9t} = T_{5t}$. Then, it is checked if the nozzle is chocked, computing the critical pressure p_9^*:

$$p_9^* = p_{9t}\left(1 - \frac{1}{\eta_n}\frac{\gamma-1}{\gamma+1}\right)^{\frac{\gamma}{\gamma-1}} \tag{5.53}$$

Then, two different cases appear. If the nozzle is chocked ($p_9^* \leq p_{19}$), the Mach is imposed, and the pressure is set to the critical one, instead of p_{19}:

- Mach number: $M_9 = 1$.
- Static pressure: $p_9 = p_9^*$.
- Static temperature: $T_9 = \frac{2}{\gamma+1}T_{9t}$.
- Velocity: $u_9 = \sqrt{\gamma R T_9}$.

If the nozzle is adapted ($p_9^* > p_{19}$), p_{19} can be reached:

- Static pressure: $p_9 = p_{19}$.
- Static temperature:

$$T_9 = T_{9t}\left\{1 - \eta_n\left[1 - \left(\frac{p_9}{p_{5t}}\right)^{\frac{\gamma-1}{\gamma}}\right]\right\}. \tag{5.54}$$

- Velocity: $u_9 = \sqrt{2C_p\left(T_{9t} - T_9\right)}$.
- Mach number: $M_9 = u_9\left(\gamma R T_9\right)^{-1/2}$.

Finally, the total pressure, density and mass flow is obtained

$$p_{9t} = p_9\left(1 + \frac{\gamma-1}{2}M_9^2\right)^{\frac{\gamma}{\gamma-1}}, \tag{5.55}$$

$$\rho_9 = \frac{p_9}{RT_9}, \tag{5.56}$$

$$\dot{m}_\pi = \rho_9 A_9 u_9. \tag{5.57}$$

At this point, if the internal mass flow is not equivalent to the one imposed at the intake in section 5.4.2, the iterative process is repeated before solving the downstream stage.

5.4.10 Downstream

The downstream module solves the flow mixing between 19 and 9 to reach the conditions in *down*. The inputs of this module are:

- Total temperature at 9: T_{9t}.
- Total temperature at 19: T_{19t}.
- Internal mass flow: $\dot{m}_\pi$.
- External mass flow: $\dot{m}_\beta$.
- Static pressure downstream: p_{down}.

The outputs of this module are:

- Total temperature: $T_{t,down}$.
- Static temperature: T_{down}.
- Mach number: M_{down}.
- External mass flow: $\dot{m}_\beta$.
- Downstream speed: u_{down}.

Firstly, the conditions *down* are computed. The total temperature is a mixture of the internal and external flow:

$$T_{t,down} = \frac{T_{19t}\dot{m}_\beta + T_{9t}\dot{m}_\pi}{\dot{m}}. \tag{5.58}$$

With the total temperature ($T_{t,down}$) and the static pressure (p_{down}), also the mass flow ($\dot{m}$) and the cross area (A_{tube}), using the continuity equation (see appendix B.1.1) the Mach number M_{down} can be computed. Then:

$$T_{down} = T_{t,down}\left(1 + \frac{\gamma+1}{2}M_{down}^2\right)^{-1}, \tag{5.59}$$

$$p_{t,down} = p_{down}\left(1 + \frac{\gamma+1}{2}M_{down}^2\right)^{\frac{\gamma}{\gamma-1}}, \tag{5.60}$$

$$u_{down} = M_{down}\sqrt{\gamma R T_{down}}. \tag{5.61}$$

Now, the current duct is solved for the external flow from downstream to upstream. The hypothesis assumed between 19 and 100 is that a mixture in total temperature happens (or energy) as equation (5.58) describes, but a mixture of total pressure (or momentum) does not occur. That means that the p_{19t} computed in section 5.4.5 should be equal to the $p_{t,down}$ computed in equation (5.60).

However, closing the iterative loop with total pressures is not numerically stable; this is why the external mass flow is used instead. The new mass flow is recomputed using all the parameters at 19 except for the total pressure: T_{19t}, $p_{t,down}$, A_{19} and M_{19}. The continuity equation is the following:

$$\dot{m}_\beta = \frac{A_{19} p_{t,down}}{T_{19t}} \sqrt{\frac{\gamma}{R}} M_{19} \left(1 + \frac{\gamma - 1}{2} M_{19}^2\right)^{-\frac{\gamma+1}{2(\gamma-1)}} . \tag{5.62}$$

This new external mass flow may be different to the one already defined. An iteration process is required to match both computations. The iteration starts from station 1 (section 5.4.1), imposing the new external mass flow, which implies a new total mass flow as, initially, the internal one is not modified.

5.5 Tube Thermodynamics

This section has been removed due to the NDA signed between the parts Sergio Hoyas and Zeleros Global SL.

5.6 Non-thermodynamic models

This section details the computations performed in the remaining modules appearing in the diagram from figure 5.5, which are the *Commanded N* and *Battery discharge* from the *Step 2: Thermodynamic model*; and all the forces required in *Step 3: Dynamic problem*.

5.6.1 Forces

The inputs of this module are:

- x_0: capsule position at the current time step.
- v_0: capsule speed at the current time step.

The outputs of this module are

- F_{brake}: braking force, a sum of the friction brake (FB) force F_{FB} and the magnetic brake (MB) force F_{MB}.
- F_{MB}: magnetic brake force.
- F_{LM}: linear motor force.
- F_{rol}: rolling friction force.
- F_{mag}: magnetic drag force.

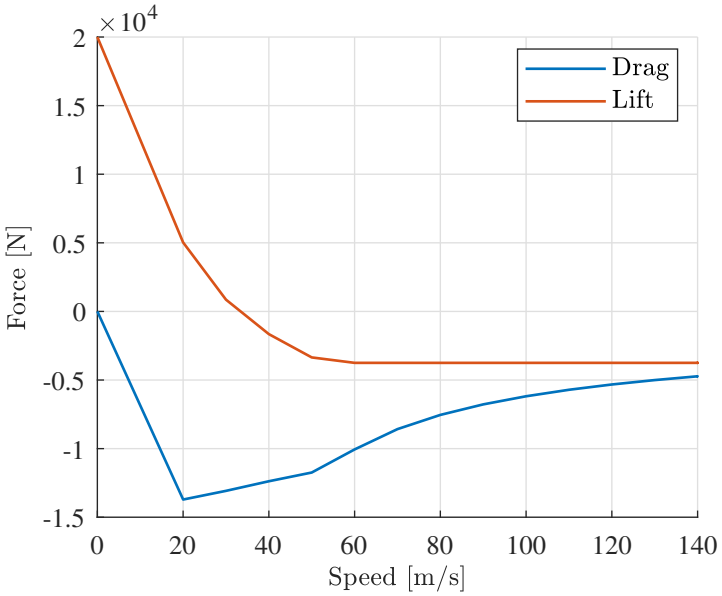

Figure 5.11: Magnetic brake map.

5.6.1.1 Friction brake

The input parameters are:

- μ_{FB}: Friction coefficient.
- n_{FB}: number of brakes.
- N_{FB}: normal force exerted by each brake.

Then, the output force is:

$$F_x = -\mu_{FB} n_{FB} N_{FB}. \tag{5.63}$$

The friction brake is only enabled when the speed is below a specific value $v \leq v_{tr}$.

5.6.1.2 Magnetic brake

The magnetic brake data includes the force in longitudinal direction x and vertical direction y as a function of the speed. The magnetic force depends on the relative speed, air gap between the magnets and the rail, and the electric current on the coils. As the airgap is fixed throughout the whole mission, and the required current is adjusted to avoid large vertical forces, only one dof is remaining: the speed. The map is shown in figure 5.11.

Note that an attractive force tends to pull the vehicle to the ground at high speeds, and a lift force pushes it to the ceiling at lower speeds.

The results of this model are the lift and drag forces of the brake, multiplied by the number of brakes n_{MB}, at the speed provided by the current time step:

$$F_{MB,x} = n_{MB} Drag\,(v)\,, \tag{5.64}$$
$$F_{MB,y} = n_{MB} Lift\,(v)\,. \tag{5.65}$$

The magnetic brake is only enabled when the speed is above a certain value $v \geq v_{tr}$.

5.6.1.3 Linear motor

For the linear motor, the input parameters are the following:

- P_{LM}: maximum mechanical power.
- a_{LM}: maximum acceleration of the linear motor.

The force provided by the linear motor is modelled as:

$$F_{LM} = \min\left(a_{LM} m_{pod}, \frac{P_{LM}}{v}\right) \lambda_{LM}, \tag{5.66}$$

where λ_{LM} is a factor that tried to determine if the Pod is within the linear motor range, or at least partially. This parameter accounts for this value:

$$\lambda_{LM} = \begin{cases} 0, & x_r > x_{LM}, \\ \frac{x_{LM} - x_r}{x_f - x_r}, & x_f > x_{LM} > x_r, \\ 1, & x_f < x_{LM}. \end{cases} \tag{5.67}$$

This way of expressing the force of the linear motor combines two regions. In the first one, the maximum force is reached, but the speed is not enough to achieve the maximum power. In the second region, the maximum force can no longer be obtained, and it starts to decrease hyperbolically with the speed.

5.6.1.4 Rolling friction

The rolling friction is modelled using the normal force and the rolling friction coefficient:

$$F_{rol} = -\mu_r \left(m_{pod} g + F_{MB,y}\right), \tag{5.68}$$

where the rolling friction coefficient is a function of the speed.

5.6.1.5 Magnetic drag

The magnetic drag is modelled equivalently to the rolling friction force, proportional to the weight of the vehicle with a factor λ_{mag}:

$$F_{mag} = -\lambda_{mag} m_{pod} g. \tag{5.69}$$

The factor λ_{mag} is a function of the speed. However, as this effect is quite slight, it has been neglected.

5.6.2 Battery discharge model

The battery is formed by connecting n_s cells in series and n_p cells in parallel. The cells in series are required to reach the motor voltage, while the parallel branches are needed to provide the target current.

5.6.2.1 Mathematical model

The total voltage provided by the battery V is the following:

$$V = n_s V_{cell}\left(I_{cell}, DOD\right), \tag{5.70}$$

The voltage of the cell is obtained from its map, which can be seen in figure 5.12.

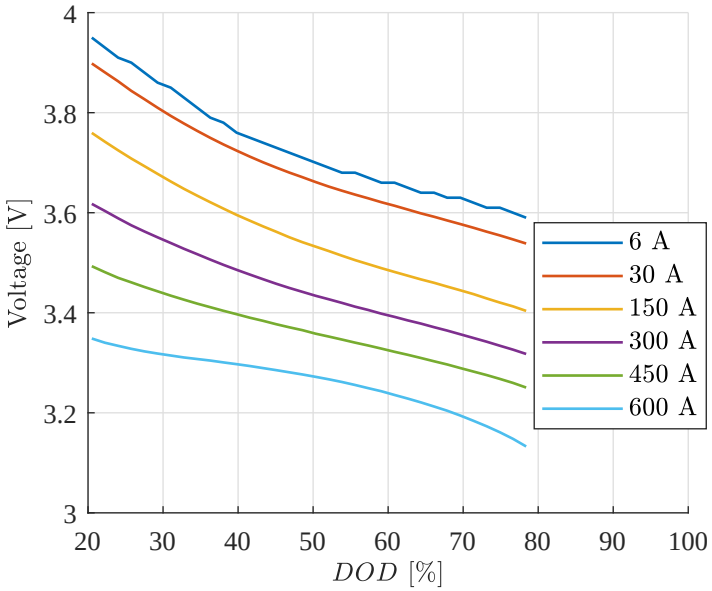

Figure 5.12: Battery map for one cell. Source: manufacturer.

To know the current drawn from each series branch, a power balance between the mechanical power $\dot{W}$ and the electrical power VI through the electrical efficiency η is used:

$$\dot{W} = \eta V I \rightarrow I = \frac{\dot{W}}{\eta V}. \tag{5.71}$$

Combining equation (5.70) and (5.71):

$$I = \frac{P}{n_s V_{cell}\left(I/n_p, DOD\right)\eta}. \tag{5.72}$$

Note that this is an implicit function $I = I\left(DOD\right)$ that is solved iteratively. Also, note that the current through the cell has been replaced by $I_{cell} = I/n_p$.

The relation between the charge of the cell and the current drawn is the following:

$$\frac{\mathrm{d}q_{cell}}{\mathrm{d}t} = I_{cell}. \tag{5.73}$$

The differential equation is reformulated considering the ratio between the charge of the cell q_{cell}, its maximum capacity q_{max}, and the DOD:

$$q_{max}\frac{\mathrm{d}DOD}{\mathrm{d}t} = \frac{I}{n_p}. \tag{5.74}$$

So, the differential system to solve is described by equations (5.74) and (5.72).

5.6.2.2 Numeric solution

Crank-Nicholson method is used on equation (5.74):

$$\frac{DOD - DOD_0}{\Delta t} = \frac{I + I_0}{2n_p q_{max}} \rightarrow DOD = DOD_0 + \frac{\Delta t}{2n_p q_{max}}\left(I + I_0\right). \tag{5.75}$$

Now, an iterative method based on I is used. For the first step, $I' = I_0$, and for the rest:

$$DOD = DOD_0 + \frac{\Delta t}{2n_p q_{max}}\left(I' + I_0\right),$$
$$I = \frac{P}{n_s V_{cell}\left(I'/n_p, DOD\right)\eta}.$$

Then, the tolerance between I and I' is checked. If it is above tolerance, $I' = I$ and the algorithm is repeated.

5.6.3 Commanded N

The compressor speed N_n in current time is computed in this module. There are different ways in which this value is obtained:

- Braking phase. During the braking phase, the motor is left free, and the compressor acts as a windmill. Then the aerodynamic torque can brake the fan. So, $T_{mot} = 0$.
- Torque imposed. During the acceleration or cruise phase, the torque of the motor is equal to the maximum value. So, $T_{mot} = T_{max}$.
- Torque not imposed. During the acceleration or cruise phase, the speed of the motor follows a parabolic evolution, as explained below.

If the torque is imposed, the speed for the current time step can be computed from the previous one:

$$N_n = \frac{T_{mot}\eta_{mech} - T_{aero,n-1}}{I_{shaft}}\Delta t + N_{n-1}. \tag{5.76}$$

If the torque is not imposed, a parabolic evolution dependent on time is followed:

$$N_n = \begin{cases} N_0 & \text{if} \quad t \leq t_0, \\ a\,t^2 + b\,t + c & \text{if} \quad t_0 < t < t_{max}, \\ N_{max} & \text{if} \quad t \geq t_{max}, \end{cases} \tag{5.77}$$

where the constants a, b and c are function the parameters that define the curve:

- N_0: initial speed.
- N_{max}: maximum speed.
- t_0: time where $N = N_0$.
- t_{max}: time where $N = N_{max}$. This may not be accomplished due to torque limitations.

The values for the constants are:

$$c = \frac{N_0 + N_{max}\left[\left(\frac{t_0}{t_{max}}\right)^2 - 2\left(\frac{t_0}{t_{max}}\right)\right]}{\left(\frac{t_0}{t_{max}} - 1\right)^2}, \tag{5.78}$$

$$b = 2\frac{N_{max} - c}{t_{max}}, \tag{5.79}$$

$$a = \frac{c - N_{max}}{t_{max}^2}. \tag{5.80}$$

Then, the torque of the motor T_{mot} should not surpass the maximum torque allowed T_{max}:

$$T_{mot} = \frac{1}{\eta_{mech}}\left(T_{aero} + \frac{N_n - N_{n-1}}{\Delta t} I_{shaft}\right). \tag{5.81}$$

If the computed torque is greater than the maximum torque, equation (5.76) is used again to compute the current N_n assuming $T_{mot} = T_{max}$.

Then, the motor power is also computed:

$$\dot{W}_{mot} = T_{mot} N_{n-1}. \tag{5.82}$$

If the computed power is greater than the maximum power equation, (5.82) is rearranged to compute the new torque:

$$T_{mot} = \frac{\dot{W}_{max}}{N_{n-1}}. \tag{5.83}$$

Then, the new speed can be computed using equation (5.76).

The last check uses the speed limit of the motor $N_{max,V}$ according to the voltage provided. It is used the voltage in the current time step V_n:

$$N_{max,V} = K_V V_n. \tag{5.84}$$

If $N_n > N_{max,V}$ then $N_n = N_{max,V}$ and equation (5.81) is used to compute the new torque and equation (5.82) to compute the new power.

5.7 Tube ambient temperature model

The ambient temperature inside the tube on the model is assumed to be constant on the simulator. However, considering effects such as solar radiation (see figure 5.13), the temperature may be far from constant, and, what is even worse, it can reach high levels even before the operation of the vehicle. At this point, the thermal model used for the tube temperature prediction is described, and some results are exposed.

The heat equation used for this calculus is 0D. The effects on the tube width are negligible compared to the characteristic times of integration (1 year), and the evolution in length is neglected, assuming an infinite tube in the axial direction. Then, only time remains in the heat equation for the tube as the independent variable.

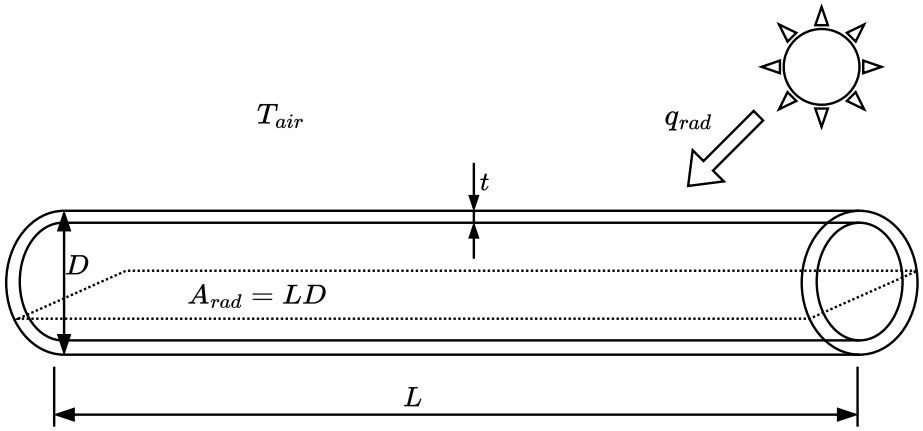

Figure 5.13: Tube heating problem.

The inner air T_i is assumed uniform in temperature, neglecting air convection. This hypothesis is not as valid as the one in the tube wall, but in this way, the system is largely simplified, as instead of a PDE system, the problem is solved with an ODE.

For the tube, there are no heat sources but three different components that introduce thermal energy to the solid:

- $q_{conv,ext} = h_e \left(T_{air} - T_w\right) A_{conv}$: heat transfer to the external air by convection.
- $q_{conv,int} = h_i \left(T_w - T_i\right) A_{conv}$: heat introduced by radiation.
- $q_{rad,ext} = \varepsilon q_{rad,0} A_{rad}$: heat transferred to the inner air by convection.

By his part, the inner air has only the convection with the tube wall, or $q_{conv,int}$, neglecting the direct sun radiation that can surpass the tube wall:

So, the equation system used is the following:

$$\rho_{tube} V_{tube} C_{p,tube} \frac{\mathrm{d}T_w}{\mathrm{d}t} = q_{conv,ext} + q_{rad,ext} - q_{conv,int}, \tag{5.85}$$

$$\rho_{air} V_{air} C_{p,air} \frac{\mathrm{d}T_i}{\mathrm{d}t} = -q_{conv,int}. \tag{5.86}$$

Symbol	Description	Formula	Value	Origin
D	Tube external diameter	-	2.5 m	Defined by project
t	Tube thickness	-	0.03 m	10% of the diameter
L	Tube length	-	1	Not necessary
A_{conv}	Area affected by convection	πDL	7.854 m^2	Wet area of the tube
h_e	External film coefficient	(5.89)	Variable	Correlation [133]
h_i	Internal film coefficient	(5.89)	Variable	Correlation [133]
T_{air}	External air temperature	-	Variable	Meteorological data [134]
A_{rad}	Area affected by radiation	DL	2.5 m^2	Horizontal projection
$q_{rad,0}$	Global horizontal irradiance	-	Variable	Meteorological from [134]
ε	Tube absortance	-	0.76	Steel absortance

Table 5.4: Different parameters used for the tube air temperature computation.

The different terms used in this model are described in table 5.4.

The tube is supposed to be made of standard structural steel, so its properties are the following:

- Density: 7800 kg/m^3.
- Specific heat: 502.416 J/(kg K).
- Absortance: 0.76[1].

The equation to compute the film coefficient is obtained from [133]. First, the Rayleigh number is obtained:

$$Ra = \frac{g\beta_{air}\left|T_w - T_{air}\right| D^3}{\alpha_{air}\nu_{air}}, \tag{5.87}$$

where $\beta_{air} = 1/T_a$ is the thermal expansion coefficient, ν_{air} is the kinematic viscosity, α_{air} is the thermal diffusivity, and g the gravity.

Then, the Prandtl Pr number is computed:

$$Pr = \frac{\nu_{air}}{\alpha_{air}}. \tag{5.88}$$

Furthermore, finally the Nusselt Nu number using the correlation:

$$Nu = \left\{ 0.60 + \frac{0.387Ra^{1/6}}{\left[1 + \left(\frac{0.559}{Pr}\right)^{9/16}\right]^{8/27}} \right\}^2. \tag{5.89}$$

From the Nusselt number, the film coefficient is derived:

$$h = \frac{Nuk_{air}}{D}, \tag{5.90}$$

[1]Reference: `https://www.engineeringtoolbox.com/solar-radiation-absorbed-materials-d_1568.html`, last accessed 20-01-2022

where k_{air} is the thermal conductivity.

The time step used is 240 seconds. This large time step is because the gradients on the characteristic variables are large (hour-based).

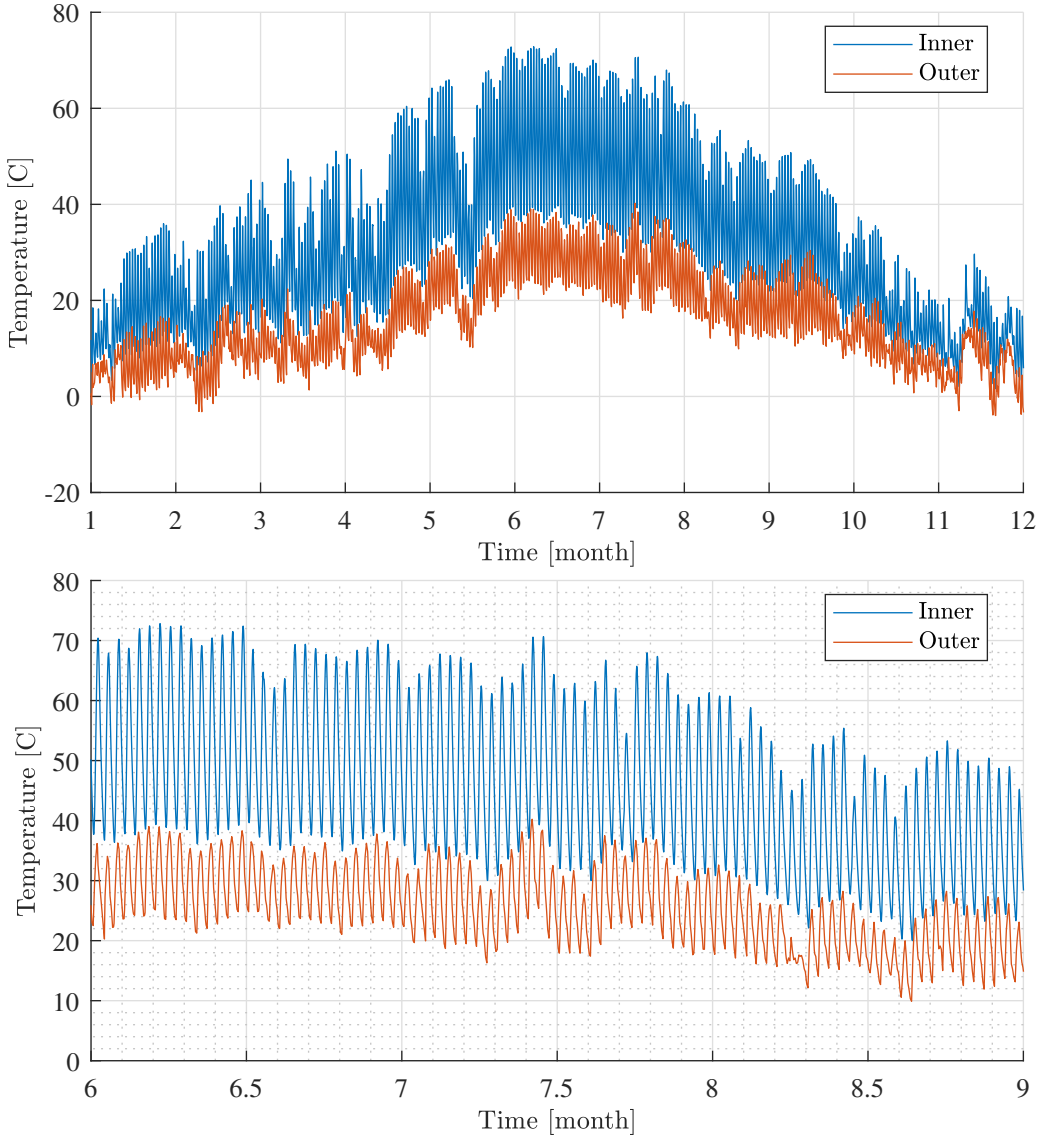

Figure 5.14: Inner and outer air temperature during one year with an absorptance of 0.76.

The results for the air temperature are plotted in figure 5.14. It is shown a whole year of temperature evolution for the internal air (from the simulation output) and the external air (input from meteorology data). There is a zoom for June to August on the bottom graph where the day-night cycles can be differentiated.

The film coefficient is computed for each time step and plotted in figure 5.15 for the internal and external interface. Note that h is not constant throughout the day or the year.

The main conclusion from this study is that the tube can reach very high temperatures

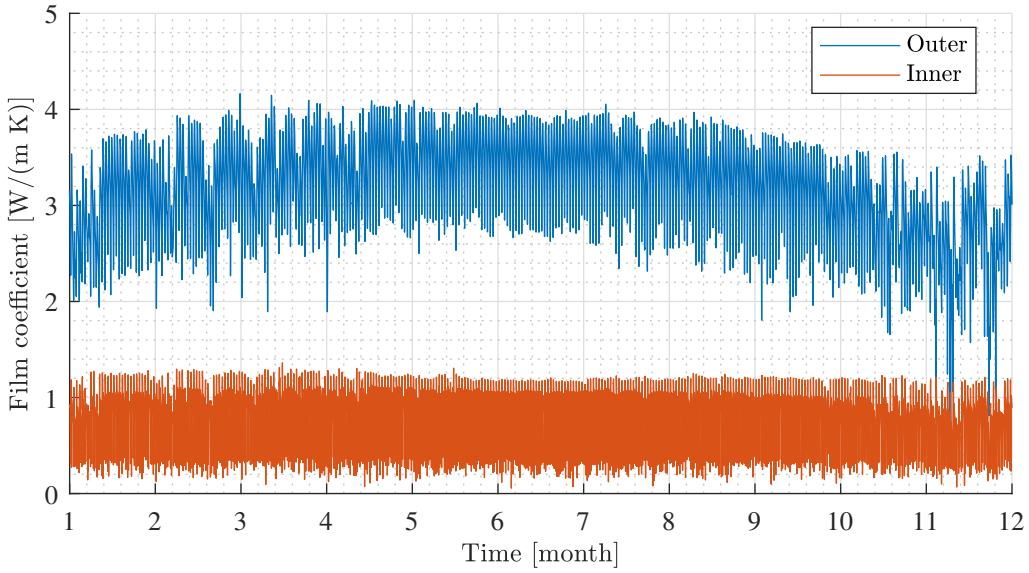

Figure 5.15: Inner and outer film coefficient during one year with an absorptance of 0.76.

during summer, in the order of 70°C. The main reason is the energy absorbed by sun radiation. In order to keep the temperature below a reasonable value, the radiation has to be minimised. The best way to do this is to cover the tube with solar cells, which avoids the radiation on its surface and helps recover part of this thermal energy as electricity.

To validate this hypothesis, the results are repeated, substituting the absorptance value from 0.76 to 0.24, which is a reasonable value for white-painted steel. The plot is represented in figure 5.16, where the maximum air temperature inside the tube is 47°C, which is reasonable.

If solar panels cover the tube, the radiation reaching its surface may be close to zero, decreasing even more the air temperature.

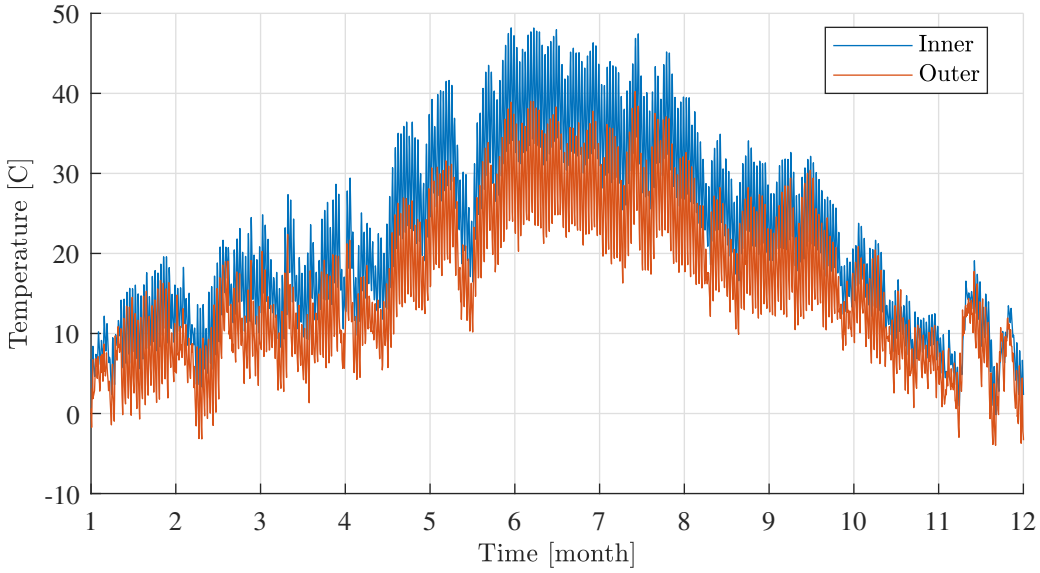

Figure 5.16: Inner and outer air temperature during one year with an absorptance of 0.24.

5.8 Results

The results presented for the module are focused on describing the outputs obtained from the simulator to the mission. The parameters used for the mission are the following:

- Cruise speed: $v_{cru} = 500$ km/h.
- Mass of the vehicle: $m_{pod} = 2500$ kg.
- Length of the track: $L_{track} = 3000$ m.
- Braking transition speed: $v_{tr} = 20$ m/s.
- Linear motor length: $x_{LM} = 800$ m.
- Braking distance: 750 meters from the end (2250 m from the beginning).
- Tube pressure: $p_0 = 10$ kPa.
- Tube temperature: $T_0 = 308$ K.

5.8.1 Mission profile

The velocity profile is the most important parameter to obtain when analysing a mission. Figure 5.17 represents the velocity and acceleration evolution with respect to the position in the track. For this and the rest of the cases, the front position of the capsule is used.

The target speed of 500 km/h is reached during the acceleration phase, just before reaching 800 meters. In this stage, the acceleration is dominated by the linear motor, which provides a hyperbolic evolution as the motor power limits the curve.

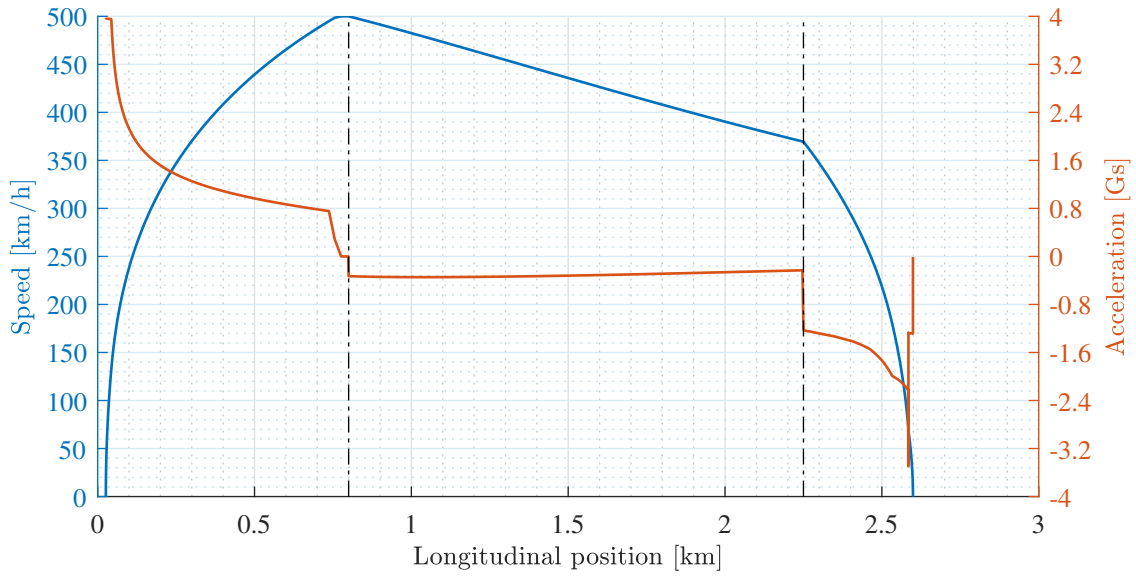

Figure 5.17: Velocity and acceleration profile. The two vertical lines represent the transition to the cruise and braking phase.

The velocity of 500 km/h is maintained constant a few meters before the end of the linear motor. From there, a nearly constant deceleration of around 0.3 Gs progressively reduces the speed of the vehicle. The reason is that the compressor does not provide enough power to the fluid to maintain a constant speed at this regime.

Finally, at the end of the cruise phase (2250 meters), the velocity decreases faster due to the actuation of the brakes. The deceleration is modified in two different stages. Firstly due to the magnetic brake, until 20 m/s (72 km/h) are reached. Secondly, the friction brakes actuate until the vehicle is stopped. Note that there are a few meters where both brakes are actuated.

Another way to explain the effects on the capsule speed and acceleration is by analysing the longitudinal forces over it. The linear motor acceleration force, aerodynamic force (or net thrust) and braking force are represented in figure 5.18. Notice that the net thrust is negative due to the drag overcoming the thrust. This leads to a negative acceleration even during the cruise phase, as seen previously in the velocity profile.

The linear motor force reaches an order of magnitude higher (up to 100 kN, although the plot is capped for convenience) than the aerodynamic one (8 kN). That means that during acceleration, the aerodynamic effects can be neglected.

The mission time is not represented in that graph; it is represented in figure 5.19. In general, the time does not provide useful information; that is why the rest of the plots use the position as the independent variable. However, the total run time is a relevant output: 27 seconds.

Before analysing other variables, the time step requires attention. As mentioned in section 5.3.2.1, the Δt is variable, function of the gradients of the solution. That is why, if represented in figure 5.20, a non-constant time step is plotted. Note that the time step is

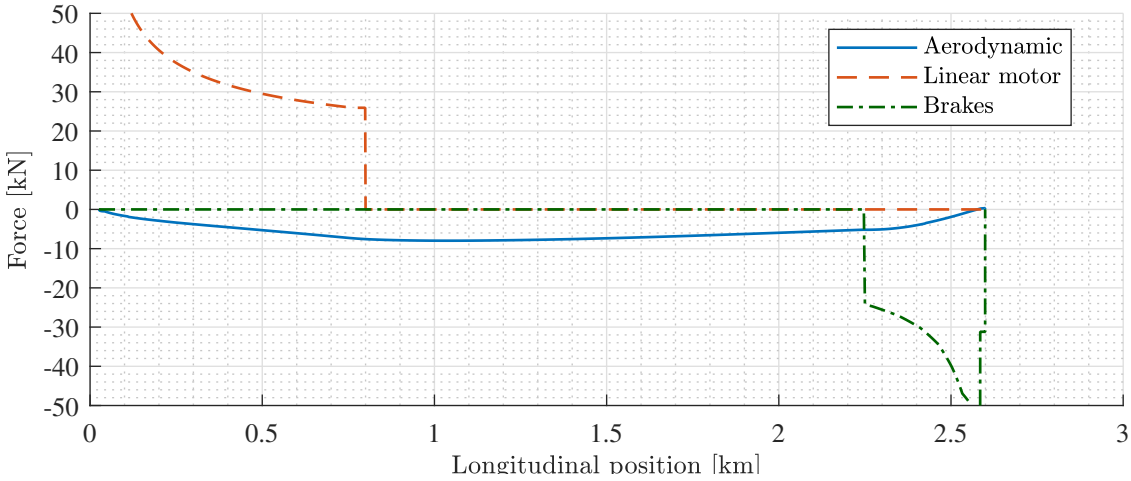

Figure 5.18: Longitudinal forces acting on the capsule versus the position.

quite large during the cruise phase, as there are no significant gradients during that stage. However, at both ends, the time step must be reduced to ensure the stability and accuracy of the solution. The reason is the proximity of the walls and the operation of the compressor in the sub-idle region. The consequence is large variations in the channel flow (see figure 5.22) and in the tube pressure.

Another part where refinement is required is the transition between phases. Near these points, discontinuities appear due to the change in the applied models, leading to numerical instabilities damped by stretching the step.

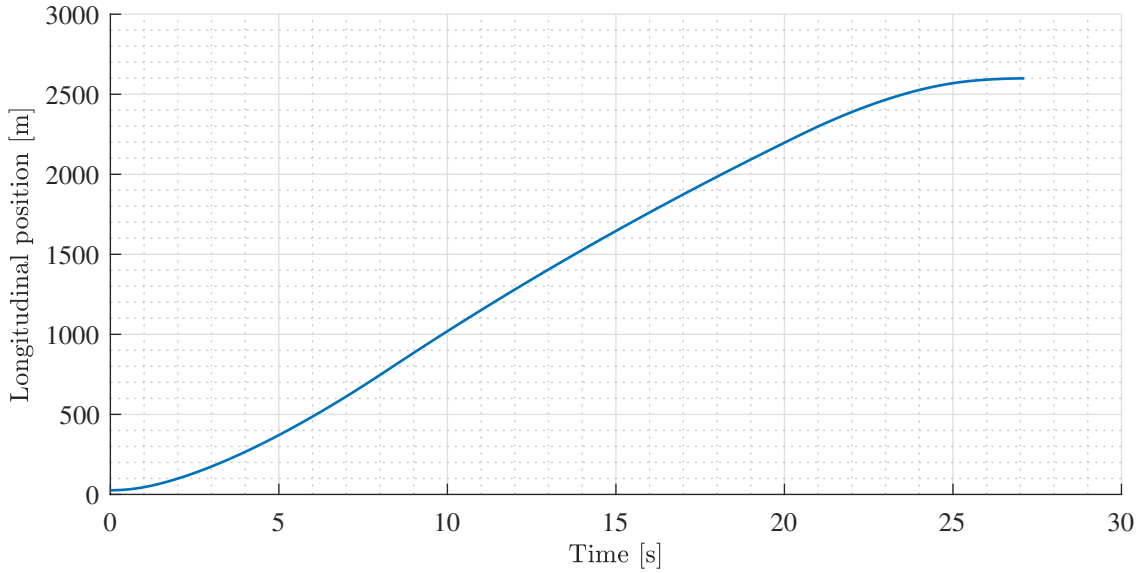

Figure 5.19: Position versus time.

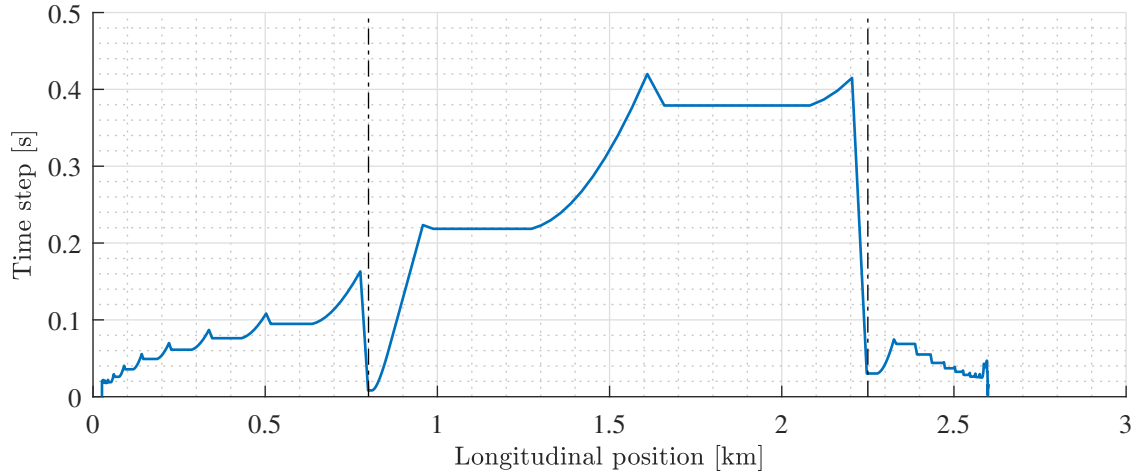

Figure 5.20: Time step versus the capsule position.

5.8.2 Tube thermodynamic variables

One of the most important outputs of the tube model is the pressure and temperature in the front and rear control volume. The rear pressure decreases significantly initially because the capsule accelerates quite fast, thanks to the linear motor. The compressor cannot shallow enough mass flow to compensate for this vacuum. The same reason explains why the front pressure increases.

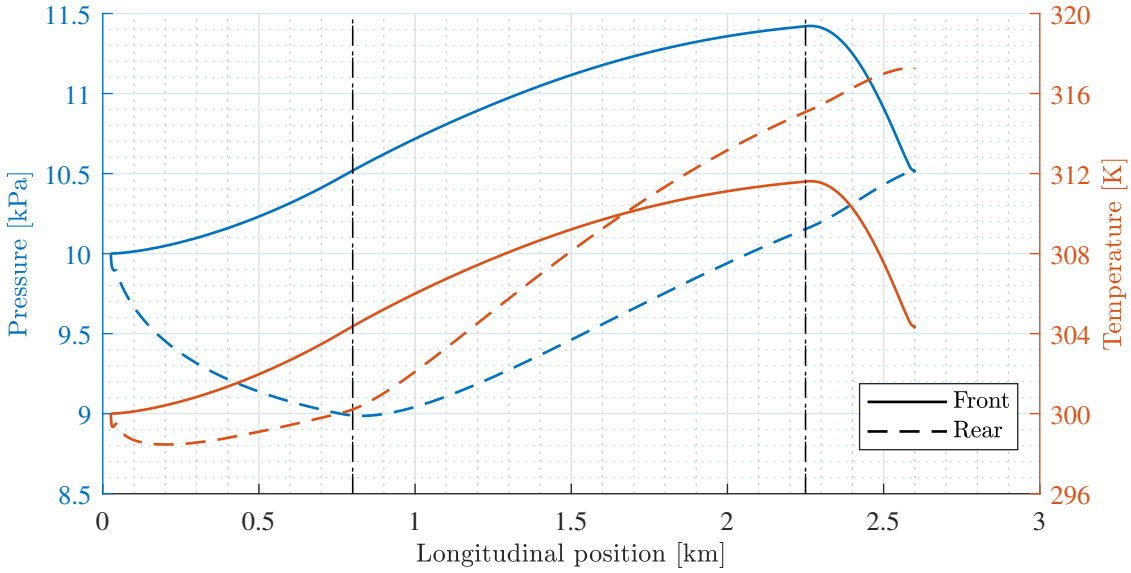

Figure 5.21: Tube font and rear pressures and temperatures versus position. Continuous line for front variables and dashed line for rear ones.

As the acceleration from the linear motor decreases and the compressor shallows more mass flow, the slope in the rear pressure decreases. Its minimum occurs where the cruise phase starts (800 meters). There, the acceleration is negligible and the rear volume can be filled again.

As the end of the tube approaches, the front pressure increases due to the piston effect. The volume displaced by the vehicle is higher than the one the channel and compressor can transfer. The rear pressure also increases as the pressure delta on the capsule and the compressor help transfer enough mass. Also, as the rear end of the tube is further than at the beginning, there is more air volume that damps the depression.

When the braking phase starts (2250 meters), the speed of the capsule reduces, and the mass flow through the channel and the compressor (acting as a windmill) can cover the volume displaced by the vehicle.

Note that the pressure level at the end of the mission is matched between the rear and the front parts. However, the value is 500 Pa higher than the one at the beginning due to the thermodynamic losses.

Regarding the temperatures, they follow the same trend as the pressure, except that the front and rear values do not match at the end. This is a consequence of the low thermal diffusion speed.

If the tube were not considered adiabatic, the front and rear temperatures would reach the values from the beginning of the simulation due to the thermal equilibrium with the exterior air. Consequently, the pressure would reach 10 kPa again, as no mass has been added to the system.

The trends observed in the pressures and temperatures are a response to the mass flows, shown in figure 5.23. There, the channel and compressor mass flow are plotted. Also, the total mass flow (sum of both variables) and the tube mass flow (the derivative of the mass displaced by the capsule control volume) are represented. To avoid any piston effect, the total mass flow should be equal to the tube mass flow.

However, this does not happen during acceleration (only very close to the beginning) or the cruise phases, as the total mass flow is considerably lower than the tube one. This explains why the piston effects provoked the pressure difference seen in figure 5.21. During these phases, the channel and compressor cannot transfer enough mass from the front to the rear control volumes, and part of the mass displaced by the vehicle remains at its front.

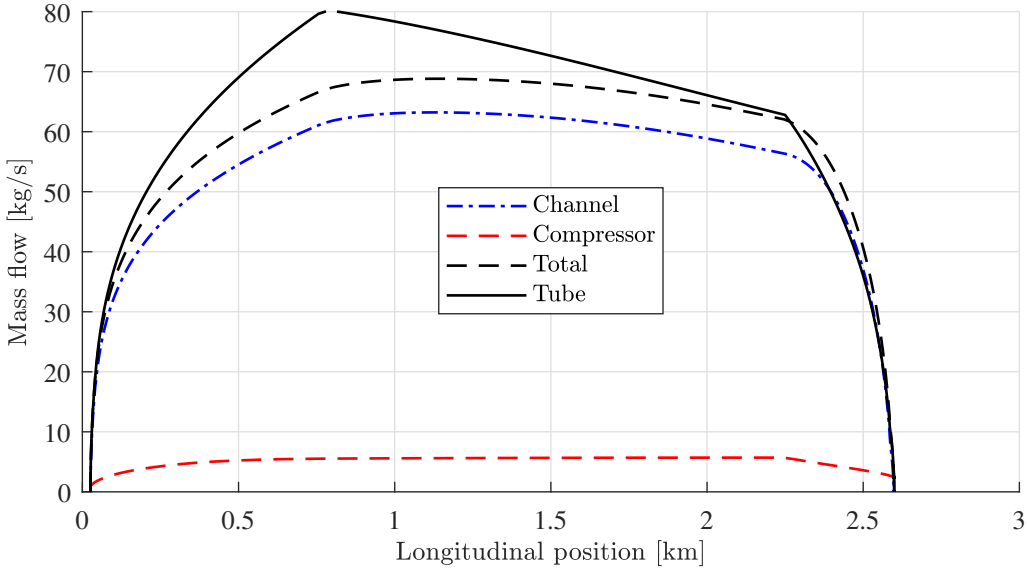

Figure 5.22: Different mass flows that cross the capsule versus position.

During the braking phase, the total mass flow overcomes the tube mass flow. Then, air accumulation no longer happens, leading to the pressure equilibrium already described.

Note that the compressor mass flow is far below the mass flow on the channel, so a better performance on the system using a larger compressor can be reached. This also explains why during the cruise phase there was a negative acceleration (see figure 5.17).

In the same line as the previous plots, the physical mass filling the front and rear volumes is represented in figure 5.23. Note how the front air mass is progressively transferred to the rear control volume.

With this plot, the mass conservation on the numeric solution can be checked, as the sum of both variables is constant.

A consequence of the air accumulation already described appears in the flow speed. The

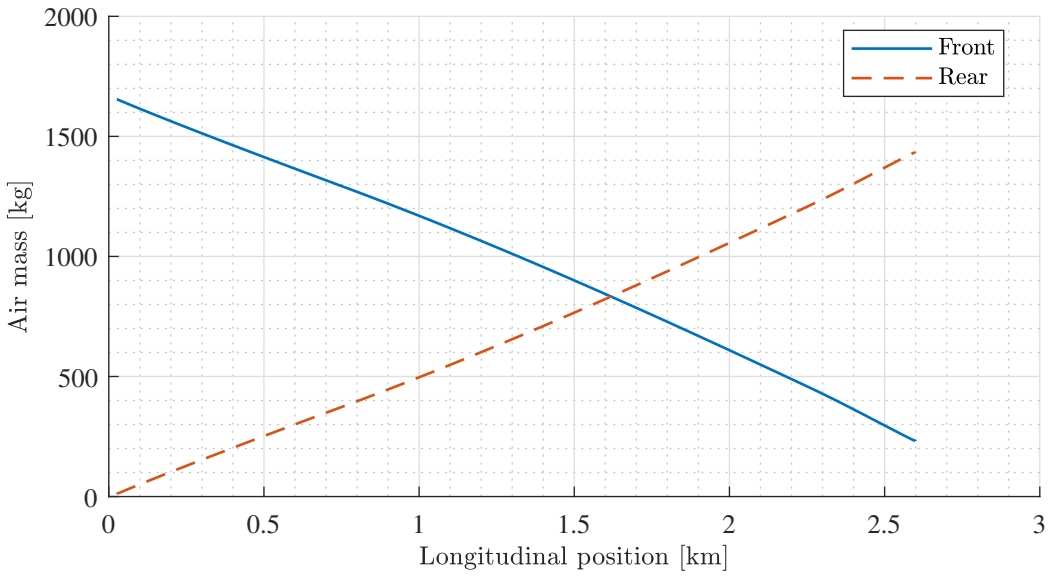

Figure 5.23: Tube front and rear air masses versus position.

vehicle does not face its wall speed but a slightly lower one in the front and rear boundary conditions. The difference between the wall and air speed is named induced speed. Up to 10 m/s (36 km/h), or 7 % of the maximum speed, is reached in the front boundary. The maximum occurs just before the end of the cruise phase (around 2000 meters) for the same reason as the accumulation was maximum at that point (front pressure in figure 5.21).

As for the rear induced speed, 14 m/s (50 km/h), or 10 % of the maximum speed, is reached. This peak occurs at the end of the acceleration due to the vacuum generated by the rapid acceleration of the linear motor. Also, it is located where the minimum of the rear pressure happened in figure 5.21.

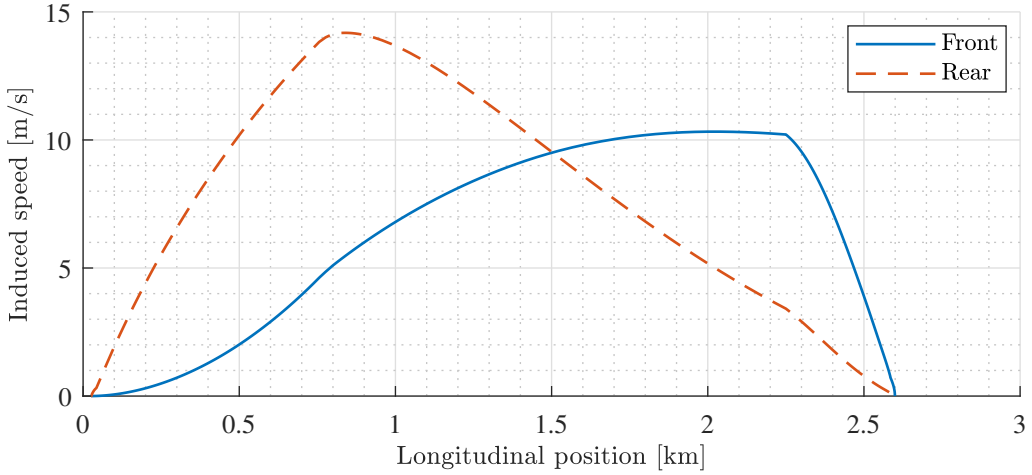

Figure 5.24: Induced front and rear speeds versus position.

5.8.3 Internal thermodynamic variables

This section analyses what occurs in the internal cycle of the vehicle. Over a hundred variables are obtained: static and total pressures, temperatures and densities, mass flow, speed, and Mach number in each station. However, only the most relevant are represented.

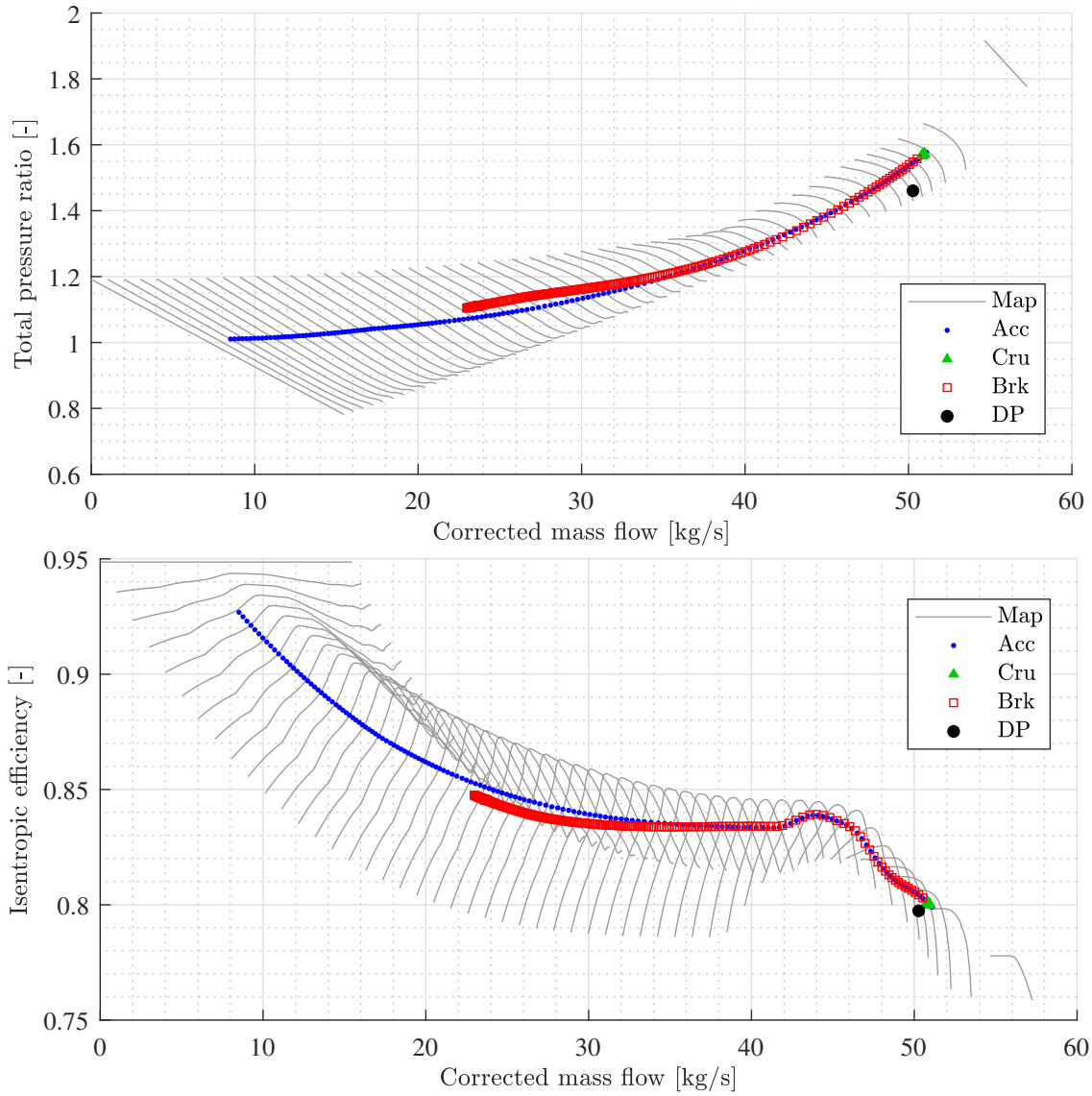

Figure 5.25: Compressor map overlapped with the operation line during the mission. Acc, Cru and Brk stand for acceleration, cruise and braking phases respectively. DP is the Design Point. Only one in two speed lines is plotted.

Firstly, the compressor map is represented again (as shown in figure 5.10) but overlapping the operation line in the mission. This is done in figure 5.25, differentiating the three mission phases. Note that all the operation line is within the bounds of the compressor

maps, which is highly important. Particularly significant is to run far from the surge limit to ensure a safe operation of the turbomachine.

The acceleration covers almost all the map, while the braking phase stops before reaching the lowest values. This is because when the simulation ends the blades are still spinning. It is remarkable the hysteresis that happens between the acceleration and braking curves, as they do not follow the same path. This is a typical effect in the operation of gas turbines [135].

The cruise is represented by many nearly overlapped points close to the maximum speed. This indicates that, during this stage, the compressor operates approximately at the same point.

Focusing on the efficiency map, the operation line closely follows the maximum at each speed, which indicates that the design point has been properly selected.

The design point is also represented in the map (DP). The operation line is close but does not intersect with this value. The non-negligible variations in the front and rear pressure, temperatures and speeds make it extremely complicated to go through the exact same boundary conditions used in the design point during a mission.

The final plot includes the Mach number in the most relevant stations in the cycle, represented in figure 5.26.

The Fanno flow explains the difference between M_3 and M_4. Note that the internal duct is far from being choked, as its maximum Mach number is 0.52.

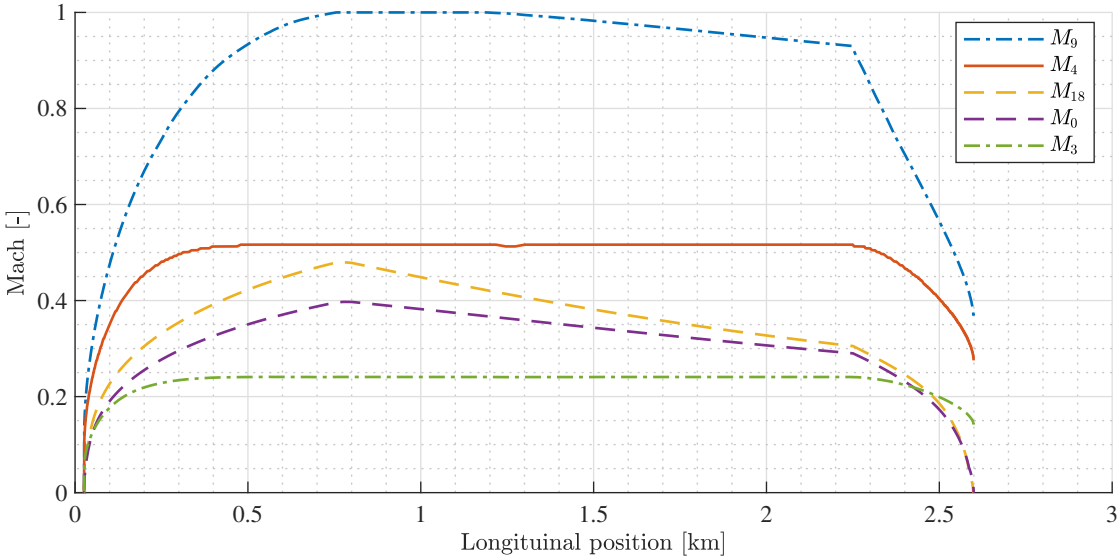

Figure 5.26: Mach number in different thermodynamic stages versus position.

Regarding the rear behaviour, the nozzle is choked during a large part of the cruise phase. It reaches $M_9 = 1$ just before the end of the linear motor and remains there for 400 meters (around 3 seconds of the mission). This way, the operation on the compressor map is also restricted, making it easier to prevent aerodynamic instabilities on the turbomachinery.

The external channel Mach, M_{18}, reaches its maximum when the capsule Mach is the highest ($M_0 = 0.4$) and is also far from blocking, reaching 0.48.

5.8.4 Component performance

Finally, the performance of the modelled non-thermodynamic components is analysed, particularly the batteries and electric motor.

As for the energy storage, figure 5.27 represents the voltage and current drawn from the batteries, and figure 5.28 the Deep Of Discharge (DOD). Note that the voltage drops rapidly from more than 820 V to a nominal around 730 V during the cruise. There, the current is near its maximum (between 450 and 470 A).

The current peak occurs just before the end of acceleration (500 m). The mechanical power required at this point is the largest as the compressor is already at its maximum speed (see figure 5.29) and the capsule is not at its maximum speed yet (see figure 5.17).

Once the cruise is completed and the power is cut off, the voltage is partially recovered and the current is null. Note that the battery losses more than 10 V in a mission.

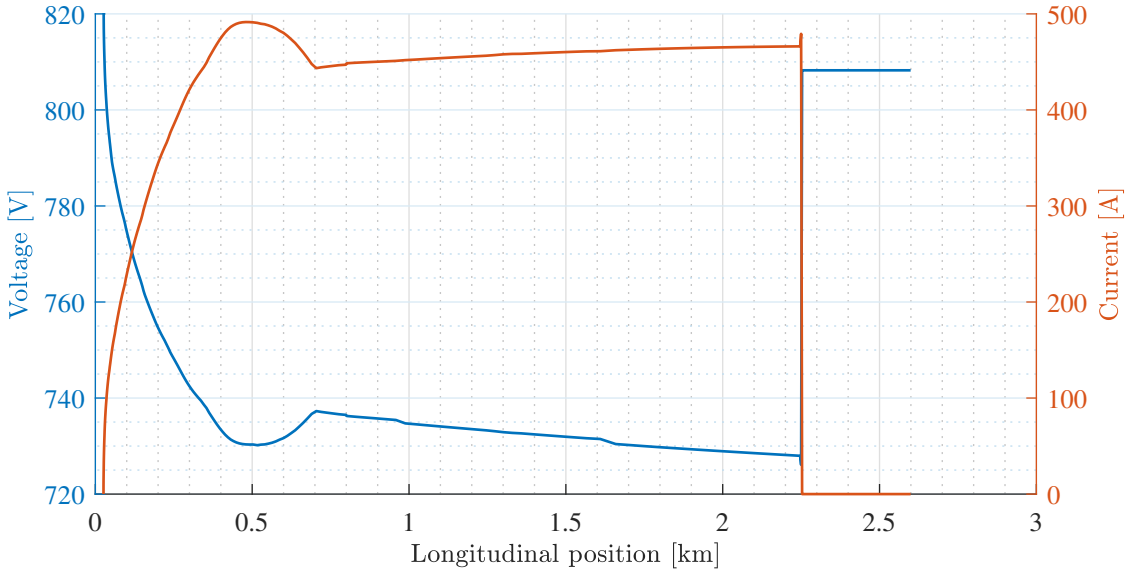

Figure 5.27: Voltage and current drawn from the batteries versus position.

By his part, the DOD increases from 30 % to 40 %, which means that the storage system can handle one mission. So, the battery will be able to provide energy for more missions.

Finally, the electric motor parameters are represented in figure 5.29. As already discussed, the power is maximum just before the end of the acceleration phase. The torque follows a similar trend, although its maximum occurs at the beginning due to the excess of power at low speeds.

Regarding the motor speed, it reaches its maximum at around 600 meters during the acceleration phase. During braking, the system acts as a windmill and the speed decreases due to the inertia of the system and the aerodynamic torque. Note that, when the simulation ends because the pod stops, the compressor remains spinning at around 35 %, as already discussed in the map in figure 5.25.

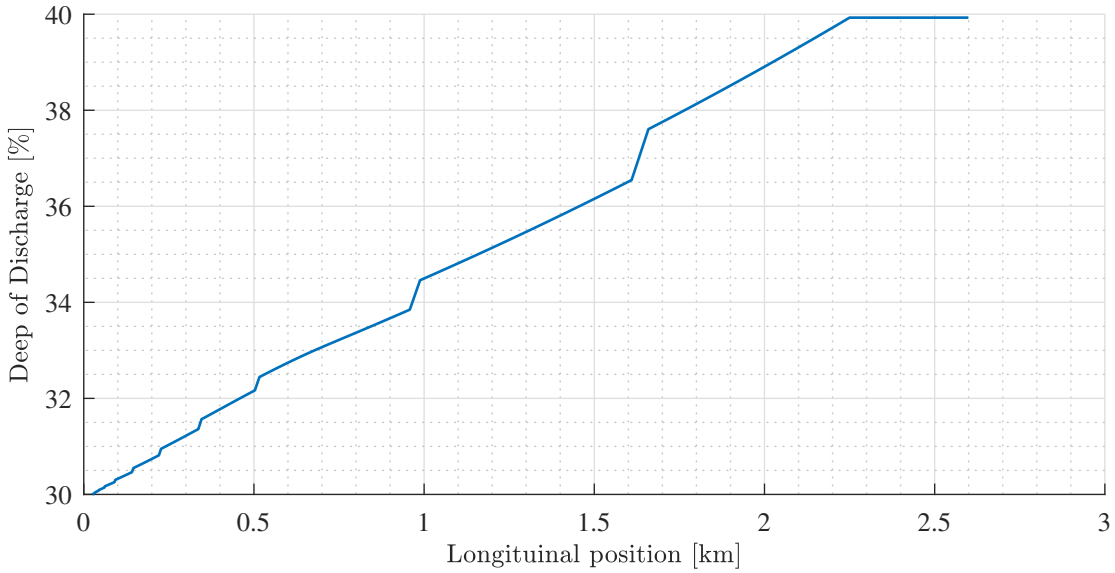

Figure 5.28: Deep of discharge of the battery versus position.

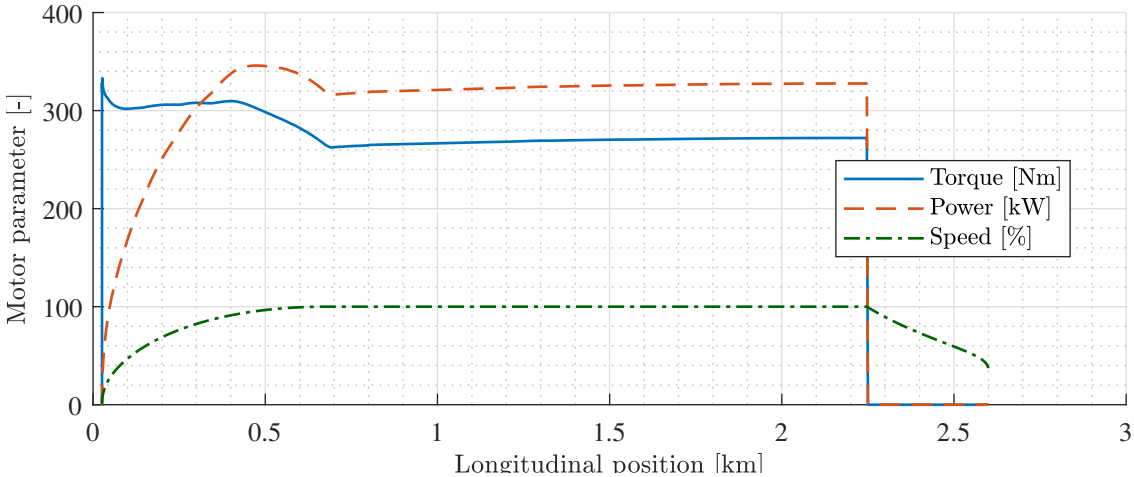

Figure 5.29: Mechanical power, torque and electric motor speed versus position.

5.9 Future work

Several improvements can be made to the model. The first one is to implement the closed-loop control of the only dof of the system: the compressor speed N. Now, a parabolic evolution is followed, limited by the motor torque and power in open loop. However, the goal of the mission is to maintain a constant speed. For that purpose, the speed of the vehicle must be read to modify the input power to the motor to modify its speed and get the net thrust necessary to follow the imposed velocity profile.

Regarding the numeric solver, the time adaptive model can be improved, as in some cases ripple in the solution may appear due to the numerical integration. Numerical problems have also appeared in the external loop (see figure 5.9), the one that iterates over $\dot{m}_\beta$ and estimates the induced pressure. The hypothesis of $p_{t,down} = p_{19t}$ and assuming a perfect mixture in temperatures and not in pressures between stations 19 and *down* seem to fail in some cases. Also, the effects of station 9 to compute *down* should be considered.

Furthermore, this code does not solve the problem correctly if the external channel is blocked. This model can be included, as it was developed successfully for the real-scale simulator (chapter 4).

Finally, instead of assuming an infinite sound speed, the 0D near-field solution can be coupled with a 1D wave propagation problem, which is valid for the tube thermodynamic solution. This will help compute the evolution of the thermodynamic variables throughout the tunnel and have the proper boundary conditions every time step on the capsule.

Currently, *Zeleros* is developing the second version of this simulator, including all the items proposed in this section. It also models the heating of the critical components. This new model is being developed in Matlab/Simulink instead of Python to take advantage of the tools that this platform offer. This simulator is oriented to implement Software-in-the-Loop (SiL) techniques.

Chapter 6

Conclusions

The goals of this thesis have been thoroughly completed. Chapter 1 conducted the proposed literature review, including all the hyperloop-alike projects and technologies used in the past and being developed currently. Moreover, this literature review could contextualise the concept of *Zeleros*.

The two proposed simulators were developed. Before, an aerodynamic study of the capsule was conducted in chapter 2, and the detail of the Fanno flow model was described in chapter 3. The simulator for the real-scale prototype appeared in chapter 4. After an optimisation process, a hyperloop vehicle was described. The thermodynamic cycle, overall performance, mass, length and power requirements were stated. Moreover, the proposed system was compared with other existing transport solutions such as aeroplanes, HSRs and maglev trains.

The model for the middle-scale system was described in chapter 5. This second simulator included a new implementation of hyperloop modelling, where the transient effects were considered. Using this capability, all the relevant parameters for the mission were represented and analysed.

Although the thesis goals were completed, some issues may have improved the present work.

The models used are, on the whole, quite robust. However, both models can apply improvements to the rear expansion approach. In particular, a pressure match between the external and internal flow in the real-scale model is difficult to achieve.

Another critical point is the experimental realisation. Experimental data would have improved the accuracy of the models, particularly for the subsystem models implemented in the middle-scale simulator. Only experiments for the levitation system were conducted in [68], and for the linear motor statically in [69].

Also, the middle-scale prototype has not been manufactured. That means that no system tests have been conducted. Quite valuable feedback would come from comparing the simulated and measured mission data (speeds, pressures, temperatures...). This would have also been useful for the real-scale approach.

More specific conclusions are detailed in the following section for each chapter of the present work.

6.1 Introduction

The literature review shows that the hyperloop approach was firstly proposed by the British inventor George Medhurst in 1799, more than two centuries ago. However, it was not until the release of the Hyperloop Alpha by Elon Musk in 2013 that the world names this system as *hyperloop*.

Two are the most similar approaches to hyperloop that have been invented and worked commercially. The first one is the atmospheric railway. Developed firstly during the XIX century, currently, the Brazilian company Aeromovel operates two (in Brazil and Indonesia), but at low speeds.

The other important hyperloop-alike technology is the maglev train. Several low-speed maglevs have been in operation. Although in Europe, Birmingham and Berlin installed maglevs in the past, nowadays, only China, Japan and South Korea have maglevs operating with passengers.

As for high-speeds, two are the main projects around the world. The German Transrapid was tested in Germany more than a decade ago. Since 2002 it has been commercially available in Shanghai, China, at a commercial speed of 431 km/h. The other important maglev is the Chuo Shinkansen developed in Japan. It uses superconductive technology for propulsion and levitation and operates at 500 km/h. It is expected to enter into service in 2027.

The analysis of the technologies used by maglev and hyperloop lead to several conclusions about the *Zeleros* approach. A similar levitation system has been working at high-speed in the Transrapid for more than 20 years. In terms of propulsion, the proposal is unique. Neither the aerodynamic propulsion nor the Linear Switched Reluctance Motor (LSRM) is proposed by other hyperloop projects. However, all the hyperloop projects plan on using a linear motor for the acceleration phase.

Regarding pressure, only the Swissmetro approach targets aerospace levels, as *Zeleros* does. The rest of the proposals aim for pressures in the order of 100 Pa or even lower.

Another important conclusion is that a few initiatives share the current hyperloop development. As far as the author knows, only seven private companies exist. Universities started their research with the Hyperloop Pod Competition by Elon Musk and now with the European Hyperloop Week. On the latter, the development of levitation systems and linear motors integrated into a vehicle has already been conducted.

6.2 Aerodynamic study of the capsule

After comparing the thermodynamic behaviour of a capsule inside a low-pressure tunnel using and not using a compressor, conclusions can be presented.

Several relevant points arise from the set-up of the cases. On the one hand, the pressure-based steady solved, although theoretically not as accurate as the Riemann transient solver for these supersonic cases, showed a difference in the drag of less than 1 %, making it feasible for this study. On the other hand, among the two possible inlet boundary conditions analysed, mass flow or total pressure imposed, a significant difference in the results is reported. The first has been chosen as it is more representative of a closed environment

where the flow cannot escape. Thus, an average result is provided.

The addition of the compressor to the simulation reduces the required power to maintain a constant speed for high blockage ratios. At low BRs (around 0.2), avoiding using the compressor can even be beneficial, as the flow is entirely subsonic. However, as the tunnel gets smaller and transonic and supersonic effects appear, the power consumed by the *base* case grows exponentially. In those cases, the compressor consumes considerably less power. This reduction grows asymptotically to a value around 70 % at a BR between 0.35 and 0.5. Higher blockage ratios do not increase the improvement of the compressor.

The capsule and the tunnel behave similarly to a converging-diverging nozzle. Once critical conditions are reached, the flow becomes supersonic downstream, enforcing the appearance of oblique shock waves. The analysis of the flow patterns has shown that adding the compressor can remove these waves in all the simulated cases, even if they reach sonic conditions. Thus, the flow behaviour is qualitatively independent of the size of the tunnel.

Not only the mitigation of shock waves is an effect of the turbomachinery, but also, for the geometry studied, the downstream separation is removed. There, the nozzle substitutes the wall at the tail of the capsule.

The delay in the transonic effects is also evident when analysing the induced speed on the inlet of the domain. The *compressor* case can maintain the inlet speed equal to the capsule speed, especially at 500 km/h, as the case is always below the Kantrowitz limit. For higher speeds, the induced speed is still negligible compared to the *base* case, in which the induced effect increases linearly with the BR independently of the reference speed. This is because this effect is mainly dependent on the geometry.

The benefits of installing a compressor can also be evaluated with the point at which the critical Mach number is reached. The turbomachinery enables the vehicle to operate subsonic in a wider range, which explains the reduction in power consumption. For 700 km/h the BR limit increases from $\beta = 0.18$ to somewhere in between 0.5 and 0.6. With regard to 500 km/h, *compressor* never blocks in the studied range. Moreover, it is remarkable how the isentropic approximation accurately follows the trend of the CFD simulation when evaluating the Mach number on the passage.

In other terms, until the *compressor* case blocks, it can operate with tunnels of 2.8 times lower cross-sectional area for the same capsule section, independently of the speed. This is a considerable reduction in the tunnel size and the infrastructure cost.

If future ground transport wants to overcome 500 km/h, a new concept where ambient pressure can be decreased must be proposed. This allows decreasing the drag of the capsuled linearly with this parameter, leading to acceptable air resistance even at very high-speeds and in small tunnels. Moreover, the system performance improves considerably when installing a compressor due to the delay in the Kantrowitz limit.

6.3 Fanno model

This work developed a 1D simplified equation to model the Couette-Poisuille compressible flow in an annular domain with friction effects. The *modified* model is based on the standard Fanno flow equation, named *original* approach, but using an equivalent diameter instead of

the hydraulic one. A *numeric* model based on integrating the 1D ODE was also developed for reference.

The equivalent diameter is shown to be higher than the hydraulic one, indicating that the friction effects are less effective when moving one of the walls, also reducing the critical length. When the wall speed equals to flow speed, the equivalent diameter is twice the hydraulic one. Moreover, the smaller the BR, the larger the equivalent diameter.

Although the accuracy of the *modified* is not extremely high, the computational cost of its evaluation is negligible compared to extensive CFD techniques or even solving a 1D ODE.

Compared to CFD, the *modified* approach is almost as close as the *numeric* to the Fluent solution. The maximum deviation shown is 5 % in the pressure ratio, normally underpredicted. The solution is more accurate the lower the BR or Fanno factor is.

The *simplified* model provides accurate results compared with CFD simulations with the same conditions. However, due to the 1D hypothesis, the accuracy is worse the larger the Fanno parameter is, no matter the blockage ratio used.

As for the critical length, the *original* approach does not predict any variation with the wall speed, but the *modified* and *numeric* do predict the same evolution. However, the *modified* approach overpredicts the critical length, a maximum of 10 % in the range analysed. This study also shows that that the dependence of the critical length with the Reynolds is negligible as long as it is turbulent.

The friction coefficient variation is predicted correctly by the *numeric* approach, the only one capable of providing this output. Regardless of the wall speed, the interior friction coefficient is underpredicted, and the exterior is overpredicted. However, both are close to the Fluent solution, always with less than a 7 % deviation.

The *numeric* also considers the variation of the Reynolds number in its integration. However, for turbulent flows, this effect is negligible. Only for laminar flows, the Reynolds cannot be assumed constant.

The results regarding the critical length and the pressure ratio, and the low computation cost, made the *modified* approach the selected one for the hyperloop models in chapters 4 and 5. This approach allows for quick and accurate approximations of the flow on the channel between a hyperloop capsule and the tube.

6.4 Real-scale system

This section developed a successful simulator for the real-scale model. The results were validated with respect to CFD in a test case. The deviation is less than 10 % in all parameters, except for the Fanno losses. Apart from the friction difference, the most significant error occurred in p_{19}, which is a challenging value to reproduce as pressure loss and even separation occur in this region.

The parametric study shows a large pressure difference between 9 and 19 in the outlet that may occur depending on the nozzle area. These are non-physical solutions of the simulator, as the mixing process is not modelled. Then, these solutions must be avoided.

Moreover, the thrust in this problem is dominated by the pressure term. The net thrust increases when the nozzle pressure increases and the momentum is lower. This explains

why the optimum values have the nozzle adapted.

Also, when the channel is blocked, the total pressure and temperature upstream of the vehicle must increase to allow transferring all the mass flow. For larger nozzle areas, the throat is in 19. For lower A_9 values, the channel behaves as a naval nozzle with the throat in 15.

The total power optimum does not match the lowest energy consumption. Compressing more the flow to reduce the cabin diameter and having excess energy at the end of the duct is more efficient. Then, the turbine can recover part of this energy to avoid more thrust than required.

Moreover, the lower the internal mass flow, the lower the total and net powers. So, the optimum occurs for the lowest mass flow with a physical solution. The physical meaning is that, as far as possible, the compressor should shallow the lowest mass flow possible as the energy required to increase its pressure is larger than the external friction losses when the external flow is greater. This also implies that the pressure ratio is the lowest possible, as the less internal mass flow, the less internal Fanno losses.

Furthermore, as the tube gets smaller, the energy requirements are higher. The reason is that less space is left for the flow and more Fanno losses in the channel occur. Moreover, the compressor mass flow must be higher for smaller tubes. As the space left around the vehicle is smaller, the compressor must shallow more flow to avoid significant external Fanno losses. Then, the pressure ratio must also increase to overcome the larger pressure drop due to the increased mass flow in the duct. Consequently, the recovery factor has to be higher, as there is an excess of energy in the internal flow to surpass the cabin.

Although the optimum may seem to increase the tube size, the infrastructure cost will also increase, which has not been considered in the model. Considering the cost instead of the energy as the target for the optimisation, the optimum value should not correspond to the biggest infrastructure diameter possible.

Comparing the Z50 and Z150, the energy requirements for the former are lower as this vehicle is smaller. However, in terms of specific energy, the Z150 capsule performs better as, only doubling the required energy, it can transport three times more passengers.

The internal thermodynamics in a hyperloop vehicle is similar to a Bryton cycle. The main difference is the no energy addition between 3 and 4 as no combustion chamber is included in hyperloop. Another difference is that the compressor enthalpy jump and the turbine jump do not have to be equal, as the system is not mechanically coupled. Moreover, the nozzle adapted pressure does not have to match the far-field pressure as there is a pressure loss around the capsule, which reduces the downstream ambient pressure.

Finally, the specific energy consumption in a hyperloop vehicle is closer to the maglev than for the aeroplane. Hyperloop efficiency is between three and five times higher than air systems.

Regarding the average speed, hyperloop is more competitive than the plane on 800 km or shorter routes. Remarkably, the mean speed in an air route can be as low as 300 km/h on short routes. Compared to the HSR, hyperloop is up to three times faster.

6.5 Middle-scale system

The development of the middle-scale simulator allowed obtaining the time evolution of many variables throughout a mission, which was not possible on the real-scale model.

The simulator is quite robust. It can model the mass flow accumulation and the point of operation in the compressor map each time step. Also, an adaptive time method has been successfully implemented. In critical parts of the mission, it automatically stretches the time step to prevent numeric instabilities and inaccuracies.

However, the current design does not reach the required net thrust in the cruise phase, and deceleration of 0.3 Gs occurs. The mass flow shallowed by the compressor is far below the one on the tube, which explains why the aero-engine cannot provide enough thrust compared to the drag of the system. This is not considered a problem, as the technology demonstration is the primary goal of the prototype. A larger compressor would be able to shallow more mass flow and thus provide the required thrust for the mission.

Another way to see the lack of compressor mass flow is through the pressure accumulation in front of the capsule. The air displaced by the moving control volume of the vehicle is not transferred by the sum of the compressor and channel mass flows. Then, the air accumulates in front of the prototype, increasing the front pressure (11.5 %) and temperature (4 %), and provoking an induced air speed (10 %). In the rear part of the vehicle, a vacuum effect is generated, leading to a pressure and temperature decrease.

One of the most important outputs is the operation line over the compressor map. The capsule can operate throughout all the mission leaving enough surge margin.

Furthermore, other non-thermodynamic components are also solved. The voltage and current drawn from the battery are computed, and, most importantly, the discharge level of the pack. Thanks to this figure, the energy left in the battery can be estimated. Moreover, the power and torque of the electric motor are computed each time step.

Another relevant conclusion from this chapter is that the air temperature inside the tube can reach values up to 70^{o}C, which will prevent the prototype from being tested on those days. The proposed solution is to paint the tube white or cover it with solar panels, which decreases 23^{o}C the temperature.

References

[1] Eurocontrol. Aviation Outlook 2050. Technical report, Eurocontrol, 2022.

[2] Boeing Commercial Airplanes. *High-speed civil transport study.* Langley Research Center, 1989.

[3] Xue-song Jin. Key problems faced in high-speed train operation. *Journal of Zhejiang University SCIENCE A*, 15:936–945, dec 2014.

[4] Elon Musk. Hyperloop Alpha. Technical report, SpaceX, Hawthorne, LA, 2013.

[5] J A G Fernández. *Ingeniería de Vías Férreas.* Lulu.com, 2017.

[6] D K Clark. Railway machinery: a treatise on the mechanical engineering of railways: embracing the principles and construction of rolling and fixed plant; illustrated by a series of plates on a large scale, and by numerous engravings on wood, 1855.

[7] A Gordon. *A Treatise Upon Elemental Locomotion: And Interior Communication, Wherein are Explained and Illustrated, the History, Practice, and Prospects of Steam Carriages, and the Comparative Value of Turnpike Roads, Railways, and Canals.* T. Tegg & Son, 3 edition, 1836.

[8] J R Stevens. *Pioneers of Electric Railroading: Their Story in Words and Pictures.* Electric Railroaders' Association, 1991.

[9] John S. Reid. Robert Davidson – pioneer electrician.

[10] Peter Hall and Peter Fox. *No Preserved Coaching Stock of British Railways: BR Design Stock Pt. 1.* Platform 5 Publishing Ltd, London, first edition, 1994.

[11] George Medhurst. *On the Properties, Power, & Application of the Aeolian Engine, with a plan and particulars for carrying it into execution, etc.* Proprietor, London, 1805.

[12] George Medhurst. *A New Method of conveying Letters and Goods with great certainty and rapidity by air.* D. N. Shury, London, 1810.

[13] George Medhurst. *Calculations and Remarks, tending to prove the practicability of a plan for the rapid conveyance of goods and passengers upon an iron road through a tube of 30 feet in area, by the power and velocity of air.* D. N. Shury, London, 1812.

[14] George Medhurst. *A New System of Inland Conveyance, for Goods and Passengers, Capable of Being Applied and Extended Throughout the Country: And of Conveying All Kinds of Goods, Cattle, and Passengers, with the Velocity of Sixty Miles in an Hour, at an Expense that Will No.* T. Brettell, London, 1827.

[15] Grace's Guide to British Industrial History. Atmospheric Railway, 2020.

[16] William Little. The Kingston and Dalkey Atmopsheric Railway, 1844.

[17] Garrett Lyons. *Steaming to Kingstown and sucking up to Dalkey : the story of the Dublin and Kingstown Railway.* Londubh, Dublin, 2015.

[18] C F Mallet. *Rapport Sur Le Chemin de Fer Établi Suivant Le Système Atmosphérique de Kingstown À Dalkey, en Irlande: Et Sur Lapplication de Ce Système Aux Chemins de Fer en Général.* Carilian-Gœury et V. Dalmont, 1844.

[19] Train History. Atmospheric Railway History and Facts, 2020.

[20] H O Hardenberg and S A E Historical Committee. *The Middle Ages of the Internal-combustion Engine, 1794-1886.* R.: Society of Automotive Engineers. Society of Automotive Engineers, Warrendale, 1999.

[21] C Hadfield. *Atmospheric Railways: A Victorian Venture in Silent Speed.* Mechanical might-have-beens. David & Charles, 1967.

[22] Grace's Guide. Lamson Pneumatic Tube Co, 2022.

[23] J. McGregor. *Pneumatic Dispatch*, volume 18. Encyclopaedia Britannica, London, 1957.

[24] J E Connor. The Crystal Palace Pneumatic Tube Railway. *The London Railway Record*, 2003.

[25] Alan Chodos and Michael Lucibella. February 26, 1870: First pneumatic powered subway line in New York City. *APS News*, 12(2), 2013.

[26] Oliver E. Allen. New York's Secret Subway. *Invention & Technology Magazine*, 12(3), 1997.

[27] Esther C Goddard. Vacuum tube transportation system, 1945.

[28] Inventors of maglev technologies, 2022.

[29] Anatoly Zaitsev, Johannes Klühspies, Roland Kircher, Eckert Fritz, and Michael Witt. *Maglev 2018 - Abstracts of the 24th International Conference in St. Petersburg, Russian Federation.* sep 2018.

[30] Boris Weinberg. Five Hundred Miles an Hour. *Popular Science Monthly*, page 705, 1919.

[31] Emile Bachelet. Levitating transmitting apparatus, 1912.

[32] Hermann Kemper. Magnetic Levitation Pionner, 2022.

[33] C. Kerr and C. Lyn. The Roller Road. *Westinghouse Engineer*, 1961.

[34] James R Powell. The Magnetic Road: A New Form of Transport. In *ASME Railroad Conference*, apr 1963.

[35] James R Powell and Gordon T Danby. Electromagnetic inductive suspension and stabilization system for a ground vehicle, 1969.

[36] Rua David Oskar H. W. Coester. Pneumatic Propulsion System for Freight and/or Passenger Vehicles, 1984.

[37] Banning Garrett. The inherent economic and environmental advantages of Aeromovel technology. Technical report, Aeromovel, Brazil, 2018.

[38] J L He, D M Rote, and H T Coffey. Survey of foreign maglev systems. 1992.

[39] Angelo Jacob and Nuno Monteiro. A new concept of superelevation in magnetic levitation – prodynamic. *Transportation systems and technology*, 4:77–111, dec 2018.

[40] D Y Park, B C Shin, and H Han. Korea's Urban Maglev Program. *Proceedings of the IEEE*, 97(11):1886–1891, 2009.

[41] Zhiwei Zhang. New maglev train improves service in Hunan, 2021.

[42] South China Morning Post. Is this Chinese prototype the shape of maglev train tech to come?, 2021.

[43] BRIAN SANDS. The German Magnetic Levitation Train (Transrapid). *Built Environment (1978-)*, 19(3/4):244–256, aug 1993.

[44] Zhendong Liu, Sebastian Stichel, and Mats Berg. Technology and Development of Maglev and yperloop Systems. Technical report, KTH - Royal Institute of Technology, Stokholm, 2022.

[45] Hyung-Woo Lee, Ki-Chan Kim, and Ju Lee. Review of maglev train technologies. *IEEE Transactions on Magnetics*, 42(7):1917–1925, 2006.

[46] Takagi H. Maglev in Japan - Yamanashi test line. In *2nd National Swissmetro Day*, Zurich, 1996.

[47] Mamoru Uno. Chuo Shinkansen Project using Superconducting Maglev System. Technical report, JR Central, Tokyo, oct 2016.

[48] Hyung-Suk Han and Dong-Sung Kim. *Magnetic levitation*. Springer tracts on transportation and traffic. Springer, Dordrecht, Netherlands, 1 edition, 2016.

[49] Tim Howgego. Transportation Futuristics – Pneumatic Transportation – Bay Area Gravity-Vacuum Transit, jun 2022.

[50] Joseph V. Foa. Transportations Means and Method, 1965.

[51] W. B. Brower. An Introduction to the Project Tubeflight. Technical report, Rensselaer Polytechnic Institute, Troy, NY, 1966.

[52] J. Dill and D. Meeker. Maglifter Tradeoff study and subscale system demonstrations. Technical report, National Aeronautics & Space Administration, Waltham, MA, 2000.

[53] J Meunier. *On the Fast Track: French Railway Modernization and the Origins of the TGV, 1944-1983*. Praeger, 2002.

[54] M R Doyle, D J Samuel, T Conway, and R R Klimowski. Electromagnetic aircraft launch system-EMALS. *IEEE Transactions on Magnetics*, 31(1):528–533, 1995.

[55] Marcel Jufer and A Cassat. Collaboration with the Korean Railroad Research Institute (KRRI) Status Synthesis of the Swissmetro Project Swissmetro Maglev and KRRI Tube Train Developments. Technical report, dec 2010.

[56] Michele Mossi and Stefano Sibilla. Swissmetro : aerodynamic drag and wave effects in tunnels under partial vacuum. In *Proceedings of the 17th International Conference on Magnetically Levitated Systems and Linear Drives*, pages 156–163, Lausanne, Switzerland, 2002.

[57] Aldo D'Arrigo and Alfred Rufer. Design of an Integrated Electromagnetic Levitation and Guidance System for SwissMetro. jan 1999.

[58] Airbus. E-Fan X, 2021.

[59] Airbus. CityAirbus NextGen, 2021.

[60] P Kshirsagar, J Ewanchuk, B van Hassel, R Taylor, S Dwari, J Rheaume, and C Lents. Anatomy of a 20 MW Electrified Aircraft: Metrics and Technology Drivers. In *2020 AIAA/IEEE Electric Aircraft Technologies Symposium (EATS)*, pages 1–9, 2020.

[61] Arbi G. Siraki. Hyperloop, the new mode of transportation. In *Proceedings of the 13th International Symposium on Linear Drives for Industry Application*, Los Angeles, CA, 2021. Virgin Hyperloop.

[62] A. Jedinger. Homopolar Linear Synchronous Machine, 2020.

[63] Ryan Janzen. TransPod Ultra-High-Speed Tube Transportation: Dynamics of Vehicles and Infrastructure. In *Procedia Engineering*, volume 199, pages 8–17. Elsevier Ltd, 2017.

[64] Type Certificate Data Sheet No. A45EU. Technical report, Federal Aviation Administration, Washington D.C., 1979.

[65] U.S. Standard Atmosphere NASA-TM-X-74335. Technical report, NASA, Washington D.C., 1976.

[66] J. K. van Leeuwen, J. M. P. Lohle, T. R. Speelman, Y. van der Tang, M. H. Teeuwen, and T. Vlesshouwer. The future of hyperloop. Technical report, Delft University of Technology, Delft, 2019.

[67] Kenneth Decker, Jeffrey Chin, Andi Peng, Colin Summers, Golda Nguyen, Andrew Oberlander, Gazi Sakib, Nariman Sharifrazi, Christopher Heath, Justin Gray, and Robert Falck. Conceptual Feasibility Study of the Hyperloop Vehicle for Next-Generation Transport. Technical report, NASA Glenn Research Center, Cleveland, 2017.

[68] Jose F. Gonzalez-Rojo, Federico Lluesma-Rodríguez, and Temoatzin González. A hybrid EMS system for a Hyperloop prototype vehicle. In *The 9th International Symposium on Speed-up and Sustainable Technology for Railway and Maglev Systems (STECH2021)*, Chiba, Japan, 2021.

[69] J F G Rojo, F Lluesma-Rodríguez, D F Sánchez, A P Sabogal, and G R Pérez. Validation of a Linear Motor for Hyperloop Applications using a 3-axis Static Test Bench. In *2021 13th International Symposium on Linear Drives for Industry Applications (LDIA)*, pages 1–4, 2021.

[70] A Veltman, P van der Hulst, M Jonker, and H Polinder. Tunnel-Vision on Economic Linear Propulsion? In *2019 12th International Symposium on Linear Drives for Industry Applications (LDIA)*, pages 1–6, 2019.

[71] Guang He, Jie Li, and Peng Cui. Decoupling control design for the module suspension control system in maglev train. *Mathematical Problems in Engineering*, 2015, jan 2015.

[72] R P Talukdar and S Talukdar. Dynamic Analysis of High-Speed MAGLEV Vehicle–Guideway System: An Approach in Block Diagram Environment. *Urban Rail Transit*, 2(2):71–84, 2016.

[73] Shu Guangwei, Reinhold Meisinger, and Shen Gang. Modeling and Simulation of Shanghai MAGLEV Train Transrapid with Random Track Irregularities. Technical report, 2007.

[74] D Tudor and M Paolone. Optimal Design of the Propulsion System of a Hyperloop Capsule. *IEEE Transactions on Transportation Electrification*, 5(4):1406–1418, 2019.

[75] Philippe Kirschen and Edward Burnell. Hyperloop System Optimization, 2021.

[76] P K Senecal and F Leach. Diversity in transportation: Why a mix of propulsion technologies is the way forward for the future fleet. *Results in Engineering*, 4, 2019.

[77] F Alkam, I Pereira, and T Lahmer. Qualitatively-improved identified parameters of prestressed concrete catenary poles using sensitivity-based Bayesian approach. *Results in Engineering*, 6, 2020.

[78] Moshe Givoni, Francis Ltd, and Sgm. Development and impact of the modern high-speed train: a review. *Transport Reviews*, 26:593–611, oct 2006.

[79] K Ehrendorfer, M Reiterer, and H Sockel. Numerical Investigation of the Micro Pressure Wave. In Burkhard Schulte-Werning, Rémi Grégoire, Antonio Malfatti, and Gerd Matschke, editors, *Transaero*, pages 321–341, Berlin, Heidelberg, 2002. Springer Berlin Heidelberg.

[80] Hyeok-bin Kown, Ki-hyeok Jang, Yu-shin Kim, Kwan-jung Yee, and Dong-ho Lee. Nose Shape Optimization of High-speed Train for Minimization of Tunnel Sonic Boom. *JSME International Journal Series C Mechanical Systems, Machine Elements and Manufacturing*, 44(3):890–899, 2001.

[81] Joong-Keun Choi and Kyu-Hong Kim. Effects of nose shape and tunnel cross-sectional area on aerodynamic drag of train traveling in tunnels. *Tunnelling and Underground Space Technology*, 41:62–73, 2014.

[82] Xiaohan Zhang, Yao Jiang, and Tian Li. Effect of Streamlined Nose Length on the Aerodynamic Performance of a 800 km/h Evacuated Tube Train. *Fluid Dynamics & Materials Processing*, 15:67–76, 2019.

[83] Yaoping Zhang. Numerical simulation and analysis of aerodynamic drag on a subsonic train in evacuated tube transportation. *Journal of Modern Transportation*, 20(1):44–48, 2012.

[84] Brijesh Pandey and Sujay Mukherjea. Aerodynamic Simulation of Evacuated Tube Transport Trains With Suction at Tail. *ASME International Mechanical Engineering Congress and Exposition, Proceedings (IMECE)*, 12, nov 2014.

[85] Tae Kyung Kim, Kyu Hong Kim, and Hyeok Bin Kwon. Aerodynamic characteristics of a tube train. *Journal of Wind Engineering and Industrial Aerodynamics*, 99(12):1187–1196, 2011.

[86] Tian Li, Xiaohan Zhang, Yao Jiang, and Weihua Zhang. Aerodynamic Design of a Subsonic Evacuated Tube Train System. *Fluid Dynamics & Materials Processing*, 15:121–130, 2019.

[87] Jae-Sung Oh, Taehak Kang, Seokgyun Ham, Kwan-Sup Lee, Yong-Jun Jang, Hong Ryou, and Jaiyoung Ryu. Numerical Analysis of Aerodynamic Characteristics of Hyperloop System. *Energies*, 12:518, feb 2019.

[88] Xuyong Chen, Lifeng Zhao, Jiaqing Ma, and Yuansen Liu. Aerodynamic simulation of evacuated tube maglev trains with different streamlined designs. *Journal of Modern Transportation*, 20(2):115–120, jun 2013.

[89] J. Liu, J. Zhang, and W. Zhang. Analysis of aerodynamic characteristics of high-speed trains in the evacuated tube. *Journal of Mechanical Engineering*, 49(22):137–143, 2013.

[90] Yi Yang, Haiyang Wang, Moble Benedict, and David Coleman. Aerodynamic Simulation of High-Speed Capsule in the Hyperloop System. In *35th AIAA Applied Aerodynamics Conference*, page 3741, Denver, CO, USA, jun 2017.

[91] Wenguang Jia, Kai Wang, Aiping Cheng, Xiangxin Kong, Xing Cao, and Qingling Li. Air flow and differential pressure characteristics in the vacuum tube transportation system based on pressure recycle ducts. *Vacuum*, 150:58–68, 2018.

[92] Shijie Bao, Xiao Hu, Jukun Wang, Tianhao Ma, Yingyu Rao, and Zigang Deng. Numerical study on the influence of initial ambient temperature on the aerodynamic heating in the tube train system. *Advances in Aerodynamics*, 2(1):28, 2020.

[93] Chia-Ren Chu, Ssu-Ying Chien, Chung-Yue Wang, and Tso-Ren Wu. Numerical simulation of two trains intersecting in a tunnel. *Tunnelling and Underground Space Technology*, 42:161–174, 2014.

[94] Joon-Hyung Kim and Joo-Hyun Rho. Pressure wave characteristics of a high-speed train in a tunnel according to the operating conditions. *Proceedings of the Institution of Mechanical Engineers, Part F: Journal of Rail and Rapid Transit*, 232(3):928–935, apr 2017.

[95] Peng Zhou, Jiye Zhang, Tian Li, and Weihua Zhang. Numerical study on wave phenomena produced by the super high-speed evacuated tube maglev train. *Journal of Wind Engineering and Industrial Aerodynamics*, 190:61–70, 2019.

[96] Jiqiang Niu, Yang Sui, Qiujun Yu, Xiaoling Cao, and Yanping Yuan. Numerical study on the impact of Mach number on the coupling effect of aerodynamic heating and aerodynamic pressure caused by a tube train. *Journal of Wind Engineering and Industrial Aerodynamics*, 190:100–111, 2019.

[97] SpaceX. Hyperloop Pod Competition, 2016.

[98] James Braun, Jorge Sousa, and Cem Pekardan. Aerodynamic Design and Analysis of the Hyperloop. *AIAA Journal*, 55(12):4053–4060, aug 2017.

[99] Max Opgenoord and Philip Caplan. Aerodynamic Design of the Hyperloop Concept. *AIAA Journal*, 56(11):4261–4270, jul 2018.

[100] Jerrey Chin, Justin Gray, Scott Jones, and Jeff Berton. Open-Source Conceptual Sizing Models for the Hyperloop Passenger Pod. In *56th AIAA/ASCE/AHS/ASC Structures, Structural Dynamics, and Materials Conference*, jan 2015.

[101] Maglev Board. Transrapid Maglev Shanghai.

[102] Rui Li and Mei Yuangui. Study on the Aerodynamic Performance of the High-Speed Train Head with Symmetrical and Asymmetric Nose Shape. *DEStech Transactions on Engineering and Technology Research*, nov 2017.

[103] Justin Morden, Hassan Hemida, and Christopher Baker. Comparison of RANS and detached eddy simulation results to wind-tunnel data for the surface pressures upon a class 43 high-speed train. *Journal of Fluids Engineering*, 137(4), apr 2015.

[104] Adif. Tunel de Guadarrama. Technical report, Adif, 2007.

[105] RENFE. AVE Serie 102 / 112, 2020.

[106] A. Kantrowitz and C. Donaldson. Preliminary Investigation of Supersonic Diffusers. Technical report, Advance Con dential Report L5D20, National Advisory Committee on Aeronautics, Langley Memorial Aeronautical Laboratory, Langley Field, Virginia, 1945.

[107] G A Bird. Molecular gas dynamics. *NASA STI/Recon Technical Report A*, 76:40225, jan 1976.

[108] V Lijo, H D Kim, and T Setoguchi. Analysis of Choked Viscous Flows through a Constant Area Duct. *Proceedings of the Institution of Mechanical Engineers, Part G: Journal of Aerospace Engineering*, 224(11):1151–1162, may 2010.

[109] A. H. Shapiro. *The dynamics and thermodynamics of compressible fluid flow*. Ronald Press, New York, 1953.

[110] V Avsarkisov, S Hoyas, M Oberlack, and J. P. García-Galache. Turbulent plane Couette flow at moderately high Reynolds number. *Journal of Fluid Mechanics*, 751:R1, 2014.

[111] Sergio Hoyas and Javier Jiménez. Scaling of the velocity fluctuations in turbulent channels up to Re_{tau} = 2003. *Physics of Fluids - PHYS FLUIDS*, 18, jan 2006.

[112] Sergio Gandía-Barberá, Sergio Hoyas, Martin Oberlack, and Stefanie Kraheberger. Letter: The link between the Reynolds shear stress and the large structures of turbulent Couette-Poiseuille flow. *Physics of Fluids*, 30:41702, apr 2018.

[113] E M Thurlow and J C Klewicki. Experimental study of turbulent Poiseuille-Couette flow. *Physics of Fluids*, 12(4):865–875, 2000.

[114] F D Hains. Stability of plane Couette-Poiseuille flow. *Physics of Fluids*, 10(9):2079–2080, 1967.

[115] L Klotz, G Lemoult, I Frontczak, L S Tuckerman, and J E Wesfreid. Couette-Poiseuille flow experiment with zero mean advection velocity: Subcritical transition to turbulence. *Physical Review Fluids*, 2(4), 2017.

[116] L Klotz, A M Pavlenko, and J E Wesfreid. Experimental measurements in plane Couette–Poiseuille flow: dynamics of the large- and small-scale flow. *Journal of Fluid Mechanics*, 912:A24, 2021.

[117] Sean Hu and Xiaolin Zhong. Linear stability of viscous supersonic plane Couette flow. *Physics of Fluids*, 10(3):709–729, 1998.

[118] Yuhua Zhu and Rolf Reitz. A 1-D gas dynamics code for subsonic and supersonic flows applied to predict EGR levels in a heavy-duty diesel engine. *International Journal of Vehicle Design*, 22, jan 1999.

[119] F Durst, S Ray, B Ünsal, and O A Bayoumi. The development lengths of laminar pipe and channel flows. *Journal of Fluids Engineering, Transactions of the ASME*, 127(6):1154–1160, 2005.

[120] Yoshiaki Miyazato, Shota Sakamoto, and Kazuyasu Matsuo. An Experiment on Choking Phenomena in Supersonic Fanno Flows. *Transactions of the Japan Society of Mechanical Engineers Series B*, 73:2393–2396, dec 2007.

[121] T Mullin. Experimental studies of transition to turbulence in a pipe. *Annual Review of Fluid Mechanics*, 43:1–24, 2011.

[122] Takahiro Ishida, Yohann Duguet, and Takahiro Tsukahara. Transitional structures in annular Poiseuille flow depending on radius ratio. *Journal of Fluid Mechanics*, 794:R2, 2016.

[123] Kohei Kunii, Takahiro Ishida, Yohann Duguet, and Takahiro Tsukahara. Laminar–turbulent coexistence in annular Couette flow. *Journal of Fluid Mechanics*, 879:579–603, oct 2019.

[124] S V Chandrasekhar. Annular Couette–Poiseuille flow and heat transfer of a power-law fluid – analytical solutions. *Journal of Non-Newtonian Fluid Mechanics*, 286, 2020.

[125] Matthew Maclean. Detailed Derivation of Fanno Flow Relationships. Technical report, SUNY University, Buffalo, 2013.

[126] Federico Lluesma-Rodríguez, Temoatzin González, and Sergio Hoyas. CFD simulation of a hyperloop capsule inside a closed environment. *Results in Engineering*, 9:100196, 2021.

[127] Klaus Hèunecke. *Jet engines : fundamentals of theory, design, and operation* . Motorbooks International, Osceola, WI, USA, 2005.

[128] Juan Manuel Rivero, Ezequiel González-Martínez, and Manuel Rodríguez-Fernández. Description of the flow equations around a high speed train inside a tunnel. *Journal of Wind Engineering and Industrial Aerodynamics*, 172:212–229, 2018.

[129] Richard H Byrd, Mary E Hribar, and Jorge Nocedal. An Interior Point Algorithm for Large-Scale Nonlinear Programming. *SIAM Journal on Optimization*, 9(4):877–900, 1999.

[130] Ajay Misra. Evolution of Fundamental Technologies for Future Electrified Aircraft. In *Electric and Hybrid Aerospace Technology Symposium*, Cologne, Germany, 2018. NASA Glenn Research Center.

[131] Eckert Fritz, Johannes Kluhspies, Roland Kircher, Michael Witt, and Laurence E Blow. *Energy Consumption of Track-based High-speed Transportation Systems*. 2022.

[132] Jacobs Consultancy Canada Inc. Canadian Aviation and Greenhouse Gases. Technical report, Jacobs Consultancy Canada Inc, Ottawa, 2007.

[133] Stuart W Churchill and Humbert H S Chu. Correlating equations for laminar and turbulent free convection from a horizontal cylinder. *International Journal of Heat and Mass Transfer*, 18(9):1049–1053, 1975.

[134] NASA. Power Data Access Viewer, 2022.

[135] J L Montañés. *Actuaciones, diseño y ensayos de aerorreactores*. Escuela Técnica Superior de Ingeniería Aeronáutica y del Espacio, Madrid, 2016.

[136] Lewis F. Moody. Friction Factors for Pipe Flow. *Transactions of American Society Mechanical Engineers*, 66(8):671–684, 1944.

[137] S.W. Churchill. Friction factor equation spans all fluid-flow regimes. *Chemical Engineering*, 84(24):91–92, 1977.

Appendix A

Fanno model

A.1 Development of ODEs

In this appendix, the Fanno ODE system from the original Fanno differential equation (3.27) is developed. The equation is repeated for convenience:

$$\frac{\mathrm{d}p}{\frac{\gamma}{2}pM^2} + 2u\frac{\mathrm{d}u}{u^2} = g\left(u\right)\mathrm{d}x. \tag{A.1}$$

The equation is reordered as follows:

$$\frac{2}{\gamma M^2}\frac{\mathrm{d}p}{p} + \frac{\mathrm{d}u^2}{u^2} = g\left(u\right)\mathrm{d}x. \tag{A.2}$$

This relation from [125] is taken into consideration:

$$\frac{\mathrm{d}p}{p} = -\left[\frac{1+\left(\gamma-1\right)M^2}{2}\right]\frac{\mathrm{d}u^2}{u^2}, \tag{A.3}$$

to reexpress equation (A.2) as:

$$\frac{-2}{\gamma M^2}\left[\frac{1+\left(\gamma-1\right)M^2}{2}\right]\frac{\mathrm{d}u^2}{u^2} + \frac{\mathrm{d}u^2}{u^2} = g\left(u\right)\mathrm{d}x. \tag{A.4}$$

Reordering:

$$\frac{\mathrm{d}u^2}{\mathrm{d}x} = \frac{\gamma M^2}{M^2-1}u^2 g\left(u\right). \tag{A.5}$$

For the temperature equation, starting from the total temperature definition:

$$T_t = T + \frac{u^2}{2c_p}, \tag{A.6}$$

and taking the derivative with respect to x:

$$\frac{\mathrm{d}T_t}{\mathrm{d}x} = \frac{\mathrm{d}T}{\mathrm{d}x} + \frac{1}{2c_p}\frac{\mathrm{d}u^2}{\mathrm{d}x}. \tag{A.7}$$

As the total temperature is constant $\mathrm{d}T_t = 0$:

$$\frac{\mathrm{d}T}{\mathrm{d}x} = \frac{-1}{2c_p}\frac{\mathrm{d}u^2}{\mathrm{d}x}. \tag{A.8}$$

Taking equations (A.5) and (A.8) the ODE system is obtained:

$$\left\{ \begin{array}{c} \frac{\mathrm{d}u^2}{\mathrm{d}x} \\ \frac{\mathrm{d}T}{\mathrm{d}x} \end{array} \right\} = \left\{ \begin{array}{c} 1 \\ \frac{-1}{2c_p} \end{array} \right\} \frac{\gamma M^2}{M^2 - 1} u^2 g\left(u\right). \tag{A.9}$$

And, if $M^2 = u^2/\left(\gamma RT\right)$ is taken into account:

$$\left\{ \begin{array}{c} \frac{\mathrm{d}u^2}{\mathrm{d}x} \\ \frac{\mathrm{d}T}{\mathrm{d}x} \end{array} \right\} = \left\{ \begin{array}{c} 1 \\ \frac{-1}{2c_p} \end{array} \right\} \frac{\gamma}{1 - \frac{\gamma RT}{u^2}} u^2 g\left(u\right). \tag{A.10}$$

Now, the system is reformulated to use M and T as dependent variables. The differential equation $\mathrm{d}M/\mathrm{d}x$ is obtained from [125]:

$$\frac{M^2 - 1}{\gamma M^2}(1 + \frac{\gamma - 1}{2}M^2)^{-1}\frac{2M}{M^2}\frac{\mathrm{d}M}{\mathrm{d}x} = g\left(u\right). \tag{A.11}$$

From this equation, $\mathrm{d}M/\mathrm{d}x$ is obtained directly:

$$\frac{\mathrm{d}M}{\mathrm{d}x} = \frac{1}{2}\frac{\gamma M^2}{M^2 - 1}\left(1 + \frac{\gamma - 1}{2}M^2\right) M g\left(u\right). \tag{A.12}$$

Now, taking the Mach definition:

$$u^2 = M^2 \gamma RT. \tag{A.13}$$

Differentiating:

$$\mathrm{d}u^2 = 2\gamma RTM\mathrm{d}M + \gamma RM^2\mathrm{d}T, \tag{A.14}$$

$$\frac{\mathrm{d}u^2}{u^2} = 2\frac{\mathrm{d}M}{M} + \frac{\mathrm{d}T}{T}. \tag{A.15}$$

Using equation (A.12) and (A.5):

$$\frac{\gamma M^2}{M^2 - 1} g\left(u\right)\mathrm{d}x = \frac{\gamma M^2}{M^2 - 1}\left(1 + \frac{\gamma - 1}{2}M^2\right) g\left(u\right)\mathrm{d}x + \frac{\mathrm{d}T}{T}. \tag{A.16}$$

Now $\mathrm{d}T/\mathrm{d}x$ can be obtained:

$$\frac{\mathrm{d}T}{\mathrm{d}x} = -\frac{\gamma M^2}{M^2 - 1}\frac{\gamma - 1}{2}M^2 T g\left(u\right). \tag{A.17}$$

Finally, with equations (A.12) and (A.17) the following system can be obtained:

$$\frac{\mathrm{d}M}{\mathrm{d}x} = \frac{1}{2}\frac{\gamma M^2}{M^2 - 1}\left(1 + \frac{\gamma - 1}{2}M^2\right) M g\left(u\right), \tag{A.18}$$

$$\frac{\mathrm{d}T}{\mathrm{d}x} = -\frac{\gamma M^2}{M^2 - 1}\frac{\gamma - 1}{2}M^2 T g\left(u\right). \tag{A.19}$$

This system can be reexpressed to use M as an independent variable, which is quite useful for computing the critical length:

$$\begin{Bmatrix} \frac{\mathrm{d}x}{\mathrm{d}M} \\ \frac{\mathrm{d}T}{\mathrm{d}M} \end{Bmatrix} = \begin{Bmatrix} \frac{2\left(M^2-1\right)}{\gamma M^3 g(u)} \\ (1-\gamma)\, MT \end{Bmatrix} \left(1 + \frac{\gamma-1}{2} M^2\right)^{-1}. \tag{A.20}$$

A.2 Equations for concentric circles

This section evaluates the generic Fanno expression for concentric circles, as is the case for the present problem.

Assuming the areas are concentric circles of diameters D_{int} and D_{ext}:

$$A_{int} = \pi D_{int}^2, \tag{A.21}$$
$$A_{ext} = \pi D_{ext}^2, \tag{A.22}$$
$$C_{int} = \pi D_{int}, \tag{A.23}$$
$$C_{ext} = \pi D_{ext}. \tag{A.24}$$

Then, the cross-sectional area A is the following:

$$A = A_{ext} - A_{int} = \frac{\pi}{4}\left(D_{ext}^2 - D_{int}^2\right), \tag{A.25}$$

and the hydraulic diameter D_h:

$$D_h = \frac{4A}{C_{int} + C_{ext}} = D_{ext} - D_{int}. \tag{A.26}$$

The internal and external hydraulic diameters:

$$D_{h,int} = \frac{D_{ext}^2 - D_{int}^2}{D_{int}}, \tag{A.27}$$
$$D_{h,ext} = \frac{D_{ext}^2 - D_{int}^2}{D_{ext}}. \tag{A.28}$$

By his part, the blockage ratio β is defined as follows:

$$\beta = \frac{A_{int}}{A_{ext}} = \left(\frac{D_{int}}{D_{ext}}\right)^2. \tag{A.29}$$

The equation that relates the equivalent diameter with the hydraulic diameter (3.19) can be expressed for a circle:

$$\frac{D_{eq}}{D_h} = \frac{D_{ext} + D_{int}}{\left(1 - \frac{u_w}{u}\right)^2 D_{ext} + D_{int}}. \tag{A.30}$$

And in terms of the blockage ratio:

$$\frac{D_{eq}}{D_h} = \frac{1 + \sqrt{\beta}}{\left(1 - \frac{u_w}{u}\right)^2 + \sqrt{\beta}}. \tag{A.31}$$

A.3 Friction factor

The Fanno flow makes use of the friction factor f. This section explains how this number is obtained.

As stated in section 3.2.2, the use of the friction factor f instead of the friction coefficient C_f is more practical. This friction factor is also called the Fanning friction factor, named after the American engineer John Fanning (1837–1911) [136]. The relation between these parameters is $C_f = f/4$, as stated in [125]:

$$C_f = f/4. \tag{A.32}$$

The friction factor used in the present work is the one presented by Moody [136] for pipes, also known as the Colebrook equation:

$$\frac{1}{\sqrt{f}} = -2\log_{10}\left(\frac{\epsilon/D_h}{3.7} + \frac{2.51}{Re_{D_h}\sqrt{f}}\right). \tag{A.33}$$

This equation can be solved iteratively or graphically employing the Moody diagram. Another way is to use the Churchill equation [137], at least to initialise the iterative calculus:

$$A = \left[-2.457\log\left(\left(\frac{7}{Re_{D_h}}\right)^{0.9} + \frac{\epsilon/D_h}{3.7}\right)\right]^{16}, \tag{A.34}$$

$$B = \left(\frac{37.530}{Re_{D_h}}\right)^{16}, \tag{A.35}$$

$$f = 8\left[\left(\frac{8}{Re_{D_h}}\right)^{12} + \frac{1}{(A+B)^{1.5}}\right]^{\frac{1}{12}}. \tag{A.36}$$

Moody also states in his paper that the equation can still be used for a generic form substituting the diameter with the hydraulic diameter.

A.4 Fanno flow solution

The detail of the Fanno flow is given in chapter 3. This section describes three different ways of solving the Fanno model. Due to the computational cost, the *analytic* approach is used instead of the *numeric*. All the details are given there. However, only the practical part of the simulator is reproduced in this section.

The Fanno flow is applied to solve the external channel and the internal duct. To be more generic, number 1 is used as the inlet and 2 as the outlet. If specified the stations used in the models:

- For the real-scale model the channel goes from 13 to 15 and the duct from 31 to 4.
- For the middle-scale model the channel goes from 12 to 18 and the duct from 31 to 4.

The input parameters are the conditions in station 1: p_{1t}, T_{1t}, and M_1. The length and equivalent diameter is also required. For the duct, as it has only one wall, the equivalent diameter is equal to the hydraulic diameter:

$$D_{eq,duct} = D_{h,duct} = \frac{4A_{duct}}{P_{duct}} = D_{duct}. \tag{A.37}$$

Note that the expression has been evaluated on a circular duct.

For the channel, modelled as a concentric annular flow with different speeds on each wall, the formula is the following:

$$K_{Fanno} = \left(1 - \frac{u_0}{u_1}\right)^2 \frac{D_0}{D_{pod}}, \tag{A.38}$$

$$D_{eq,ch} = \frac{D_0^2 - D_{pod}^2}{D_{pod}\left(K_{Fanno} + 1\right)}. \tag{A.39}$$

Note that u_0 refers to the station 0 velocity equivalent to the external wall speed or capsule speed.

Then, the Reynolds number is computed as:

$$Re_1 = \frac{D_h}{\mu}\sqrt{\frac{\gamma}{R}}\frac{p_{1t}}{\sqrt{T_{1t}}}M_1\left(1 + \frac{\gamma - 1}{2}M_1^2\right)^{-\frac{\gamma+1}{2(\gamma-1)}}. \tag{A.40}$$

Using the Reynolds number, the Colebrook factor is also obtained:

$$\frac{1}{f} = \left[-2\log_{10}\left(\frac{\varepsilon}{3.7D_h} + \frac{2.51}{Re\sqrt{f}}\right)\right]^2. \tag{A.41}$$

After that, the critical length is determined:

$$L_{crit} = \frac{D_{eq}}{f}\left[\frac{1 - M_2^2}{\gamma M_2^2} + \frac{\gamma + 1}{2\gamma}\log\left(\frac{\frac{\gamma+1}{2}M_2^2}{1 + \frac{\gamma-1}{2}M_2^2}\right)\right]. \tag{A.42}$$

To solve the Fanno flow, the following equation is used:

$$\frac{fL}{D_{eq}} = \left[\frac{\gamma + 1}{2\gamma}\log\left(\frac{1}{M_2^{-2} + \frac{\gamma-1}{2}}\right) - \frac{1}{\gamma M_2^2}\right] - \left[\frac{\gamma + 1}{2\gamma}\log\left(\frac{1}{M_1^{-2} + \frac{\gamma-1}{2}}\right) - \frac{1}{\gamma M_1^2}\right]. \tag{A.43}$$

Three different cases are solved in this code:

- M_1 is known and M_2 is computed.
- M_2 is known and M_1 is computed. Note that this case is iterative for the external channel, as the equivalent diameter depends on the speed at station 1 u_1, which implies that the thermodynamic conditions in 1 should already be known.

- The case is blocked and M_2 is set to 1, obtaining M_1. This case has the same iterative implication as the previous point.

If $L < L_{crit}$, the input is M_1 and the output is M_2, while if not, M_2 is set to 1 and M_1 is computed. There are some cases in which M_2 is also imposed to some value lower than 1 to compute M_1.

The other output obtained from the Fanno solution is the total pressure ratio between the inlet and the outlet:

$$\pi_{12} = \frac{M_1}{M_2} \left(\frac{1 + \frac{\gamma-1}{2} M_2^2}{1 + \frac{\gamma-1}{2} M_1^2} \right)^{\frac{\gamma+1}{2(\gamma-1)}} . \tag{A.44}$$

Appendix B

Real-scale model

B.1 Compressible continuity solver

In this section the solution for the Mach on the continuity equation is given for a generic station using the total temperature, mass flow and static pressure (section B.1.1) or the total pressure (section B.1.2). They are only valid for subsonic flow.

B.1.1 Using static pressure

In some cases, the continuity is solved using total temperature and static pressure:

$$\dot{m} = \rho A u = AM\sqrt{\frac{\gamma}{R}}\frac{p}{\sqrt{T_t}}\sqrt{1+\frac{\gamma+1}{2}M^2}. \tag{B.1}$$

This equation has an analytic solution for the Mach number:

$$M = \sqrt{\frac{\sqrt{1+2\left(\gamma-1\right)\left(\frac{\dot{m}}{Ap}\right)^2 T_t\frac{R}{\gamma}}-1}{\gamma-1}}. \tag{B.2}$$

B.1.2 Using total pressure

The continuity equation solves the Mach in different stages, for that reason, is highly important to have an efficient method to compute it. The equation to solve is the following:

$$\dot{m} = \frac{Ap_t}{T_t}\sqrt{\frac{\gamma}{R}}M\left(1+\frac{\gamma+1}{2}M^2\right)^{-\frac{\gamma+1}{2(\gamma-1)}}. \tag{B.3}$$

Performing the following identification:

$$K \equiv \frac{\dot{m}\sqrt{T_t}}{Ap_t}\sqrt{\frac{R}{\gamma}} = M\left(1+\frac{\gamma+1}{2}M^2\right)^{-\frac{\gamma+1}{2(\gamma-1)}}, \tag{B.4}$$

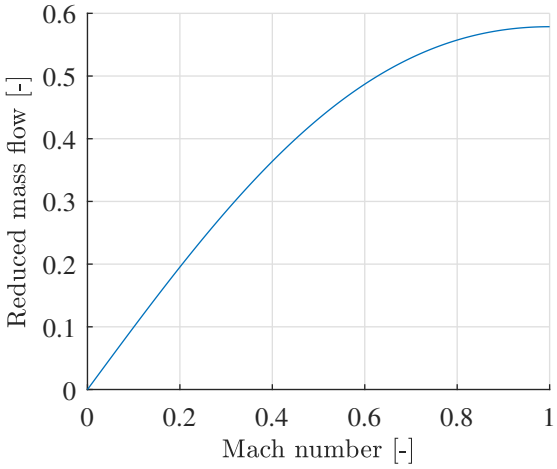

Figure B.1: Reduced mass flow with respect to the Mach number.

note that K, or the reduced mass flow, is only a function of M and γ, so, $K = K(M, \gamma)$. For the air, this magnitude is represented in figure B.1.

The function is increasing in all the range, except at the point where Mach equals 1. Also, this function has these mathematical characteristics:

- $K(0, \gamma) = 0$,
- $K(1, \gamma) = \left(\frac{\gamma+1}{2}\right)^{-\frac{\gamma+1}{2(\gamma-1)}} \equiv C(\gamma)$,
- $\left.\frac{\partial K(M,\gamma)}{\partial M}\right|_{M=1} = 0$.

A second-order polynomial fitting can be proposed to fit the reduced mass flow function, as seen in figure B.1, where the curve has a parabolic trend. The polynomial is the following:

$$K_{fit}(M, \gamma) = a(\gamma) M^2 + b(\gamma) M + c(\gamma). \tag{B.5}$$

Using the three proposed restrictions, the parameters of the parabola can be obtained, leading to this solution:

$$K_{fit}(M, \gamma) = C(M) M (2 - M). \tag{B.6}$$

The comparison between the fitted curve from equation (B.6) and the analytic solution from equation (B.4) is presented in figure B.2.

Equation (B.6) can be solved to obtain the Mach number analytically:

$$M(K, \gamma) = 1 - \sqrt{1 - \frac{K}{C(\gamma)}}. \tag{B.7}$$

With that in mind, the Mach obtained numerically solving equation (B.4), M_{num}, and analytically from equation (B.7) M_{fit} are compared, obtaining the absolute error:

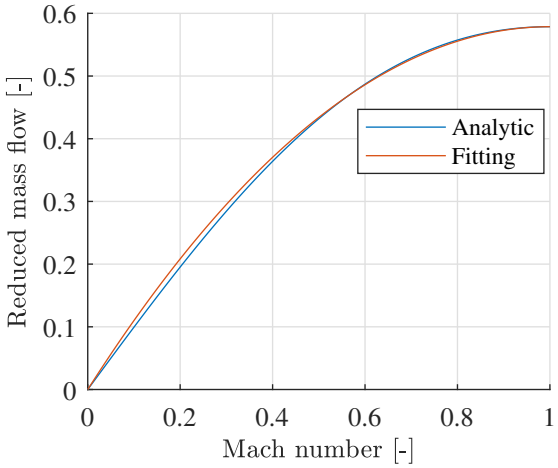

Figure B.2: Comparison between the analytical and the fitted reduced mass flow function.

$$\varepsilon_{Mach} = |M_{num} - M_{fit}|\,, \tag{B.8}$$

The error is represented in figure B.3. As can be seen, it is quite low, being the maximum deviation of 0.0142 in Mach number, a 1% of the domain of the function.

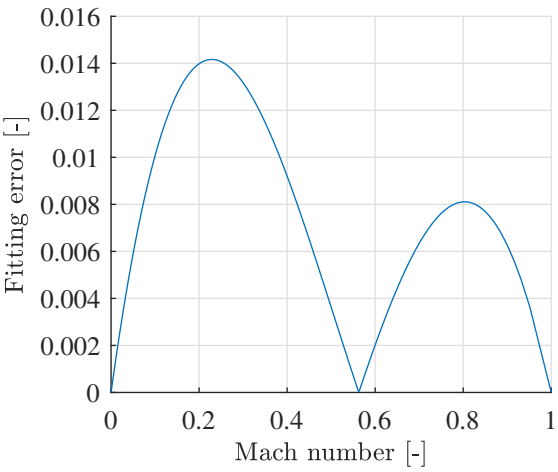

Figure B.3: Error between the Mach number from the analytical and numerical solution.

Lastly, it is explained how the Mach is solved numerically. An iterative method is used, assuming a certain Mach as an initial condition and solving for the following term from equation (B.4):

$$M = K\left(1 + \frac{\gamma+1}{2}M^2\right)^{\frac{\gamma+1}{2(\gamma-1)}}. \tag{B.9}$$

Until the error between the Mach plugged into the right-hand side, and the one obtained is below a certain tolerance, the equation is iterated.

Lastly, the process followed to solve for a Mach according to a specific reduced mass flow is obtaining the initial condition with the analytic approximation, instead of guessing this value. Then, the equation is iterated until the tolerance is reached. This way, the number of iterations is minimised.

B.2 Analytic solution for the chocked channel

This section has been removed due to the NDA signed between the parts Sergio Hoyas and Zeleros Global SL.

B.3 Cabin dimensions in *D-duct*

From the sketch in figure B.4, the cross area of the duct and the cabin must be computed to know how much space is left for the different components (passengers, air, batteries...). The figure has several new parameters represented. The equations that define them are described below.

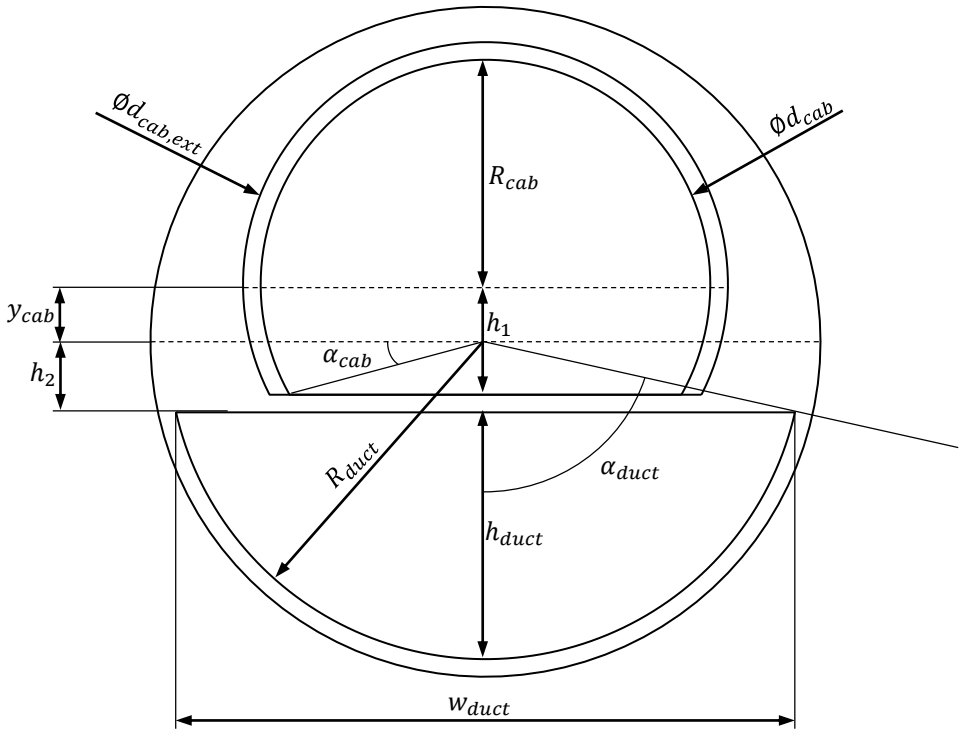

Figure B.4: Dimensions used to make advanced calculus.

For the cabin:

$$R_{cab} = \frac{d_{cab}}{2}, \tag{B.10}$$

$$R_{cab,ext} = \frac{d_{cab,ext}}{2}, \tag{B.11}$$

$$h_1 = h_{cab} - R_{cab}, \tag{B.12}$$

$$\alpha_{cab} = \text{asin}\left(\frac{h_1}{R_{cab}}\right), \tag{B.13}$$

$$\alpha_{cab,ext} = \text{asin}\left(\frac{h_1}{R_{cab,ext}}\right), \tag{B.14}$$

$$y_{cab} = \frac{d_{pod}}{2} - \delta_{lev} - R_{cab,ext}\alpha_{tube} = \text{acos}\left(\frac{R_{tube} - h_{tube}}{R_{tube}}\right), \tag{B.15}$$

$$w_{cab,ext} = 2\cos\left(\alpha_{cab,ext}\right) R_{cab,ext}. \tag{B.16}$$

For the duct:

$$h_2 = \frac{d_{pod}}{2} - h_{duct}, \tag{B.17}$$

$$h_{duct} = d_{pod} - \delta_{bottom} - \delta_{lev} - R_{cab,ext} - h_1 - \delta_{floor}, \tag{B.18}$$

$$R_{duct} = R_{pod} - \delta_{bottom}, \tag{B.19}$$

$$w_{duct} = 2R_{duct}\sin\left(\alpha_{duct}\right) \tag{B.20}$$

The area of the duct is computed as follows:

$$A_{duct} = \alpha_{duct}R_{duct}^2 - \frac{1}{2}w_{duct}h_2. \tag{B.21}$$

Its perimeter is obtained from:

$$P_{duct} = 2\alpha_{duct}R_{duct} + w_{duct}. \tag{B.22}$$

Then, the hydraulic diameter can also be obtained:

$$D_h = \frac{4A_{duct}}{P_{duct}}. \tag{B.23}$$

Finally, the area left to the batteries, which corresponds to the external cross area of the passengers' cabin, is computed as follows:

$$A_{bat} = \left(\alpha_{cab,ext} + \frac{\pi}{2}\right) R_{cab,ext}^2 + \frac{1}{2}w_{cab,ext}h_1. \tag{B.24}$$

B.4 Computation of η_f and η_r

The parameter that defines the efficiency between stations 1 and 13 is η_f, presented in equation (4.11). The equivalent between stations 15 and 19 is η_r, defined in equation (4.48).

These are extremely important for the solution provided by the present code, especially the last one.

The value for these parameters is obtained from the CFD simulations performed in chapter 2. As those simulations were performed at 500 km/h and 700 km/h, two different curves can be obtained, function of the blockage ratio. These are represented in figure B.5 for both parameters.

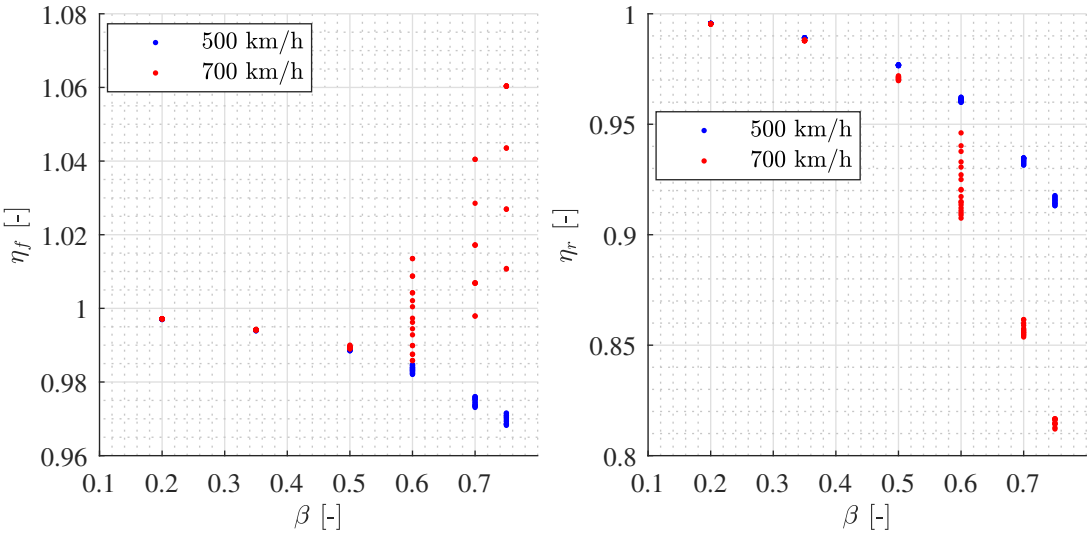

Figure B.5: Evolution of η_f and η_r with respect to the speed and blockage ratio.

At some points, there is a significant dispersion due to other factors that may affect the simulation not represented as independent variables, for instance, the performance of the compressor and the turbine.

It is important to highlight that the trends differ from one variable to the other. As for η_f, the value is close to 1 in the whole range, and it can be even higher due to the acceleration of the flow in a convergent geometry. As no clear trend is shown for this parameter, a constant value of 0.99 is chosen.

For η_r, the dependency with speed is more evident: the higher the speed, the lower the efficiency. Even the dependency with the blockage ratio is clearer, as it has a parabolic evolution. Thanks to this dependency, a curve fitting is performed for η_r for the two different speeds and BR to consider these effects on the simulator. The fitted curves are the following:

$$\eta_r = \begin{cases} \frac{-15.49\beta+16.84}{\beta^2-15.67\beta+16.90}, & u = 500\,\text{km/h}, \\ -0.586\beta^4 - 0.0276\beta^3 + 0.0430\beta^2 - 0.0135\beta + 0.998, & u = 700\,\text{km/h}, \end{cases} \tag{B.25}$$

while for other speeds different than the simulated ones, a linear fitting with a maximum value in 1 is performed.

The reason why the larger the blockage ratio the lower the efficiency is conceptualised in figure B.7. On the one hand, the higher the BR, the more momentum the flow has at

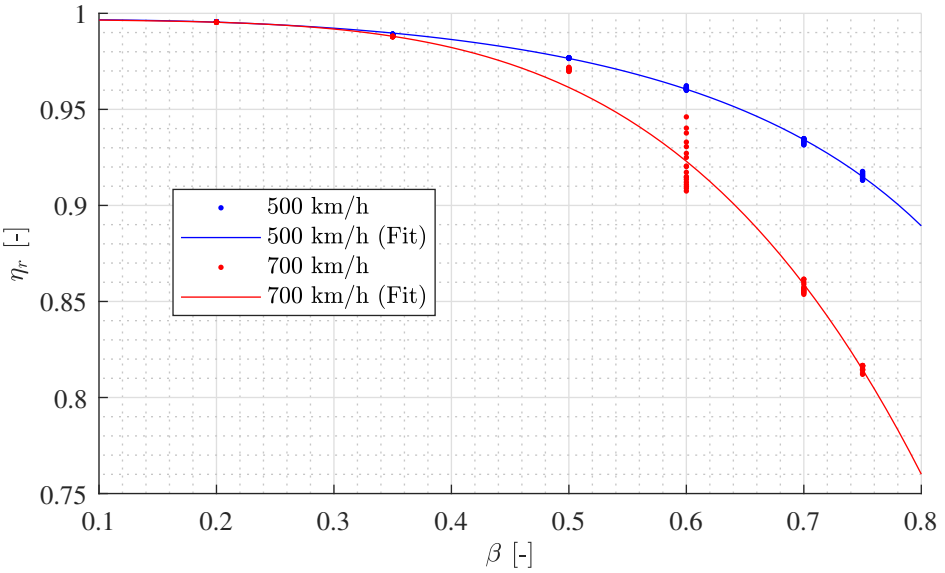

Figure B.6: Comparison between the CFD values for η_r and the fitted ones.

the outlet of the Fanno flow, leading to more detachment in the divergent region. On the other hand, the lower the blockage ratio, the larger the radial space between the walls of the vehicle and the tube, which means that the influence of a local separation on the capsule is lower compared to the whole area covered by the station 19.

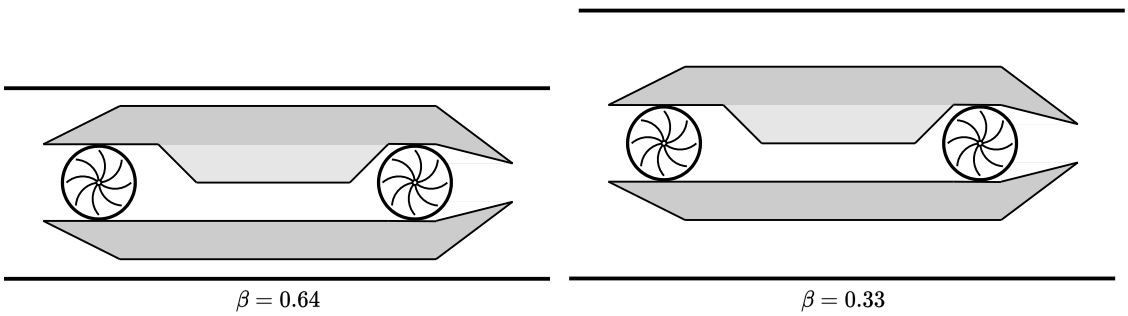

Figure B.7: Hyperloop concept for two different blockage ratios.

B.5 Optimisation plots

This section includes the plots from the optimisation process conducted for the real-scale model in chapter 4. These figures represent the total power with respect to the required power for different cabin diameters and compressor mass flows.

In these figures, the grey points correspond to the values not belonging to the mass flow represented in each plot. For convenience, only one in six points is represented.

B.5.1 Z50 and 5-meter tube

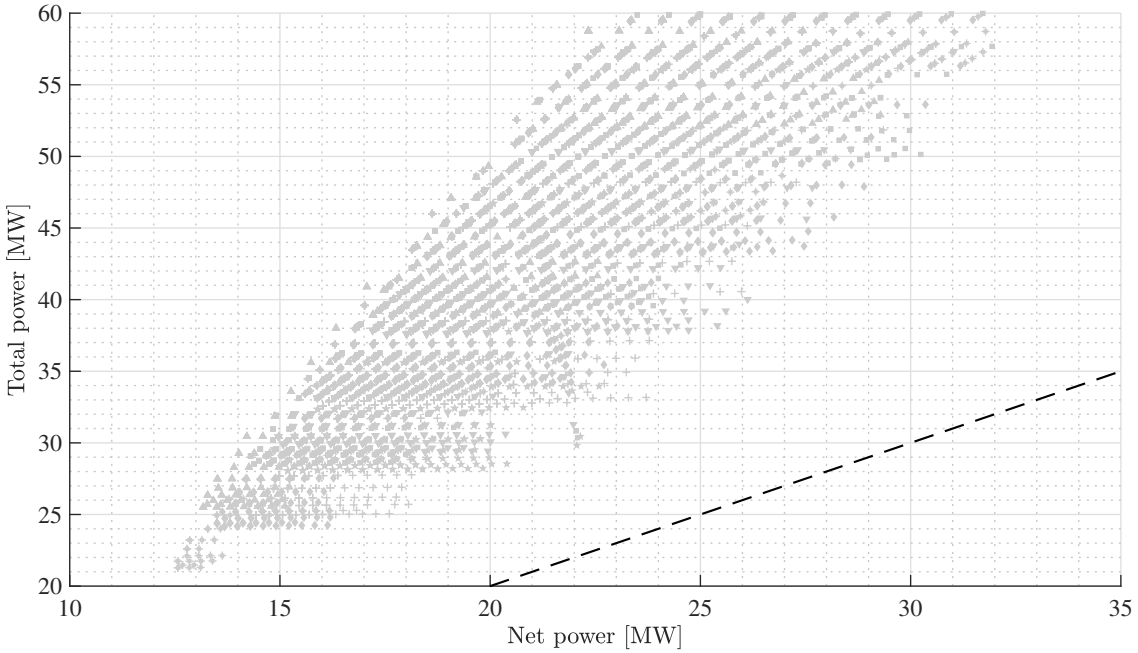

Figure B.8: Total versus required power for different cabin dimensions and compressor mass flows. Z50, $D_{tube} = 5$ m and $\dot{m}_{\pi} = 130$ kg/s.

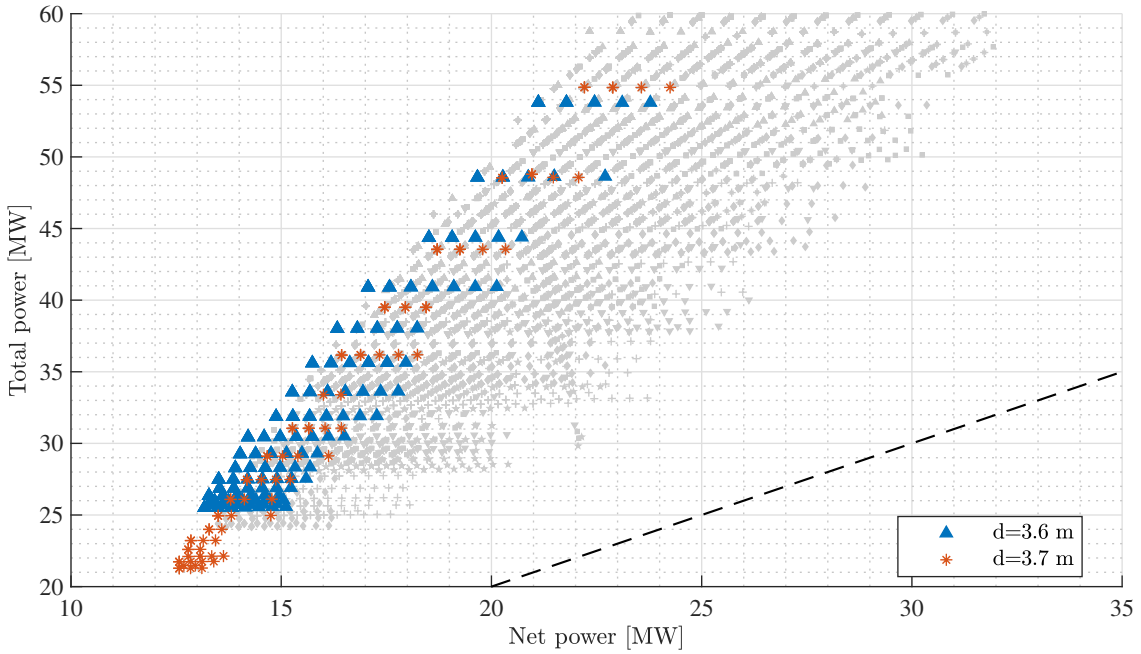

Figure B.9: Total versus required power for different cabin dimensions and compressor mass flows. Z50, $D_{tube} = 5$ m and $\dot{m}_{\pi} = 165$ kg/s.

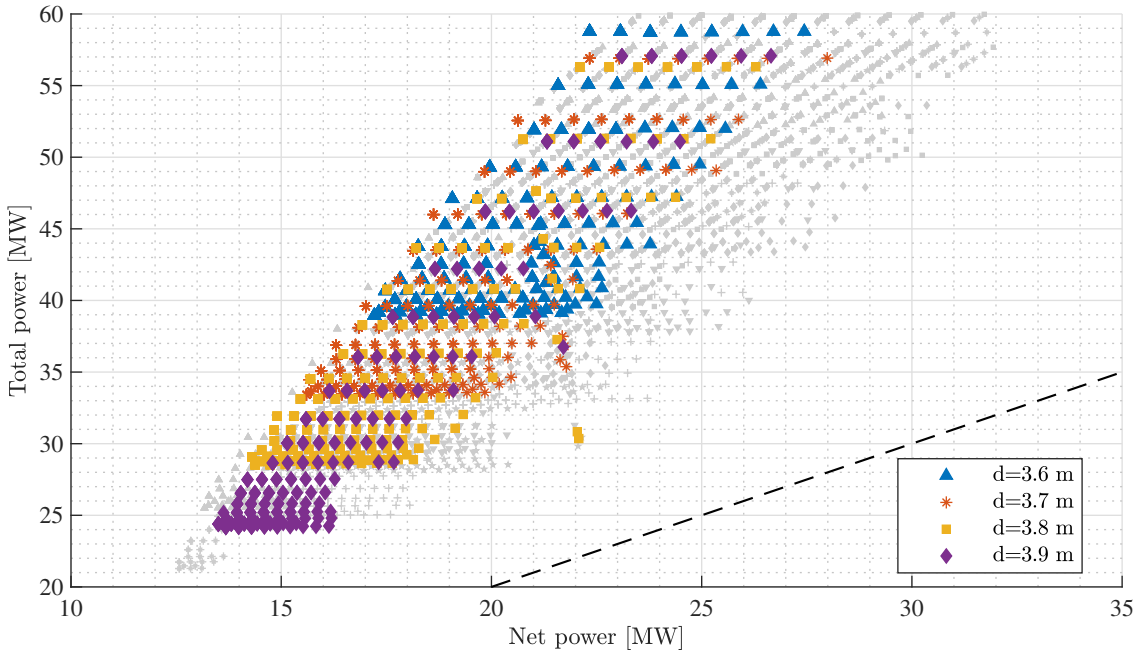

Figure B.10: Total versus required power for different cabin dimensions and compressor mass flows. Z50, $D_{tube} = 5$ m and $\dot{m}_{\pi} = 200$ kg/s.

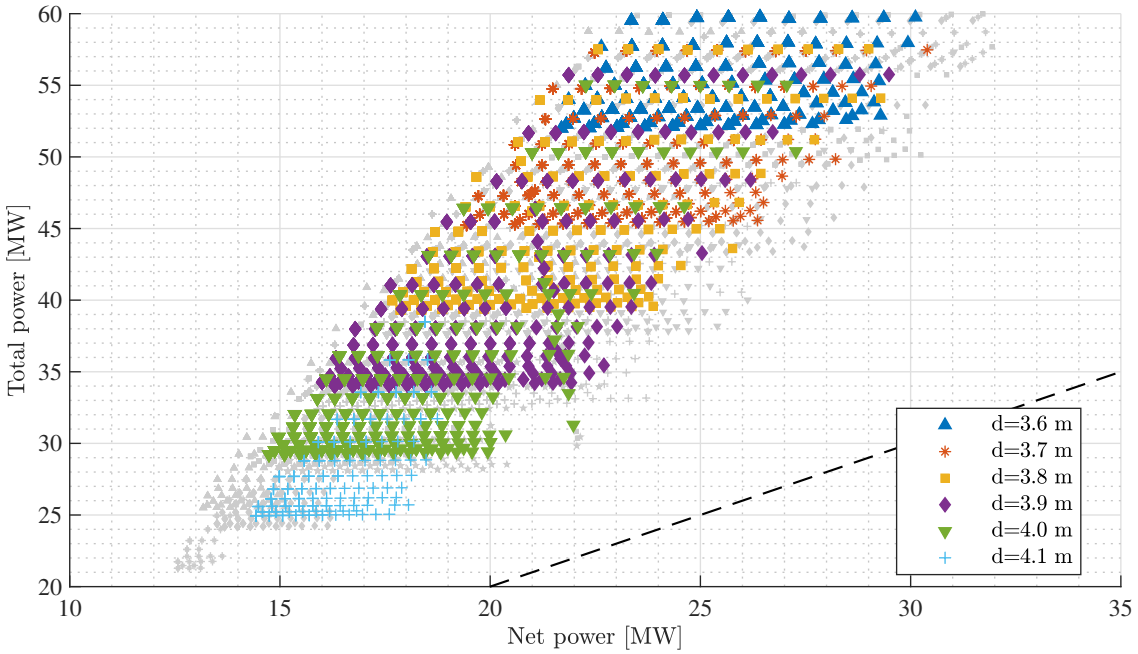

Figure B.11: Total versus required power for different cabin dimensions and compressor mass flows. Z50, $D_{tube} = 5$ m and $\dot{m}_{\pi} = 230$ kg/s.

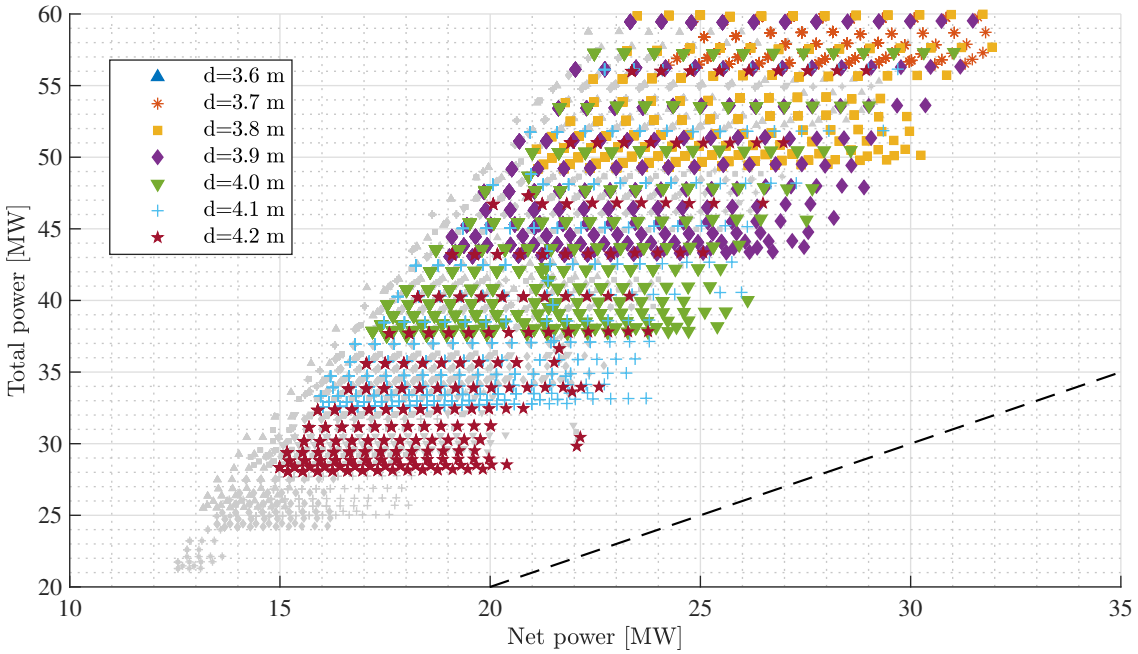

Figure B.12: Total versus required power for different cabin dimensions and compressor mass flows. Z50, $D_{tube} = 5$ m and $\dot{m}_{\pi} = 255$ kg/s.

B.5.2 Z50 and 6-meter tube

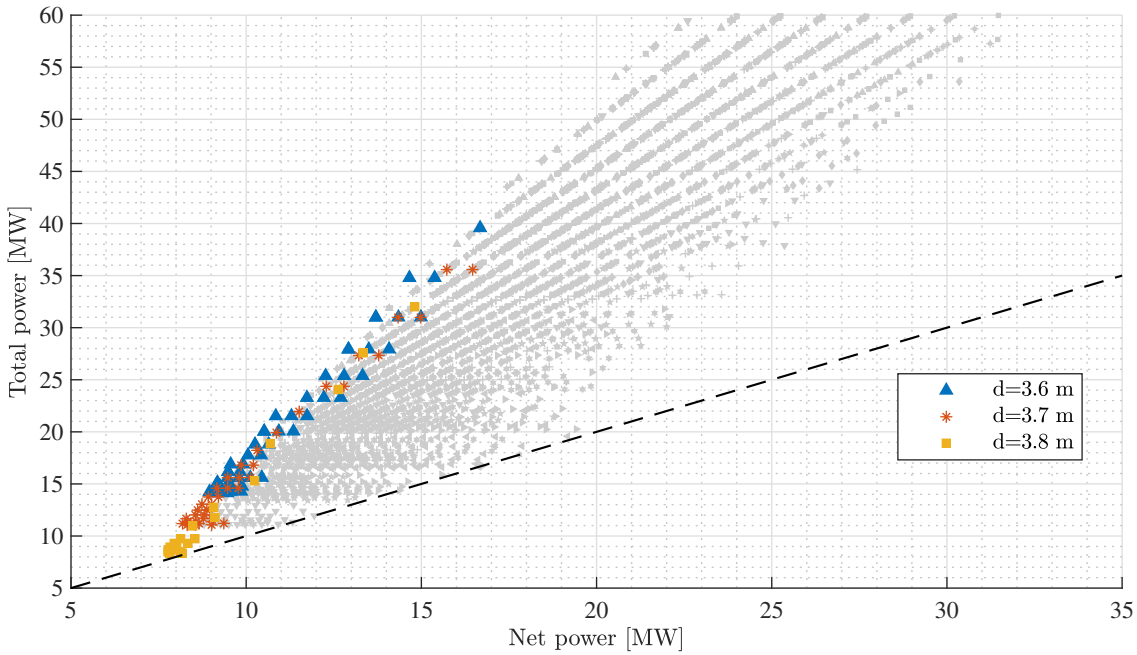

Figure B.13: Total versus required power for different cabin dimensions and compressor mass flows. Z50, $D_{tube} = 6$ m and $\dot{m}_{\pi} = 130$ kg/s.

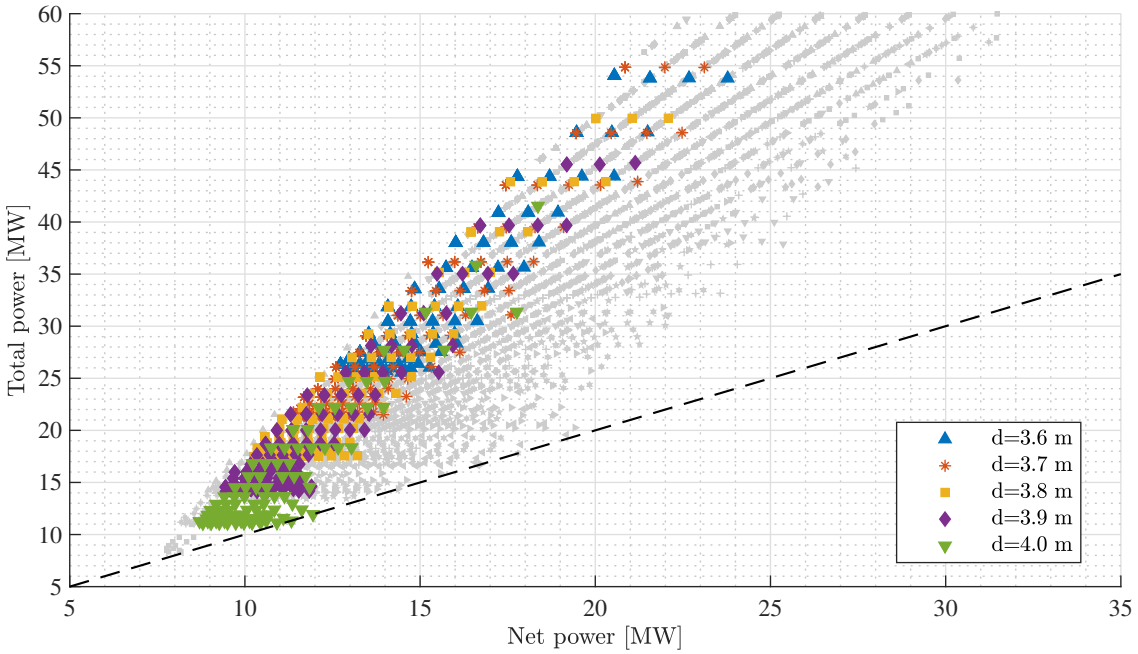

Figure B.14: Total versus required power for different cabin dimensions and compressor mass flows. Z50, $D_{tube} = 6$ m and $\dot{m}_{\pi} = 165$ kg/s.

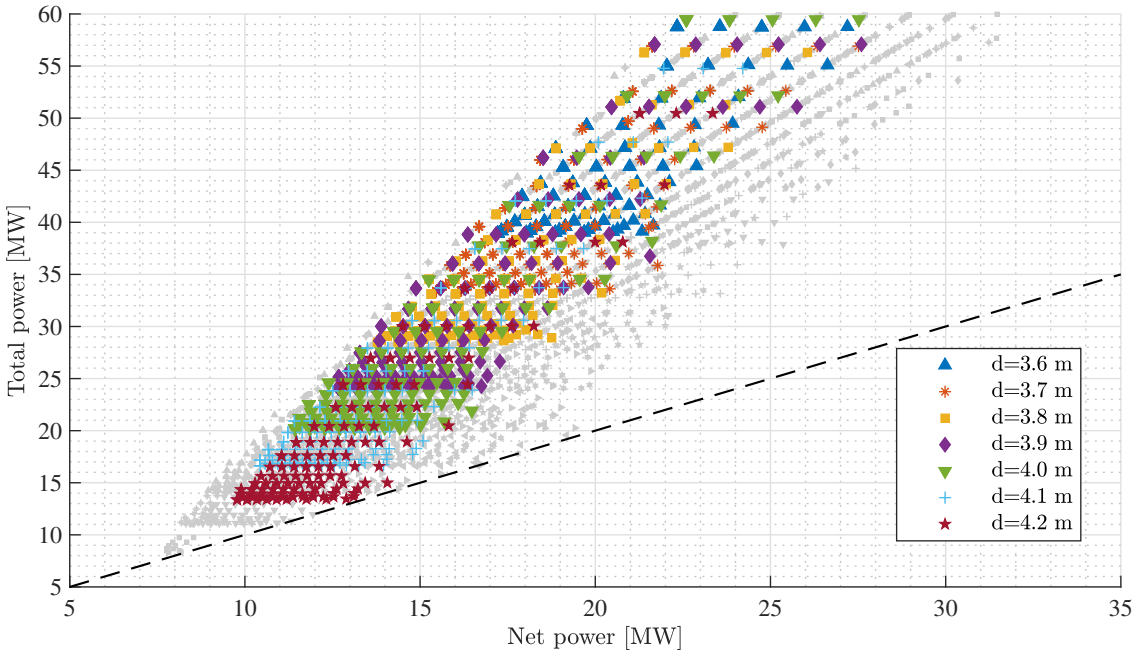

Figure B.15: Total versus required power for different cabin dimensions and compressor mass flows. Z50, $D_{tube} = 6$ m and $\dot{m}_{\pi} = 200$ kg/s.

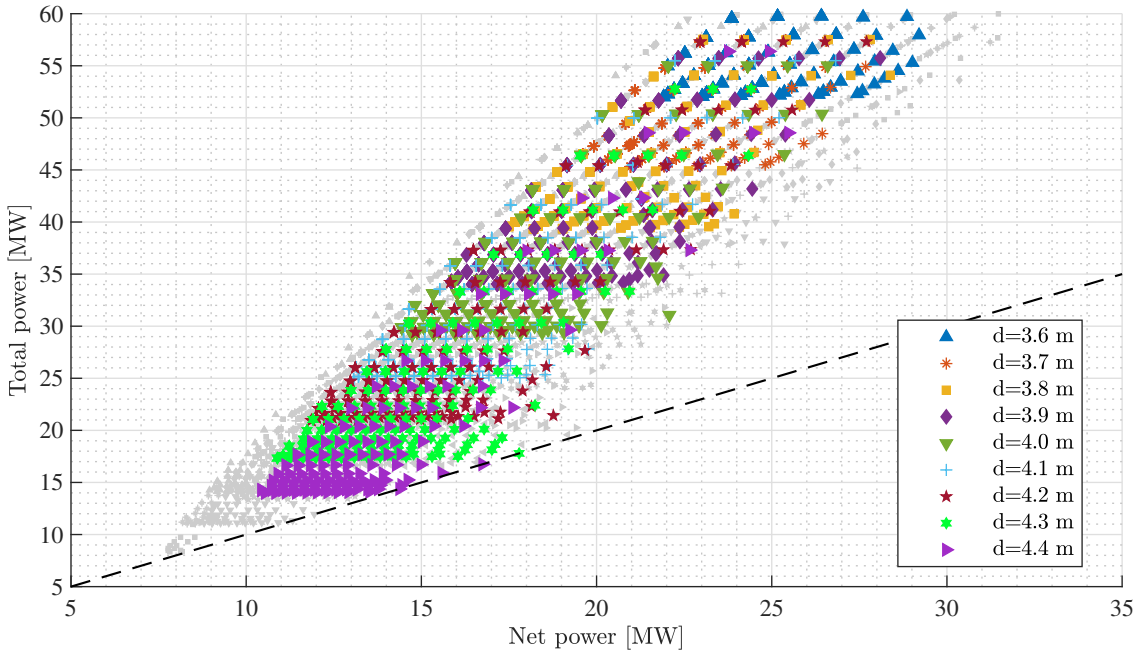

Figure B.16: Total versus required power for different cabin dimensions and compressor mass flows. Z50, $D_{tube} = 6$ m and $\dot{m}_{\pi} = 230$ kg/s.

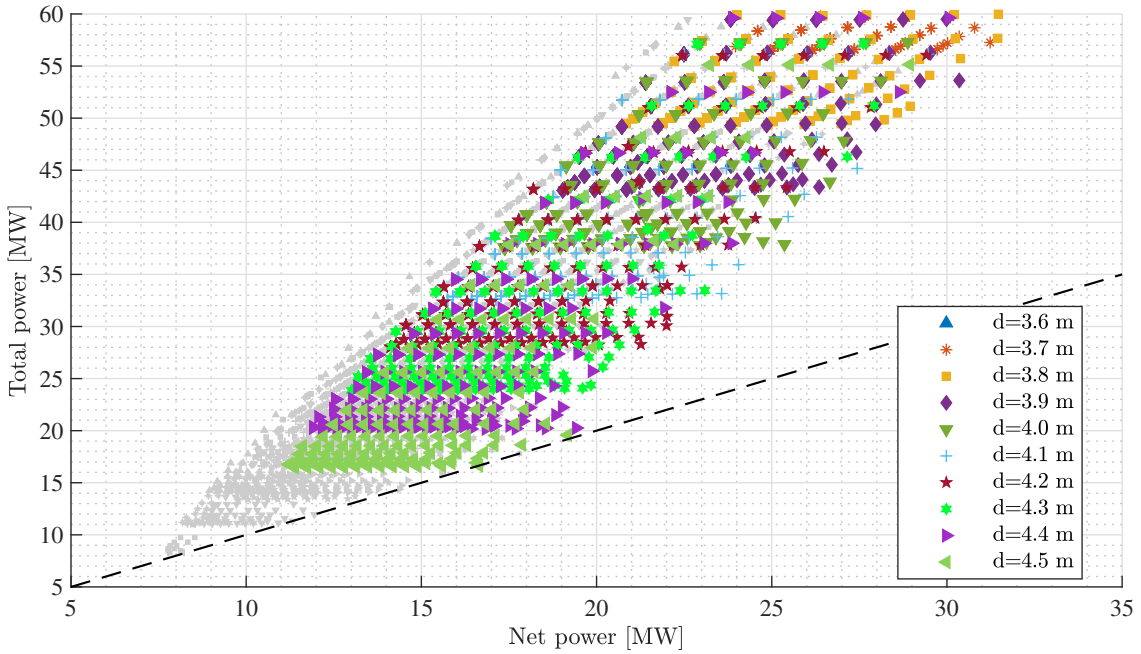

Figure B.17: Total versus required power for different cabin dimensions and compressor mass flows. Z50, $D_{tube} = 6$ m and $\dot{m}_{\pi} = 255$ kg/s.

B.5.3 Z150 and 5-meter tube

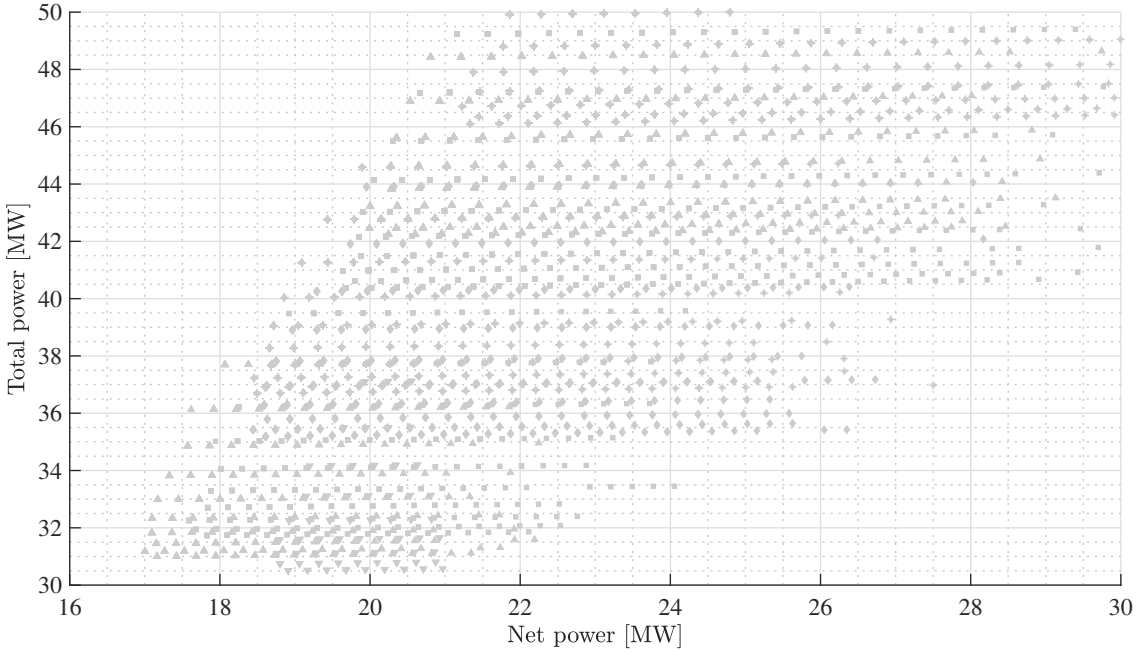

Figure B.18: Total versus required power for different cabin dimensions and compressor mass flows. Z150, $D_{tube} = 5$ m and $\dot{m}_{\pi} = 130$ kg/s.

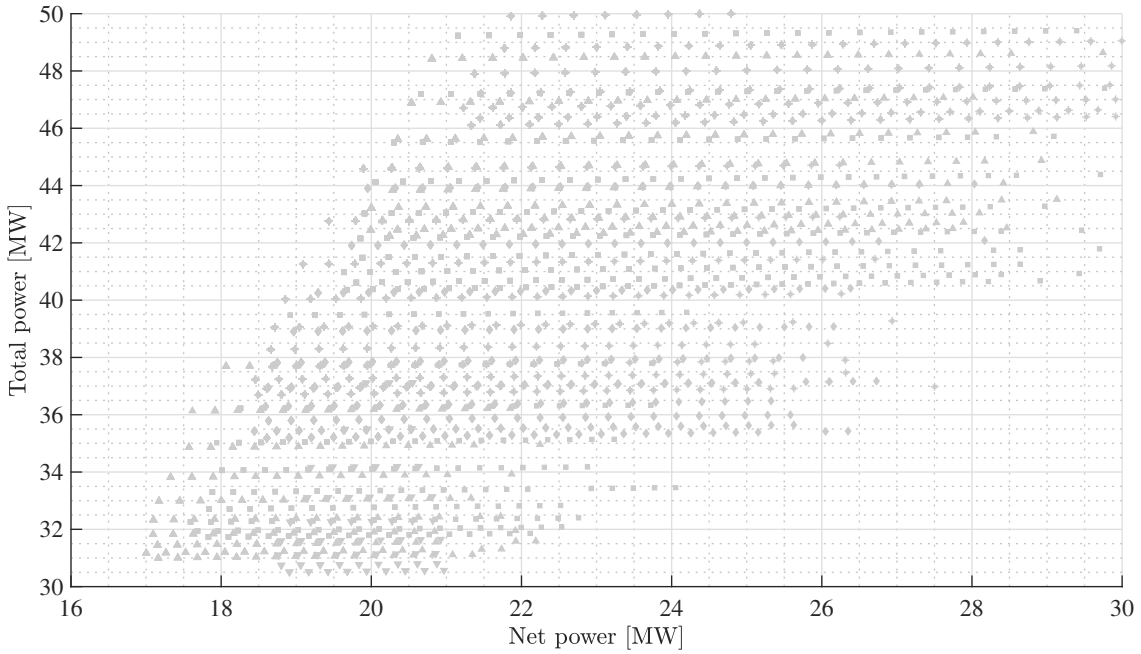

Figure B.19: Total versus required power for different cabin dimensions and compressor mass flows. Z150, $D_{tube} = 5$ m and $\dot{m}_{\pi} = 165$ kg/s.

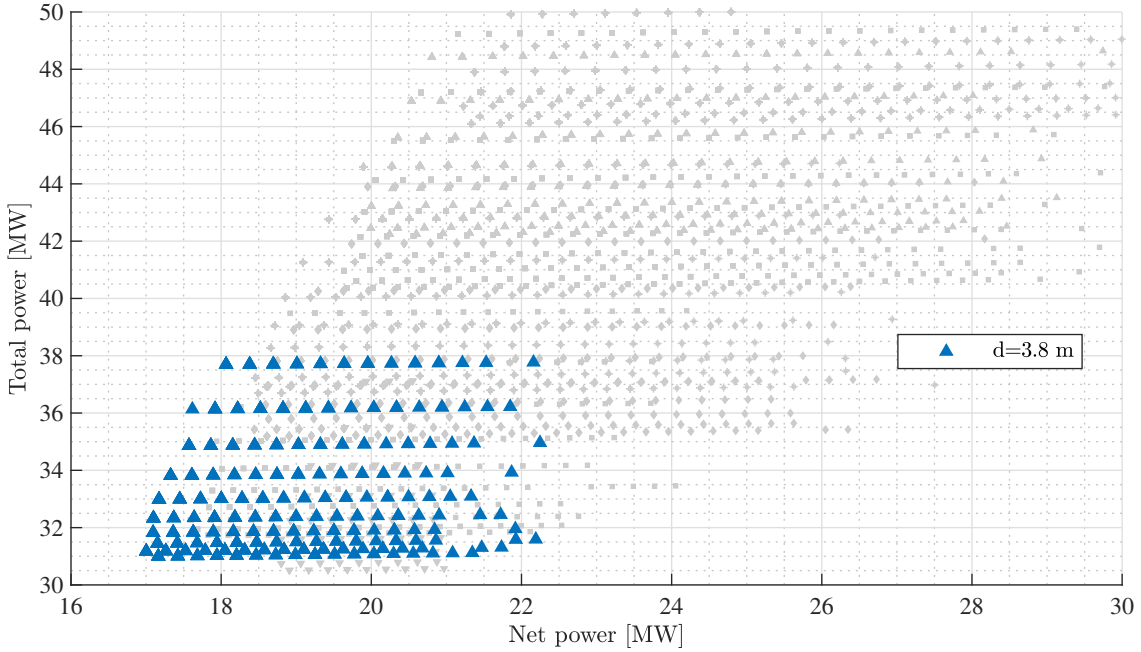

Figure B.20: Total versus required power for different cabin dimensions and compressor mass flows. Z150, $D_{tube} = 5$ m and $\dot{m}_{\pi} = 200$ kg/s.

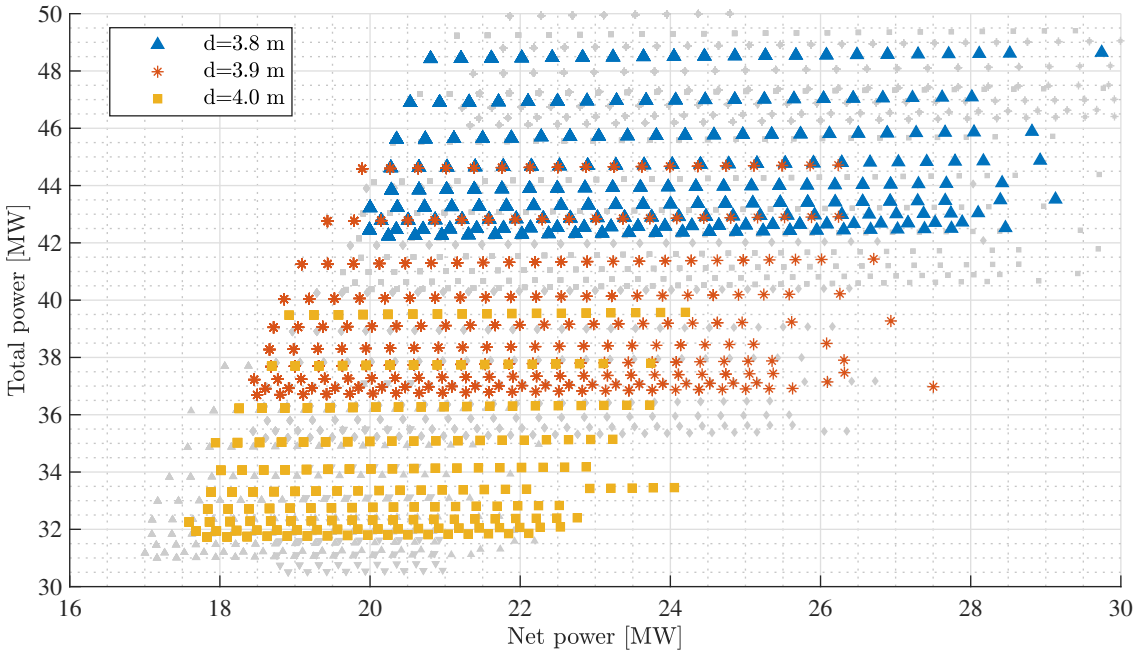

Figure B.21: Total versus required power for different cabin dimensions and compressor mass flows. Z150, $D_{tube} = 5$ m and $\dot{m}_{\pi} = 230$ kg/s.

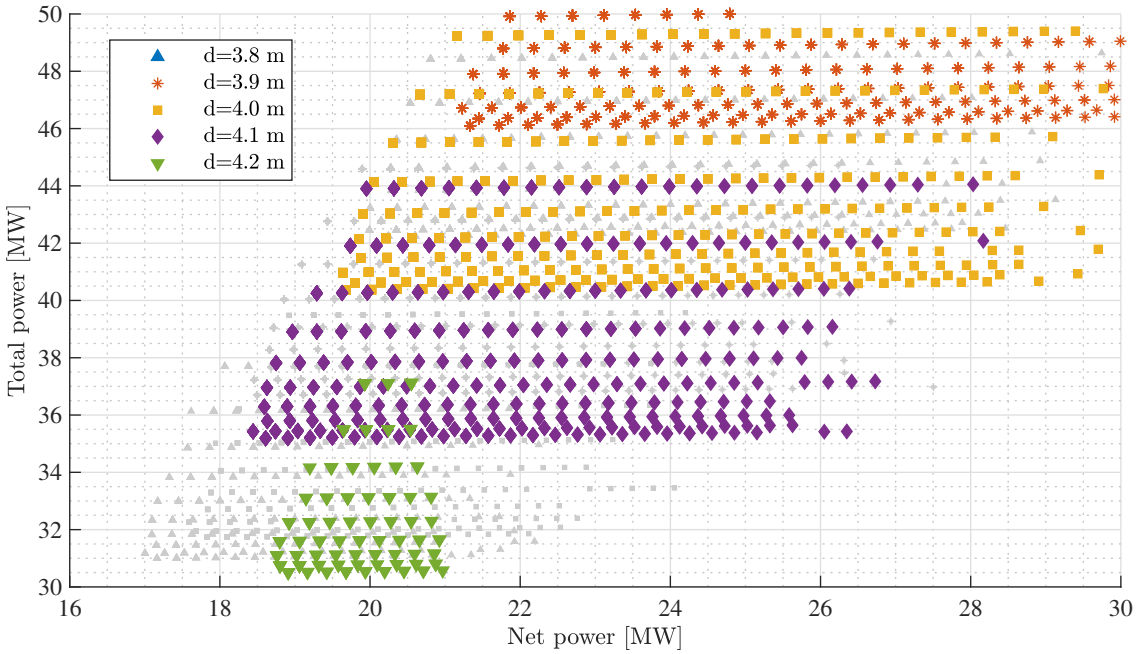

Figure B.22: Total versus required power for different cabin dimensions and compressor mass flows. Z150, $D_{tube} = 5$ m and $\dot{m}_{\pi} = 255$ kg/s.

B.5.4 Z150 and 6-meter tube

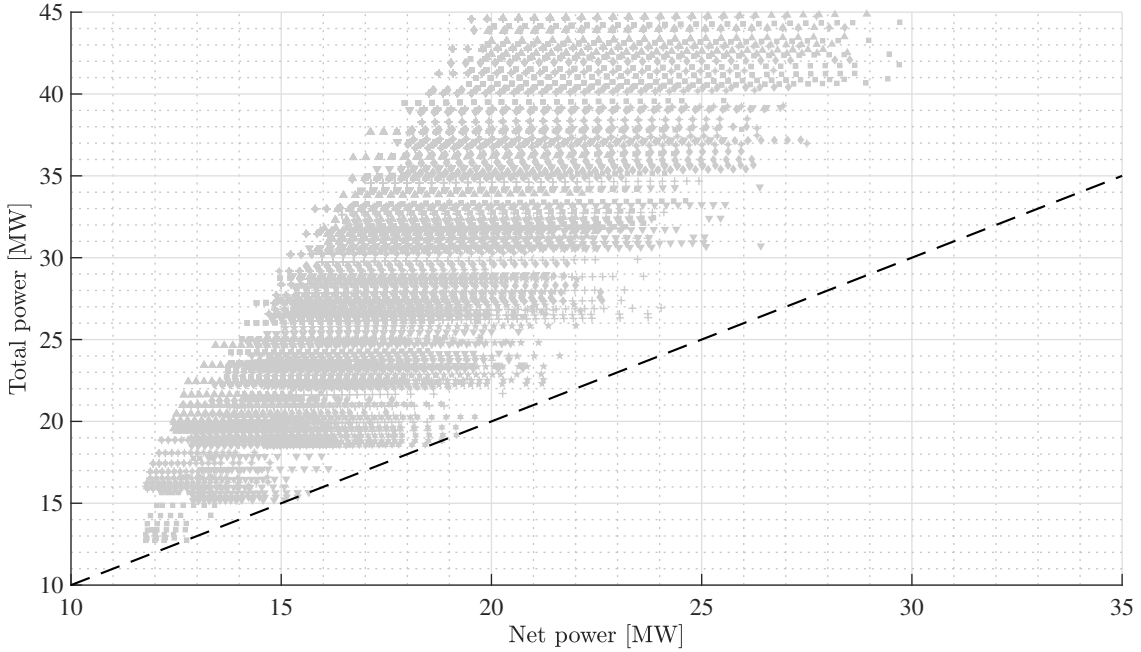

Figure B.23: Total versus required power for different cabin dimensions and compressor mass flows. Z150, $D_{tube} = 6$ m and $\dot{m}_{\pi} = 130$ kg/s.

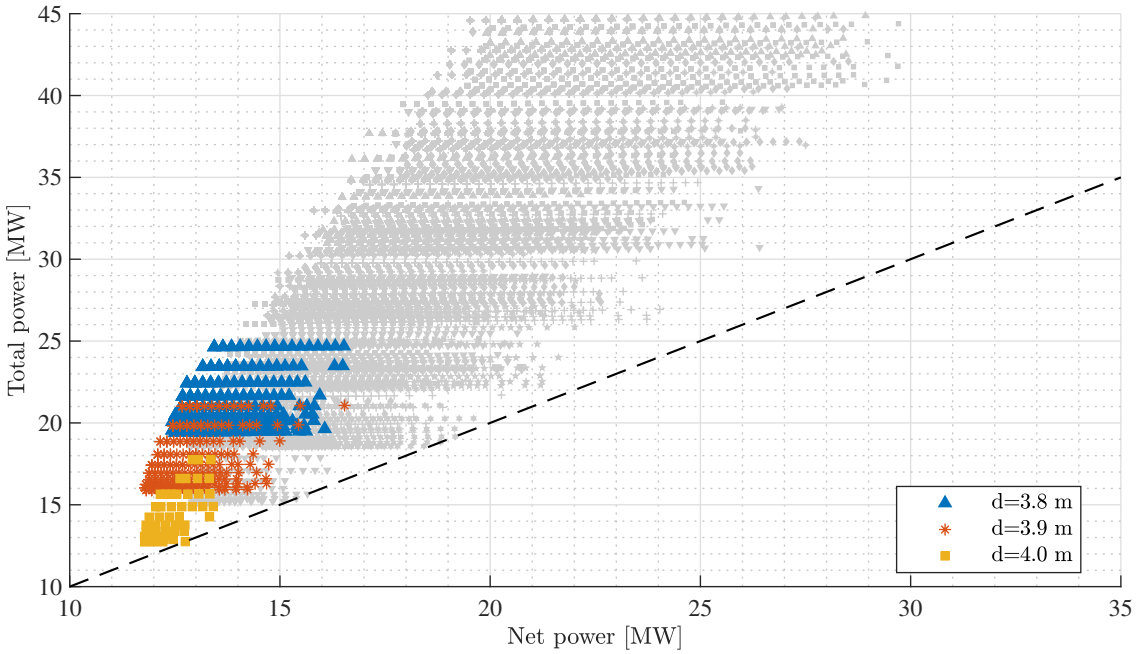

Figure B.24: Total versus required power for different cabin dimensions and compressor mass flows. Z150, $D_{tube} = 6$ m and $\dot{m}_{\pi} = 165$ kg/s.

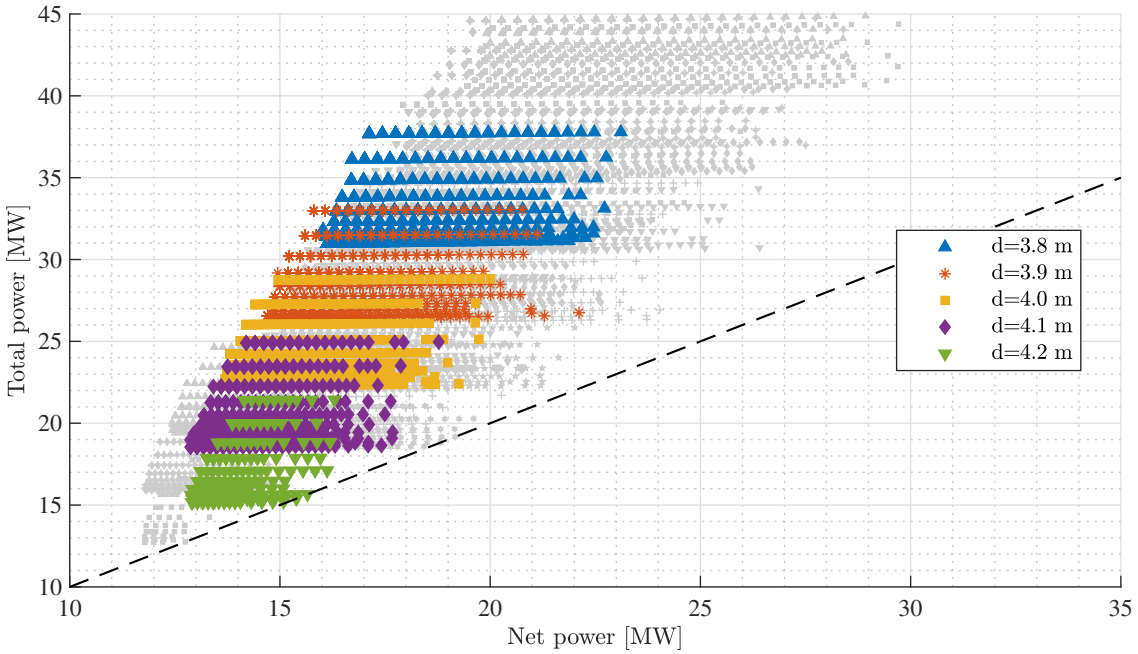

Figure B.25: Total versus required power for different cabin dimensions and compressor mass flows. Z150, $D_{tube} = 6$ m and $\dot{m}_{\pi} = 200$ kg/s.

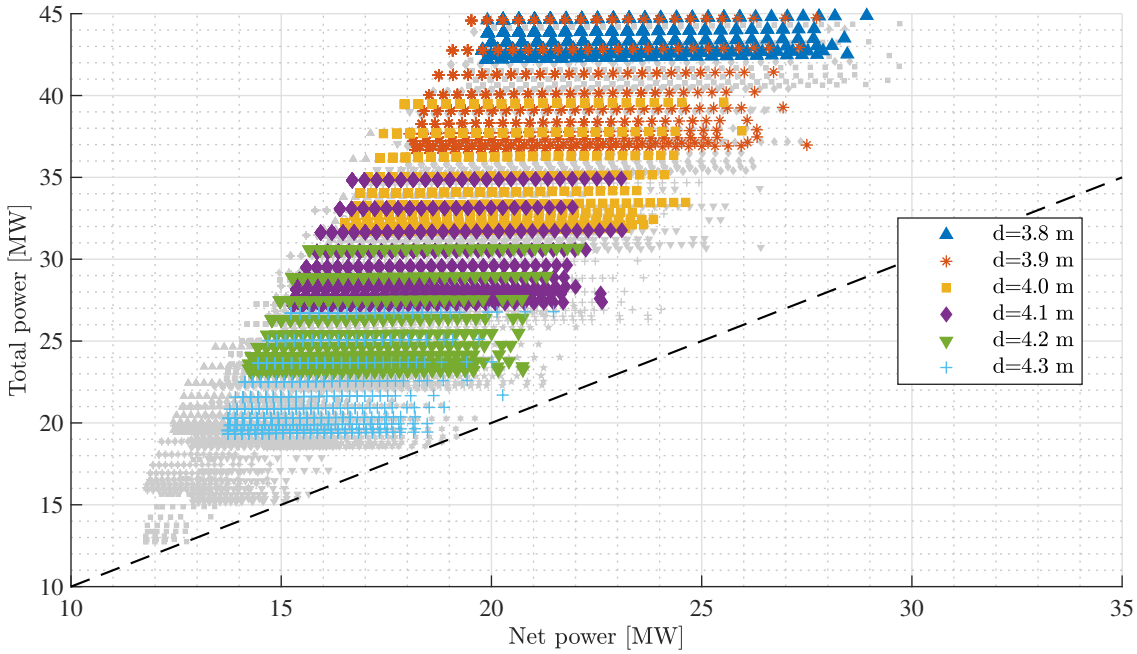

Figure B.26: Total versus required power for different cabin dimensions and compressor mass flows. Z150, $D_{tube} = 6$ m and $\dot{m}_{\pi} = 230$ kg/s.

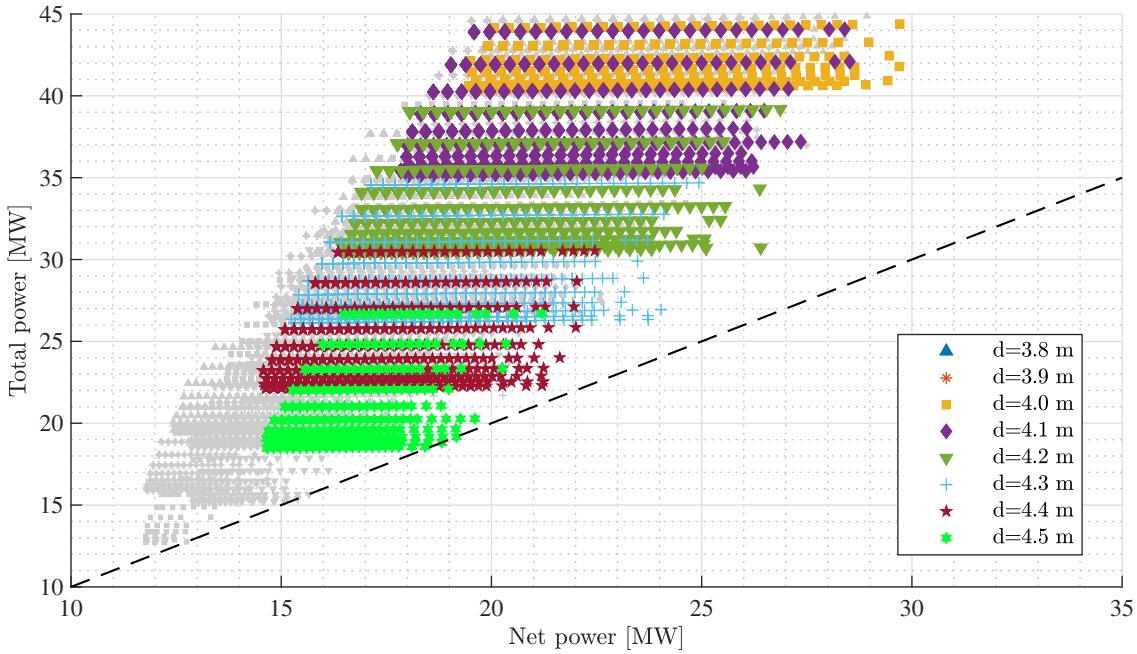

Figure B.27: Total versus required power for different cabin dimensions and compressor mass flows. Z150, $D_{tube} = 6$ m and $\dot{m}_{\pi} = 255$ kg/s.